Earthquakes and Active Tectonics of the South Caspian region, Central Asia



Neill Russell Marshall
Worcester College
University of Oxford

A thesis submitted for the degree of
Doctor of Philosophy
Michaelmas 2023

Declaration of Authorship

The contents of this thesis are my own work, except were stated otherwise. The views and opinions expressed herein are mine and not necessarily those of any other person or body unless so attributed.

Signed: 

Date: 05/10/2023

Abstract

Earthquakes and Active Tectonics of the South Caspian Region, Central Asia

Neill Russell Marshall

Worcester College

University of Oxford

Michaelmas Term, 2023

The study of earthquakes and active faulting is vitally important at multiple scales. At a local level, analysis of past earthquakes and surface ruptures provides insight and source parameters that are critically important for effective seismic hazard assessment. More regionally, understanding characteristic earthquakes and active faulting helps reveal plate tectonic motion that influences deformation and sedimentation. Globally, as populations have expanded the number of people effected by earthquakes and active faulting has increased. By working in regions where environmental conditions allow earthquake and active fault signals to be well preserved, insight into fundamental earthquake rupture processes and complex rupture patterns can be gained. I investigate single complex events, such as the 1948 Ashgabat M 7.3 earthquake, using a combination of seismic and geomorphic data. I find that this is one of the most devastating earthquakes in the 20th Century occurring on a secondary active fault with a complicated rupture. From analysis of digitised seismograms, the earthquake had a strike-slip focal mechanism and had a hypocentroidal depth of 12 km. I examine geomorphic displacements and identify active faults in Ashgabat using high resolution satellite imagery. After reviewing historical records, imagery and rupture maps, I determine that the earthquake did not rupture the main tectonic fault (Main Kopeh Dagh Fault) in the region, but a secondary right-lateral strike-slip fault southeast of Ashgabat.

Further west from Ashgabat, I look to use our understanding of active faulting to help constrain regional landscape evolution and paleoclimate signals. I investigate geomorphic displacements and stratigraphy along the Main Kopeh Dagh Fault and in the east Caspian lowlands. I build the first late-Quaternary stratigraphy in the Turkmen Kopeh Dagh and east Caspian lowlands, observing five different generations of alluvial fan deposits. I recalculate the geologic slip-rate

on the Main Kopeh Dagh Fault to 9.2 ± 1.5 mm/yr and develop a new method that uses measurements of offset drainage channels and the geologic slip-rate to constrain the timing of alluvial fan incision. I find clusters of drainage channel displacements that I date, using the slip-rates, at 2 – 3 ka, 3 – 4 ka, 8 – 12 ka, 24 – 33 ka, 38 – 52 ka, 56 – 78 ka and 94 – 130 ka. I interpret these special and temporal clusters as periods on heightened incision, providing insights into the regional environment during the Holocene and late-Pleistocene.

On the west and northwest margins of the South Caspian Basin I provide the first robust geomorphic evidence for active right-lateral strike-slip faulting. The Shirvan fault is one of several parallel to sub-parallel strands showing several right-laterally deflected stream channels and follows mud volcano alignments. I show that mud volcanoes predominately occur at fault bends and anticlinal folding along fault traces. By mapping the mud volcano distribution and alignment I estimate the total length of the fault at ~ 150 km. I estimate the slip-rate at 3.9 - 4.8 mm/yr based on a displaced terrace riser of assumed age. Two paleoseismic trenches reveal between four and six surface rupturing events. Quaternary dating constrains these events to the last 3000 years, and therefore an average recurrence of 500 – 750 years. From earthquake scaling relationships I expect rupture of the entire fault length to produce Mw 7.5 events with average slip of 3 m, which is consistent with the smaller lateral offsets (2-3 m) that I identify in imagery. However, a lack of historical earthquakes combined with inferences on fault behaviour within the fluid-rich Kura basin sediments leads to speculation that the ruptures may represent aseismic slip events. The Shirvan and adjacent strike-slip faults play an important role in accommodating tectonic plate motion at the margin of the South Caspian Basin, presenting a significant seismic hazard for communities and infrastructure in the vicinity.

Extended Abstract

Earthquakes and Active Tectonics of the South Caspian Region, Central Asia

Neill Russell Marshall

Worcester College

University of Oxford

Michaelmas Term, 2023

This thesis aims to enhance our understanding of earthquakes, active faulting and tectonics in regions of continental collision and the inherent seismic hazard that they pose. I therefore focus on eastern and western margins of the South Caspian Basin, which is an ideal environment to study past earthquakes and active faulting due to the well-preserved geomorphic surfaces and long historical records. This research centres on building records of past earthquakes and their source parameters, identifying and mapping active faults and geomorphic surfaces, with the goal of enhancing our understanding of the active tectonics and seismic hazard. Chapter 1 provides a brief introduction to the tectonics of the Arabian-Eurasian collision and provides an earthquake history within the study areas. Chapters 2, 3 and 4 presents three independent research projects with its own objectives and conclusions. Chapter 5 provides an overall conclusion to the three study projects within a regional framework.

Chapter 2 focusses on the devastating M 7.3 1948 Ashgabat earthquake. Despite the size and scale of the destruction, little is known about the style, location, and causative fault. I use a combination of seismic and geomorphic methods and historical records to locate the epicentre, calculate focal mechanism solutions, and map reported surface rupture and active faults in the area. I digitise historical seismograms and find that the earthquake was most likely strike-slip at a depth of 12 km with an estimated M_w 7.3. The earthquake ruptured a right-lateral strike-slip fault to the southeast of Ashgabat, and also reactivated a subparallel concealed thrust east of the city. The earthquake potentially also ruptured a right-lateral segment northwest of Ashgabat, which does not have an identifiable expression in the landscape. Using high-resolution satellite imagery and digital elevation models I investigate the geomorphology of

active faulting around Ashgabat and adjacent parts of the Kopeh Dagh mountain rangefront, showing that there are significant strike-slip and oblique strike-slip segments adjacent to the city that apparently did not rupture in 1948, and yet show clear geomorphic expression and potential right-lateral displacement of Parthian-era (~2000 year) and post-Sassanian era (~1500 year) archaeological remains. Luminescence dating of displaced fluvial terraces west of Ashgabat yields a vertical displacement rate of 0.6 mm/yr, though the strike-slip rate remains undetermined.

Chapter 3 focusses on the eastern margin of the South Caspian Basin. By measuring on-fault offset drainage channels and using cumulative offset probability distributions I obtain peak offsets at 23.5, 30, 88.5, 256, 402, 600, 1000 m. Using the long-term geologic slip-rate on the Main Kopeh Dagh Fault of 9.2 ± 1.5 mm/yr we provide age constraints on these peaks in offset measurements. I find peak incision occurring between 2-3 ka, 10 ka, 28 ka, 44 ka, 65 ka and 109 ka. Using satellite data and field observations, I build a Quaternary stratigraphy for ~100 km of the Kopeh Dagh rangefront and east Caspian lowlands. I also present dating results from 2017 and 2019 field campaigns in Turkmenistan. From geomorphic mapping and Quaternary dating, I constrain alluvial fan surfaces and paleoshoreline deposits on the margins of the Caspian Sea. I map two prominent shorelines at 0 m and 47 m above sea level (a.s.l.). Radiocarbon dating of marine shells in a beach deposit at 0 m (a.s.l.) yields an age of 12.5 kyrs cal BP, suggesting the 0 m (a.s.l.) shoreline was formed after the Last Glacial Maximum.

Chapter 4 focusses on the western and north-western margins of the South Caspian Basin. I find the first robust evidence for active right-lateral strike-slip faulting in this region. The Shirvan fault is one of several parallel to sub-parallel strands in the region and I find a series of right-lateral stream deflections and mud volcano alignments. Mud volcanoes occur predominantly at bends and anticlinal folding along the otherwise strike-slip trace, indicating a structural control on emplacement. From Mud volcano distribution and alignments in seismicity, I infer a total fault length of ~150 km. I estimate a minimum slip-rate of 3.9-4.8 mm/yr averaged over the Holocene, based upon a displaced terrace riser of assumed age. Two paleoseismic trenches reveal between four and six surface rupture events over the last 3000 years, a seventh prior to that, and an average recurrence interval of 500-750 years. The events are unevenly spaced in time, with a significant cluster of 2 or 3 events in the last 600 years, and much longer intervals earlier. From earthquake scaling relationships I expect rupture of the

entire fault length to produce M_w 7.5 events with average slip of 3 m, which is consistent with the smaller lateral offsets (2-3 m) that we identify in imagery. However, a lack of historical earthquakes combined with inferences on fault behaviour within the fluid-rich Kura basin sediments lead me to speculate that the ruptures may represent aseismic slip events. The Shirvan and adjacent strike-slip faults play an important role in accommodating tectonic plate motion at the margin of the South Caspian Basin, and presents a significant seismic hazard for communities and infrastructure in the vicinity.

In Chapter 5 I provide some concluding remarks from each study and discuss possible further research opportunities and directions.

Acknowledgements

Firstly, I would like to thank my primary supervisor, Richard Walker, for his unwavering support and invaluable guidance during this project. His encouragement and the opportunity he provided me to explore the world have been instrumental to my academic journey.

I also extend my heartfelt thanks to my secondary supervisors, Christoph Grützner and Mike Kendall, for their significant contributions and continuous support throughout my DPhil studies. Their expertise has been pivotal in shaping my research.

I am deeply appreciative of Ian Pierce, who introduced me to the field of paleoseismology and enriched my understanding of geomorphology and remote sensing techniques. His mentorship has been instrumental in my academic growth.

I would like to acknowledge Rich Koehler and Gordon Seitz for generously sharing their wealth of experience, knowledge, and expertise in the realms of geomorphic processes and paleoseismic investigations. Their insights have been invaluable to my research endeavours. My thanks go to James Hammond and Gerald Roberts who have acted as academic mentors and introduced me to earthquakes and active tectonics. Additional thanks go to Bob Hilton and Laura Gregory for reading, reviewing and challenging this research.

My gratitude goes to James Jackson for facilitating access to the Bullard Labs (Cambridge) library and the many interesting and helpful discussions we have had on Iranian and Caspian tectonics. I would also like to thank my colleagues at the University of Oxford, specifically, Nick Dodds, Wendy Tsai, Ben Johnson, Roberta Wilkinson, Tamarah King and Qi Ou, for their help and support during my studies.

I would like to thank my parents Graeme and Judith, as well as my sister, Grace, and brother-in-law, Stephen, for their unwavering love and support in every endeavour I've undertaken.
I want to extend my appreciation to my delightful nephews, Artie and Xander, whose presence never fails to bring a smile to my face.

Lastly, I am profoundly thankful to my partner, Lucy, who has shown tireless commitment, made numerous sacrifices, and offered unwavering love and support throughout my academic journey. Lucy has been there with me through all the ups and downs of my studies.

I am truly grateful for the guidance and contributions of these individuals, which have played a crucial role in my academic and research journey.

Dedicated to my family.

Table of Contents

DECLARATION OF AUTHORSHIP ..... **I**

ABSTRACT ..... **II**

EXTENDED ABSTRACT ..... **V**

ACKNOWLEDGEMENTS ..... **IX**

TABLE OF FIGURES ..... **XIV**

LIST OF TABLES ..... **XXII**

1 INTRODUCTION **1**

1.1 Motivation and Background 1

1.2 Geographic and tectonic setting 4

1.3 Earthquake history 5

1.4 Overview of the text 7

1.5 Publications from this thesis 8

CHAPTER 2 ..... **11**

Seismotectonic aspects of the Ms 7.3 1948 October 5th Ashgabat (Ashgabat) earthquake, Turkmenistan: right-lateral rupture across multiple fault segments, and continuing urban hazard 11

2.1 Introduction 12

2.2 Background and regional setting 13

2.2.1 Tectonics *13*

2.2.2 Earthquakes *13*

2.3 Methods 17

2.4 The October 5th 1948 Ashgabat earthquake (M7.3) 18

2.4.1 Overview and macroseismic effects *18*

2.4.2 Ruptures and surface deformation *20*

2.4.3 Published source parameters from seismology *23*

2.5 Re-analysis of the 1948 earthquake 23

2.5.1 Collection and digitisation of seismic records *23*

2.5.2 Epicentral location *25*

2.5.3 Focal depth *26*

2.5.4 Focal mechanism calculation *27*

5.5. Magnitude determination *29*

2.6 Tectonic geomorphology 30

2.6.1. Gyaursdag anticline *31*

2.6.2 Southeast of Ashgabat *31*

2.6.3 Ashgabat *33*

2.6.4 West of Ashgabat *35*
2.7. DISCUSSION 40
2.7.1 Multi-segmented rupture *40*
2.8 CONCLUSION 44
ACKNOWLEDGEMENTS 44
DATA TABLES 45
CHAPTER 3 56
CONSTRAINING LANDSCAPE EVOLUTION OF THE KOPEH DAGH, TURKMENISTAN, USING OPTICAL IMAGERY AND LONG-TERM GEOLOGIC SLIP-RATES 56
3.1 INTRODUCTION 57
3.2 GEOGRAPHIC AND TECTONIC SETTING 58
3.2.1 Active tectonics *58*
3.2.2 Geomorphology of Turkmenistan *59*
3.2.3 Late Quaternary paleoclimate of the Caspian Lowlands *60*
3.2.3 Caspian Sea level in the late Quaternary *62*
3.3 METHODS 63
3.3.1 Satellite imagery *63*
3.3.2 Fault mapping *63*
3.3.3 Geomorphic mapping *64*
3.3.4 Offset measurements *64*
3.3.5 Quaternary dating *65*
3.4 LATE-PLEISTOCENE STRATIGRAPHY OF THE KOPEH DAGH, TURKMENISTAN 66
3.4.1 Relative stratigraphy *66*
3.4.2 Slip-rate and incision age constraints *69*
3.4.3 Cumulative offset peaks *69*
3.4.3 Age control *75*
3.5 EAST CASPIAN LOWLANDS 76
3.5.1 Oglanly *77*
3.5.2 Belek Turrkmenskiy *78*
3.5.3 Kum Dag *82*
3.6 DISCUSSION 84
3.6.1 Paleoclimate in the late-Pleistocene *84*
3.6.2 Caspian Sea level *86*
3.7 CONCLUSION 86
ACKNOWLEDGEMENTS 87
CHAPTER 4 89
PALEOSEISMOLOGY OF THE SHIRVAN STRIKE-SLIP FAULT ZONE (WEST CASPIAN FAULT), AZERBAIJAN: IMPLICATIONS FOR SEISMIC HAZARD AND SOUTH CASPIAN TECTONICS 89
ABSTRACT 89

4.1 INTRODUCTION 90
4.2 GEOGRAPHIC AND TECTONIC SETTING 91
4.2.1 The Kura Basin *91*
4.2.2 The South Caspian Basin (SCB) *93*
4.2.3 Caspian Sea level *95*
4.3 METHODS 97
4.3.1 Satellite imagery *97*
4.3.2 Structure from motion (Surveys using Unmanned Aerial Vehicle) *97*
4.3.3 Geomorphic and fault mapping *97*
4.3.4 Paleoseismic Trenching *98*
4.3.5 Quaternary dating *99*
4.4 RIGHT-LATERAL STRIKE-SLIP FAULTING IN THE KURA BASIN 100
4.4.1 The Shirvan fault zone *100*
4.4.2. The Alat fault system *105*
4.4.3. Faulting inferred from mud volcanism and seismicity *108*
4.5 PALEOSEISMOLOGY OF THE SHIRVAN FAULT 108
4.5.1 Geomorphology *108*
4.5.2 Trench 1 ..... *110*
4.5.3 Trench 2 ..... *114*
4.5.4. Age control *116*
4.6 PALEO-EARTHQUAKES AND SLIP-RATE OF THE SHIRVAN FAULT ZONE 117
4.6.1. Paleo-earthquake history *117*
4.6.2. Slip-rate estimate *122*
4.7. DISCUSSION 122
4.8 CONCLUSION 127
ACKNOWLEDGEMENTS 127
DATA TABLES 129
5 CONCLUDING REMARKS 131
5.1 CONCLUSIONS FROM THE THESIS 131
5.2 SUGGESTIONS FOR FUTURE WORK 132
REFERENCES 134

Table of Figures

Fig. 1.1	Map showing earthquakes, black dots from the International Seismological Centre-Global Earthquake Model (ISC-GEM) catalogue from 1904 – 2014 with magnitudes > 5.0 (Di Giacomo et al., 2018) and plate boundaries (red) defined by the USGS.	2
Fig. 1.2	SRTM 30 m DEM showing active faults (white lines), black arrows show the GNSS velocity vectors (Khorrami et al., 2019), the black boxes indicate the three study areas and main fault structures in the region.	3
Fig. 1.3	SRTM 30 m DEM showing active faults (white lines), GNSS velocity vectors (Khorrami et al., 2019), earthquake locations from Ambraseys and Melville (1982) (white dots) between 3000BC – 1954, earthquake locations and focal mechanisms from ISC-GEM catalogue (coloured by depth and sized by magnitude).	5
Fig. 2.1	Tectonic map of the Arabian/Eurasian plate collision zone. Black arrows represent GPS velocity vectors after Khorrami et al., (2019) relative to Eurasia. Waveform-modelled focal mechanism solutions and locations for earthquakes greater than Mw 3.5 between 1917 and 2017 from the catalogue created by Wimpenny and Watson (2020); black lines show active faults in the region (Walker et al., 2021). Digital Elevation Model (DEM) from SRTM 90m. Main Kopeh Dagh Fault zone – MKDF; South Caspian Basin – SCB.	12
Fig. 2.2	(A) Hypocentral locations of earthquakes between 1929 and 2019 scaled by magnitude with 90% confidence interval (Table 2.2). Locations are calibrated using the Hypocentroidal Decomposition technique. The earthquakes are coloured by focal depth. DEM is from SRTM 30 m. (B) Hypocentre location of the 1948 Ashgabat earthquake located using the ISC phase arrival data (black dot) (Table 2.1); the ISC phase arrival data combined with phase arrivals from the digitised waveforms (blue) (Table 2.1); coloured circles are the calibrated earthquake locations calculated using the hypocentroidal decomposition relative relocation method and sized relative to magnitude (Fig 2.2A). Dotted blue lines represent confidence intervals showing a measurement of the error in the location. DEM is from SRTM 30m.	14
Fig. 2.3	Ashgabat region showing reported earthquake ruptures. Black lines are active faults (mapped by the authors) and red lines are 1948 ruptures digitised from the Gorkoshev 1949 geologic study (Rogozhin, 1994). Difficulties in georeferencing means that the rupture locations should be used as an approximate guide only. The ruptures are separated into three main areas of rupture (A, B, C). MSK isoseismal contours are from Berberian and Yeats (2001), who combined several other sources along with their own intensity observations in Iran.	17
Fig. 2.4	(a) Oblique view to the ESE from a viewpoint above Asgabat (Fig. 2.3) showing the Gyaursdag anticline in the foreground and the Manysh syncline behind. The axis of the Gyaursdag fold are shown in yellow, and the Kharvardagh right-lateral fault in red. (b) Apparent bedding-slip thrusts within the northern limb of the Gyaursdag fold near	

	Yashlyk. (c and d) Satellite image of Kuru Gaudan showing ruptures associated with the 1948 earthquake (Tchalenko, per. Comm.)	20
Fig. 2.5	(a) Global coverage of first motion data from ISC records and ISS bulletins (red) and from waveforms digitised within this study (blue). Dots represent the station location, with lines showing the azimuth from the event. (b) Global coverage of stations that have digitised waveforms used for amplitude ratio focal mechanism calculation.	22
Fig. 2.6	Focal Mechanism beach-ball lower hemisphere projection for first motion polarities of P-wave arrivals. Blue triangles are compressions; Red triangles are compressions; grey nodal planes are a random sample of 1000 solutions within 1% of the maximum probability of the Bayesian inversion; purple nodal plane represents the best fit.	26
Fig. 2.7	Amplitude ratio focal mechanism results with fixed strike at 120 ° and depth at 12 km. Dip and rake are calculated at 10 ° and 20 ° increments, respectively. The mechanisms are scaled by the misfit to the model, with larger mechanisms having the lowest misfit.	28
Fig. 2.8	(a) Heritage Corona imagery from 1967 showing the region from Nisa in the northwest, to Nokhandan in the southeast (see Fig. 2.3 for location). Major fold axes are shown in yellow, and active faults in red. Three landslides south and west of Manysh are marked in green. Areas shown in later panels are marked. (b) aligned right-lateral stream displacements marked by white arrows. (c-d) Apparent qanat offsets of ~5 m. (e) Possible fault scarp south of Ashgabat, running between thick white arrows, with a further potential qanat offset marked by a thin white arrow.	31
Fig. 2.9	(a) Pleiades-derived DEM showing post-earthquake mapped ruptures southeast of Ashgabat (yellow lines) adjacent to two scarps with cumulative right-lateral displacement of minor drainage channels within an incised alluvial fan surface, which we infer to be the scarps that ruptured in the earthquake. The resolution of the georeferenced mapped ruptures is low, and these may not exactly locate the ruptured fault. Towards the top of the image, a third fault scarp with clear up to the north displacement is visible, but does not appear to have ruptured at the surface in 1948. (b) Close-up of the two fault scarps with cumulative right-lateral stream displacements marked.	29
Fig. 2.10	World View 3 DEM of the Ashgabat area. White triangles show limits of folding as identified from topographic profiles. The red triangles show offset qanats (c.f. Fig. 8c-d).	34
Fig. 2.11	**(A)** DEM derived from WorldView 3 stereo imagery of the ancient city of Nisa. Triangles delineate the fault trace of the right-lateral MKDF. Box shown in (B). **(B)** Shows the zoomed DEM of the archaeological site New Nisa. The west wall shows an apparent offset at the fault trace. Profiles A-A' and B-B' show a scarp at the fault trace	35

	(at triangles). **(C)** Clipped (B) along the fault trace. Restoring the west wall of New Nisa measures at 20.1 m.	
Fig. 2.12	(A) Pleiades DEM and geomorphic map of the region just to west of Ashgabat. Profiles show elevation taken from the DEM. The oldest geomorphic surface was sampled and IRSL ages calculated. Q5 is dated at 99-103 +/- 11k years (see text). (B) Photograph taken looking East at the sample site (white dot) on the Q5 surface shown in A. (C) Photographs taken facing west at the sample site in (A).	37
Fig. 2.13	Perspective view looking west across the Main *Kopeh Dagh* fault, running between the thick white arrows, ~5 km northwest from the region shown in Fig. 12a (centre coordinate at 38.072590N, 57.975358E, see Fig. 3 for location). The fault trace cuts across hillslopes (scarps shown by vertical white arrows) and has right-laterally displaced the lower portions of the hillslopes, which now form shutter ridges. Drainage channels (blue) are displaced by ~150 m around the ends of these shutter ridges.	38
Fig. 3.1	Neotectonic map of the eastern Caspian lowlands showing the north-eastern edge of the Arabian-Eurasian collision zone. Motion on the faults indicates westwards extrusion of the South Caspian Basin. Topography is from SRTM (30 m resolution), GNSS velocity vectors – black arrows (after Khorrami et al., 2019), active faults – black lines (adapted after Walker et al., 2021 and Dodds et al., 2022).	58
Fig. 3.2	SRTM DEM (30 m resolution) of a 100 km segment of the Main Kopeh Dagh Fault with Quaternary alluvial fans mapped according to relative age. Black lines – active faults; yellow dots – offset drainage measurement sites; alluvial fan stratigraphy shown in the bottom left insert. Topographic profiles are from SPOT 6 stereo imagery derived DEMs. Blue dotted line is the 47 m (a.s.l.) elevation contour extracted from the SRTM DEM.	66
Fig. 3.3	Panel A shows WorldView 2 panchromatic optical imagery. Topographic profile C-C' is taken from the SPOT 6 stereo DEM. We show speculated fault locations and geometries on the topographic profile. Panel B shows the alluvial fan stratigraphy mapped using a combination of optical and DEM data. Active faults are the black lines with yellow dots showing the offset measurements. Active faults are also mapped using a combination of satellite optical and DEM data.	67
Fig. 3.4	Panel A shows WorldView 2 panchromatic optical imagery. Topographic profiles A-A' and B-B' are taken from the SPOT 6 stereo DEM. White lines show fault trace and dotted yellow line shows a speculated anti-form axis. White arrows show the location of dextral offset drainages. Panel B shows the alluvial fan stratigraphy mapped using a combination of optical and DEM data. Active faults are the black lines with yellow dots showing the offset measurements. Profile A-A' shows a topographic profile perpendicular to the strike of the MKDF, the fault geometry is speculative showing the location along the profile. Profile B-B' runs parallel to strike of the MKDF. It shows the	68

	elevation of the alluvial fan units Qaf 2 – Qaf 5. Older exposed surfaces are at higher elevations, we speculate these were abandoned, incised and uplifted.	
Fig. 3.5	Offset drainage channels across the Main Kopeh Dagh Fault. Panel A shows WorldView 2 pansharpened false-colour composite satellite image showing the MKDF (red arrows). Yellow dots show IRSL sample sites from Walker et al. (2021). Panel B shows the relative alluvial fan units Qaf 1 – 5 (Figs 3.3 and 3.4). Black lines show the fault trace, yellow dotted line shows the thalweg offset by the fault, blue dotted lines are the nearest risers and the distance between these represents a minimum offset measurement, red dotted lines are the furthest risers representing a maximum offset measurement.	69
Fig. 3.6	Simplified alluvial fan, incision and faulting schematic model for drainage channel offset measurements. Panel A shows alluvial fan deposition out of a catchment occurring during cooler and arid climatic conditions, the fan buries the active fault trace. Panel B shows the fan being incised by multiple drainages and the formation of a main channel during wetter climatic periods. Panel C shows the right-lateral movement on the fault beheading the drainages and offsetting the main channel through the alluvial fan. The main drainage is diverted along strike of the fault. The fault moves with a slip-rate, from this rate and measured offsets the minimum incision timing can be determined.	72
Fig. 3.7	Panel A is an active fault map of the Main Kopeh Dagh Fault on SRTM derived DEM. Yellow dots show measured offset drainage and terrace riser sites. The white bracketed measurements are displayed on panel D. Panels B, C and D show the measurement method at two different sites shown on panel A. The blue lines are linear traces of the thalweg – this is our best offset measurement; the yellow lines trace the closest offset risers – representing the minimum offset; the red lines are the furthest risers – representing the maximum possible offset. Panel E shows the triangular Cumulative Offset Probability Distribution (COPD) for the section of the fault detailed in A. We show the combined COPD in Fig. 3.8 used to determine peaks in the COPD.	73
Fig. 3.8	Shows the combined COPD results from our offset measurements. Quality has been assessed to each individual measurement as per the methods section. We see seven peaks in offset displacement at 23.3 m, 30 m, 88.5 m, 256 m, 402 m, 600 m and 1000 m. The number of measurements decreases as the offset displacement increases.	74
Fig. 3.9	SRTM DEM (30 m resolution) of the East Caspian lowlands in Turkmenistan. The blues contours are at 0 m (a.s.l.) and 47 m (a.s.l.) and have been extracted from the SRTM DEM. We observe shoreline morphology at these contours that are from Caspian Sea highstands at 11-13.5 ka (0 m asl) and 33 - 35 ka (47 - 50 m asl) ((Leroy et al., 2020).	75
Fig. 3.10	Panel A is a Bing Aerial image of the study area near Oglanly (Fig. 3.8). We observe two scarps and have sampled sediments for IRSL dating. Panel B shows a geomorphic map and we observe five different alluvial fan surfaces (Qaf 1-5). Yellow dots show sample sites. Panel C shows sample site TK19 – 01/02/03.	

		77
Fig. 3.11	Panel A shows a Bing Aerial image of a shoreline sample site between Balkanabat and Turkmenbashi (Fig. 3.8). The blue contour lines show elevation at 0 m (a.s.l.) and 47 m (a.s.l.), the contours are at paleoshorelines. Panel B shows the Quaternary stratigraphy of the area. Qaf 1 – 4 are alluvial fan deposits; Qb 1 - 4 are beach deposits; and Qla is a lacustrine deposit. Age relationships are determined by elevation and cross-cutting relationships. Shorelines follow the 0 m and 47 m (a.s.l.) contours. Dated shells from Qb2 give a maximum age of 12.74 k cal. BP and are consistent with the end-Pleistocene high stand. Panel A shows a Bing Aerial image of a shoreline sample site between Balkanabat and Turkmenbashi (Fig. 3.8). The blue contour lines show elevation at 0 m (a.s.l.) and 47 m (a.s.l.), the contours are at paleoshorelines. Panel B shows the Quaternary stratigraphy of the area. Qaf 1 – 4 are alluvial fan deposits; Qb 1 - 4 are beach deposits; and Qla is a lacustrine deposit. Age relationships are determined by elevation and cross-cutting relationships. Shorelines follow the 0 m and 47 m (a.s.l.) contours. Dated shells from Qb2 give a maximum age of 12.74 k cal. BP and are consistent with the end-Pleistocene high stand.	78
Fig. 3.12	OxCal v4.4.4 probability distribution of calibrated age results from the Ap17-1a and b using the Marine20 curve.	79
Fig. 3.13	A – Radiocarbon sample site for Ap17-1a/b, beach gravels and quarry site. B – shells sampled from beach gravels in A. C Shoreline deposit showing cross bedded gravels and sands capped with horizontal beach gravels. Interpreted as paleoshoreline at 47 m (asl).	80
Fig. 3.14	Panel A is a Bing Aerial image of the sample site to the southeast of Kum Dag (Fig. 3.8). Panel B shows the Quaternary stratigraphy and three generations of alluvial fan deposition (Qaf 1-3). We sampled sediments at the sample site (yellow dot) and use IRSL to constrain the age of deposition.	81
Fig. 3.15	Benthic $\delta^{18}O$ ($^{0}/_{00}$) curve for the last 150 kyrs (Lisiecki and Raymo, 2005). Yellow dotted lines show Marine Isotope Stages and black bars show sub-stages. Grey blocks show minimum, best and maximum incision ages from peaks in the cumulative offset probability distribution (COPD) in Fig. 3.7 and Table 3.1. Red line is the age from the best measurement.	85
Fig. 4.1	**A:** Tectonic map of the South Caspian Basin. Black arrows show GNSS velocity data relative to Eurasia is after Khorrami et al. (2019). Thick black lines are faults mapped in this study, black lines with teeth are active thrust fault, thick dark grey lines are from Walker et al. (2021), and thin light grey lines are taken from the Neotectonics Group, Moscow active fault map (Zelenin et al., 2022). The map shows the northern zone of Arabian-Eurasian collision with the main fault zones named in the white boxes. The	

	yellow box is our study area. Note that GNSS velocity vectors drop significantly north of the Greater Caucasus. The motion of the GNSS and on the faults shows the westward extrusions of the South Caspian Basin and the subduction beneath the Alborz and Talesh. **B:** Velocity triangle showing motion of the South Caspian Basin relative to Eurasia (Dodds et al., 2022b). The Turkish-Iranian Plateau (TIP) motion is determined by averaging GNSS velocity vectors from Khorrami et al. (2019) relative to Eurasia. Solving between these two vectors gives SCB-TIP motion of 7.5 mm/yr. **C:** Takes the average strike of the Shirvan Fault (345º) to solve for the shortening (7.2 mm/yr) and 1.9 mm/yr of right-lateral shear.	90
Fig. 4.2	A - Seismotectonic map of Azerbaijan and Trans-Caspian region (inset). GNSS velocity vectors are from Khorrami et al. (2019), relocated seismicity is from Gunnels et al. (2021), and focal mechanisms are taken from the ISC catalogue. Black lines show the major faults and light grey shows active faults from Zelenin et al. (2022). Digital elevation data is from SRTM (30 m resolution) and Bathymetric data is from the Global Oceans (https://www.gebco.net/data_and_products/gridded_bathymetry_data/). B – Dotted black line show lineation of mud volcanoes in five main areas (1a – Shamakhi to Shirvan, 1b – Salyan to offshore South Caspian Basin, 2 – offshore southwest Alat, 3 – Alat (NW-SE) trend, 4 – north Alat offshore). Trend 5 is a linear NNW-SSE trend is seismicity with strike-slip focal mechanisms.	91
Fig. 4.3	Active faults in the Shirvan region and GNSS velocity vectors for the area (after Khorrami et al. 2019). Brown triangles show the location of active mud volcanoes, black lines show the fault mapping in this study, grey lines are active faults from Zelenin et al. (2022). The blue line shows the 0 m above sea level (a.s.l.) contour which is dated at 11,000 – 13,500 years BP. Highlighted on this map are four study areas (see below). Elevation data is from SRTM and has been overlaid on to a Google Earth image.	95
Fig. 4.4	NNW-SSE striking strike-slip faulting between Shirvan and Shamakhi (Fig. 4.2). A - shows reverse and strike-slip faulting on Bing Aerial imagery. Mud volcanoes form in a lineation along fault strike. B – Pleiades stereo DEM showing a linear break in slope that crosscuts topography. The faulting forms a sharp linear scarp through the mud volcano at the SSE of the panel.	100
Fig. 4.5	Rupture map from Shirvan. Panel D shows the rupture trace in three strands that have created scarps in the topography. The topographic profile XX' shows the scarps. There is also an offset drainage along strike of the rupture trace at the NW of the panel. Pleiades satellite derived DEM at 1 m resolution. Panel B shows the rupture trace and a transpresional step-over (pop-up) structure. Panel C – rupture trace showing scarps and trantensional pull-apart basin where there is a step-over in the rupture trace. This is seen	

	in the topographic profile YY'. Panel D – two rupture traces, scarp and offset drainage channels with measurements between 5m and 22m. Scarps can be seen in the topographic profile ZZ'.	101
Fig. 4.6	Pleiades derived DEM of the Salyan region of the Shirvan fault zone. White lines delineate active faulting from our field and remote mapping. We see the fault bend from a N-S to NW-SE trend. We see antithetic R' sinistral faulting (Fig. 4.7). Trench site is shown in the yellow box on panel B. Blue lines on inset panel show 0 m a.s.l.	102
Fig. 4.7	Field photographs of the Shirvan fault zone. A and B show two offsets at the Shirvan site in Fig. 4.5 (d). Panels C and D are oblique drone images of the trench site at Salyan (Fig. 4.6). E shows the 7.5 m offset riser. F shows an oblique drone image of antithetic left-lateral faulted vertical bedding planes.	103
Fig. 4.8	Fault trace near Alat (Fig. 4.3) shown on ERSI imagery. Shutter ridges, deflected drainage channels and scarps can be seen on panels B and C. We see a mud volcano near to the fault trace. Motion determined by offset drainages is consistent with dextral strike-slip faulting.	104
Fig. 4.9	Northwest of Alat (Fig. 4.3) ERSI imagery showing fault scarps, offset drainages and a mud volcano at the NW end of the panel. Panel B shows a fault scarp with offset drainage channels. Panel C shows two parallel fault scarps and offset drainage channels. The offset drainage channels indicate a dextral motion of the fault. Panel D shows an oblique drone image of faulting. It shows offset drainages, scarps and mud volcanoes.	106
Fig. 4.10	UAV derived DEM of the trench site near Salyan on the Shirvan fault zone. Panel 1 shows a geomorphic map and the fault trace. Panel 2 is a hillshade of the UAV DEM showing the sample site, Trench 1 and Trench 2. We see a dextral riser offset of 53 m. Profile AA' shows the marine terrace at an elevation of 0 m a.s.l. Panel C shows a slope map of from the UAV DEM data, showing the offset Qt1 riser and Qt1 tread. The matched riser profiles are restored using LaDiCoaz method, the result is shown in panel D showing a 7.5 m offset.	108
Fig. 4.11	Trench 1 – photo-orthomosaic and trench log of the NNW wall of Trench 1 (Fig. 4.6). The trench has two fault zones (F1 and F2) and seven possible events (E1-7).	111
Fig. 4.12	Trench 2 – photo-orthomosaic of the NNW wall of Trench 2. Trench log shows fluvial sediments in the Qt1 surface (Fig. 4.6). There are two fault zones (F1 and F2) and up to three events (E1-3).	114

Fig. 4.13	Event evidence from trenches 1 and 2. Units and event labels are consistent with the trench logs in Figs *4*.11 & *4*.12. Trench 1 has evidence for at least 4 and up to 7 events. Ages are from IRSL and radiocarbon dating techniques (Tables *4*.1 & *4*.2).	117
Fig. 4.14	Stratigraphic log of the sample site, Trench 1 and Trench 2. Unit descriptions in the text section 3.2.1. Red and blue lines show sediment ages that match at the different trenches.	120
Fig. 4.15	Offset drainage measurements along fault strike in the Shirvan and Salyan sections. Blue circles are offset measurements and yellow line shows the Shirvan fault trace.	123
Fig. 4.16	A – Fault 1 (F1) Trench 1 (Fig. *4*.11) IRSL sample locations detailed in the trench log. B – Fault 2 (F2) Trench 2 (Fig. *4*.12) IRSL sample locations detailed in trench log 2 (Fig. 12). C – Shell in situ taken from the top of U60 in Trench 1 (Fig. 11) calibrated ages in Table *4*.2. D – photo of sample pit wall (Fig. 6) with a charcoal burn layer sampled and dated using radiocarbon (Table 2). E – close photo of removed (C) in tact shell from U60. F – Close up photo of burn layer in D.	125

List of Tables

2.1	Phase arrival times from the 1948 Ashgabat earthquake from a global network of seismometers constructed from the ISC Bulletin database (International Seismological Centre, 2022) and the digitised waveforms.	43
2.2	Earthquake catalogue showing the location, depth and magnitude of relocated events using the MLOC method of Hypocentroidal decomposition.	47
2.3	Polarity data used to calculate focal mechanism solutions from the first arrival data. The table shows if the record has come from digitised seismograms or/and from the ISC catalogue (International Seismological Centre, 2020). Station locations are taken from Charlier and Van Gils (1953), and International Seismological Centre (2020). Take-off angles are calculated using Pho and Behe (1972).	51
2.4	Inferred Stimulated Luminescence results from sediments taken from terrace site at 38.043°N/58.026°E. A 1.2m sample pit was excavated in the Q5 surface (Fig. 2.12), sediments were sampled at depths above.	52
3.1	Shows the alluvial fan age based on slip-rate and peak fault offset displacement measurements shown in *F*igs *3.6* and *3.7*. We show the alluvial fan ages for the long-term geologic and geodetic slip-rates (*this study* and Dodds et al. (2022), respectively).	70
3.2	Calibrated radiocarbon carbon ages at the sample location (Figs 9 & 10). The table shows the raw ages and calibrated date range using the Marine20 curve and ΔR value from sites around the Caspian. Samples are from shoreline deposits at 39.9327ºN/58.8723ºE, 0 m (asl).	76
3.3	Infrared Stimulated Luminescence results from sediment samples taken from alluvial fan sites at listed locations showing calculated group ages.	79
4.1	Shows the location and age of the IRSL samples from trenches 1 and 2. The location in the cross section is shown in Figs 4.11, 4.12, and 4.13.	122
4.2	Shows the location and type of material sampled for radiocarbon dating. The ages have been calibrated using the OxCal v4.4.4 model using the Marine 20 curve and delta R adjustment from previous studies around the Caspian Sea.	123

1 Introduction

1.1 Motivation and Background

In the past century, there has been an exceptional increase in urban expansion in regions prone to earthquakes within the continents (England and Jackson, 2011). In contrast to areas near the edges of oceans, where earthquake hazards are typically concentrated in narrow zones along tectonic plate boundaries, the occurrence of active faulting within the interiors of continents is spread across extensive areas (Fig. 1.1). Moreover, significant periods, ranging from hundreds to even thousands of years, can pass between occurrences of large earthquakes in any given region. These lengthy intervals between events present difficulties in identifying active faults (e.g., Grützner et al., 2017). Furthermore, our understanding of fault rupture processes within such areas is constrained by the scarcity of available data concerning recent significant earthquakes. (e.g., Hamling et al., 2017).

Understanding the attributes of previous earthquakes provides valuable insights into the dynamics of plate tectonics, ongoing fault activity, and the inherent seismic hazard. In areas where earthquakes are infrequent but have a historical pattern, it becomes crucial to maximize our understanding of documented seismic incidents. Nevertheless, it is often encountered that historical records are either sparse or non-existent, necessitating the analysis of landforms and geomorphic features to uncover indications of prior earthquakes.

In regions where the intervals between large earthquakes is long, relying solely on instrumental seismic data might prove inadequate in fully assessing potential hazards. This limitation poses challenges for making informed decisions in engineering design, urban planning, and risk mitigation. Creating reliable hazard assessments for regions within continents hinges on precise mapping of active faults, combined with establishing limits on the potential highest magnitudes and the average time spans between consecutive occurrences (e.g., Field et al., 2014).

The South Caspian region presents unique opportunities for investigating ongoing tectonic activities and the evolution of landscapes. The pristine and comparably dry natural

surroundings provide optimal circumstances for conserving geomorphic features and earthquake surface ruptures (e.g., Dodds et al., 2022a). This environment allows us to construct records of earthquake occurrences and observe active fault behaviour directly from the landforms.

Furthermore, the South Caspian region hosts several significant tectonic fault structures (Allen et al., 2004; Forte et al., 2010; Jackson et al., 2002; Walker et al., 2021) that are not fully understood. This thesis focuses on two of these faults, the Main Kopeh Dagh Fault (Turkmenistan) and the Shirvan Fault zone (Azerbaijan) (Fig. 1.2).

A comprehensive record of earthquakes in this area, particularly within Iran, is available, covering a considerable time span, ranging from hundreds to thousands of years (Ambraseys and Melville, 1982). Nevertheless, as we move northwards, the documentation becomes scarcer and active faulting is poorly constrained.

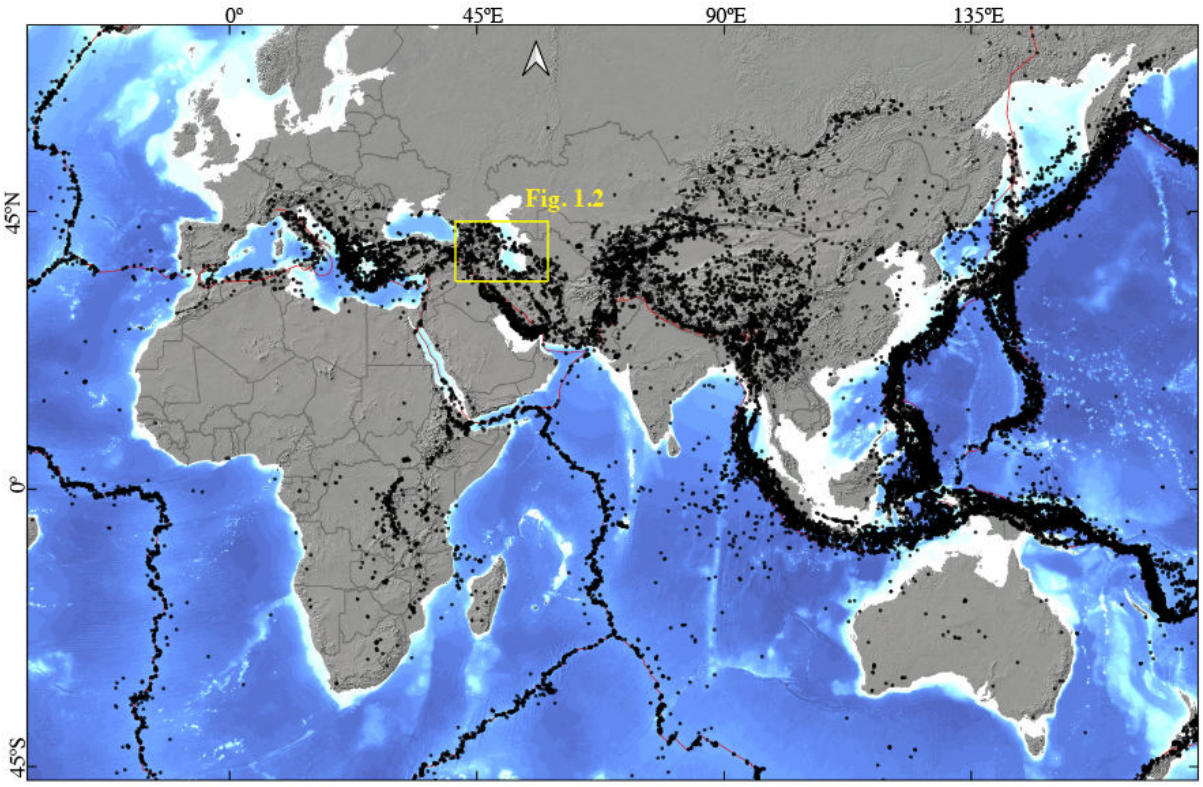


Figure 1.1 – Map showing earthquakes, black dots from the International Seismological Centre-Global Earthquake Model (ISC-GEM) catalogue from 1904 – 2014 with magnitudes > 5.0 (Di Giacomo et al., 2018) and plate boundaries (red) defined by the USGS.

The South Caspian region also offers the opportunity to address wider questions in earthquake science and tectonic geomorphology. Several recent examples of large earthquakes (e.g. the

2022 M 7.8 and 7.5 Kahramanmaras and the M 7.1 2019 Ridgecrest) show the potential for ruptures to propagate through multiple faults and fault segments (Barbot et al., 2023; Antoine et al., 2021). This is an important fundamental consideration for hazard and fault rupture modelling when undertaking scenario analyse. Therefore, having numerous example earthquakes that have ruptured multiple faults and fault segments provides a richer reference dataset when building models. More broadly, we can use these example events to increase our understanding of structural barriers to rupture propagation (e.g. Wesnousky, 2006; Biasi and Wesnousky, 2016).

Typical seismic hazard models assume that seismicity is randomly distributed across earthquake faults through time (Petersen et al., 2014), yet contrary to these models, earthquakes are increasingly witnessed to occur in spatiotemporal clusters spanning decades, such as the 1997-2016 cluster of destructive earthquakes in Central Italy (Caporali et al., 2019). Additionally, Pierce (2022) finds similar clustered earthquake behaviour in the western Basin and Range (USA) with four large events over a 200-year timespan in a region expected to produce one event every 1000-2000 years. These results, combined with other such historical examples of earthquake sequences that exhibits clustering behaviour, contradicts what might be expected in seismic hazard models that assume randomly distributed seismicity through time. By using paleoseismic methods of trenching and slip-rate analysis, we can look to evaluate earthquake recurrence on active fault strands.

Understanding landscape evolution and past climate conditions is an important consideration when undertaking active tectonic and paleoseismic research (McCalpin, 2009). One of the main tools involves dating geomorphic landforms and their fault related displacements to build slip-rates (e.g. Walker et al., 2021). Reversing this method, assuming a constant long-term slip-rate, allows for constraints on the timing of incision. By analysing this timing we are able to start to construct a model of past climate.

1.2 Geographic, geologic and tectonic setting

The South Caspian region sits at the northern boundary of the Arabian-Eurasian collision zone which forms part of the Alpine-Himalayan collision belt (Copley and Jackson, 2006; Jackson and McKenzie, 1984). The region consists of five main mountain belts and two sedimentary basins (Fig. 1.2). The Kopeh Dagh mountains sit at the northeast boundary and forms the border region between NE Iran and Turkmenistan (Fig. 1.2).

The Kopeh Dagh range is believed to be an uplifted and inverted Mesozoic extensional basin with a poorly understood basement. The oldest rocks correlate to the Lower-Middle Triassic basin, that consists of arc-related marine succession. Basin fill continued, without magmatism, of carbonates and siliciclastics deposits from the Middle Jurassic to the Late Eocene when the

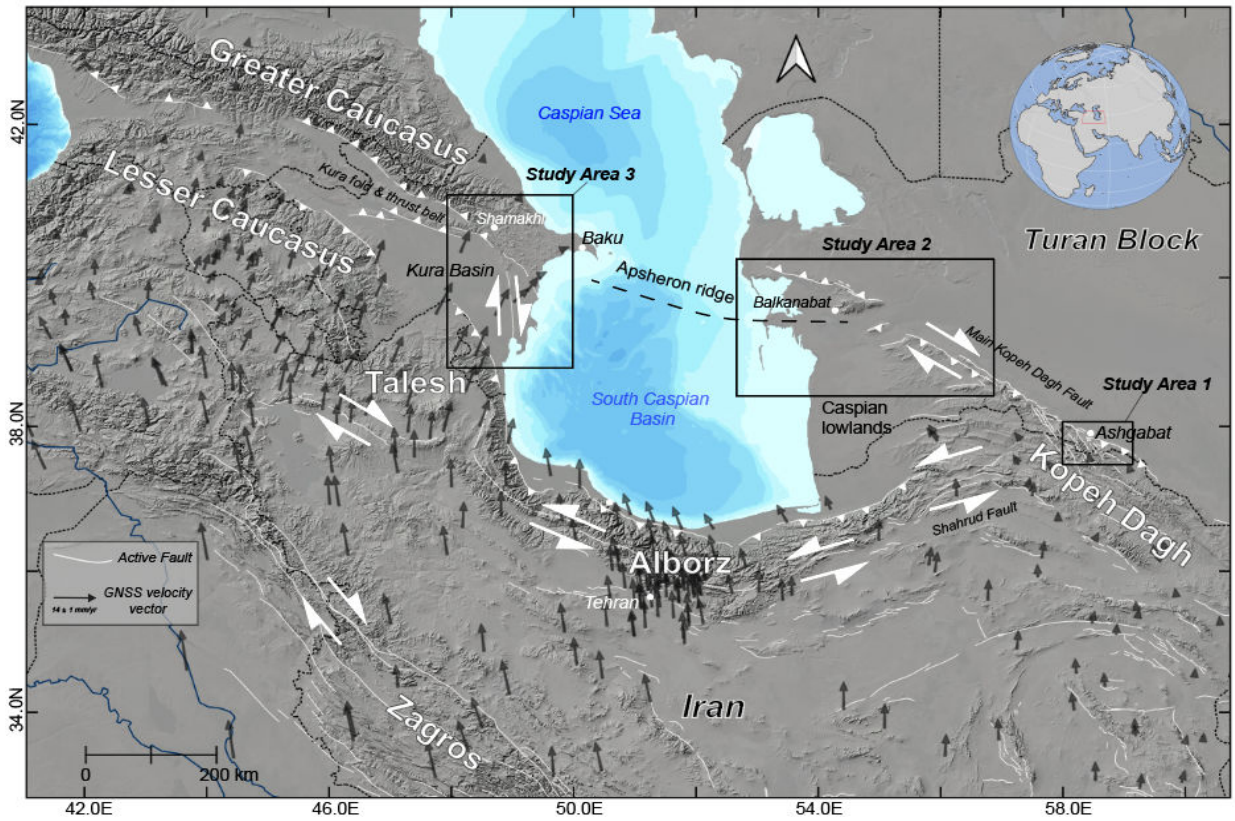


Figure 1.2 SRTM 30 m DEM showing active faults (white lines), black arrows show the GNSS velocity vectors (Khorrami et al., 2019), the black boxes indicate the three study areas and main fault structures in the region.

first signs of basin inversion begin. Major shortening of the basin occurred during the Oligocene to Miocene folding and faulting the inverted basin (Ghassemi and Garzanti, 2019). The pre-existing fold and thrust belt is bisected by a series of NW-SE striking dextral strike-slip faults and bound at the range front by a major right-lateral fault (Main Kopeh Dagh Fault

– MKDF) stretching ~ 400 km out into the east Caspian lowlands (Hollingsworth et al., 2006; Robert et al., 2014; Shabanian et al., 2009; Walker et al., 2021).

There are no historical records of this fault rupturing, but a recent study by Dodds et al. (2022a) shows evidence for a large medieval earthquake that caused at least a 200 km surface rupture. There is also a gap in instrumental seismicity on this fault (Fig. 1.3) and geodetic observations show the fault is not releasing strain through aseismic creep (Dodds et al., 2022b). Geomorphic analysis shows a high long-term slip-rate of 9.1 ± 1.4 mm/yr (Walker et al., 2021).

The right-lateral Main Kopeh Dagh Fault and conjugate left-lateral Shahrud Fault zone form the eastern margins of the South Caspian Basin (Fig. 1.2). The South Caspian Basin is believed to be an aseismic block moving independently of its surrounds. The South Caspian Basin consists of 15 -20 km of sediments with a 10 – 15 km basaltic like basement beneath (Jackson et al., 2002). The South Caspian Basin thought to subduct beneath at the northern boundary under the raised Apsheron ridge (Fig. 1.2). The southern boundaries the South Caspian Basin is thought to subduct beneath the Alborz and Talesh mountains (Iran) (Fig. 1.2 & 1.3). However, the relative motions along the northwest and northeast boundaries are less well constrained. These two areas form the basis for studies 2 and 3 (Chapters 3 and 4).

1.3 Earthquake history

Northeast Iran and Turkmenistan

There is a long history of major (M_w > 7.0) and destructive earthquakes in northeast Iran (e.g., Ambraseys and Jackson, 1998; Ambraseys and Melville, 1982; Berberian and Yeats, 1999; Dodds et al., 2022; Hollingsworth et al., 2010; Jackson et al., 2002) (Fig. 1.3). However, little is known about earthquakes in Turkmenistan earlier to the 19th century with evidence for one medieval event of M_w 7.6 ± 0.4 bracketed at 600 – 800 BP (Dodds et al., 2022a). The lack of events could represent an absence of seismicity or a lack of historical records.

In the lowlands of the eastern Caspian region, there exists a comparatively extensive contemporary record of earthquakes. The 1895 Krasnovodsk (Turkmenbashi) earthquake, with a magnitude of approximately M_s 7.5, stands as one of the earliest notable seismic events recorded in Turkmenistan (Ambraseys, 1997). The 1946 Balkan earthquake (M_s 7.0) is thought to have occurred in a similar area. The 1983 Kum Dag (M_b 5.2) and the 1984 Burun (M_w 5.7) earthquakes have centroid depths of 27 km and 31 km, respectively (Jackson et al., 2002). Both

earthquakes have surface ruptures in the eastern Caspian lowlands (Trifonov et al., 1986). The 2000 Balkanabat earthquake (M_w 7.0) had a centroid depth of 31 km, a thrust focal mechanism but no reported surface ruptures (Jackson et al., 2002) (Fig. 1.3).

To the east of the Main Kopeh Dagh Fault there are a series of NNW-SSE striking strike-slip faults that have hosted five earthquakes (e.g., 1851, 1871, 1872, 1893, and 1895) in the Quchan earthquake sequence with magnitudes of 6.8 – 7.2 and the 1929 M7.0 Baghan earthquake which produce a 50 km long surface rupture (Tchalenko and Skempton, 1975) (Fig. 1.3). At the eastern edge of this zone is the capital of Turkmenistan, Ashgabat. In 1948 Ashgabat was hit by a large earthquake (M 7.3) with a centroidal depth of 12 km (Fig. 1.3). This was a devasting event that is believed to have killed in excess of 38,000 people (Sidorin, 2019). Despite the scale of the devastation little is known about this event and active faulting near Ashgabat, and this is discussed in more detail in Chapter 2.

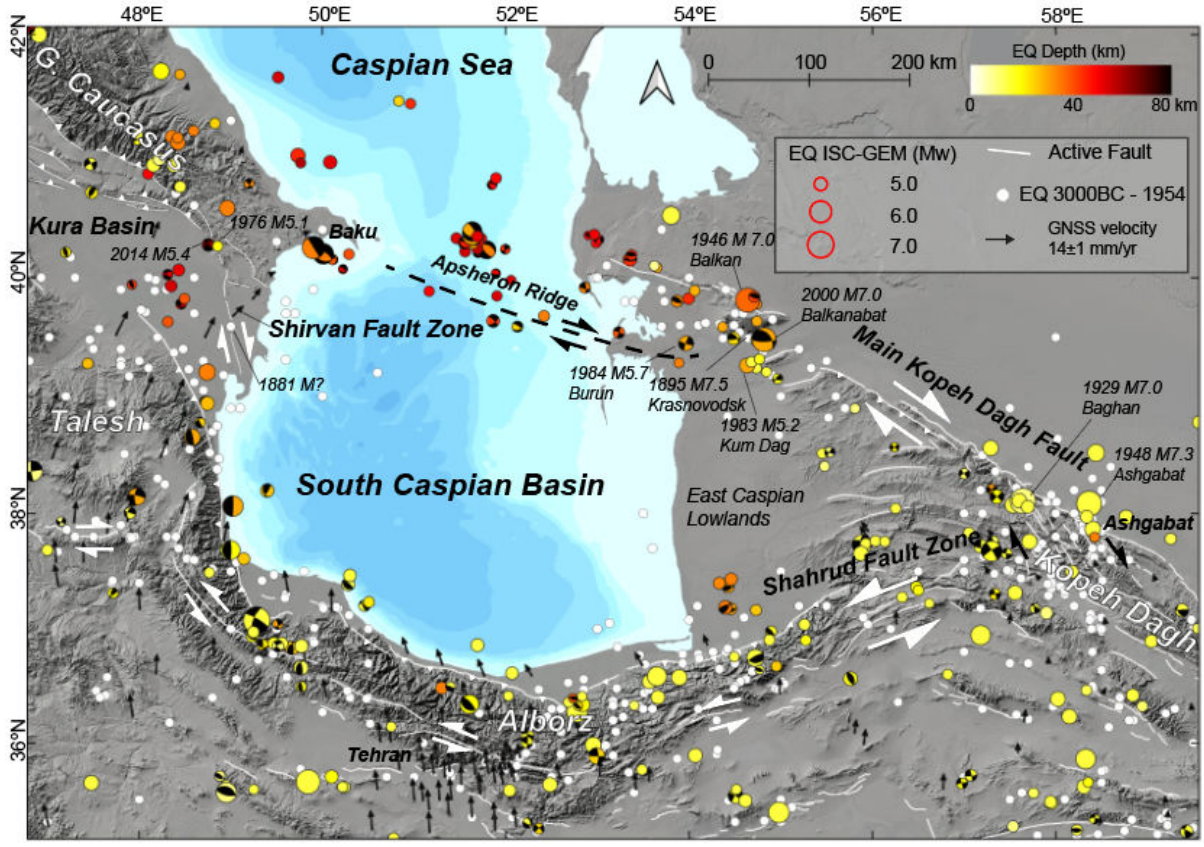


Figure 1.3 SRTM 30 m DEM showing active faults (white lines), GNSS velocity vectors (Khorrami et al., 2019), earthquake locations from Ambraseys and Melville (1982) (white dots) between 3000BC – 1954, earthquake locations and focal mechanisms from ISC-GEM catalogue (coloured by depth and sized by magnitude).

In the eastern Alborz Mountain range, there is evidence for left-lateral motion on the Shahrud Fault Zone (Figs 1.2 & 1.3). There is paleoseismic evidence for rupture on the Astaneh segment during the early medieval (before 1300 C.E.), between 600 – 4600 and 4600 – 9600 B.C.E. (Hollingsworth et al., 2010b).

Azerbaijan

Earthquake records at the western edges of South Caspian Basin are limited. On the Shirvan Fault zone there is geomorphic evidence for right-lateral strike-slip faulting but few recorded earthquakes. Instrumental seismic data show earthquakes to the west of the Shirvan Fault zone. There are only three onshore events that are near to the Shirvan Fault zone in 1881 (magnitude unknown), 1976 (M 5.1) and 2014 (M 5.4) (Fig. 1.3). Therefore, this region warrants further geomorphic investigation (see Chapter 4).

1.4 Overview of the text

This body of work is split into three main studies (Chapters 2 – 4) with an introduction (Chapter 1) and conclusion (Chapter 5). Each study is in research paper form and includes some contributions from other authors, detailed at the end of each chapter.

The first study (Chapter 2) is a reassessment and analysis of the devasting M7.3 Ashgabat earthquake in Turkmenistan. Despite being one of the most devastating earthquakes in the 20th century it has remained poorly constrained and not well understood. The study uses a combination of seismic and geomorphic techniques to characterise and provide constraints on source parameters of the event. The results are combined with data and observations from previous studies to provide a reassessment of the earthquake and associated surface ruptures. The investigation assesses the seismotectonic significance of this event in the context of Arabian-Eurasian collision zone. The study also discusses the implications for regional seismic hazard and the apparent complex nature of this rupture.

The second study (Chapter 3) extends its examination westward from Ashgabat to encompass the central and western sections of the Main Kopeh Dagh Fault. In this context, the focus shifts

toward understanding the fault's long-term behaviour across numerous seismic cycles. It introduces novel techniques for utilising fault slip-rates to establish chronological boundaries for regional incision occurrences and the formation of alluvial fans. Through the utilisation of long-term geologic slip-rates, coupled with short-term geodetic rates, and remotely observed displacement of drainage channels, the study estimates the timing of incision events and consequently establishes temporal constraints for the deposition of alluvial fans. The research additionally unveils findings derived from field expeditions conducted in Turkmenistan in 2017 and 2019. Employing a synergy of field observations and remote sensing methodologies, the study effectively charts the geomorphic features within the area, establishing a stratigraphy. These outcomes hold significant relevance for late-Pleistocene paleoclimatic conditions and the historical levels of the Caspian Sea. Such factors are crucial considerations in the context of utilising geomorphic surfaces to tackle tectonic inquiries.

The final study (Chapter 4) focusses on active faulting of the western margins of the South Caspian (Fig. 1.2). The study uses remote sensing and paleoseismic techniques to map active faults and past surface ruptures. A paleoseismic investigation builds source parameters of a previously unknown strike-slip fault in the region with the potential of producing large magnitude earthquakes (> M 7.0). The results provide constraints on slip-rate and earthquake recurrence during the Holocene, which has important implications for seismic hazard and regional tectonics.

1.5 Publications from this thesis

Chapter 2 has been submitted and is currently in pre-print at Geophysical Journal International as:

Seismotectonic aspects of the Ms 7.3 1948 October 5th Ashgabat (Ashgabat) earthquake, Turkmenistan: right-lateral rupture across multiple fault segments, and continuing urban hazard.

N. Marshall[1], Q. Ou[1,5], G. Begenjev[2], E. Bergman[3], Y. Bezmenov[2], N. Dodds[1], C. Gruetzner[4], T. Hudson[1], I. Pierce[1], R. Mirzin[2], E. Rhodes[6,7], R.T Walker[1], P. Wordsworth[8]

1 - COMET, Department of Earth Sciences, Oxford University, Oxford, OX1 3AN, UK.

2 - Institute of Seismology and Physics of the Atmosphere, National Academy of Sciences of Turkmenistan, Ashgabat, Turkmenistan.
3 - Global Seismological Services, 1900 19th St., Golden, Colorado 80401, U.S.A.
4 - Friedrich Schiller University Jena, Institute of Geological Sciences, Jena, Germany.
5 - COMET, University of Leeds
6 - Department of Geography, University of Sheffield, Sheffield, S10 2TN, UK.
7 - Department of Earth, Planetary, and Space Sciences, University of California Los Angeles, Los Angeles, CA 90095-1567, USA.
8 - School of Archaeology, Oxford

Chapter 3 will be submitted for publication as:
Constraining landscape evolution of the Kopeh Dagh, Turkmenistan, using optical imagery and long-term geologic slip-rates.

N. Marshall[1], G. Begenjev[2], Y. Bezmenov[2], N. Dodds[1], C. Gruetzner[3], R. Mirzin[2], E. Rhodes[4,5], R.T Walker[1]

1 - COMET, Department of Earth Sciences, Oxford University, Oxford, OX1 3AN, UK.
2 - Institute of Seismology and Physics of the Atmosphere, National Academy of Sciences of Türkmenistan, Aşgabat, Türkmenistan.
3 - Friedrich Schiller University Jena, Institute of Geological Sciences, Jena, Germany.
4 - Department of Geography, University of Sheffield, Sheffield, S10 2TN, UK.
5 - Department of Earth, Planetary, and Space Sciences, University of California Los Angeles, Los Angeles, CA 90095-1567, USA.

Chapter 4 will be submitted for publication as:
Paleoseismology of the Shirvan Strike-slip fault zone (West Caspian Fault), Azerbaijan: implications for seismic hazard and South Caspian tectonics.

N. Marshall[1], S. Kazimova[3], I. Pierce[1], E. Rhodes[4,5], R.T Walker[1], R. Javanshir[1,2], B. Johnson[1], G. P. De Pascale[6], I. Guliyev[2], G. Yetirmishli[3], R. Muradov[3].

1 - COMET, Department of Earth Sciences, Oxford University, Oxford, OX1 3AN, UK.

2 - Azerbaijan National Academy of Science, Baku, Azerbaijan.

3 - Republican Seismic Survey Center of Azerbaijan National Academy of Science, Baku, Azerbaijan

4 - Department of Geography, University of Sheffield, Sheffield, S10 2TN, UK.

5 - Department of Earth, Planetary, and Space Sciences, University of California Los Angeles, Los Angeles, CA 90095-1567, USA.

6 - School of Engineering and Natural Sciences, University of Iceland, Reykjavík, Iceland.

Chapter 2

Seismotectonic aspects of the Ms 7.3 1948 October 5th Ashgabat (Ashgabat) earthquake, Turkmenistan: right-lateral rupture across multiple fault segments, and continuing urban hazard.

Abstract

The Ms 7.3 1948 Ashgabat earthquake was one of the most devastating earthquakes of the 20th century, yet little is known about its location, style, and causative fault. In this study, we bring together new seismic and geomorphic observations with previously published descriptions of surface rupture and damage distributions to determine the likely source of the earthquake. We determine the epicentre and focal mechanism of this earthquake from digitised historical seismograms and the relocation of regional seismicity to show that the earthquake most likely nucleated close to the city of Ashgabat. The earthquake ruptured a right-lateral strike-slip fault to the southeast of the city, which has a clear long-term expression in the landscape, and also likely reactivated a subparallel concealed thrust along the Gyaursdag anticline east of the city. The earthquake potentially also ruptured a right-lateral segment northwest of Ashgabat, which does not have an identifiable expression in the landscape. Using high-resolution satellite imagery and digital elevation models we investigate the geomorphology of active faulting around Ashgabat and adjacent parts of the Kopeh Dagh (Köpetdag) mountain range front, showing that there are significant strike-slip and oblique strike-slip segments adjacent to the city that apparently did not rupture in 1948, and yet show clear geomorphic expression and potential right-lateral displacement of Parthian-era (~2000 year) and post-Sassanian era (~1500 year) archaeological remains. Luminescence dating of displaced fluvial terraces west of Ashgabat yields a vertical displacement rate of 0.6 mm/yr, though the strike-slip rate remains undetermined.

2.1 Introduction

At 01:15AM local time on 5th October 1948 a Ms 7.3 earthquake occurred near the city of Ashgabat in present-day Turkmenistan (Sidorin, 2019). The city was almost completely destroyed, and its population devastated by the mainshock and subsequent aftershocks. It is estimated that 90% of all buildings in the city collapsed killing between 38,000 and 120,000 people (Nikonov, 1998; Sidorin, 2019) making this one of the most damaging earthquakes recorded in the 20th century (England and Jackson, 2011). Despite the size and impact of this earthquake, there are continuing uncertainties in the location, mechanism, and causative fault. There is disagreement about the mechanism of this earthquake, which range between strike-slip and thrust mechanisms (Rezanov, 1957; Shirokova, 1967; Mckenzie, 1972; Tchalenko, 1975; Nikonov, 1998; Sidorin, 2019; Berberian and Yeats, 2001). A wide array of surface ruptures were reported in earlier publications (e.g., Rogozhin, 1994; Sidorin, 2019), though significant urban expansion and regional development during the last 30 years may have masked any residual surface signals that could have been preserved. Furthermore, the active faulting around Ashgabat and surrounding areas has not been mapped in detail, such that the tectonic context of the 1948 earthquake is not clear.

Determining the location, magnitude, focal mechanism and rupture style of large earthquakes that occur in this region is of vital importance for understanding local seismic hazard, and for improving our broader understanding of the regional tectonics and large-scale fault systems that accommodate shortening (e.g. Walker et al., 2021). The potential for step-over during the Ashgabat rupture may allow this earthquake to help us understand the processes that control multi-fault and multi-segment ruptures, which have been shown to be important through several strike-slip occurrences in recent years (e.g. the M 7.8 & 7.5 2023 Kahramanmaraş (Barbot et al., 2023) and the M 7.1 2019 Ridgecrest (Antoine et al., 2021) earthquakes.

In this chapter, we investigate the source of the 1948 Ashgabat earthquake. We combine seismic investigations, intensity distributions, contemporary mapping of surface rupture and analysis of high-resolution optical satellite data and derived topographic datasets, and field-based quaternary dating. Our seismic investigations of the earthquake source parameters are aided by digitised analogue seismograms sourced from a range of global archives and through compilation of bulletin arrival times. Epicentral location and depths of earthquakes in

Turkmenistan are determined using a calibrated multiple event relocation technique (Bergman et al., 2022).

2.2 Background and regional setting

2.2.1 Tectonics

Ashgabat (Aşgabat) (population 864,000 (https://data.worldbank.org/)) is the capital city of Turkmenistan (Türkmenistan) and sits at the northernmost edge of the Eurasia-Arabia continental collision (Fig 2.1). Deformation in Turkmenistan results from a combination of north-south shortening associated with the Eurasia-Arabia collision, and by the motion of the South Caspian Basin (SCB). The South Caspian Basin is an aseismic block moving independently of its surroundings, with a rate of 10 ± 2 mm/yr in direction 330º ± 10º relative to Eurasia (Jackson et al., 2002; Copley & Jackson 2006; Djamour et al., 2010; Walker et al. 2021; Dodds et al., 2022). The South Caspian's motion relative to its surroundings is accommodated along left-lateral strike-slip faults of the Alborz mountains in Iran, and along the oblique right-lateral reverse Main Kopeh Dagh fault (MKDF) in Turkmenistan, which has a geologic slip-rate at 9.1 ± -1.3mm/yr (Walker et al., 2021) and InSAR-derived geodetic right-lateral slip-rate 7.2 ± 2.4 mm/yr, and a shortening rate of 4 ± 2 mm/yr (Dodds et al., 2022).

The tectonics of the Kopeh Dagh (Köpetdag) range change along strike, from rapid right-lateral faulting related to South Caspian Basin-Eurasia in the west, through to north-south Arabia-Eurasia shortening in the east. The transition between these two domains likely occurs within the Barharden-Quchan fault zone (BQFZ) (Fig. 2.1), centred on longitude ~58ºE, which consists of an array of NNW-SSE trending right-lateral faults that cut through the Kopeh Dagh range (Hollingsworth et al. 2006; Shabanian et al., 2009). Ashgabat, where the destructive 1948 earthquake occurred, lies near the eastern margin of the BQFZ.

2.2.2 Earthquakes

The 1948 earthquake is the most destructive event in Turkmenistan, though not the only significant event in recent history (Ambraseys, 1997; Berberian and Yeats, 2001; Dodds et al.,

2022). Significant earthquakes in 1895, 1946, 1983, 1984 and 2000 have occurred in the eastern Caspian lowlands (Fig. 2.2. also see Section 2.4.3.). The 1983 and 1984 events were associated with surface rupture near Kumdag town (Fig 2.2a), indicative of right-lateral faulting on a NW-SE trend (e.g. Jackson et al., 2002). Closer to Ashgabat there have been several large earthquakes on the right-lateral faults of the BQFZ, within the interior of the Kopeh Dagh. These include the 1851, 1871, 1872, 1893 and 1895 Quchan earthquake sequence with M ~ 6.8–7.2, the May 1st 1929 (Ms ~7) Baghan earthquake, which produced up to 50 km of surface rupture (Tchalenko, 1975), and the February 4th 1997 Bojnurd earthquake with MW 6.4 (Hollingsworth et al., 2006).

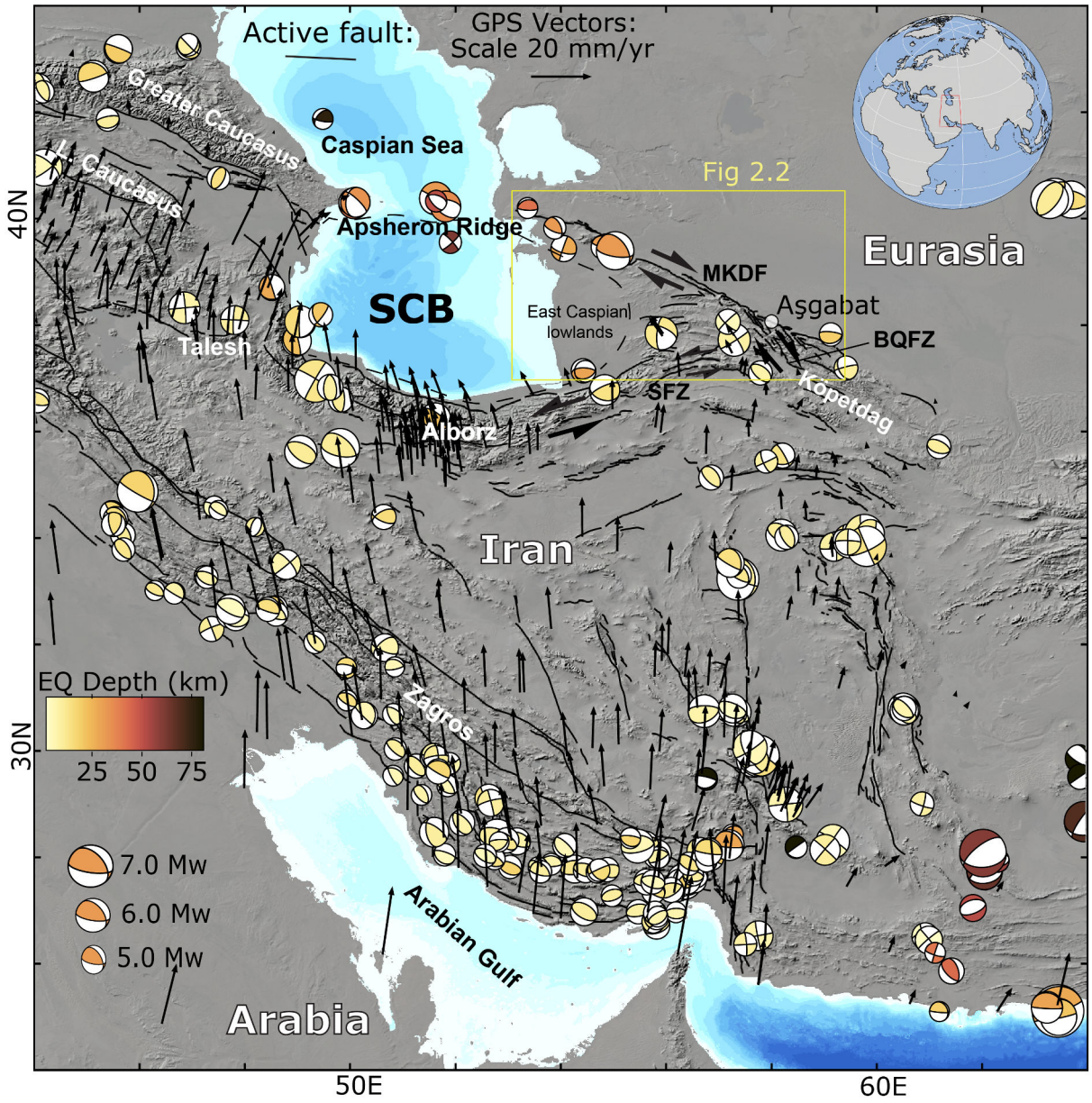


Figure 2.1 Tectonic map of the Arabian/Eurasian plate collision zone. Black arrows represent GPS velocity vectors after Khorrami et al., (2019) relative to Eurasia. Waveform-modelled focal mechanism solutions and locations for earthquakes greater than Mw 3.5 between 1917 and 2017 from the catalogue created by Wimpenny

and Watson (2020); black lines show active faults in the region (Walker et al., 2021). Digital Elevation Model (DEM) from SRTM 90m. Main Kopeh Dagh Fault zone – MKDF; South Caspian Basin – SCB.

Instrumentally recorded earthquakes in the eastern part of Turkmenistan and adjacent parts of Iran, east of longitude 55ºE, have centroid depths typically less than 20 km, whereas those west of 55ºE are deeper, with centroid depths ranging between 20 and 50 km (Jackson et al. 2002; Walker et al., 2021). The deeper earthquakes west of 55ºE are likely to reflect increasing thickness of sediment in the east Caspian lowlands, and the influence of the South Caspian basement. Available focal mechanisms show strike-slip faulting (right-lateral on NW-SE planes, or left-lateral on NE-SW planes) as far east as 60ºE.

There are relatively few recorded earthquakes along the Kopeh Dagh rangefront between Ashgabat and Bereket. Dodds et al (2022a) observed a single paleo-earthquake ruptures with average offsets of ~7.5 m along a ~200 km-long section of the MKDF from Bereket to Arçman. They estimate a magnitude of Mw 7.8 and an age of 600-800 years based on trenching and the displacement of cultural features of presumed Medieval age. East of Arçman to Asgabat the Kopeh Dagh rangefront is more segmented, and is separated into the Baharly, Dowgala and Goktepe segments. The only constraint on earthquake timing along this part of the range-front is provided by two Infra-red-stimulated luminescence (IRSL) ages of 3.4 ± 0.5 26 ka and 2.5 ± 0.2 ka from a river cutting exposure of an offset alluvial deposit along the Baharly segment predating the most-recent surface rupture (Dodds et al., 2022b).

Berberian and Yeats (2001) report archaeological evidence for destructive earthquakes in proximity to Ashgabat, with inferred earthquake damage at the Parthian city of Old Nisa dated from the first century 179 B.C.E to the first century C.E. (Pilipko, 2007) and from the Bronze Age settlement of Ak-Depe at 3000-2000 B.C.E (Liapin, 2006). However, as noted by Dodds et al., (2022a), both the interpretation of the damage and the dating are ambiguous, and other potential dates of earthquake damage are possible. For instance, a date of the fifth century C.E. is proposed by earlier excavators at Nisa, but does not appear in later publications (Davidovich, 1951).

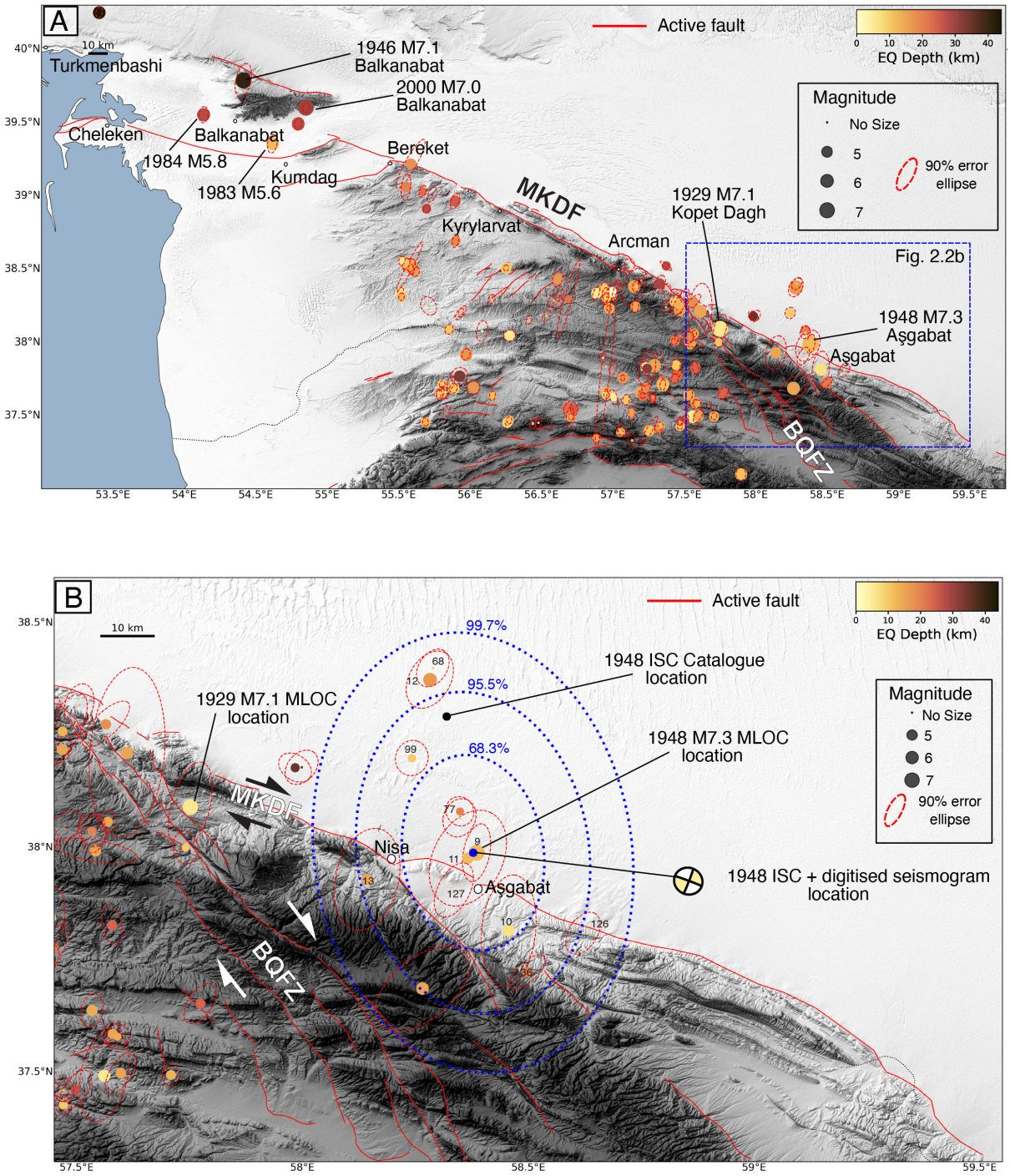


Figure 2.2 (A) Hypocentral locations of earthquakes between 1929 and 2019 scaled by magnitude with 90% confidence interval (Table 2.2). Locations are calibrated using the Hypocentroidal Decomposition technique. The earthquakes are coloured by focal depth. DEM is from SRTM 30 m. (B) Hypocentre location of the 1948 Ashgabat earthquake located using the ISC phase arrival data (black dot) (Table 2.1); the ISC phase arrival data combined with phase arrivals from the digitised waveforms (blue) (Table 2.1); coloured circles are the calibrated earthquake locations calculated using the hypocentroidal decomposition relative relocation method and sized relative to magnitude (Fig 2.2A). Dotted blue lines represent confidence intervals showing a measurement of the error in the location. DEM is from SRTM 30m.

2.3 Methods

We map active faults using a combination of modern imagery of different resolutions and digitise historical fault, rupture, and intensity maps recorded by Soviet scientists after the 1948 earthquake (Rogozhin, 1994; Sidorin, 2019). The Soviet records have been georeferenced using the QGIS 3.16 software (QGIS Development Team, 2021), though challenges in accurately georeferencing the maps to modern imagery means they should be used as a guide only. We trace from these maps the reported and recorded ruptures shown in Fig. 2.3.

To analyse the geomorphological signature of earthquake ruptures and fault scarps we use tri-stereo high-resolution Pléiades imagery and bi-stereo Worldview 3 satellites to produce Digital Elevation Models (DEM). Agisoft Metashape Professional software was used to build a point cloud data set of matched points in each of the images. The dense cloud of point data was then rasterised to build an elevation model of the area. Using the Pléiades satellite imagery, we build an elevation model with 1 m horizontal resolution. The Worldview-3 imagery yielded a DEM with 50 cm horizontal resolution. Additionally, we used legacy Corona imagery from 1967 to observe the ground surface prior to major urbanisation of Ashgabat. Faults are mapped using the QGIS software and defined by scarps, offset drainages, shutter ridges and offsets in Anthropocene features.

Age control on alluvial fans displaced by faulting came from single-grain Infra-red-stimulated luminescence (IRSL) dating of feldspar grains, using methods as described in Walker et al., (2021) and Rhodes (2015). To collect the samples, we dug a 1.2 m sample pit into an uplifted alluvial surface at 38.043°N/58.026°E. The stratigraphy (bottom to top) consisted of a 20 cm fine grained and silt layer capped by 30 cm of blocky gravels. Above this there is 20 cm compact loess layer with a less well consolidated 50 cm loess cap. We took two adjacent sample tubes at a depth 100 cm (TK19-09 and TK19-10) in the fine-sand/silt layer and a further sample tube (TK19-11) at a depth of 55 cm in the compact loess deposit (Table 2.3). Samples were collected in metal tubes hammered horizontally into the fine-sand/silt and loess layers. The sample grains were prepared by selecting a suitable grain size using wet sieving and we administered a dilute HCl treatment to remove carbonate. The samples were the dried. K-feldspar fractions were then separated from the quartz, plagioclase and heavy minerals by flotation in a centrifuge using a lithium metatungstate (LTM) solution. The separated k-feldspar

was then rinsed to remove the LTM and treated to remove the outer surfaces (or dark coating), presumed to absorb light (Rhodes, 2015). IRSL measurements were then made in a standard Risø TL-DA-20D automated luminescence reader. Details regarding the machine calibration and filters can be found in Rhodes (2015).

The various seismic methods of epicentre location and relocation, and focal mechanism calculation are described in detail in the Section 2.5.

2.4 The October 5th 1948 Ashgabat earthquake (M7.3)

2.4.1 Overview and macroseismic effects

The Ms 7.3 Ashgabat earthquake occurred at 20.12.07 GMT on the 5th October 1948, corresponding to 1:12 am local time on the 6th October. It was followed by a number of strong aftershocks in the following days, including at 6 am and 10 am local time on the 6th October (as reported by Federov, 1998), and another on the 8th that caused additional deaths. The Ashgabat seismic station recorded 138 aftershocks over the month from October 20th to November 20th 1948. The mainshock largely destroyed the city of Ashgabat and caused heavy damage over a wide region. Within Ashgabat and surroundings there was near total collapse of brick buildings, heavy damage to concrete structures and infrastructure, and the destruction of all medical facilities (Sidorin, 2019). All utility networks in the city other than water were rendered inoperable. The city was cut off from the outside world, resulting in considerable delay in activating relief efforts.

The death toll in the earthquake is not known precisely due to a combination of information restrictions in the USSR at that time and imprecise estimates of the immediate post-war population (Sidorin, 2019). Estimates vary between 10,000 and 120,000 casualties, with most recent publications suggesting ~40,000 deaths (35,000 in Ashgabat) as the most likely figure (Sidorin, 2019). The earthquake and its effects are a major feature within the cultural memory of Turkmenistan. Casualties and damage extended over the border into Iran, with destruction of over thirty villages, and more than 350 people killed in the Darrez Gaz region.

Several isoseismal maps have been published (Sukacheva and Kazanli, 1949; Rezanov, 1959; Rustanovich, 1967; Golinskiy and Nepesov, 1968; Shebalin, 1974; Gorshkov, 1984; Berberian and Yeats, 2001). There are variations between these in the exact shape of the contours, and in the peak intensity. All agree on an overall elongate NW-SE ellipse, with wider contour spacing to the northeast side of the epicentral zone (e.g. Fig. 2.3). The isoseismal contours are misaligned with the Kopeh Dagh range front, extending into the mountains in the southeast and into the piedmont in the northwest. Irregularities in the shape that have been used by Berberian and Yeats, (2001) to infer rupture on more than one misaligned fault. Peak intensities of X were recorded at Gyaurs and Kuru Gaudan, and IX at Asgabat, Nisa, and Änew (Fig. 2.3). Rogozhin (1994) suggests that the large intensities at Kura Gaudan may be related to site effects, with the water table near to the surface in this region.

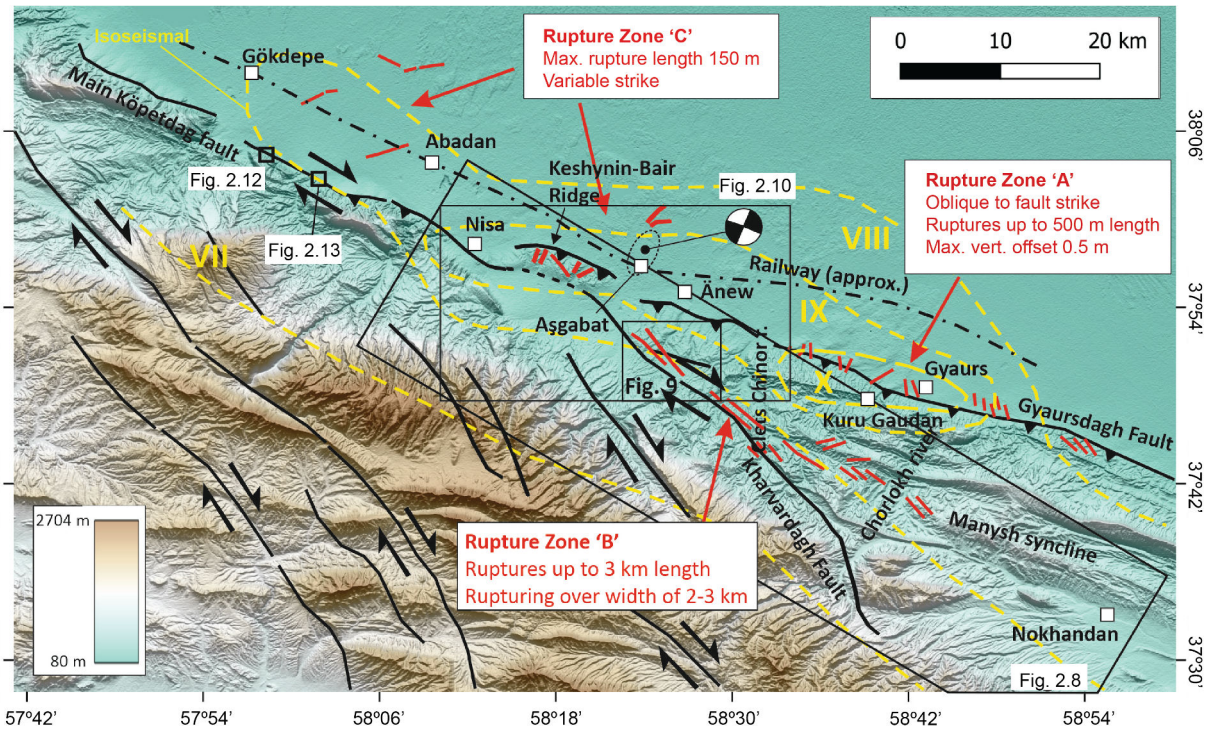


Figure 2.3: Ashgabat region showing reported earthquake ruptures. Black lines are active faults (mapped by the authors) and red lines are 1948 ruptures digitised from the Gorkoshev 1949 geologic study (Rogozhin, 1994). Difficulties in georeferencing means that the rupture locations should be used as an approximate guide only. The ruptures are separated into three main areas of rupture (A, B, C). MSK isoseismal contours are from Berberian and Yeats (2001), who combined several other sources along with their own intensity observations in Iran.

2.4.2 Ruptures and surface deformation

Surface ruptures have been reported in several previous studies, based on observations made in 1948, and contained in reports that are not publicly available (Rogozhin, 1994; Sidorin, 2019). There are remaining uncertainties in the exact positioning of each reported rupture, but by comparing to our satellite derived DEMs we identify nearby indications of active faulting that we infer to have ruptured in the earthquake.

Ground displacements mapped after the 1948 earthquake occur in three main zones (Sidorin, 2019; Rogozhin, 2012 & 1994; Nikonov, 1998; Rezanov, 1958), extending both northwest (zone C) and southeast (zone B) of Ashgabat, and east (zone A) of Ashgabat within the Gyaurs anticline near Kuru Gaudan, as shown in Fig. 2.3. Fractures were also mapped on the Keshenyn-Bair ridge that runs between Ashgabat and Nisa, close to the Änew mosque, and along the highway ~8 km south of Änew (Fig. 2.3). Authors disagree on the extent to which any or all of the dislocations represent primary fault rupture, secondary faulting, or associated fissuring caused by hydrological changes (Rezanov, 1958; Rustanovich, 1964; Rogozhin, 1994; Rogozhin, 2012). The rupture zones are discontinuous, but define an overall end-to-end length of ~80 km. None of the rupture zones align with the main range-bounding faults of the Kopeh Dagh, despite careful field checking of these faults by Gorshkov (1957). We provide further interpretation of the surface ruptures and the active faulting below.

The first area of reported rupture (Zone A on Fig. 2.3) is found east of Ashgabat along the frontal (northern) limb of the Gyaursdag anticline and fault striking WNW-ESE with a concentration of reported ruptures at the village of Kuru Gaudan. The length of this rupture zone is ~40 km, with the individual fractures perpendicular to the roughly east-west strike of the anticline. Individual ruptures are up to 500 m in length and have a maximum vertical offset of 0.5 m (Sidorin, 2019; Rogozhin 2012; Rezaonov, 1958). A detailed map of one section of these perpendicular fractures near the settlement of Kuru Gaudan, from Tchlenko's personal documents, is shown in Fig 2.4. Here, ruptures with relative displacements of up to 1 m form complex stepped horsts and grabens that are up to 1 m wide (Rogozhin, 1994). Ejections of sediments and mud volcanoes (up to 20 m in diameter with a height of 0.5 m) were also observed near Kuru Gaudan (Sidorin, 2019; Rogozhin, 1994), which can be interpreted as liquefaction features.

Rogozhin (1994) suggests that the fractures observed along the Gyaursdag anticline are gravitational, though the apparently right-stepping arrangement of fractures may indicate a combination of fold growth and right-lateral motion above a blind fault tip, as seen for instance in the 1957 Gobi-Altay earthquake in Mongolia (Kurushin et al., 1998). Indications of co-seismic shortening across the Gyaursdag anticline come from reports of damaged water pipes in several places at Kuru Gaudan, with pipes buckled to heights of 1 m, and the telescoping of one pipeline over a length of 3 m (Butovskaya and Kovalenko, 1955).

The second rupture zone (Zone B) coincides with the Kharvardagh geological fault zone and is orientated NW-SE (Fig. 2.3). It begins ~5 km southeast of Asgabat and extends further southeast for a distance of ~ 35 - 40 km within the Manysh syncline (Fig. 2.3). Reported individual rupture lengths range from several hundred meters in the west to 3 km across a 2 - 3 km wide zone (Sidorin, 2019; Rogozhin, 1994). Rogozhin (1994) separates the ruptures into north and south zones. The northern one is ~6 km in total length, beginning near the headwaters of the Celts-Chinor river (Fig. 2.3). The southern one extended a further 15 km to the southeast, ending at the headwaters of the Chorlokh river (Fig. 2.3). The NW-SE ruptures tracked across undulating topography caused by multiple minor northeast-flowing drainages. Along the northern section upslope-facing scarps ~0.5 m high formed to the northern sides of the valleys, potentially suggesting lateral displacement of topography.

The third zone of rupturing (Zone C in Fig. 2.3) occurs northwest of Ashgabat in a low relief area north of the Kopeh Dagh rangefront. Individual ruptures (cracks) were short (< 150 m) in length and discontinuous (Sidorin, 2019; Rogozhin, 1994), with trends of 0 °, 60°, 90°, 290º and 300º. The ruptures are described as consisting both of fissures up to 30 - 40 cm wide and with a vertical displacement of up to 20 – 30 cm, and compressive features accompanied by warping of the ground and eruptions of mud. Rogozhin (1994) and others have suggested that these ruptures are associated with local geologic conditions such as a groundwater and swelling of sediment and mud volcanoes.

Post-earthquake resurveying of the Trans-Caspian railroad (approximate route shown in Fig. 2.3) provides an additional constraint on surface deformation at various points within the epicentral zone. Re-levelling revealed varying vertical displacements, ranging from 22 cm of

subsidence at Änew (Anau) east of Ashgabat (Butovskaya and Kovalenko, 1955; Rezanov, 1958; Kolibaev, 1962), to uplift of 33 cm at Büzmeýin (Bezmein/Abadan) west of Ashgabat. Within Ashgabat itself the levelling data shows almost pure right lateral displacement of 178-190 cm, that we are not able to accurately locate in the available imagery.

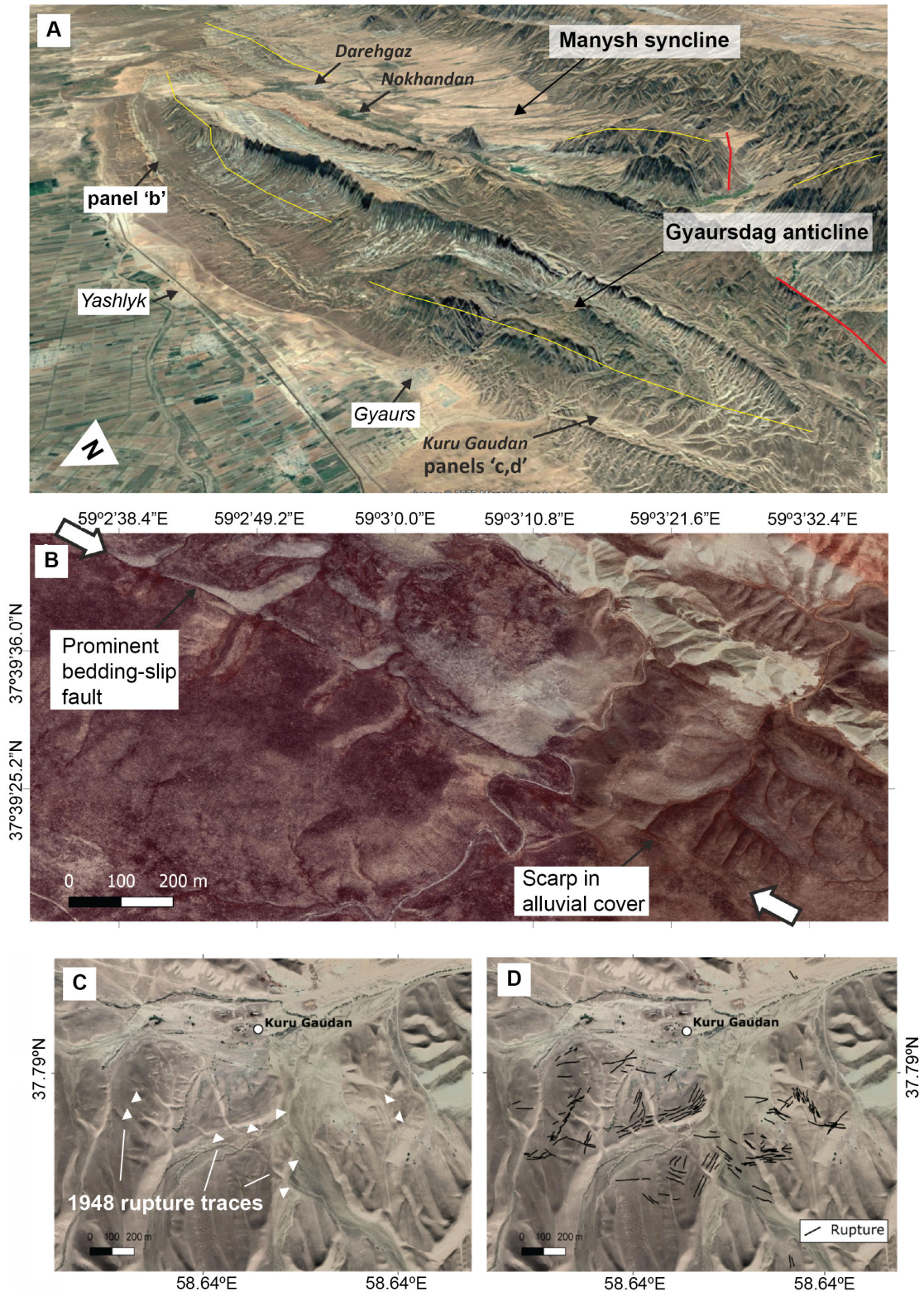


Figure 2.4 (a) Oblique view to the ESE from a viewpoint above Asgabat (Fig. 2.3) showing the Gyaursdag anticline in the foreground and the Manysh syncline behind. The axis of the Gyaursdag fold are shown in yellow, and the Kharvardagh right-lateral fault in red. (b) Apparent bedding-slip thrusts within the northern limb of the Gyaursdag fold near Yashlyk. (c and d) Satellite image of Kuru Gaudan showing ruptures associated with the 1948 earthquake (Tchalenko, per. Comm.)

2.4.3 Published source parameters from seismology

Published focal mechanisms of the 1948 earthquake show predominantly reverse faulting striking 110°-290°, with one nodal plane nearly vertical with uplift to the north, and the other plane nearly horizontal plane indicating thrusting of the southern block to the NNE (Rustanovitch & Shirokova 1964; McKenzie 1972). The focal mechanism has been used to suggest predominantly thrust motion in the earthquake, though the nodal planes are not well constrained, particularly for the very gently south-dipping plane (Jackson and Mackenzie, 1984).

Aftershock studies using temporary seismic networks were carried out in June-October 1949 and in June-September 1953 (Rustanovitch, 1957), revealing concentrations at Kuru Gaudan and at Bezmein, near the SE and NW ends of the zone of maximum destruction. The majority of aftershocks occurred at depths of 10-12 km. We provide epicentres of larger aftershocks and seismicity in Section 5.2 (Table 2.2).

2.5 Re-analysis of the 1948 earthquake

2.5.1 Collection and digitisation of seismic records

Our analysis of the Ashgabat earthquake involved the collection, digitisation, and analysis of seismic data from bulletins and seismograms. The International Seismological Centre (ISC) online bulletin (http://www.isc.ac.uk/iscbulletin/) records 175 stations reporting phase arrivals for the 1948 Ashgabat earthquake (International Seismological Centre, 2022). However, due to war damage, fire, misplacement and untracked lending over the decades following the event (Okal, 2015), it is no longer possible to recover all the original records. We collated phase arrival information from ISS bulletins (http://www.isc.ac.uk/iscbulletin/) and

recovered original seismograms for the 1948 earthquake from 21 stations of which 18 are usable (Fig 2.5) due to the quality of the record and companion metadata. The azimuthal distribution shows a good level of coverage to the NW but this is poor in the southern hemisphere. We have been unable to obtain seismogram records from neighbouring countries, and the only station in Turkmenistan at that time was destroyed in the earthquake (Sidorin, 2019). All arrival time data is presented in Table 2.1.

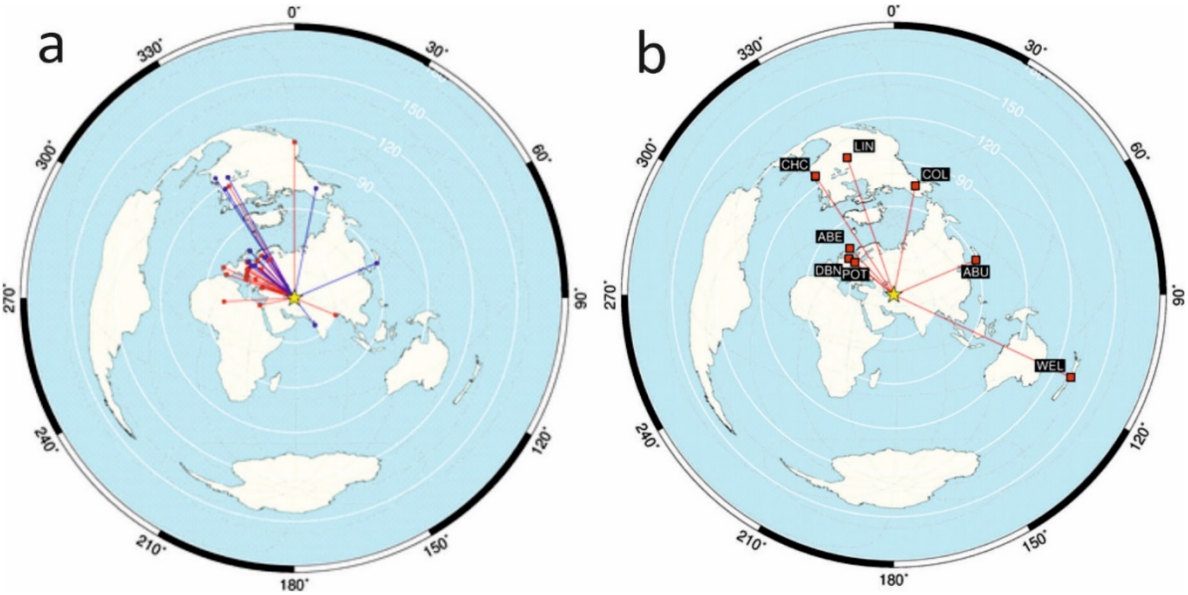


Figure 2.5 (a) Global coverage of first motion data from ISC records and ISS bulletins (red) and from waveforms digitised within this study (blue). Dots represent the station location, with lines showing the azimuth from the event. (b) Global coverage of stations that have digitised waveforms used for amplitude ratio focal mechanism calculation.

We digitized scanned paper seismograms using the same process as detailed in Ou et al. (2020). We first digitise the waveforms by tracing over the recorded signal by hand as a Bezier curve in version 2.10 of the GNU Image Manipulation Program (https://www.gimp.org). We begin the trace at the minute mark 3 minutes prior to the first arrival and cease when the waveform can no longer be traced due to saturation, the trace breaks due to dislocation of the stylus or at the edge of the seismogram if the trace cannot be reliably joined. We account for differences in resolutions of the scanned seismograms with the methods used in Ou et al. (2020) and Kulikova & Krüger (2015). The seismograms are recorded on different instruments and due to the mechanical designs of these instruments, corrections for geometrical artifacts such as curvature and slant have been made consistent with the methods detailed in Ou et al. (2020)

and Kulikova & Krüger (2015). We use the same inversion algorithm developed at the University of Potsdam (see Kulikova & Krüger, 2015) to restore the symmetry of the waveforms. We collate the instrument parameters, station location and altitude (detailed in Table 2.3) from the seismograms, station bulletins and from data in Chalier (1953). Where the damping constant or ratio was not available in the literature, we calculate this from the calibration pulse at the start of the seismogram. If there was no such pulse, we chose a best estimate of the most common damping constant or ratio for that particular instrument from Chalier (1953).

2.5.2 Epicentral location

To improve the location of the 1948 earthquake, and others in nearby parts of Turkmenistan, we use a relocation method based on the Hypocentroidal decomposition (HD) approach for multiple event relocation (Jordan & Sverdrup, 1981), but extended to develop calibrated locations (minimally biased by unknown Earth structure, with credible uncertainties) with suitable data sets (Bergman et al, 2022). The HD algorithm separates the relocation problem into two parts, with iteration between the two inversions. Firstly, vectors describing the relative locations in space and time of each event in the cluster are determined relative to the hypocentroid, or geometrical centre of the cluster. Secondly, the hypocentroid itself is located. The cluster vectors are then added to the new hypocentroid to obtain updated coordinates for each event. The method has been applied to over 300 clusters of earthquakes worldwide (Bergman et al., 2022) and in many individual studies, e.g., Walker et al., 2011, Hayes et al. (2013), Mackey and Bergman (2014), Yeck et al. (2016), and Karasözen et al. (2019). We use a cluster of 152 recorded earthquakes in the calibrated location analysis, detailed in Table 2.2.

We independently determined the 1948 epicentre from bulletin arrival times and phase arrivals picked from digitised waveforms. We picked arrival times for P, PP, PPP, S, SS and SSS phases from the digitised waveforms using the Snuffler module of the Pyrocko application toolbox (Heimann, 2019). We prioritised arrival times picked from the vertical component (Z) if available and chose the arrival time picked from the horizontal component better oriented to record a given phase from records from other stations. Once we have picked the phase arrivals, we use version 6.0c of the Hyposat inversion algorithm (Schweitzer, 2001) to calculate the

location of the hypocentre based on the Crust 1.0 and AK135 velocity models (Kennett et al., 1995; Laske et al., 2013). The algorithm uses first arrival times and time travel differences to iterate a best fit hypocentre and phases showing higher residuals were iteratively removed (greater than 30s) from the calculation, consistent with the methods in previous studies by Ou et al. (2020) and Kulikova et al (2017). We calculate three inversions independent of each other. The first uses phase arrival times from the ISC catalogue, the second uses a combination of phase arrival times we picked and the ISC dataset. The differences in epicentral location are shown in Fig. 2.2b.

Combining the phase arrival times from the digitised waveforms and the ISS bulletin data we calculate, using a 1D velocity model, a new hypocentre of the 1948 Ashgabat earthquake. Due to the trade-off between onset time and depth we have calculated hypocentres at a variety of depths and show results at different confidence intervals. Fig. 2.2(b) shows the epicentral locations and HD calibrated relocation with the error ellipses at different confidence intervals. The results show the possible locations of the hypocentre within three confidence intervals at 1, 2 and 3 standard deviations away from the centre at a fixed depth of 12 km, within the error bounds of a floating result. A fixed depth at 12km is taken from the depth estimate from the HD calibrated results that provide better depth resolution than the 1D location results.

The calibrated HD hypocentre is also plotted showing the horizontal error with a confidence interval of 90%. We show relocated earthquake hypocentres from 1929 to 2019 (Fig. 2.2) in the eastern South Caspian region. The cluster locations were calibrated using Iranian seismic network data. The inclusion of calibration data from the south only may produce an unknown amount of bias in the location.

2.5.3 Focal depth

In the calibrated relocation analysis using MLOC, focal depths may be treated as a free parameter if the arrival time data set includes readings at epicentral distances that are comparable to the focal depth and if such data is available for all or most of the events in the cluster. This is rarely the case, so most calibrated clusters are based on focal depths set manually and fixed for the relocation. Focal depths may be set by several means, depending on the specific composition of an event's arrival time data set. Many events have no suitable data

to constrain focal depth and must be set at some default value if they are to be included in a calibrated cluster (Bergman et al., 2022). For the Ashgabat cluster, which includes several very old events, there is a wide range of circumstances. For the 10 events prior to 1950, focal depths for five are constrained by teleseismic depth phases and the other five are set at a default value of 15 km. More recent events all have depth constraint, mainly from arrival time data at near-source or local-distances, with uncertainties of 3-4 km. Eleven events have depth constraint from teleseismic depth phases, and one (20001206.1711, 7.0Mw) from waveform modelling.

The analysis of teleseismic depth phases is based on the method developed by E. R. Engdahl for the well-known EHB catalogue (Engdahl et al., 1998) with the addition of statistical testing that helps identify outlier readings (of which there are many) and provides a quantitative asymmetric estimate of depth uncertainty. For the 1948 Ashgabat mainshock the depth of 12 km is based on 9 consistent depth phases (7 were dropped as outliers) that yield an uncertainty of 6 km deeper and 4 km shallower.

2.5.4 Focal mechanism calculation

We first calculate focal mechanism solutions from the first motion polarity of P-wave arrivals (Fig. 2.6). Compressional and dilatational arrivals are derived from both the ISC records of ISS bulletins (http://www.isc.ac.uk/iscbulletin/) and from the seismogram digitisations on a lower hemisphere projection (Fig. 2.4). From historical station location records (Chalier, 1952; http://www.isc.ac.uk/iscbulletin/), we calculate ray-path back-azimuths for the ray-paths and find take-off angles from seismic tables from Pho and Behe (1972). We use the Mtfit software to find nodal plane solutions from the first motion data (Pugh and White, 2018). Mtfit uses a probabilistic Bayesian earthquake source mechanism inversion approach developed by Pugh et al., 2016, to estimate moment tensor solutions. In this study we constrain the inversion to be double-couple (DC) using first-motion polarity observations only. We run 10 million iterations of the model and sample from these results. We qualitatively weight the uncertainty in the first motion data based on the quality information in the ISS bulletin and the quality of the first arrival in the digitised waveform. This provides a DC-constrained moment tensor solution with an estimate on the uncertainty of the orientation of the nodal planes.

In Fig. 2.6 we show the first motion data (from Table 2.3) plotted on a lower hemisphere projection showing 1000 randomly sampled solutions within 1% of the maximum probability from the Bayesian inversion (Fig. 2.3). The results show that the earthquake is most likely to be a strike-slip event. The nodal planes show that strike is most likely to be at either 120° or 30°, for right-lateral and left-lateral slip respectively, and there is good constraint on the 120° nodal plane. Three of the four stations in the eastern hemisphere of the plot are from the digitised waveforms and we have a higher level of confidence in the polarities of the first motions from this data. For stations where we have both a digitised seismogram and an ISS record of the first motion, we recorded agreement in all cases.

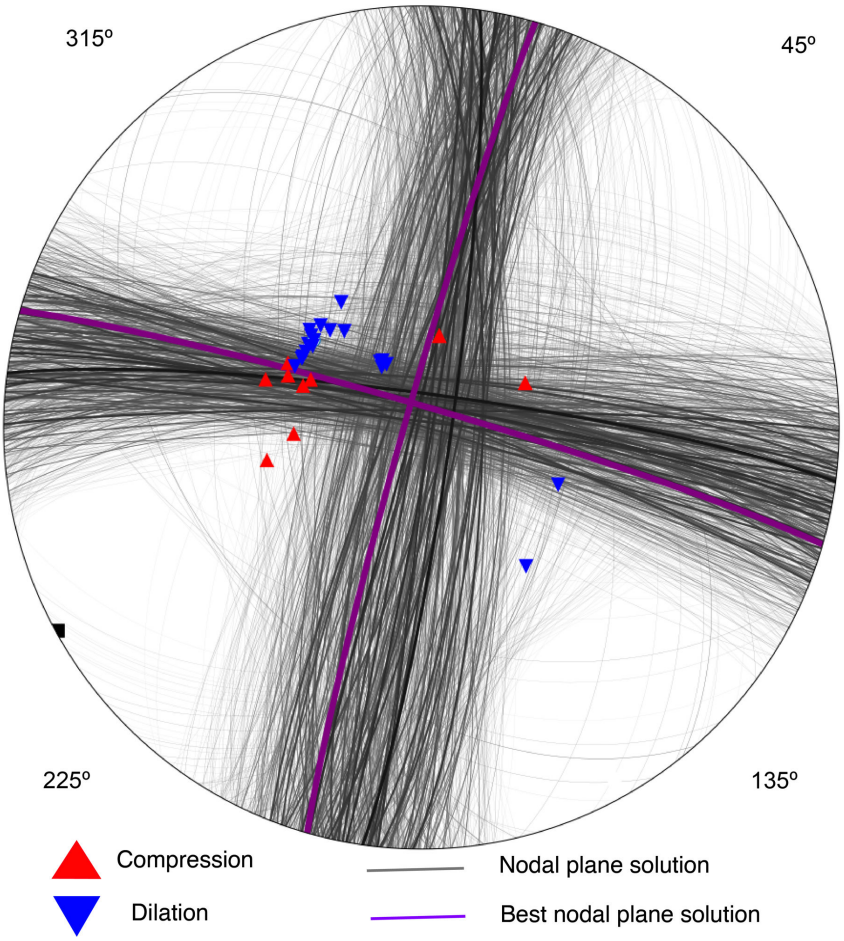


Figure 2.6. Focal Mechanism beach-ball lower hemisphere projection for first motion polarities of P-wave arrivals. Blue triangles are compressions; Red triangles are compressions; grey nodal planes are a random sample of 1000 solutions within 1% of the maximum probability of the Bayesian inversion; purple nodal plane represents the best fit.

In addition to using first motion polarities, we also determine focal mechanism solutions by fitting the radiation pattern in terms of the ratio between P- and S-phase amplitudes (Fig. 2.7).

We use the method detailed in Ou et al. (2020) modified for our station network distribution and instrument components. We perform a grid search through strikes between 20° and 180°, dips between 20° and 90° and rakes between -180° and 180°. We varied the depth between 10 km and 20 km to establish the depth sensitivity of the results and fix a depth at 12 km from the depth determined for the calibrated hypocentre using the MLOC method. Fig. 2.7 shows the best fit strike, dip and rake for a centroid depth of 12 km. We also fix strike at 120° taken from the first motion focal mechanism solution and this is within trend of the main faulting in this region (Rozoghin et al., 1994; Walker et al., 2021).

The focal mechanisms in Fig. 2.7 are sized inversely proportional to the misfit between the result and the model, with the largest mechanisms having the smallest misfit. The best solution from this analysis also shows that the mechanism is most likely to be strike-slip. However, due to the coverage of usable waveforms (Fig 5b) we cannot constrain the dip. The rake shows better constraint with the best solutions occurring at 160° to 180° degrees or -20° to 0° degrees depending on whether this event is left- or right-lateral.

5.5. Magnitude determination

Previous studies calculate a surface-wave magnitude of 7.3 (Shebalin & Tatevossian, 1996). We estimate mB and Mw following Bormann 2012 and Bormann & Saul, 2008 using the following equations:

$$m_B = \log\left(\frac{A_H}{T}\right)_{max} + Q(\Delta), \quad (1)$$

$$M_w = 1.33 m_B - 2.36 \quad (2)$$

where A_H is the vectorially combined horizontal phase amplitude in μm and T is the corresponding period in s. Δ is the epicentral distance, and Q is a distance- and phase-dependent calibration value tabulated in Gutenberg and Richter (1956).

We use the 5 stations that have vertical components from our digitised catalogue and measure A_H and T from the P and PP phases. This yields an estimate of $m_B = 7.26 \pm 1.0$ and $M_w = 7.29 \pm 1.4$. The high levels of uncertainty in our magnitude estimates reflect data quality issues with instrument parameters. As a result, we decided not to perform moment magnitude (M_w) calculation using waveform modelling as in Kulikova & Krüger, 2015, 2017; Kulikova et al.,2016; and Ou et al. 2020.

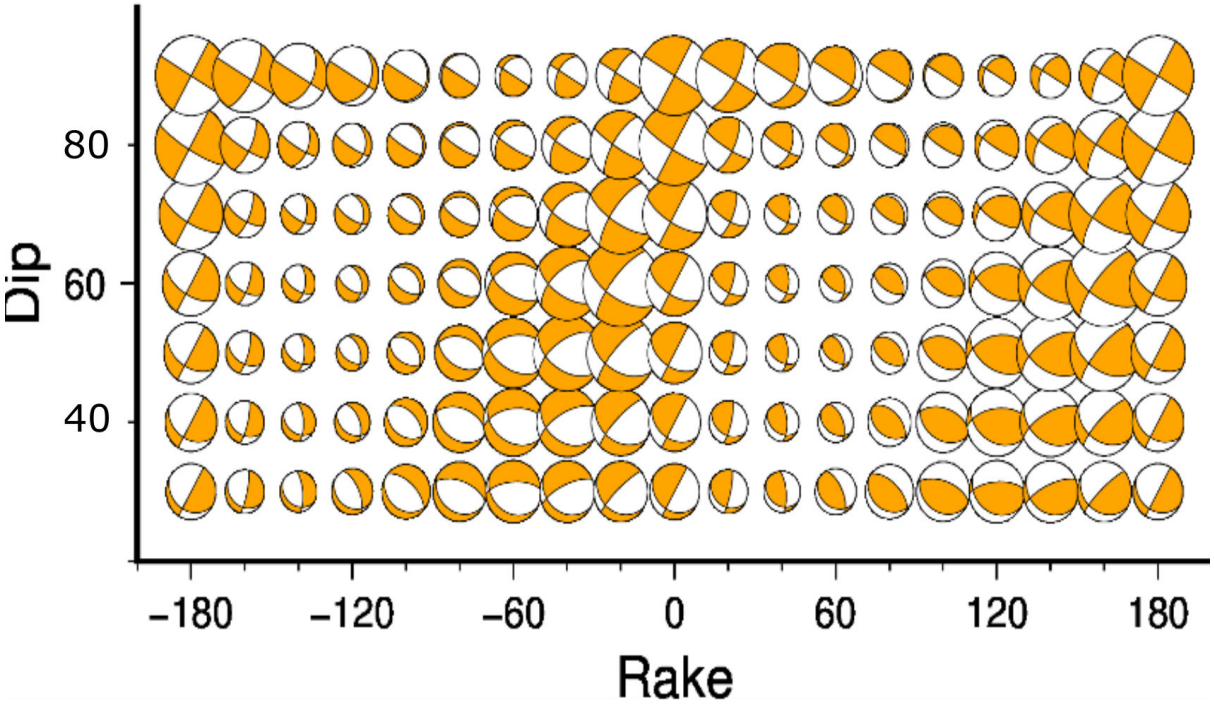


Figure 2.7. Amplitude ratio focal mechanism results with fixed strike at 120˚ and depth at 12 km. Dip and rake are calculated at 10˚ and 20 ° increments, respectively. The mechanisms are scaled by the misfit to the model, with larger mechanisms having the lowest misfit.

2.6 Tectonic geomorphology

We combine the seismic analyses and contemporary studies of surface rupture and intensities from the 1948 earthquake with an investigation of the tectonic geomorphology of the Ashgabat region, using archive Corona satellite imagery from 1967, modern high-resolution satellite imagery, and derived DEMs to identify active faults from their expression in the landscape. This analysis allows us to identify potential causative faults of the 1948 earthquake, and to identify fault traces that do not appear to have ruptured the surface. The analysis allows us to better understand the tectonic context of the Ashgabat region, as well as to identify and characterise faults that pose continuing risk to the city and nearby regions. We characterise the active faulting in the area south and east of Ashgabat, in which 1948 earthquake ruptures were reported, both within the city itself and along the range front adjacent to Bezmein (Abadan) to the west of Ashgabat.

2.6.1. Gyaursdag anticline

Surface displacements were mapped within the northern limb of the Gyaursdag anticline (Figs 2.3 and 2.4). The Gyaursdag anticline is asymmetric, with its core sited close to its northern margin. This arrangement is suggestive of a fault-related fold forming due to slip above a south-dipping thrust fault. No discrete fault scarps are visible at the northern edge of the fold, suggesting that the underlying thrust tip is buried. The preservation of both fold limbs is also strong corroborating evidence that the fault does not reach the surface.

Prominent south-facing scarps are visible in satellite imagery along the northern fold limb (e.g. Fig. 2.4b). These scarps run parallel to north-tilted bedding in basin sediments, and are visible also in young alluvial materials. We interpret them as bedding slip faults resulting from fold growth (e.g., Cooke and Pollard, 1997; Nicol and Nathan, 2010). The mapped 1948 ruptures (Fig. 2.3) show an en-echelon arrangement that may represent a lateral component of slip, suggestive of a tectonic origin. However, the detailed example from Kuru Gaudan shown in Figs 2.4(c and d) show correlation between the locations of the surface deformation and the local topography, suggesting that they may relate, in part, to secondary deformation caused by shaking.

2.6.2 Southeast of Ashgabat

Some of the most extensive ruptures reported from the 1948 occurred southeast of Ashgabat, along the Kharvardaghskiy fault, referred to as rupture zone B (Fig. 2.3). In Fig. 2.8a we show a Corona satellite image from 1967, extending from Ashgabat in the northwest to Nokhandan, in Iran, in the southeast, with the Kharvardaghskiy fault extending through the central part of the image. We have mapped geomorphic fault traces onto this image (in red) and the axes of major folds in bedrock (in yellow).

The Corona imagery was acquired 18 years after the earthquake and is more likely to retain evidence of ground deformation from the 1948 earthquake, and potentially also from older events, than modern imagery. Near Manysh, we identify three ‘fresh’ landslide scars visible in proximity to the fault trace (green circles in Fig. 2.8(a)). We also identify a sharp NW-SE trace within alluvial surfaces, accompanied by consistent small stream displacements of ~ 15 m, as identified by shadowing, and marked by white arrows in Fig. 8b. It is possible, though not

confirmed, that this surface trace in the Corona image represents surface rupturing from the 1948 earthquake. It is no longer visible in modern imagery due to urban development.

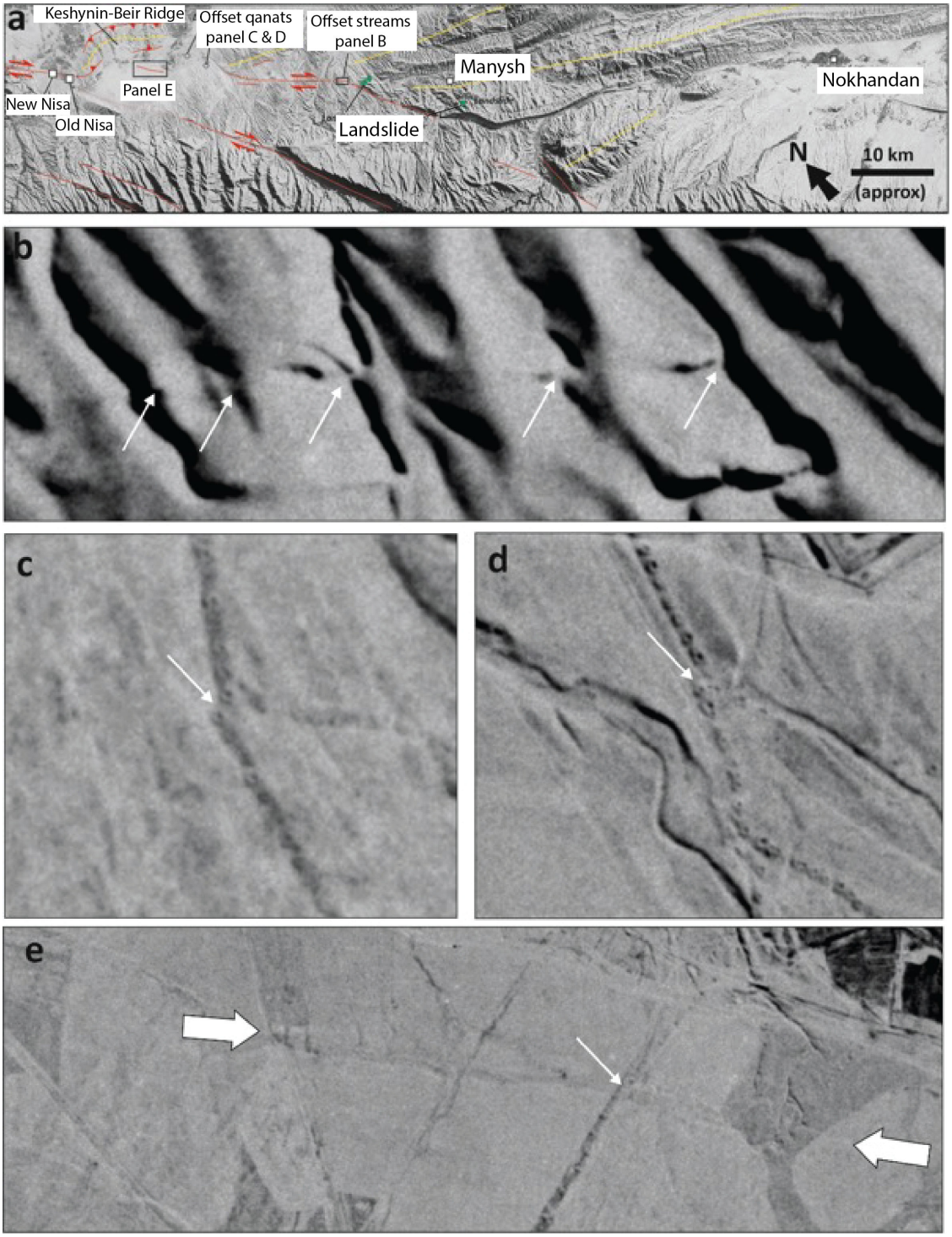


Figure 2.8 (a) Heritage Corona imagery from 1967 showing the region from Nisa in the northwest, to Nokhandan in the southeast (see Fig. 2.3 for location). Major fold axes are shown in yellow, and active faults in red. Three landslides south and west of Manysh are marked in green. Areas shown in later panels are marked. (b) aligned right-lateral stream displacements marked by white arrows. (c-d) Apparent qanat offsets of ~5 m. (e) Possible

fault scarp south of Ashgabat, running between thick white arrows, with a further potential qanat offset marked by a thin white arrow.

There is evidence for cumulative late Quaternary displacement along the Kharvardaghskiy fault in the form of scarps in alluvial terraces, and the right-lateral displacement of streams and rivers. In Fig. 2.9(a) we show a Pleiades-derived DEM of the fault zone crossing heavily incised alluvial fan deposits immediately southeast of Ashgabat, at the very northern end of the mapped Rupture Zone B (Fig. 2.3). Georeferenced rupture locations from Rogozhin (1994) are shown as yellow lines (note that the locations are not necessarily accurate). In red, we highlight minor drainage channels within the alluvial fan that appear to be displaced right-laterally by ~40m across two closely spaced fault traces, near the yellow lines. The northern of these two faults has a vertical component, with the northern side uplifted relative to the southern side. A third fault trace, again with a greater total uplift of the northern side, is visible near the top of Fig 2.9(a). We could not find evidence of rupture from the 1948 earth along the third fault.

2.6.3 Ashgabat

Ashgabat city lies on an ~5-km-wide low-relief plain, occupying the area between the low hills of the Gyaursdag anticline to the southeast, and the Keshenyn-Bair ridge to the northwest. The Keshenyn-Bair ridge is a narrow (3 km wide) asymmetric anticline, with a maximum relief of ~70 m above the surrounding plains. It has a slight northward vergence, though with localised steepening on its southern side towards both east and western fold tips. Tilted basin sediments are exposed within drainage incised into the fold. The basin sediments are overlain by alluvial gravels that are parallel to the fold shape. Discontinuous ground deformations were observed within the ridge after the 1948 earthquake (e.g. Fig. 2.3).

No surface ruptures were reported in the region between the Keshenyn-Bair ridge and the Gyaursdag hills, in the region closest to Ashgabat itself. In Fig. 2.8c-d we show apparent right-lateral offsets of two qanats (underground canals, identified from the aligned access shafts and spoil heaps), which are in a direct alignment between the south-eastern margin of the Keshenyn-Bair ridge and the right-lateral faults we identify in Fig. 2.9(a), which are part of Rupture zone B. In both cases the qanats are offset by an amount equal to the width of the spoil heaps, which is ~5m, thought to be Sassanian or younger, > 200 C.E. A second possible fault

scarp is identified south of the Keshenyn-Bair ridge (Fig. 2.8e), along which there is a third possible qanat displacement.

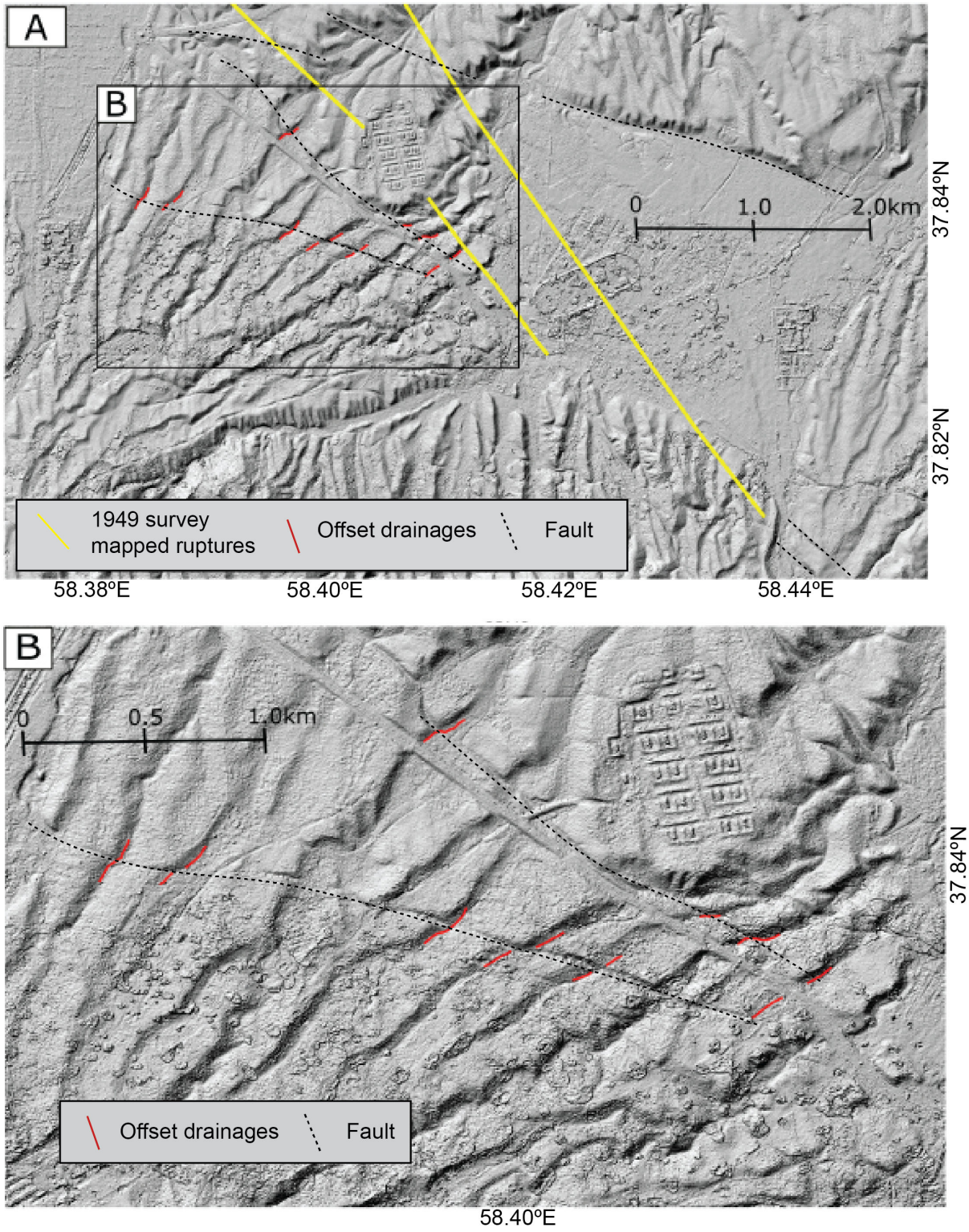


Figure 2.9 (a) Pleiades-derived DEM showing post-earthquake mapped ruptures southeast of Ashgabat (yellow lines) adjacent to two scarps with cumulative right-lateral displacement of minor drainage channels within an incised alluvial fan surface, which we infer to be the scarps that ruptured in the earthquake. The resolution of the georeferenced mapped ruptures is low, and these may not exactly locate the ruptured fault. Towards the top of the

image, a third fault scarp with clear up to the north displacement is visible, but does not appear to have ruptured at the surface in 1948. (b) Close-up of the two fault scarps with cumulative right-lateral stream displacements marked.

To further investigate the potential for faulting extending through the southern districts of Ashgabat, and connecting Rupture zone B to the Keshenyn-Bair ridge (Rupture zone C) (Fig. 2.3), we extract a number of topographic profiles through Pleiades-derived digital topography (Fig. 2.10). Each of the profiles shows slight warping and folding of the alluvial surface, with the width and amplitude of the fold increasing to the southeast, and with a general change from northward vergence in the northwest to southward vergence in the southeast. In Fig. 2.10 we mark the margins of the topographic folding as white arrows, and also mark the positions of the two offset qanats. There is close alignment in the positions of the offset qanat and the fold margin in profile B, whereas in profile A the offset qanat lies ~2 km south of the visible folding.

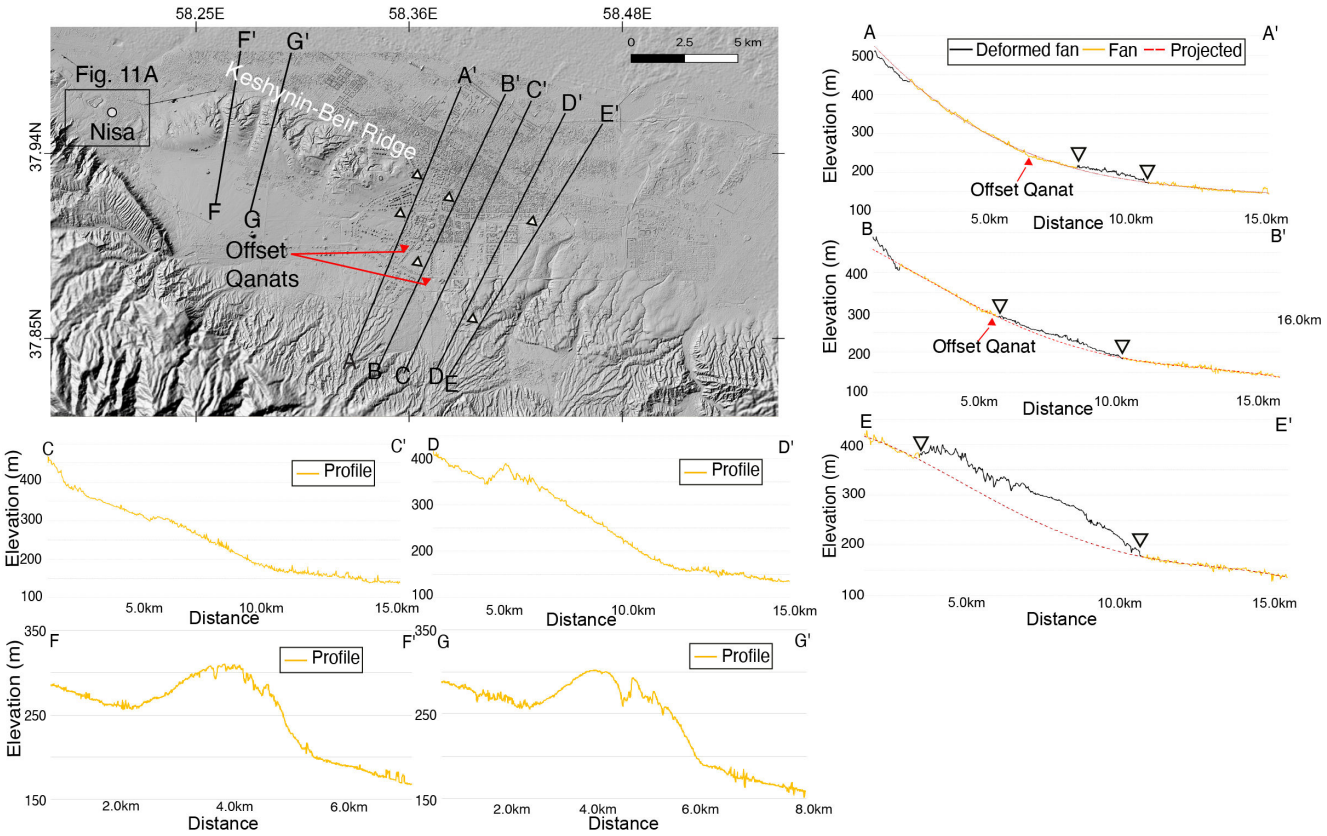


Figure 2.10 World View 3 DEM of the Ashgabat area. White triangles show limits of folding as identified from topographic profiles. The red triangles show offset qanats (c.f. Fig. 8c-d).

2.6.4 West of Ashgabat

West of Ashgabat an active fault extends northwest from the Keshenyn-Bair ridge, traverses a low relief area at Nisa, and localises along the base of the Kopeh Dagh mountains (Fig. 2.10a). This section of fault is the easternmost 'Gökdepe' segment of the Main Kopeh Dagh fault (MKDF) as defined by Dodds et al., (2022). There are a number of archaeological sites in the region, but by far the most famous are the twin settlement mounds of Nisa.

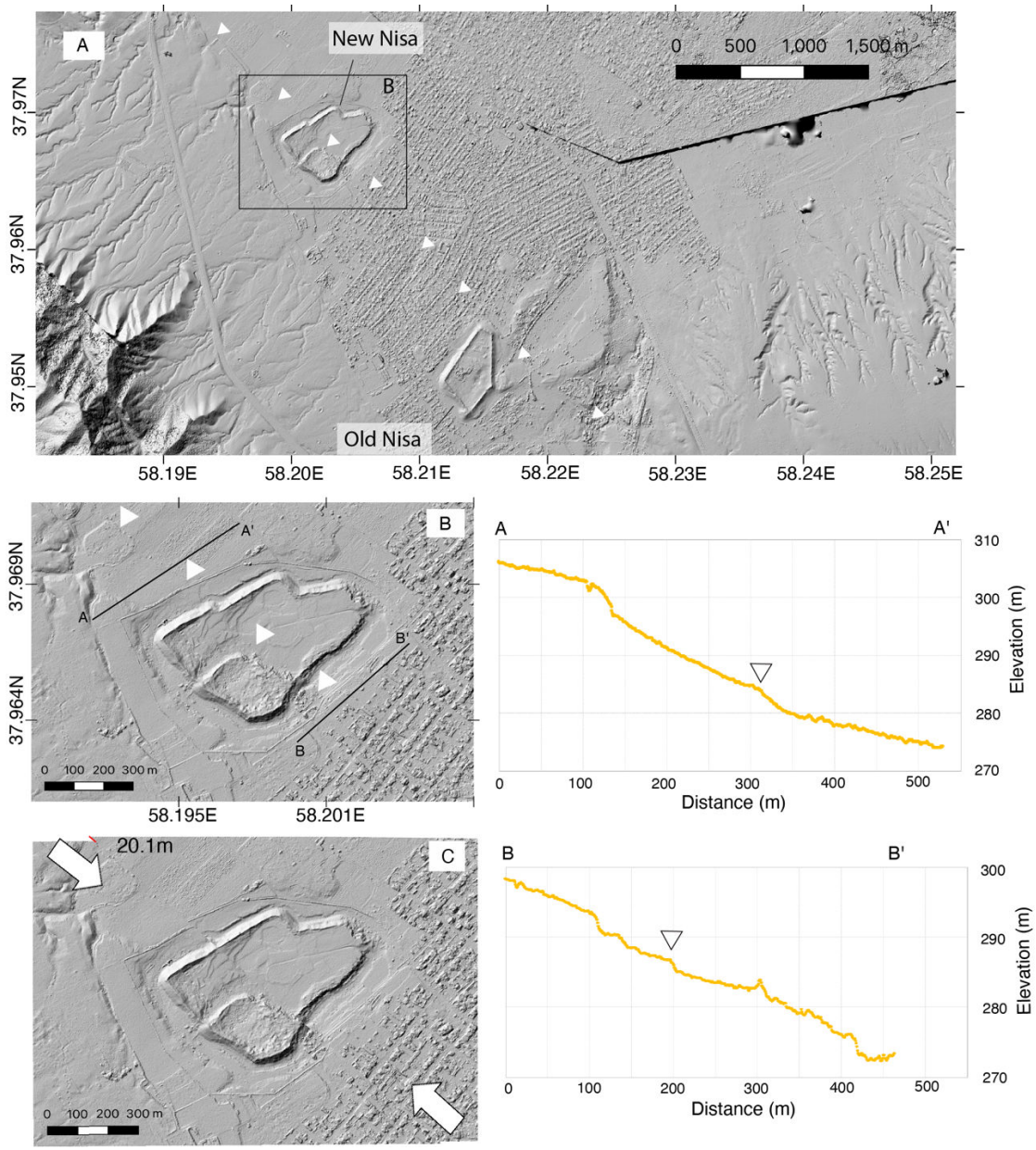


Figure 2.11 **(A)** DEM derived from WorldView 3 stereo imagery of the ancient city of Nisa. Triangles delineate the fault trace of the right-lateral MKDF. Box shown in (B). **(B)** Shows the zoomed DEM of the archaeological site New Nisa. The west wall shows an apparent offset at the fault trace. Profiles A-A' and B-B' show a scarp at the fault trace (at triangles). **(C)** Clipped (B) along the fault trace. Restoring the west wall of New Nisa measures at 20.1 m.

Both of these mounds show traces of early occupation in the Parthian era (ca. 247 BCE – 224 CE), but are then subsequently reoccupied, with substantial settlement in and around the

northernmost mound (Fig. 2.10a). The fault trace passes immediately north of 'Old' Nisa, and cuts through the centre of 'New' Nisa (Fig. 2.11a).

The fault scarp at New Nisa has a consistent northeast-facing scarp of ~5 m height. The north-western wall of the walled city shows a sharp deflection at the scarp, consistent with ~20 m of right-lateral displacement (Fig. 2.11). This misalignment was seemingly first identified by Poletaev (1986) through an examination of aerial photography and in the field. From current satellite imagery, the south-eastern wall of the city does not show a clear displacement at the fault trace. If this apparent displacement is real, it suggests that the eastern wall of the fortress was rebuilt and realigned.

West of Nisa the fault runs along the base of the Kopeh Dagh. Uplift of the southern side is apparent from suites of fluvial-alluvial terraces truncated at the fault. In Fig. 2.12 we show a suite of five terraces (labelled Q1 to Q5) preserved on the southern side of the Chuli river catchment. Here the terrace treads are extensive and well-preserved (Figs 2.12a and b), though modified by the presence of ancient sites of unknown age (particularly on the Q4 surface). The youngest surface (Q1) has no visible scarp at the fault. Topographic profiles through Q3, Q4 and Q5 show vertical displacement of 10.4 ± 0.3 m, 24.1 ± 0.4 m and 59.1 ± 0.5 m. It is likely that these vertical displacements are accompanied by significant amounts of right-lateral slip.

Roughly 5 km further west along the range front the fault cuts slightly into the range-front, forming shutter ridges with ~150 m of displacement (Fig. 2.13), though there are no markers of lateral displacement here site from which we can determine a strike-slip rate.

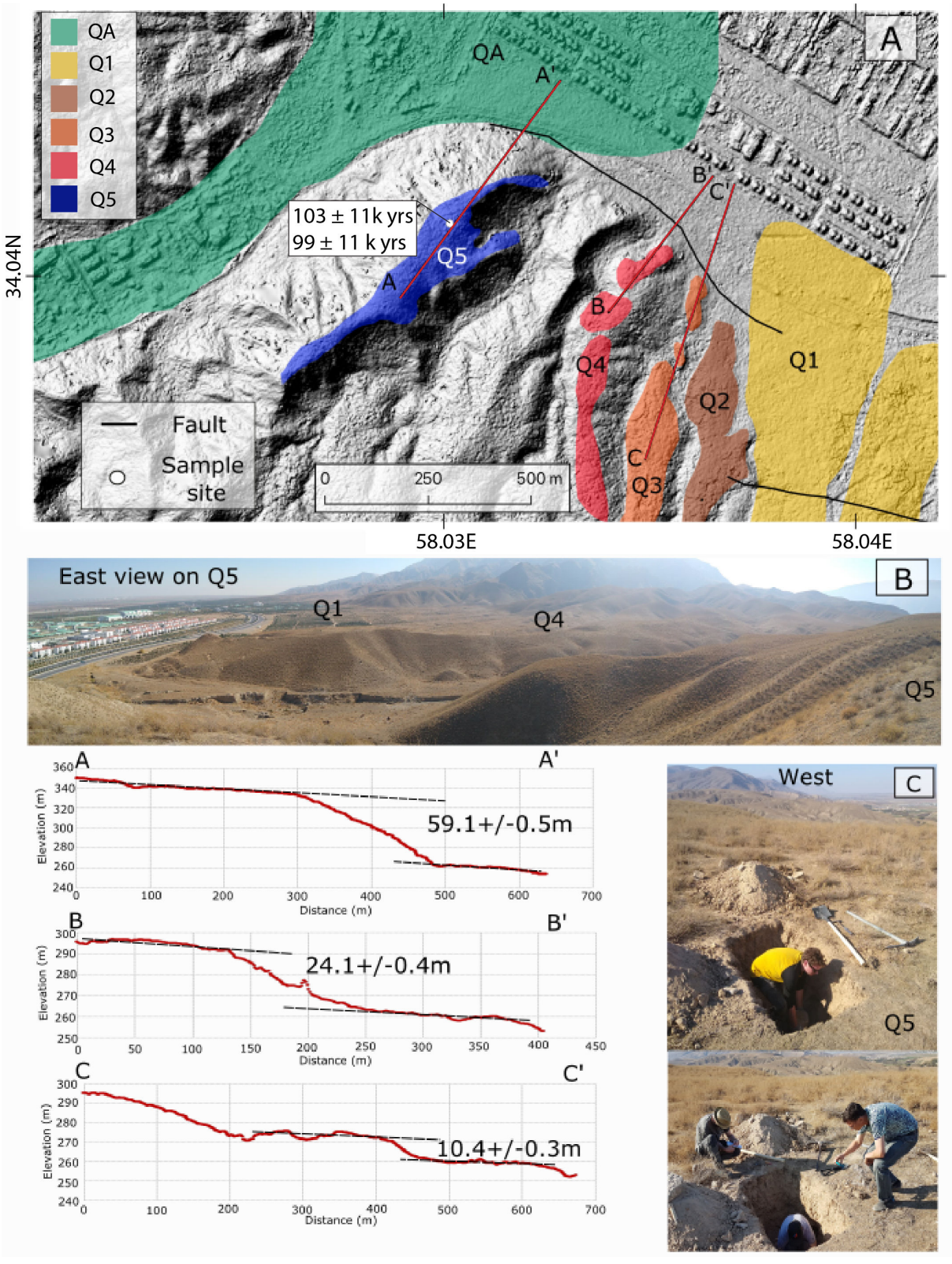


Figure 2.12 (A) Pleiades DEM and geomorphic map of the region just to west of Ashgabat. Profiles show elevation taken from the DEM. The oldest geomorphic surface was sampled and IRSL ages calculated. Q5 is dated at 99-103 +/- 11k years (see text). (B) Photograph taken looking East at the sample site (white dot) on the Q5 surface shown in A. (C) Photographs taken facing west at the sample site in (A).

In order to determine the long-term dip-slip rate across the MKDF in this segment we collected three samples for Infrared Stimulated Luminescence (IRSL) dating, from a soil pit dug into the Q5 surface. The IRSL samples returned ages of 3.61 ± 0.88ka (100 cm), 98.8 ± 11ka (55 cm) and 102.7 ± 11ka (100 cm) (Table 2.4), which we note are similar in age to the prominent alluvial fan surfaces dated at 100 ± 5 ka by Walker et al., (2021), from 150 km further northwest along the range front. The sample TK19-09 returning an age of 3.61 ± 0.88ka was produced by 4 grains. The surface shows evidence for human activity and is a possible source for contamination causing the outlying age, but this does not appear to have affected the loess layer above. The ~100 ka age of Q5, combined with a vertical offset of ~60 m allows us to estimate an uplift rate of ~ 0.6 mm/yr. This rate assumes no erosion or deposition since the formation of Q5 and the vertical rate will be accompanied by an unknown, dominant, right-lateral strike-slip component.

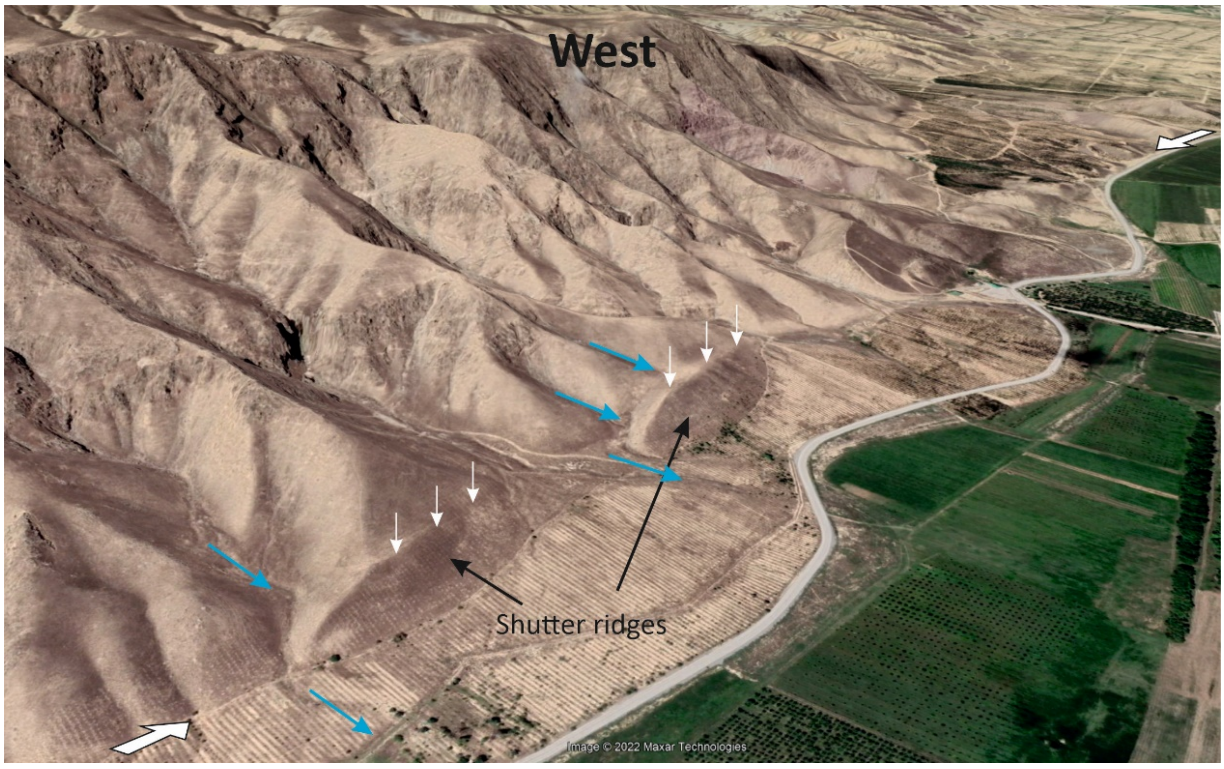


Figure 2.13 Perspective view looking west across the Main Kopeh Dagh fault, running between the thick white arrows, ~5 km northwest from the region shown in Fig. 12a (centre coordinate at 38.072590N, 57.975358E, see Fig. 3 for location). The fault trace cuts across hillslopes (scarps shown by vertical white arrows) and has right-laterally displaced the lower portions of the hillslopes, which now form shutter ridges. Drainage channels (blue) are displaced by ~150 m around the ends of these shutter ridges.

2.7. Discussion

2.7.1 Multi-segmented rupture

By combining the focal mechanism and epicentral results (as summarised on Fig. 3) from this study with the isoseismal maps and the mapped ruptures from the 1949 survey (also on Fig. 3) we suggest that the earthquake nucleated immediately north of the city, and is likely to have ruptured several fault segments. The first causative fault (rupture zone B) extends southeast from Ashgabat for a distance of ~40 km, following a prominent right-lateral fault. Cumulative right-lateral displacements are visible as this fault crosses alluvial fan surfaces, and potential single-event scarps and associated landslides are identified in legacy Corona imagery from 1967.

Fracturing along the northern margin of the Gyaursdag anticline (Rupture zone A) likely indicates rupture of a southward-dipping thrust fault, which may connect with Rupture zone B at depth. Although some of the ruptures along the Gyaursdag anticline may relate to secondary shaking effects, the en-echelon arrangement of fractures, the telescoping of water pipes, and the reported subsidence in the footwall of the fault from railroad levelling surveys, all suggest fault slip along the Gyaursdag structure. It is unlikely that the primary slip on the Gyaursdag fault reached the surface, with observed faulting relating to secondary fold growth structures.

Another potential rupture zone extends ~30 km northwest from the epicentre. Surface rupturing of 'Zone C' is associated with this fault segment. Although the rupturing itself is ambiguous in origin, and may be caused by liquefaction and other secondary effects, the post-1948 Railroad levelling survey indicates a mixture of uplift (33 cm at Büzmeýin (Bezmein/Abadan) west of Ashgabat, and right lateral displacement (178-190 cm at Ashgabat), both of which are sited north of the observed surface ruptures and fault scarps that we have described and we are unable to locate these sites in the recent satellite imagery. This proposed third segment does not have any visible expression at the surface, suggesting that additional active faults may exist north of the main range front of the Kopeh Dagh, as also suggested by strain accumulation ~10-30 km north of the range front, measured further northwest using InSAR (Dodds et al., 2021).

The overall rupture length is thus ~ 70 km, though with a gap in between the two main rupture zones of 10 km, giving a total of 80 km if this gap in surface observations is also included. The only measurement of co-seismic lateral displacement is 178-190 cm of the railroad at Ashgabat, near the centre of the inferred rupture.

Using Wesnousky (2008) scaling relationships we estimate the M_w and slip from the total rupture length. From the observed total rupture length of 80 km, we use the relationship

$$M_w = 5.56 + 0.87 \times \log\big(length(km)\big) \quad (3)$$

for strike-slip faulting, giving $M_w = 7.2$. To calculate the maximum slip, we use the log-linear relationship:

$$slip\ (m) = -5.02 + 5.02 \times \log\big(length\ (km)\big) = 4.5m. \quad (4)$$

These values are reasonable estimates given the previous calculations of moment magnitude of 7.3 (McKenzie, 1972; Shebalin & Tatevossian, 1996) and our estimate of $M_w = 7.29 \pm 1.4$. Given the only measurement of lateral displacement is between 1.8 – 1.9 m in rupture zone, there is still uncertainty associated with the maximum and minimum slip.

The faults that are not known to have ruptured in the 1948 earthquake are also of interest. We have identified a continuation of faulting and folding northwest of rupture zone B that extends through southern districts of the modern city to connect with the Keshynin Bair ridge. This fault zone crosses open ground outside the 1948 urban extent, and we expect that any surface ruptures upon it would have been identified in the post-earthquake surveys. We therefore consider the gap in surface rupturing to be real. Two qanat lines are displaced right-laterally across the fault trace by ~5 m, suggesting rupture in unknown prior events or postseismic deformation.

The Keshynin Bair ridge is a northward-verging anticline (e.g. Fig. 2.10), which we infer to overlie a south-dipping thrust that joins at depth with the strike-slip fault on its southern side. A number of surface cracks were observed along the apex of the Keshynin Bair ridge, which may represent co-seismic fold growth, or may represent secondary effects. Northwest of the ridge, the right-lateral strike-slip fault trace is clearly visible in satellite imagery, and appears to offset the outer walls of New Nisa, whose fortifed walls are believed to be laid out initially in the Parthian era (3rd-2nd century CE). Again, there is no record at this site of rupturing caused by the 1948 earthquake, and the archaeologists who were working at the site were most active during this period (some of the archaeologists on the team were sadly even injured or killed in

the event). The displacements of ~20 m, if real therefore, indicate several prior events have occurred since the walls were constructed.

The misalignment of the wall at New Nisa was first identified through an examination of aerial photography and in the field (Poletaev 1986). Poletaev's study identified a 1.5 m difference in height between the northeastern and southwestern sectors of the walled city, bisected by the fault. He further subdivided the southwestern sector into two distinct zones, the northwestern being slightly higher than the southern, although the latter apparently had better preservation of archaeology. This interpretation seems to be at odds, however, with the archaeological data from the site gathered by the South-Turkmenistan Archaeological Comprehensive Expedition (IuTAKE) in the 1940s, which identified the southern area as the higher mound of an inner walled citadel (Masson 1949). It is tricky, then, to disambiguate the synthetic structural components of the city, its walls and landscaping, from the perceived deformation of the land. Furthermore, it was observed already in the 1940s that local farmers were terraforming and reutilising areas of the walled city and citadel (Pugachenkova 1949).

The history of the settlement and its walls might have been disambiguated through the stratigraphy of the test-trenches and sections dug around the city, but the majority proved inconclusive in terms of determining major topographical shifts. Based on the work of the IUTAKE 1940s missions, they observed that the site was probably occupied, and indeed walled initially between the 3rd -2nd centuries BCE, with general signs of decline going into the first millennium CE (Masson 1949; Viaz'mitina 1951). According to the same authors, there is resumed activity in the 4th-8th centuries CE and then again between the 11th-13th and 15th-17th centuries, based on ceramic chronology.

It is possible to suggest that the periodic abandonment of the site might be linked to seismic activity. Based on the identification of a sudden collapse in the excavations at the nearby site of Old Nisa, Masson and colleagues proposed a date in the first century BCE or CE for a significant earthquake, which has subsequently been quoted as definitive in the major earthquake catalogues for the region (Pugachenkova 1951). An additional fifth century event was similarly identified by archaeologists at Old Nisa from collapse evidence but was later refuted and indeed is not mentioned in the interpretation of the sequence at New Nisa (Davidovich 1951).

Turning to the 8th - 10th century hiatus at New Nisa, the explanation for abandonment is unclear. It is particularly pertinent to note that evidence of significant decline includes the ruin of the city walls and their complete lack of upkeep, to the extent that domestic buildings were being built on top of the collapsed defences (Viaz'mitina 1951). As Pilipko points out, the interpretation for the stratigraphy for this period is difficult to unravel at the site, with complex reuse, and his attempts to revisit this sequence have not been able to define the abandonment more clearly (Pilipko 2010). Meanwhile 10th century historical sources on the city seem to indicate that it was flourishing, although it is unclear exactly the material on which this account is based, or indeed the specific zones of the city which are being described (al-Muqaddasi 2001). Considering this difficulty of interpretation, alongside the significant general reappraisal of medieval ceramic chronologies since the excavations took place, it might be possible to connect the later abandonment to the known catastrophic seismic event of 943CE, recorded by 12th century historian Ibn al-Athir and others. Based on additional evidence for landslides around the same time elsewhere, Melville and Ambraseys (1982) place the event instead in the southern part of the Kopeh Dagh. Until further archaeological and palaeoseismic work can refine the location and impacts of the 943 earthquake, it is possible that the traces of displacement being observed relate to this period, after which the walls are known to be rebuilt.

Finally, the improved determination of the 1948 earthquake source, and mapping of faults around the wider Ashgabat region, is useful in refining our understanding of the regional fault kinematics. We have shown that Ashgabat is sited at a transition from right-lateral faulting cutting through the interior of the Kopeh Dagh mountains as part of the BQFZ (Fig. 2.1), to faults that run along the range-front as the easternmost parts of the MKDF. As such, the faults here are likely to be contributing to the NNW motion of the South Caspian Basin relative to Eurasia. Further northwest, the MKDF has consistent long-term geological 9.1 ± 1.3 mm/yr (Walker et al., 2021), and decadal 9 ± 2 mm/yr (Dodds et al., 2021) slip rates. From existing GNSS measurements (e.g. Mousavi et al., 2013; Khorrami et al., 2019) and kinematic models (e.g. Hollingsworth et al., 2010; Walker et al., 2021) we expect those rates to decrease eastwards, as the South Caspian motion is accommodated at its eastern end by block rotations and fault slip in the BQFZ. The apparent right-lateral displacements of cultural sites around Ashgabat are interesting in this respect, as they suggest relatively rapid accumulation of slip over the last few thousand years in an area that we would expect the faults to have relatively

low overall slip-rates. Either the displacements are misleading, the fault slip-rates are higher than we expect or, potentially, we are seeing the effects of millennial -scale variability in fault slip. Detailed paleoseismic investigation and slip-rate determination are required to test which of these is correct.

2.8 Conclusion

We show that the 1948 Ashgabat earthquake was a right-lateral strike-slip event most likely nucleating immediately north of Ashgabat, and involving bilateral rupture on at least two separate faults with a total length of ~80 km. Active faults within the southern districts of Ashgabat and adjacent areas to the west do not appear to have ruptured at the surface in the 1948 earthquake, and yet show apparent significant displacement in cultural sites, including qanats (Sassanian or younger, > 200 C.E.), and the walls of Nisa (Parthian, ~200 B.C.E). These observations suggest continuing local earthquake hazard in Ashgabat. The faults involved in the 1948 earthquake are at the easternmost end of the Kopeh Dagh strike-slip fault system, and show a transition of slip from the range-front right-lateral faults to those that cut through the Kopeh Dagh interior, as part of the BQFZ. The north-western fault segment is not apparent in the geomorphology and is sited ~15 km north of the prominent range-front, highlighting the potential hazards posed by 'concealed' active faults in low-relief regions.

Acknowledgements

This work was supported by the Leverhulme Trust Research Project Grants 'EROICA' (RPG-2018-371) and 'NEPTUNE' (RPG-2018-243), by the NERC-ESRC Increasing Resilience to Natural Hazards program 'Earthquakes without Frontiers' (NE/J02001X/1), the NERC-funded COMET (GA/13/M/031), and allocation 0009090 from the Research England GCRF Support Fund. Pleiades satellite imagery was obtained through the Committee for Earth Observing satellites (CEOS) Seismic Hazard demonstrator. Worldview-3 satellite imagery was obtained through the NERC grant 'Looking into the Continents from Space' (NE/K011006/1). Maps were prepared using Generic Mapping Tools software [Wessel and Smith, 1995].

Data Tables

Table 2.1 Phase arrival times from the 1948 Ashgabat earthquake from a global network of seismometers constructed from the ISC Bulletin database (International Seismological Centre, 2022) and the digitised waveforms.

Station	Location	Phase	Arrival Time	Digitised
SAM	Samarkand, Uzbekistan	P	20:13:47	N
BAK	Baku, Azerbaijan	P	20:13:51	N
DSH	Dushanbe, Tajikistan	P	20:14:07	N
TAS	Tashkent, Uzbekistan	P	20:14:16	N
KUL	Kulyob, Tajikistan	P	20:14:17	N
CHM	Chimkent, Kazakhstan	P	20:14:23	N
GRO	Groznyy, Russia	P	20:14:44	N
ANR	Andizhan, Uzbekistan	P	20:14:44	N
LEN	Gyumri, Armenia	P	20:14:48	N
ERE	Yerevan, Armenia	P	20:14:49	N
MUR	Murghob, Tajikistan	P	20:15:02	N
PYA	Pyatigorsk, Russia	P	20:15:09	N
FRU	Bishkek, Kyrgyzstan	P	20:15:14	N
DSH	Dushanbe, Tajikistan	S	20:15:38	N
SOC	Sochi, Russia	P	20:15:39	N
AAA	Almaty, Kazakhstan	P	20:15:40	N
TAS	Tashkent, Uzbekistan	S	20:15:56	N
CHM	Chimkent, Kazakhstan	S	20:16:12	N
FEO	Feodosiya, Crimea	P	20:16:24	N
SVE	Sverdlovsk, Russia	P	20:16:25	N
KSA	Ksara, Lebonan	P	20:16:26	N
YAL	Yalta, Crimea	P	20:16:27	N
SIM	Simferopol, Crimea	P	20:16:35	N
ANR	Andizhan, Uzbekistan	S	20:16:47	N
GRO	Groznyy, Russia	S	20:16:52	N
ERE	Yerevan, Armenia	S	20:16:54	N
DDI	Dehran Dun, India	P	20:17:00	N
MOS	Moscow, Russia	P	20:17:07	N
ISK	Istanbul, Turkey	P	20:17:09	N
BOM	Bombay, India	P	20:17:14	Y
HLW	Helwan, Egypt	P	20:17:18	N

CRB	Chernovtsy, Ukraine	P	20:17:25	N
BOM	Bombay, India	PP	20:17:31	Y
PYA	Pyatigorsk, Russia	S	20:17:31	N
BUC	Bucharest, Romania	P	20:17:36	N
FRU	Bishkek, Kyrgyzstan	S	20:17:37	N
CMP	Campulung, Romania	P	20:17:44	N
HYD	Hyderabad, India	P	20:17:50	N
BEO	Belgrade, Serbia	P	20:18:08	N
BUD	Budapest, Hungary	P	20:18:08	N
CAL	Calcutta, India	P	20:18:10	N
WAR	Warsaw, Poland	P	20:18:13	N
SOC	Sochi, Russia	S	20:18:20	N
HEL	Helsinki, Finland	P	20:18:22	N
AAA	Almaty, Kazakhstan	S	20:18:27	N
RAC	Raciborz, Poland	P	20:18:29	N
TAR	Taranto, Italy	P	20:18:29	N
KOD	Kodaikanal, India	P	20:18:40	N
PRA	Prague, Czech Republic	P	20:18:46	N
CAT	Catania, Italy	P	20:18:47	N
TRS	Trieste, Italy	P	20:18:51	N
IRK	Irkutsk, Russia	P	20:18:53	Y
CLL	Collm, Germany	P	20:18:57	N
ROM	Rome, Italy	P	20:18:59	N
COP	Copenhagen, Denmark	P	20:19:03	N
CAL	Calcutta, India	PP	20:19:05	N
BOL	Bologna, Italy	P	20:19:07	N
FIR	Florence, Italy	P	20:19:07	N
COC	Colombo, Sri Lanka	P	20:19:08	N
MES	Messina, Italy	P	20:19:12	N
CHU	Chur, Switzerland	P	20:19:12	N
SAL	Salo, Italy	P	20:19:13	N
POT	Potsdam, Germany	P	20:19:17	Y
DBN	De Bilt, Holland	P	20:19:43	Y
SVE	Sverdlovsk, Russia	S	20:19:54	N
FEO	Feodosiya, Crimea	S	20:19:56	N
KSA	Ksara, Lebonan	S	20:20:07	N
SIM	Simferopol, Crimea	S	20:20:10	N
ALG	Algiers, Algeria	P	20:20:15	N
DDI	Dehran Dun, India	S	20:20:18	N
POT	Potsdam, Germany	PP	20:20:27	Y
ALI	Alicante, Spain	P	20:20:29	N
TAM	Tamanrasset, Algeria	P	20:20:41	N

ABE	Aberdeen, Scotland	P	20:20:46	Y
MOS	Moscow, Russia	S	20:21:07	N
ISK	Istanbul, Turkey	S	20:21:19	N
HLW	Helwan, Egypt	S	20:21:38	N
CRB	Chernovtsy, Ukraine	S	20:21:49	N
BUC	Bucharest, Romania	S	20:21:59	N
AIK	Aikawa, Japan	P	20:22:09	N
OWA	Owase, Japan	P	20:22:19	N
OSA	Osaka, Japan	P	20:22:22	N
KAM	Kameyama, Japan	P	20:22:24	N
HYD	Hyderabad, India	S	20:22:26	N
ABE	Aberdeen, Scotland	PP	20:22:33	Y
KOB	Kobe, Japan	P	20:22:33	N
SAP	Sapporro, Japan	P	20:22:34	N
CAL	Calcutta, India	S	20:22:45	N
BEO	Belgrade, Serbia	S	20:22:54	N
WAR	Warsaw, Poland	S	20:23:04	N
RAC	Raciborz, Poland	S	20:23:12	N
TAR	Taranto, Italy	S	20:23:16	N
BUD	Budapest, Hungary	S	20:23:17	N
HEL	Helsinki, Finland	S	20:23:21	N
KOD	Kodaikanal, India	S	20:23:40	N
COL	College, Alska, USA	P	20:24:00	Y
PRA	Prague, Czech Republic	S	20:24:02	N
COL	College, Alska, USA	P	20:24:03	Y
TRS	Trieste, Italy	S	20:24:14	N
CAT	Catania, Italy	S	20:24:15	N
CLL	Collm, Germany	S	20:24:26	N
MES	Messina, Italy	S	20:24:27	N
COP	Copenhagen, Denmark	S	20:24:35	N
ROM	Rome, Italy	S	20:24:36	N
FIR	Florence, Italy	S	20:24:41	N
BOL	Bologna, Italy	S	20:24:45	N
CHU	Chur, Switzerland	S	20:24:47	N
SAL	Salo, Italy	S	20:24:49	N
COC	Colombo, Sri Lanka	S	20:24:53	N
ABU	Abuyama, Japan	PP	20:24:56	Y
CLE	Cleveland, USA	P	20:25:37	Y
DBN	De Bilt, Holland	S	20:25:38	Y
DBN	De Bilt, Holland	S	20:26:14	Y
BUR	Burlington, USA	P	20:26:19	Y
ALG	Algiers, Algeria	S	20:26:44	N

ALI	Alicante, Spain	S	20:27:09	N
ABE	Aberdeen, Scotland	S	20:27:12	Y
TAM	Tamanrasset, Algeria	S	20:27:30	N
CLE	Cleveland, USA	S	20:29:30	Y
SJP	San Juan, Puerto Rico	PP	20:30:34	Y
SAP	Sapporro, Japan	S	20:30:38	N
KAM	Kameyama, Japan	S	20:30:44	N
OWA	Owase, Japan	S	20:30:46	N
KOB	Kobe, Japan	S	20:30:56	N
OSA	Osaka, Japan	S	20:30:56	N
CHC	Chappel Hill, USA	PP	20:31:21	Y
WEL	Wellington, New Zealand	PKIKP	20:31:58	Y
ABU	Abuyama, Japan	S	20:32:21	Y
ABU	Abuyama, Japan	S	20:32:59	Y
HUA	Huancayo, Peru	PP	20:33:30	Y
ARA	Arapuni, New Zealand	P	20:33:30	N
API	Apia, Samoa	P	20:33:37	Y
CHC	Chappel Hill, USA	S	20:33:39	Y
COL	College, Alska, USA	S	20:33:43	Y
COL	College, Alska, USA	S	20:34:09	Y
WEL	Wellington, New Zealand	Pdiff	20:35:32	Y
LIN	Lincoln, Newbraska, USA	S	20:36:48	Y
BUR	Burlington, USA	S	20:37:18	Y
COL	College, Alska, USA	SS	20:38:39	Y
ABU	Abuyama, Japan	Pdiff	20:39:18	Y
ABU	Abuyama, Japan	Pdiff	20:40:10	Y
ARA	Arapuni, New Zealand	S	20:43:30	N
API	Apia, Samoa	S	20:50:55	Y

Table 2.2 Earthquake catalogue showing the location, depth and magnitude of relocated events using the MLOC method of Hypocentroidal decomposition.

Number	Date	Time	Latitude	Longitude	Depth (km)	Magnitude
1	01/05/1929	21:17:32	38.0901	57.75175	6	7.1
2	03/05/1929	16:20:04	37.99202	57.54186	15	5.1
3	13/05/1929	13:27:12	37.83842	57.29086	15	5.8
4	13/07/1929	07:36:40	37.6855	58.2657	15	5.7
5	25/07/1929	00:17:26	38.21068	57.61191	15	5.6
6	19/09/1939	03:24:05	38.38081	57.14887	15	5.6
7	04/11/1946	21:47:49	39.78535	54.41388	41	7.1

8	18/06/1948	18:44:33	37.49156	57.56102	5	5.5
9	05/10/1948	20:12:06	37.98799	58.38585	12	7.3
10	06/10/1948	01:24:43	37.81474	58.45691	7	5.3
11	06/04/1950	02:43:30	37.9758	58.36648	12	5
12	09/05/1950	11:16:58	38.37312	58.28216	17	6.2
13	15/09/1952	04:31:31	37.92868	58.14308	15	4.9
14	12/02/1964	08:19:18	39.21631	55.58492	18	4.7
15	02/01/1966	16:33:07	37.83356	56.95344	10	
16	18/01/1966	20:54:11	37.82239	57.00199	20	
17	03/01/1969	03:16:38	37.09915	57.89763	11	5.4
18	30/07/1970	00:52:18	37.91641	55.97292	17	5.7
19	30/07/1970	02:35:11	37.76736	55.92736	33	4.9
20	30/08/1970	16:17:30	37.69081	56.02371	17	5
21	12/11/1970	13:10:02	38.39853	57.32867	29	4.7
22	12/10/1972	10:26:09	38.28453	56.58716	12	
23	07/03/1974	11:36:00	37.68516	55.88506	10	5.2
24	14/02/1976	15:29:51	37.68933	57.23338	19	4.2
25	31/05/1976	08:07:13	38.96327	55.89629	25	4.8
26	14/06/1978	16:25:31	38.04499	56.27835	5	4.9
27	08/03/1979	22:40:33	37.45993	57.4981	27	4.5
28	06/10/1979	11:55:44	38.27415	57.5647	18	4.6
29	14/03/1983	12:12:45	39.35403	54.61675	12	5.6
30	22/02/1984	05:44:40	39.55186	54.13543	28	5.8
31	21/08/1984	19:48:49	38.33267	56.88419	5	4.6
32	05/09/1984	18:50:39	38.36245	56.93677	10	4.7
33	05/09/1984	11:19:11	38.34002	56.99391	0	4.4
34	09/05/1985	14:08:34	38.26755	56.61431	15	
35	01/12/1985	20:31:47	37.55327	56.68497	23	4.7
36	05/07/1987	07:43:04	37.72232	58.49802	21	4.8
37	07/09/1987	11:32:26	39.48895	54.79772	28	5.7
38	31/05/1992	16:39:24	38.68921	55.89864	19	4.4
39	09/09/1992	19:27:34	37.39613	57.25546	11	4.7
40	06/10/1992	08:57:18	38.43091	56.61419	17	4.7
41	06/01/1993	17:16:53	37.49751	57.59755	15	4.7
42	18/02/1993	04:15:01	37.65182	57.77365	24	4.5
43	02/05/1993	04:26:38	39.05774	55.55226	20	4.5
44	01/07/1994	10:12:41	40.24923	53.404	44	5.6
45	16/10/1994	10:09:54	38.51942	57.37345	28	3.9
46	21/10/1994	11:46:24	38.32201	56.99406	10	4.8
47	04/02/1997	10:37:48	37.71772	57.35096	18	5.9
48	04/02/1997	09:53:56	37.70851	57.35052	11	5.4
49	04/02/1997	21:04:12	37.81947	57.23981	32	4.1

50	05/02/1997	07:53:46	37.63656	57.53406	14	5.1
51	18/02/1997	18:01:36	37.84267	57.44368	10	4.2
52	22/08/2000	16:55:14	38.21793	57.46804	15	5.1
53	01/09/2000	05:04:46	38.25852	57.46846	13	4.4
54	19/09/2000	15:19:09	38.27794	57.43474	8	4.7
55	06/12/2000	17:11:06	39.60021	54.85161	30	7
56	11/09/2003	14:00:34	37.82656	57.23012	4	4.5
57	21/08/2004	03:32:43	37.82644	57.5782	24	4.7
58	17/08/2005	20:55:26	38.03617	57.53407	20	4.2
59	10/09/2005	01:10:03	38.3422	57.38418	20	
60	16/09/2006	10:42:54	37.49312	57.70862	13	4.4
61	29/11/2006	21:38:49	37.51892	57.1317	15	3.5
62	20/04/2007	08:04:41	37.54408	56.7299	25	3.9
63	19/08/2007	13:45:35	38.53637	55.5894	22	4.3
64	20/08/2007	04:53:31	37.77651	57.44823	22	4.6
65	01/10/2007	03:07:08	37.44936	56.47985	10	
66	29/02/2008	19:57:40	38.24187	57.15867	15	4.4
67	01/08/2008	22:44:38	37.45504	55.68835	12	4.3
68	01/08/2008	21:13:54	38.39899	58.28896	10	
69	14/10/2008	01:59:03	37.48624	56.70201	13	
70	24/10/2008	05:14:15	38.23795	57.37276	10	
71	06/02/2009	18:14:29	38.01086	57.43507	20	4.3
72	17/02/2009	17:57:23	38.29408	56.68847	22	3.3
73	17/02/2009	18:03:34	38.33147	56.6185	10	
74	21/02/2009	21:45:26	38.04246	57.47209	20	
75	15/04/2009	07:54:01	37.6506	55.81009	10	3.2
76	11/09/2009	20:53:01	37.75063	57.43499	23	3.5
77	31/12/2009	23:16:38	38.08044	58.34872	20	3.5
78	19/04/2010	03:31:13	37.49287	56.70936	15	4.4
79	25/05/2010	13:03:19	38.17759	57.98372	35	4
80	30/05/2010	08:48:39	38.17834	57.99821	35	
81	23/07/2010	00:56:41	37.658	56.95659	13	4.8
82	08/08/2010	09:39:01	37.99966	57.74134	10	3.5
83	11/08/2010	17:26:19	37.75608	57.06982	17	5
84	18/10/2010	08:05:11	38.07559	56.08548	2	
85	15/05/2011	14:49:36	37.64743	55.78103	8	3.4
86	17/06/2011	19:55:40	37.64211	56.95522	8	4.2
87	17/06/2011	20:07:59	37.62512	57.00528	5	3.6
88	08/11/2011	20:11:12	37.65777	55.8245	5	
89	09/11/2011	01:20:39	37.71071	55.8061	9	4.2
90	13/11/2011	12:30:38	37.65051	55.79393	7	
91	26/12/2011	01:49:13	37.58472	57.57978	15	4.5

92	26/12/2011	03:25:42	37.57852	57.59052	14	3.4
93	03/02/2012	19:07:33	38.08671	55.85415	10	4.3
94	10/03/2012	15:54:28	37.32906	57.13464	10	
95	16/04/2012	04:22:21	37.38562	57.05462	10	3.9
96	19/04/2012	18:01:01	37.39816	57.06686	20	
97	08/09/2012	03:17:36	38.50429	55.60953	14	4.2
98	09/09/2012	06:46:16	38.53659	55.55283	11	3.6
99	22/09/2012	12:27:15	38.19883	58.24226	10	3.6
100	01/10/2012	08:43:49	38.54086	55.57427	13	4.4
101	01/10/2012	08:51:16	38.53371	55.59461	14	4
102	01/10/2012	14:36:11	38.49605	55.58938	14	
103	02/10/2012	20:19:49	38.51954	55.55249	13	4.2
104	23/02/2013	23:12:33	38.90967	55.69564	28	4
105	28/02/2013	11:06:02	38.05756	57.56878	15	4.5
106	30/04/2013	02:00:12	37.42845	57.33484	12	3.6
107	10/05/2013	15:55:09	37.40632	57.3211	20	3.9
108	01/07/2013	01:36:01	38.06575	58.34774	11	
109	09/12/2013	11:33:51	38.51677	55.59254	10	5.1
110	09/12/2013	23:19:45	38.49048	55.59273	15	4
111	10/12/2013	03:42:32	38.51539	55.5783	15	3.6
112	13/02/2014	08:35:50	38.5055	56.25343	10	4.8
113	10/04/2014	00:08:43	38.51957	55.57716	24	4.2
114	10/04/2014	23:13:57	38.47823	55.62252	16	3.3
115	16/04/2014	05:27:40	38.17813	56.53517	10	
116	21/04/2014	02:35:58	37.46672	56.27517	10	3.9
117	12/10/2014	00:24:14	37.34481	56.88379	15	3.4
118	27/10/2014	21:00:35	37.45186	56.26208	8	4.4
119	19/05/2015	01:45:17	38.55509	55.52408	6	3.4
120	30/05/2015	06:19:23	38.31671	57.50594	12	
121	31/05/2015	12:10:14	38.24747	55.71141	12	
122	12/10/2015	21:37:30	38.23119	56.97518	14	4.8
123	12/10/2015	21:52:47	38.29753	56.94529	7	
124	13/10/2015	17:26:23	38.33641	56.95049	6	
125	16/11/2015	17:03:12	38.30452	56.95245	9	4.1
126	19/12/2015	19:10:04	37.80859	58.62128	7	
127	02/03/2016	16:07:05	37.90475	58.3354	10	
128	04/03/2016	14:57:25	38.29113	56.15072	10	
129	26/03/2016	23:51:01	38.14846	56.41316	10	
130	29/06/2016	22:56:13	37.45244	57.46855	14	
131	14/07/2016	08:35:40	37.4267	57.47044	10	4
132	05/11/2016	18:32:33	37.72421	55.86583	7	
133	09/11/2016	04:17:05	39.00581	55.73548	30	

134	26/01/2017	02:24:48	38.37943	57.16299	8	
135	06/02/2017	23:37:18	38.21004	55.94796	10	
136	07/02/2017	00:29:01	38.19152	55.92797	10	
137	14/03/2017	04:05:21	38.34476	55.5148	5	4.1
138	16/03/2017	00:48:25	37.53072	55.83747	20	
139	19/03/2017	14:55:30	38.30881	55.52077	12	4
140	13/05/2017	18:00:59	37.65444	57.19932	14	5.5
141	14/05/2017	02:59:45	37.62543	57.28129	15	
142	19/05/2017	11:27:26	37.61425	57.27928	23	3.3
143	02/07/2017	20:50:17	39.02745	55.66965	23	3.7
144	10/07/2017	07:04:54	38.03046	57.53785	18	
145	14/09/2017	09:38:18	38.41989	57.19935	15	
146	02/10/2017	05:35:07	37.63363	56.15776	12	3.6
147	10/10/2017	17:02:19	37.45974	57.47114	10	
148	17/10/2017	18:52:37	37.63624	57.21016	22	4.6
149	17/11/2018	05:21:15	37.60644	57.09352	10	3.8
150	10/04/2019	16:17:48	37.89286	56.93078	6	
151	22/05/2019	01:52:17	37.4455	56.44118	8	
152	29/07/2019	09:27:46	38.52742	57.11668	6	

Table 2.3 Inferred Stimulated Luminescence results from sediments taken from terrace site at 38.043°N/58.026°E. A 1.2m sample pit was excavated in the Q5 surface (Fig. 2.12), sediments were sampled at depths above.

Field code	Lab code	Depth (m)	Sediment K (%)	Sediment U (µg/g)	Sediment Th (µg/g)	Dose rate mGy/yr		1 sigma uncertainty	Equivalent Dose (Gy)		1 sigma uncertainty	Age (kyr)		1 sigma uncertainty
T19-09	Shfd-20102	1.00	1.20	1.81	6.10	2.70	±	0.11	9.75	±	2.34	2.80	±	0.23
T19-10	Shfd-20103	1.00	0.70	1.07	3.70	1.95	±	0.08	200.1	±	19.8	102.7	±	11.2
T19-11	Shfd-20104	0.55	1.40	2.27	7.50	3.08	±	0.13	304.3	±	30.6	98.8	±	11.0

Table 2.4 Polarity data used to calculate focal mechanism solutions from the first arrival data. The table shows if the record has come from digitised seismograms or/and from the ISC catalogue (International Seismological Centre, 2020). Station locations are taken from Charlier and Van Gils (1953), and International Seismological Centre (2020). Take-off angles are calculated using Pho and Behe (1972).

Station	Location	Latitude	Longitude	ISS/ISC Catalogue	Digitised Waveform	Take -off angle	Compression/Dilation
BOM	Bombay, India	18.90	72.82	N	Y	34	D
ISK	Istanbul, Turkey	41.07	29.06	Y	N	32	C
HLW	Helwan, Egypt	29.86	31.34	Y	N	31	C
BEO	Beograd, Serbia	44.81	20.47	Y	N	29	C
WAR	Warsaw, Poland	52.24	21.02	Y	N	29	D
CAL	Calcutta, India	22.54	88.33	Y	N	29	D
HEL	Helsinki, Finland	60.18	24.96	Y	N	29	D
POT	Potsdam, Germany	52.38	13.07	Y	N	28	D
ROM	Rome, Italy	41.90	12.51	Y	N	28	C
COP	Copenhagen, Denmark	55.69	12.43	Y	N	28	D
POT	Potsdam, Germany	52.38	13.07	N	Y	28	D
BOL	Bologna, Italy	44.49	11.33	Y	N	27.5	D
GTT	Göttingen, Germany	50.55	9.97	N	Y	27.5	D
CHU	Chur, Switzerland	46.85	9.54	Y	N	27	D
STU	Stuttgart, Germany	48.77	9.20	Y	N	27	D
ZUR	Zurich, Switzerland	47.37	8.58	Y	N	27	D
DBN	De Bilt, Netherlands	52.10	5.18	Y	Y	27	D
UCC	Uccle, Belgium	50.80	4.36	Y	N	26.5	D

ABE	Aberdeen, Scotland	57.17	-2.10	N	Y	26	D
TAM	Tamanrasset, Algeria	22.79	5.52	Y	N	25	C
CRT	Cartuja, Spain	37.19	-3.60	Y	Y	24.5	C
UPP	Uppsala, Sweden	59.86	17.63	Y	Y	24	D
LIS	Lisbon, Portugal	38.72	-9.15	Y	N	23.5	C
ABU	Abuyama, Japan	34.87	135.57	N	Y	22	C
COL	College, Fairbanks, USA	64.86	-147.82	N	Y	18	C
OTT	Ottawa, Canada	45.39	-75.72	Y	N	15	D
BUR	Burlington, USA	44.47	-73.19	N	Y	15	C
CLE	Cleveland, USA	41.49	-81.53	Y	Y	14	D
CHC	Chapel Hill, USA	35.90	-79.05	N	Y	14	D

Statement of Authorship for joint/multi-authored papers for PGR thesis

To appear at the end of each thesis chapter submitted as an article/paper

The statement shall describe the candidate's and co-authors' independent research contributions in the thesis publications. For each publication there should exist a complete statement that is to be filled out and signed by the candidate and supervisor **(only required where there isn't already a statement of contribution within the paper itself).**

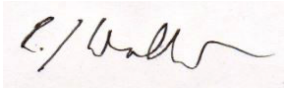
Title of Paper	Seismotectonic aspects of the Ms 7.3 1948 October 5th Ashgabat (Ashgabat) earthquake, Turkmenistan: right-lateral rupture across multiple fault segments, and continuing urban hazard.
Publication Status	□Submitted for Publication
Publication Details	Marshall, N. et al. (2023), *Geophysical Journal International*, In revision

Student Confirmation

Student Name:	Neill Marshall		
Contribution to the Paper	Performed processing, mapping and analysis of satellite and topographic data, digitisation of seismograms and seismic processing, interpretation and wrote manuscript. Relative relocation of seismicity was undertaken by Eric Bergman.		
Signature.	Neill Marshall	Date	04/10/23

Supervisor Confirmation

By signing the Statement of Authorship, you are certifying that the candidate made a substantial contribution to the publication, and that the description described above is accurate.

Supervisor name and title: Prof. Richard T. Walker			
Supervisor comments The student did indeed make substantial contribution, and led all analysis and interpretation. The paper incorporates some seismic location analyses that were performed by a collaborator, as the student states.			
Signature.		Date	05/10/23

This completed form should be included in the thesis, at the end of the relevant chapter.

Chapter 3

Constraining landscape evolution of the Kopeh Dagh, Turkmenistan, using optical imagery and long-term geologic slip-rates.

Abstract

The landscape evolution and paleoclimate north and east of the Kopeh Dagh mountains in Turkmenistan is poorly understood, which has significant implications for our understanding of past climate conditions and regional sea level. We present a new method for constraining the timing of alluvial fan incision using fault slip-rates. By measuring displacement of on-fault offset drainage channels in the Kopeh Dagh and dividing this by the long-term geologic slip-rate (9.2 ± 1.5 mm/yr) we determine the minimum timing of incision. Using cumulative offset probability distributions we find peaks in fault related drainage channel displacements at 23.5, 30, 88.5, 256, 402, 600, 1000 m. We associate these peaks to periods of increased and preserved incision. We find increased incision occurring between 2-3 ka, 10 ka, 28 ka, 44 ka, 65 ka and 109 ka, coinciding with regional precipitation trends from northern Iran. We use satellite data and field observation to build a detailed Quaternary stratigraphy for ~100 km of the Kopeh Dagh rangefront and east Caspian lowlands. From geomorphic mapping and Quaternary dating, we provide age constraints on alluvial fan surfaces and paleoshoreline deposits on the margins of the Caspian Sea. We map two prominent shorelines at 0 m and 47 m above sea level (a.s.l.). Radiocarbon dating of marine shells in a beach deposit at 0 m (a.s.l.) yields an age of 12.5 kyrs cal BP, suggesting the 0 m (a.s.l.) shoreline was formed after the Last Glacial Maximum.

3.1 Introduction

Building chronologies of late Quaternary stratigraphy and landscape development can be challenging. The identification of regionally correlated periods of alluvial fan deposition and drainage network reorganization complicated by catchment specific processes, and by the ability and means to date a sufficient number of geomorphic surfaces (Sohn et al., 2007; Walker and Fattahi, 2011; Ventra and Clarke, 2018). Nonetheless, knowing the timing of major periods of landscape change is an important constraint in establishing past environment changes, climatic conditions, and as markers to establish fault slip-rates.

The landscape of the arid lands of northeast Iran and Turkmenistan retain abundant evidence of past environmental changes, thorough the preservation of multiple generations of large alluvial fans that are at present abandoned, and then incised by rivers. Establishing the timing of these past changes is of critical importance in tectonic and earthquake hazard studies as the region is cut through by multiple major faults whose slip-rates are not known. The chronology of alluvial fan deposition is important more widely, outside tectonic studies, as it is a critical area in the expansion of early modern humans in the late Pleistocene, with wetter, greener, periods likely facilitating movement across presently arid areas (Shoaee et al., 2023). A number of constraints exist on alluvial fan deposition age, river terracing, and lake deposition, though with far from even coverage, and with individual studies suffering from limitations in sample number and precision of age measurement (e.g. Walker and Fattahi, 2011).

In this study we propose a new method to date the major periods of regional landscape change using offsets of numerous landforms displaced across the Main Kopeh Dagh Fault (MKDF), a major right-lateral strike-slip fault for which we have reliable estimates of slip-rate (Dodds et al., 2022b; Walker et al., 2021). By measuring many fault related offsets in alluvial fan surfaces, and streams incised into their surfaces, we can look for clustering in the offset measurements using a cumulative offset probability density (COPD) approach (McGill and Sieh, 1993; Tsai et al., 2022; Zielke et al., 2010), which we infer to represent more regional extensive landscape events. As we know the fault slip-rate, we can then assign ages to these clustered offsets.

To measure offsets, we use observations from sub-metre resolution optical satellite imagery, digital elevation models derived from stereo satellite imagery and field surveys combined with previously published fault slip-rate and dated geomorphic surfaces to study the landscape evolution of the Kopeh Dagh mountains and the East Caspian lowlands. We provide age constraints on past Caspian Sea level and incision events, discussing the implications for paleoclimate records during the late-Pleistocene.

In section 3.2 we introduce the regional geographical, tectonic, and paleoclimatic setting of the East Caspian lowlands. Section 3.3 details the geomorphic, remote sensing and Quaternary dating methods we have used. We describe our results in sections 3.4 and 3.5, and discuss the implications for regional climate and sea level in section 3.6.

3.2 Geographic and tectonic setting

3.2.1 Active tectonics

The Main Kopeh Dagh Fault is a major continental strike-slip fault stretching ~ 500 km along the northern edge of the Kopeh Dagh range (Fig. 3.1). The Kopeh Dagh range is the northernmost expression of the Arabia-Eurasia collision zone east of the South Caspian Basin (SCB) and accommodates ~ 2 - 4 mm/yr of shortening (Walker et al., 2021). The South Caspian Basin is an aseismic block that moves independently of its surrounds (Jackson et al., 2002). Previous tectonic studies show the westward extrusion of the South Caspian Basin, accommodated by the dextral Main Kopeh Dagh Fault and conjugate sinistral Shahroud fault zone (Dodds et al., 2022; Hollingsworth et al., 2010, 2008, 2006; Jackson et al., 2002; Walker et al., 2021). The Main Kopeh Dagh Fault is a major boundary fault, accommodating relative motion between the SCB and Eurasia to its north (Fig. 3.1).

The Main Kopeh Dagh Fault accommodates this motion with dextral strike-slip faulting at a long-term geologic slip-rate of 9.1 ± 1.3 mm/yr (Walker et al., 2021) and has a geodetic slip-rate of 7.2 ± 2.4 mm/yr (Dodds et al., 2022b). This makes it one of the most rapidly slipping faults in the Arabia-Eurasia collision zone. The onset of lateral motion in the Kopeh Dagh is debated. Studies by Shabanian et al (2009) show that lateral motion of the Kopeh Dagh belt should not have started before ~4 Ma corresponding to the reorganisation of the tectonic

deformation in the Arabia-Eurasia collision zone (Allen et al., 2004; Copley and Jackson, 2006). However, Hollingsworth et al. (2008) suggest that strike-slip motion could have initiated earlier (~10 Ma) and this is related to the westward extrusion of the South Caspian Basin relative to Eurasia. Prior to the dominance of lateral motion, the Kopeh Dagh shows fold-and-thrust belt structures and morphology with the main phase of formation occurring during the late-Eocene and early-Oligocene (Robert et al., 2014).

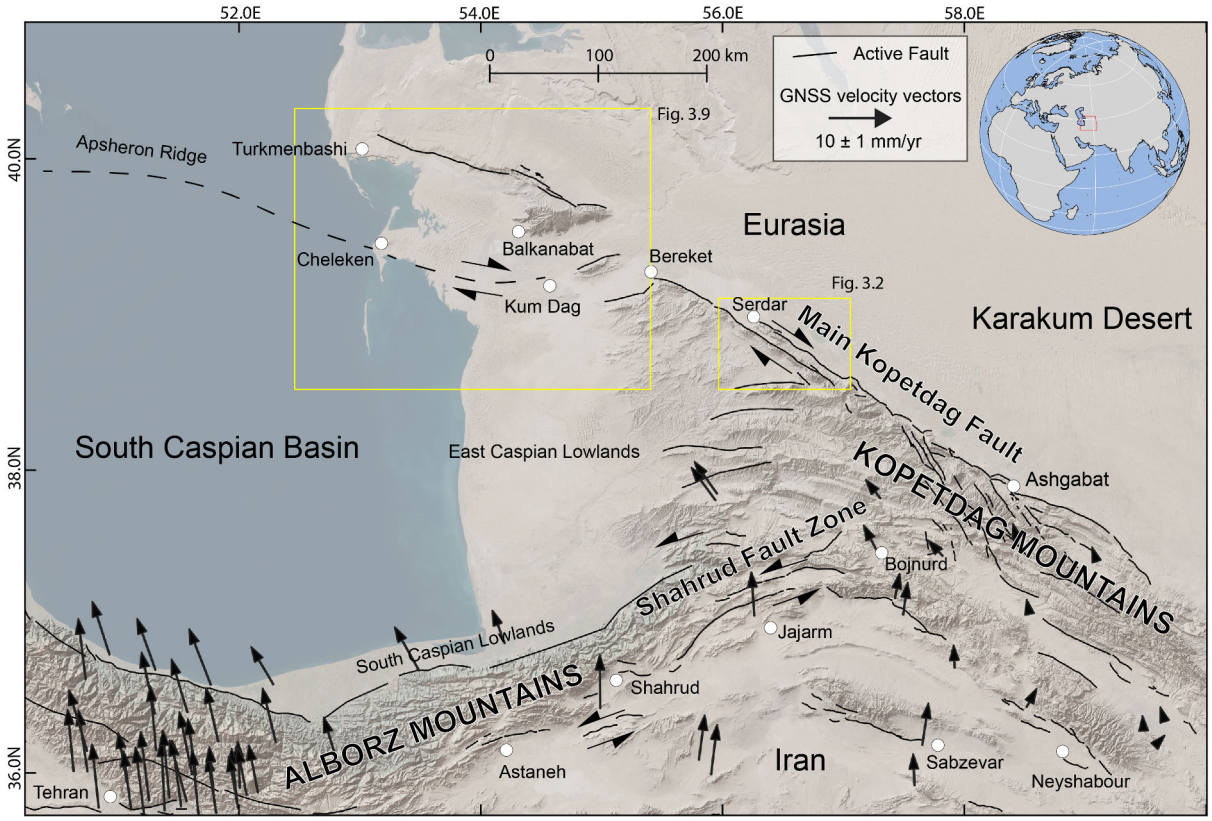


Figure 3.1: Neotectonic map of the eastern Caspian lowlands showing the north-eastern edge of the Arabian-Eurasian collision zone. Motion on the faults indicates westwards extrusion of the South Caspian Basin. Topography is from SRTM (30 m resolution), GNSS velocity vectors – black arrows (after Khorrami et al., 2019), active faults – black lines (adapted after Walker et al., 2021 and Dodds et al., 2022).

3.2.2 Geomorphology of Turkmenistan

There are relatively few published resources available in the international literature concerning the geomorphic development of Turkmenistan. A review of the general geology and geomorphology provides a general overview of the geomorphic regions (Ghassemi and Garzanti, 2019), but resolution of the Quaternary surfaces is low. The major geomorphic

regions are the Karakum desert, Kopeh Dagh rangefront, and East Caspian lowlands. The Karakum desert occupies around 70% of the country's area with the prevailing winds coming from the Kazakh steppe, suggesting this a major source of aeolian deposits (Ghassemi and Garzanti, 2019).

Our study focusses on the Kopeh Dagh rangefront and the East Caspian lowlands. The Kopeh Dagh rangefront is characterised by a suite of alluvial fan deposits and loess caps. The stratigraphy and chronology of fan emplacement and abandonment is poorly constrained. Some older fan and terrace units in the region have been dated (for tectonic studies to constrain fault slip-rates and uplift) at late-Pleistocene (e.g. Walker et al., 2021). However, there are no detailed fan chronologies, loess and paleosol studies in this area.
The East Caspian lowlands has received more attention and is a good location to observe Pleistocene and Holocene paleoclimate and Caspian Sea level. Most studies focus on the region north of the Alborz in Iran, where loess and paleosol deposits provide constraints of regional climate (e.g. Karimi et al., 2011; Kehl et al., 2021; Vlaminck et al., 2016). There are no geomorphic studies further northeast in Turkmenistan.

3.2.3 Late Quaternary paleoclimate of the Caspian Lowlands

Past climate in western Central Asia is poorly constrained. Signals of past environmental fluctuations during the late Quaternary come from lakebed sediments, loess and paleosol deposits, cave speleothem and fan abandonment interpretations in northern Iran and are correlated to Marine Isotope Stages (MIS) through the Pleistocene and Holocene.

Late-Pleistocene (130 – 11.7 ka)

Late-Pleistocene climate has changed substantially from interglacial to glacial reaching the Last Glacial Maximum at MIS 2. The Quaternary deposits observed in northern Iran and Turkmenistan provide markers of regional climate in the Caspian lowlands. Pollen studies in NW Iran show that at the last interglacial period (MIS 5e ~ 126 ka) was slightly warmer and moister than in the Holocene (Djamali et al., 2008). Dated paleosols from NE Iran show ages consistent with the last interglacial period and indicate that the climate was most likely warm and moist at this time (Karimi et al., 2011; Vlaminck et al., 2016). This was followed by two stadial (MIS 5d – 109 ka and 5b – 87 ka) and interstadial (MIS 5c – 96 ka and 5a – 82 ka)

periods with the interstadial not reaching the same conditions seen in the last interglacial (Djamali et al., 2008; Kehl, 2009). Analysis of paleosols and loess deposits in the southern Caspian lowlands shows weakly altered loess deposits correlated to the stadial phases MIS 5b and 5d as well as MIS 4 (Kehl et al., 2021). This suggests that these were periods of increased rates of dust accumulation under dry climatic conditions. Past precipitation recorded in cave stalagmites in the Alborz show dryer conditions at 88 ka, 77 ka and 73 ka that are consistent with stadial conditions during MIS 5b and possibly late MIS 5a or the onset of MIS 4 at around 71 ka (Carolin et al., 2019).

Alluvial fan abandonment ages in the Kopeh Dagh at 83 ± 4 ka (Shabanian et al., 2009), and at Neyshabour 82 ± 17 ka (Hollingsworth et al., 2010a) possibly show wetter conditions in NE Iran during MIS 5, although errors in the obtained ages at Neyshabour show this could be as late as 65 ka. Another generation of fan abandonment appears to have occurred during MIS 3 in NE Iran, dated at 35 – 60 ka at Neyshabour (Hollingsworth et al., 2010a; Walker and Fattahi, 2011) and 40 – 60 ka at Kashmar (Fattahi et al., 2007; Walker and Fattahi, 2011). Further evidence of fan abandonment is shown near the SE Alborz near Astaneh with two generations at 32 ka and 55 ka (Rizza et al., 2011).

Loess accumulation appears to have increased significantly in the southern Caspian lowlands during MIS 4 and increased again in MIS 3 (Kehl et al., 2021; Vlaminck et al., 2018), suggesting more arid conditions as climate cooled in the Last Glacial Period. Kehl et al. (2021) shows a series of weakly developed paleosols during MIS 4 to 2 suggesting reduced dust deposition and increased humidity in relatively short-lived interstadial periods, which is also supported in the Lake Van (eastern Turkey) records (McCormack et al., 2018). MIS 3 appears to be characterised by fluctuations in climate stability in the Caspian Lowlands, with evidence for multiple relatively short (millennial scale) wetter and humid periods, providing possible pathways for hominin migration in MIS 3 between 55 - 30 ka (Shoaee et al., 2023).
Despite these fluctuations the Last Glacial Period shows an overall trend of substantial dust deposition, indicative of dry arid conditions.

Holocene (11.7 ka & MIS 1)

Paleoclimate during the Holocene shows a move from the glaciation to a wetter full interglacial period. Early Holocene lacustrine deposits have been identified at Nimbluk (East Iran) dated

at ~ 9 ka (Fattahi and Walker, 2015) and peat sequences at Neor Lake in the Alborz (Sharifi et al., 2015) are indicative of wetter conditions. This is supported by paleosol development in the Alborz, Kopeh Dagh and southern Caspian Lowlands above MIS 2 loess deposits (Karimi et al., 2011; Kehl et al., 2021).

Alluvial fan abandonment has also been observed and dated to the Holocene at numerous sites in NE Iran. At Sabzevar fan abandonment is dated between 9 and 13 ka (Fattahi et al., 2006). At Kashmar (NE Iran) we see fan abandonment at ~10 ka and river terracing between 5 – 11 ka (Fattahi et al., 2007). Near Astaneh fan abandonment has been dated to occur between ~12 – 20 ka (Rizza et al., 2011), although the error is wide and could put this phase within MIS 2.

3.2.3 Caspian Sea level in the late Quaternary

The Caspian Sea is the largest endorheic body of water globally with occasional punctuated outflows towards the Black Sea in the late Pleistocene (Krijgsman et al., 2019; Leroy et al., 2020), with its current level at -27 m (a.s.l.). The main sources of water into the Caspian are the Volga, Kura and Amu-Darya (via the Aral Sea) rivers with episodic outflow occurring when lake levels are > 25 m (a.s.l). Marine transgressions and regressions are thought to have existed at different periods of the late-Pleistocene and span into the Holocene.

Transgressions are recorded and dated during MIS 5a, 3 and 2/1 (Krijgsman et al., 2019; Kroonenberg et al., 1997; Leroy et al., 2020; Pánek et al., 2016). However, there is disagreement about the exact timing and amplitude of Caspian Sea level during the MIS 2 and 3. Most studies agree that there were three major transgressions during the late-Pleistocene. Studies by Svitoch (2009), Tudryn et al. (2022) and Kuzucuoğlu and Leroy (2023) suggest that Caspian Sea level was at a ~ 50 m (a.s.l.) highstand from around 22 to 12 ka, whereas Krijgsman et al. (2019) and others put the last high stand between 11 – 15 ka with a sea level height of 0 m (a.s.l.).

3.3 Methods

3.3.1 Satellite imagery

Within the Kopeh Dagh Mountains we use high-resolution (0.4 m per pixel) pan-sharpened optical imagery from the WorldView-2 satellite (obtained through the Digital Globe Foundation) to remotely map and analyse geomorphic surfaces along a ~ 150 km section of the Main Kopeh Dagh Fault. We use a combination of true colour imagery and near-infrared false colour band combination (band 7 (near-IR 1), band 5 (red), and band 3 (green)) to highlight near-surface differences in moisture content. The WorldView-2 imagery allows us to highlight different geomorphic surface boundaries, fault related scarps and drainage channels.
The WorldView-2 dataset is complimented by Google Earth and Bing Aerial imagery, SPOT6 satellite stereo imagery and Shuttle Radar Topography Mission (SRTM) digital elevation models (DEMs). We use Agisoft Metashape software to build DEMs from the SPOT6 stereo imagery, yielding a resolution of 4 m per pixel. Elevation profiles across the Kopeh Dagh study area are taken from the SPOT6 DEMs.

In the east Caspian lowlands, we use a combination of freely available Google Earth, Bing Aerial and 30 m resolution SRTM derived DEMs to remotely map fault scarps and geomorphic surfaces. We extract elevation contours from the SRTM DEMs at 0 and 47 m above sea level (a.s.l.) that coincides with shoreline deposits located and sampled in a 2017 field campaign.

3.3.2 Fault mapping

We use a combination of remote sensing, previous earthquake and tectonic studies (Dodds et al., 2022a; Dodds et al., 2022b; Walker et al., 2021) and field observations to map active faults in the Kopeh Dagh and East Caspian lowland regions. We map typical fault associated morphology such as scarps, offset drainages, ruptures, shutter ridges and step-overs consistent with paleoseismic methods (McCaplin, 2009). These landscape discontinuities form linear trends that we associate with the presence of active faults. The data and observations are gathered and mapped in QGIS software for further analysis.

3.3.3 Geomorphic mapping

From the imagery and elevation sources described above we map alluvial fan surfaces, shorelines, beaches and marine terraces. We use QGIS software to trace around each individual geomorphic surface and convert this into a polygon.

For the alluvial fan deposits, we assign a relative age to each polygon based on qualitative assessment of the relative surface age. This qualitive assessment is based on the texture, position and geomorphic relationships (e.g. Figs 3.3 & 3.4). We assume that a surface that is smooth, with a well-developed incision and drainage network and vegetation is old. A surface that has a rough, unvegetated and immature drainage network is assumed to be young. Alluvial fan surfaces in between are classified relatively based on their textural appearance of maturity.

We use a combination of Bing Aerial and Google Earth satellite data, and field observation to map beach and shoreline deposits. We observe escarpments near to and above these deposits and measure elevation (geoid adjusted) from the SRTM 30 m DEMs. We extracted contour lines at these elevations from the SRTM elevation data for the East Caspian lowland region.

3.3.4 Offset measurement

Measuring lateral offsets in geomorphic surfaces is a method commonly used in paleoseismic investigations and active fault studies to determine individual earthquake slip and slip-rates over multiple earthquake cycles (McCaplin, 2009). We use the WorldView 2 satellite imagery to trace drainage channels at each side of the Main Kopeh Dagh fault trace where drainages are deflected. We trace the thalweg of the channel and each riser that bounds the thalweg (Fig. 3.6 b & c). At the fault the trace of the risers and thalwegs form piercing points. We remotely measure the distance between the thalweg piercing points to give an offset value. To constrain error, we measure between the nearest and furthest risers to give minimum and maximum values, respectively. We qualitatively assess each measurement based on the sinuosity and sharpness of the piercing lines and points consistent with methods described in Kurtz et al. (2018).

We construct a cumulative offset probability density (COPD) using methods detailed in previous studies (e.g., McGill and Sieh, 1993; Zielke et al., 2010). The values of the preferred offset (thalweg offset), minimum and maximum are inputs as a triangular probability density function (PDF) and these are stacked to form the COPD function. We use a triangular PDFs for individual measurements centred on the preferred offset measurement with the minimum and maximum measurements represented as the other corners of the triangle (e.g., Tsai et al., 2022). To remove the effects of the most recent earthquake cycles we focus on offsets that are greater than 20 m and focus on longer time periods (equating to 2 -3 k years at the measured fault slip-rate).

3.3.5 Quaternary dating

We collected 8 sediment tubes for Infrared Stimulated Luminescence (IRSL) analysis. Metal tubes were hammered horizontally into exposed sedimentary units and sealed from light contamination. The ends of the tubes were wrapped in aluminium foil and taped to seal. Samples were wet sieved to select a suitable grain size, treated with a dilute HCl to remove carbonate, and then dried. K-feldspar fractions were separated from quartz, plagioclase and heavy minerals by flotation using a centrifuge in a lithium metatunstate (LTM)solution. The samples were then washed to remove the LTM and treated to remove the outer dark coating on the grains (presumed to absorb light. IRSL measurements were made in a standard Risø TL-DA-20D automated luminescence reader (Rhodes, 2015). Machine calibration and filter specifications are detailed in Rhodes (2015).

We found marine bivalve shells in a shoreline deposits (Table 3.2) at 0 m a.s.l., datable using radiocarbon techniques. Two shells were analysed at Beta Analytic laboratory in Miami, Florida. Results were calibrated using OxCal v4.4 (Bronk Ramsey, 1995) and the Marine20 calibration curve was used (Heaton et al., 2020). The Caspian Sea is a unique marine setting and we used weighted average ΔR value taken from sites around the Caspian Sea from the CHRONO marine reservoir database (Reimer and Reimer, 2001).

3.4 Late-Pleistocene stratigraphy of the Kopeh Dagh, Turkmenistan

3.4.1 Relative stratigraphy

From geomorphic mapping we identify five past generations of alluvial fan deposition in the study area (Fig. 3.2). Qaf 1 is the youngest fan deposited before the currently active fans. The unit has been identified by a rough surface with poorly developed drainage networks. The surfaces are deposited adjacent to and one terrace tread above the active drainage channels. There is little vegetation observable on these surfaces suggesting that a relatively short period since deposition and vegetation on these surfaces, mainly grass and scrub bush and gravels exposed in places, suggesting a relatively young age. The elevation of the Qaf 1 surfaces tends to be the lowest in the stratigraphy, just higher than the active fans (Fig. 3.3).

From cross cutting relationships and surface texture we see that Qaf 2 is the second youngest fan deposited before Qaf 1. Qaf 2 surface has a better developed drainage network with preferential channels being developed on the surface. These channels are deeper and sharper than the relatively unorganised drainage patterns seen in Qaf 1. The surface of Qaf 2 is also smoother than Qaf 1 but remnants of the older, more active, drainage networks are still visible and overall, the surface appears rough. Vegetation varies on this surface; we no longer see exposed gravels and the surface appears to have vegetation covers with sparse clustering of scrub bushes. Qaf 2 has elevations higher than Qaf 1 and lower than Qaf 3 (Figs 3.3 & 3.4).

Qaf 3 is a smoother surface with well-defined deep incision and drainage network. The fan surface no longer shows signs of early-stage drainage channels. Qaf 3 sits at higher elevations above adjacent riverbeds to Qaf 2 and shows well developed dense vegetation at the surface (Figs 3.3 & 3.4).

Qaf 4 is a smooth fan surface with deeper incision than Qaf 3 into a well-developed drainage network. Drainage channels and triangular facets are developing on the risers into the incision network. Overall, the surface is smooth and there is not much difference in smoothness between Qaf 3 and 4, the vegetation patterns on this surface are also similar to Qaf 3. Along strike of the range front, the Qaf 4 surfaces are at higher elevations to Qaf 3 (Figs 3.3 & 3.4).

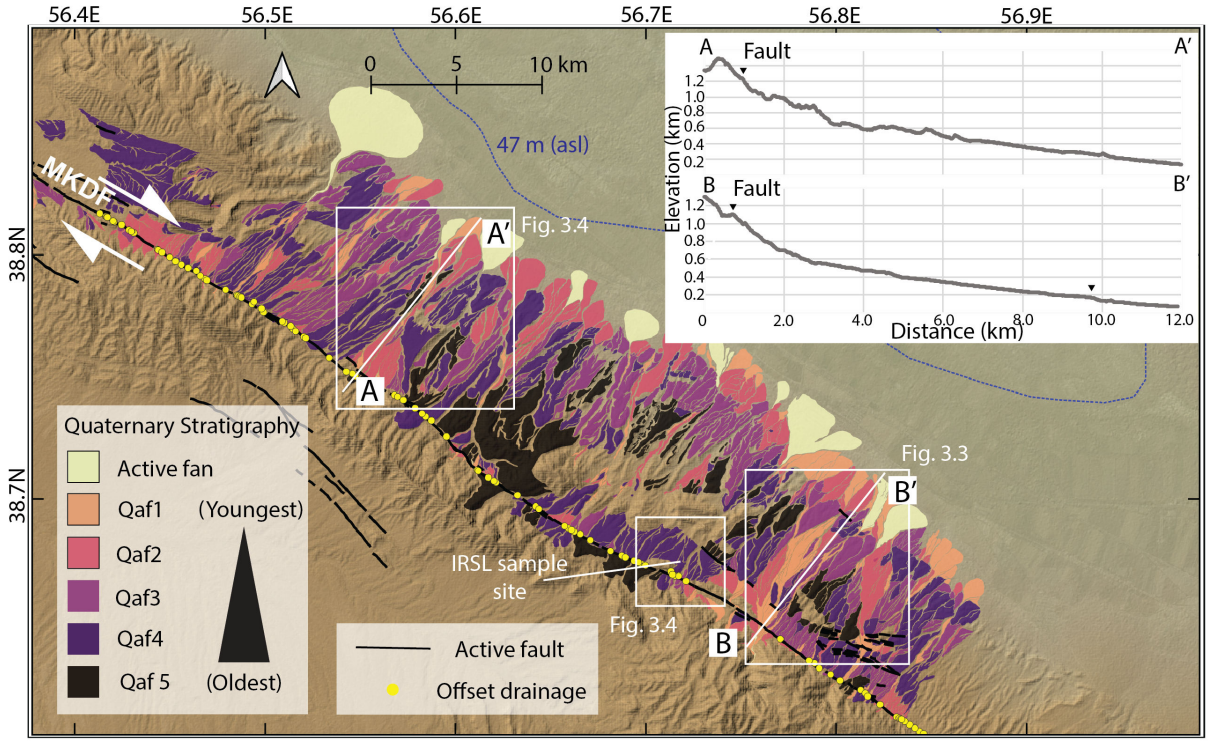


Figure 3.2: SRTM DEM (30 m resolution) of a 100 km segment of the Main Kopeh Dagh Fault with Quaternary alluvial fans mapped according to relative age. Black lines – active faults; yellow dots – offset drainage measurement sites; alluvial fan stratigraphy shown in the bottom left insert. Topographic profiles are from SPOT 6 stereo imagery derived DEMs. Blue dotted line is the 47 m (a.s.l.) elevation contour extracted from the SRTM DEM.

Qaf 5 is the oldest set of alluvial fans in the study area. The surface is deeply incised with well-developed drainage bounding the fan surface. There are steep drainage channels on the flanks fans with the fan surface eroding into thin ridgelines. The surface is smooth with little incision to the top of the surface. There is sparse vegetation on these surfaces. Qaf 5 occupies the highest elevations in our study area (Figs 3.3 & 3.4).

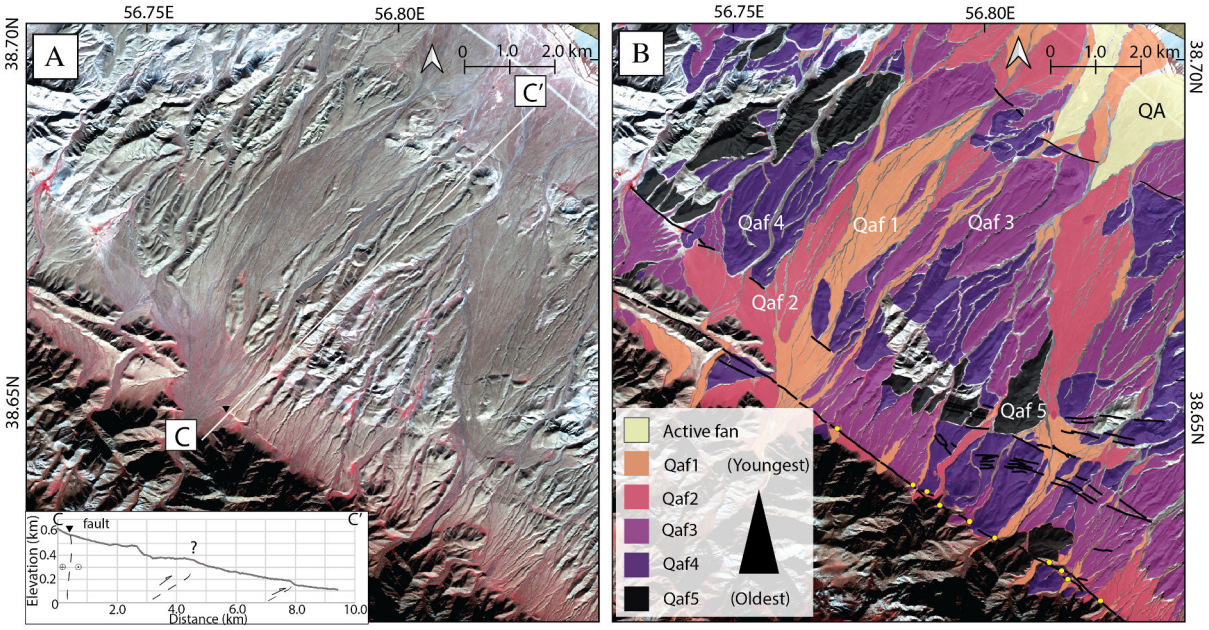


Figure 3.3: Panel A shows WorldView 2 panchromatic optical imagery. Topographic profile C-C' is taken from the SPOT 6 stereo DEM. We show speculated fault locations and geometries on the topographic profile. Panel B shows the alluvial fan stratigraphy mapped using a combination of optical and DEM data. Active faults are the black lines with yellow dots showing the offset measurements. Active faults are also mapped using a combination of satellite optical and DEM data.

3.4.2 Slip-rate and incision age constraints

From the WorldView 2 satellite data we identify the offset drainage used to calculate the long-term geologic slip-rate on the MKDF of 9.1 ± 1.3 mm/yr (Walker et al., 2021). We have measured the same offset drainage at 970 m (Fig. 3.5) and use the central IRSL age of 105 ± 5 kyrs BP to recalculate the long-term geologic slip-rate on the MKDF. From our measurement, we obtain a slip-rate of 9.2 ± 1.5 mm/yr, which is comparable to the previous geologic slip-rate 9.1 ± 1.3 mm/yr (Walker et al., 2021) and within error of the geodetic slip-rate 7.2 ± 2.4 mm/yr (Dodds et al., 2022a). We use our calculated slip-rate, 9.2 ± 1.5 mm/yr, and the peaks from the COPD analysis to constrain the timing of incision into the geomorphic surfaces along the Kopeh Dagh rangefront (Figs 3.5 and Table 3.1).

Our model of the geomorphic processes, detailed in Fig. 3.6, has three main phases. In the first phase, alluvial fans are deposited out from the main rangefront across the Main Kopeh Dagh Fault. In phase 2, the alluvial fans are then incised and faulted (right-laterally) in phase 3. Typically, there are climate controls on alluvial fan deposition (dry and arid) and incision (wetter and hotter). The incised alluvial fans are then offset away from their original

catchments. By measuring the offset drainage channels and using the long-term geologic slip-rate we can provide constraints on the timing of incision and provide a minimum age on the alluvial fan surface.

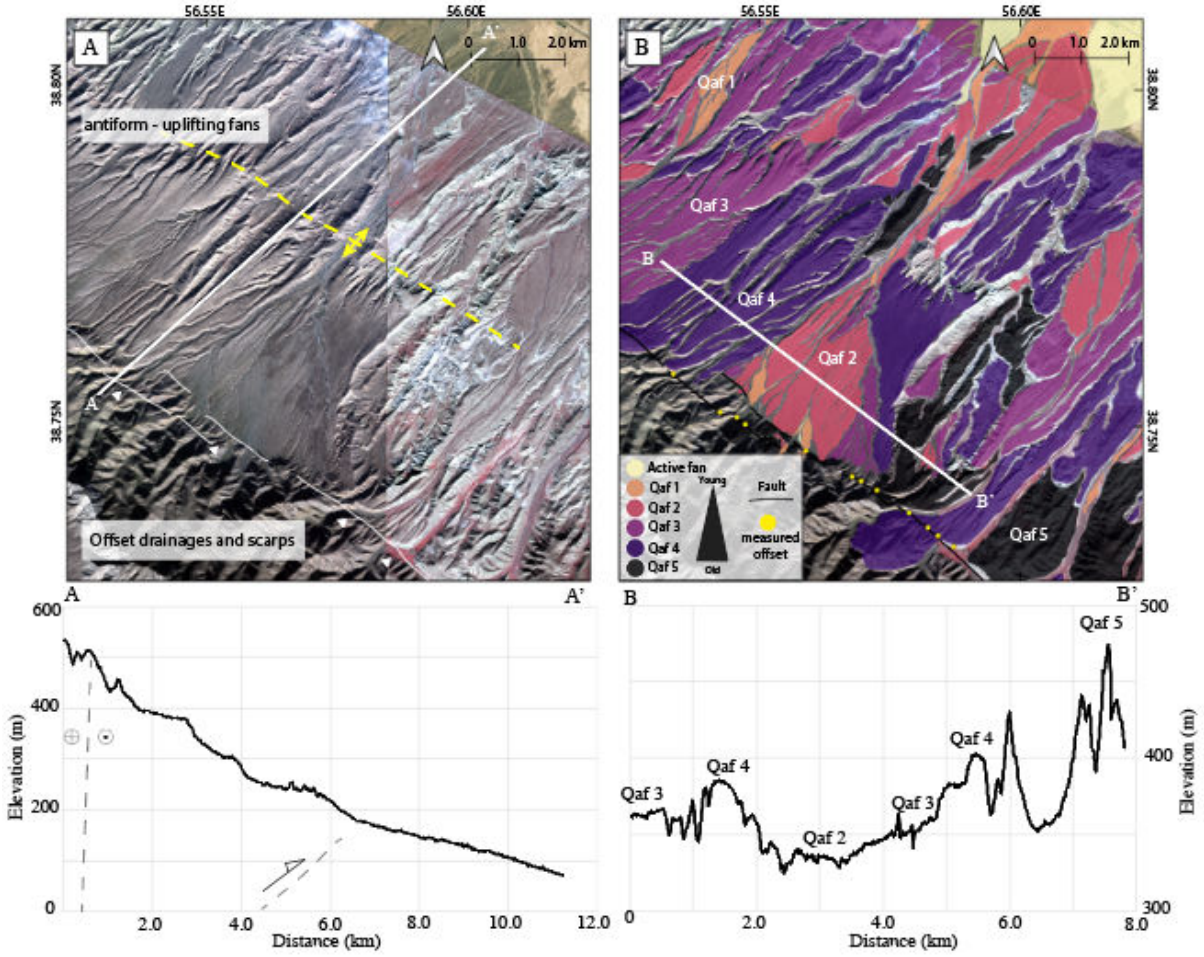


Figure 3.4: Panel A shows WorldView 2 panchromatic optical imagery. Topographic profiles A-A' and B-B' are taken from the SPOT 6 stereo DEM. White lines show fault trace and dotted yellow line shows a speculated anti-form axis. White arrows show the location of dextral offset drainages. Panel B shows the alluvial fan stratigraphy mapped using a combination of optical and DEM data. Active faults are the black lines with yellow dots showing the offset measurements. Profile A-A' shows a topographic profile perpendicular to the strike of the MKDF, the fault geometry is speculative showing the location along the profile. Profile B-B' runs parallel to strike of the MKDF. It shows the elevation of the alluvial fan units Qaf 2 – Qaf 5. Older exposed surfaces are at higher elevations, we speculate these were abandoned, incised and uplifted.

3.4.3 Cumulative offset peaks

We observed 131 offsets with maximum measurements greater than 15 m, of this we have 96 offset drainages with preferred measurements that are greater than 20 m (Fig. 3.7). From the offset measurements greater than 20 m, the COPD analysis determines several peaks in offset measurements at 23.3 m, 30 m, 88.5 m, 256 m, 402 m, 600 m and 1000 m (Figs 3.7 & 3.8). Using the long-term geologic and geodetic slip-rates on the Main Kopeh Dagh Fault of 9.2 ± 1.5 mm/yr and 7.2 ± 2.4 mm/yr (Dodds et al., 2022a) respectively, we can constrain minimum ages on alluvial surfaces that have been offset by the peak amount. These minimum surface ages are given to the other fans within the same unit. Table 3.1 shows the results of the preferred measurement peaks (Figs 3.7 and 3.8) dated using both the geologic and geodetic slip-rates. The errors are also included within the table to provide a full range on the minimum age.

Calculating the age of an COPD peak from fault slip-rates primarily gives age constraint on incision. We speculate that the COPD peaks represent periods of increased incision, and we date these periods of increased incision at 2 - 3 ka, 3 - 4 ka, 8 – 12 ka, 24 – 33 ka, 38 - 52 ka, 56 - 78 ka, and 94 - 130 ka (Table 3.1). We assume that the long-term geologic slip-rate remains broadly the same in the late-Pleistocene and Holocene.

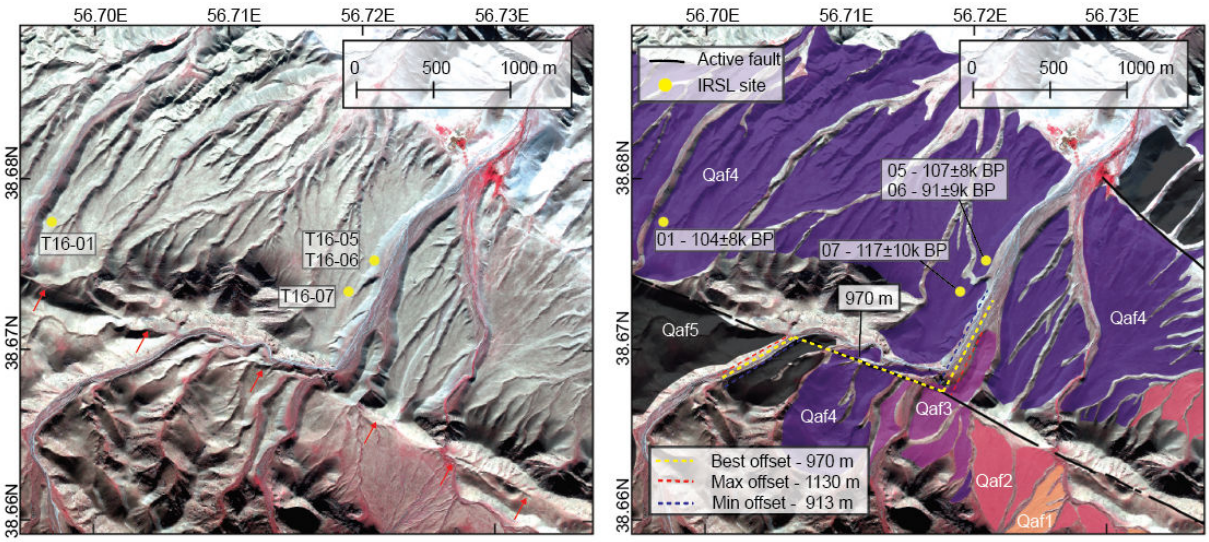


Figure 3.5: Offset drainage channels across the Main Kopeh Dagh Fault. Panel A shows WorldView 2 pansharpened false-colour composite satellite image showing the MKDF (red arrows). Yellow dots show IRSL

sample sites from Walker et al. (2021). Panel B shows the relative alluvial fan units Qaf 1 – 5 (Figs 3.3 and 3.4). Black lines show the fault trace, yellow dotted line shows the thalweg offset by the fault, blue dotted lines are the nearest risers and the distance between these represents a minimum offset measurement, red dotted lines are the furthest risers representing a maximum offset measurement.

The first two peaks from the COPD are 23.3 m and 30 m. Given the closeness in proximity in both values and age, these are difficult to separate in the stratigraphy. However, we only observe Qaf 1 surfaces with offsets at 23.3 m. Therefore, using the geologic slip-rate we assign a minimum age to Qaf 1 of 2 - 3 k years BP. For the 30 m peak offsets we observe that alluvial fans in both the Qaf 1 and Qaf 2 strata have offsets of this size. We can assign a minimum age of 3 - 4 k years BP to Qaf 2. The Qaf 1 surfaces also exhibiting 30 m offsets are within overlapping errors attached the offset measurements and could be due to error in the qualitative assessment of the surface. It is likely that because there are significantly more measurements of lower offset values (i.e. fewer larger offsets survive as sediments are more likely to be reworked with age), we have a greater age resolution between fan generations. A similar effect is seen when looking at the preservation of the most recent, penultimate and antepenultimate event offsets over shorter time scales in arid to semi-arid conditions (Reitman et al., 2023).

The third COPD peak is 88.5 m and from the long-term geologic slip-rate yields a minimum age between 8 -12 k years BP. We observe alluvial fans bound by ~ 88 m offset drainages within the Qaf 3 unit. This provides a minimum age constraint on the Qaf 3 unit of 8 - 12 k years BP.

The next COPD peak is at 256 m and yields an age of 24 - 33 k years BP (Table 3.1) which we also assign to the Qaf 3 strata based on some surfaces being bound by offsets of 256 m. We are unable to satisfactorily distinguish between the Qaf 3 surfaces offset by 88.5 m and 256 m from our remote mapping from satellite imagery. It is possible that there are two generations of sub-strata within the Qaf 3 surfaces, but further field investigation would be required to make this distinction.

The fifth COPD peak occurs at 402 m and the long-term geologic slip-rate provides a minimum age of 38 - 52 k years BP for the Qaf 4 surfaces bound by ~ 400 m offsets.
The sixth COPD peak has a preferred offset of 600 m and age of 56 -78 k years BP determined by the long-term geologic slip-rate. We observe three alluvial fans in the Qaf 4 unit that are

bound by drainages that are offset by ~ 600 m, one is high quality and well constrained measurement, the second is high quality with higher errors and the third is medium quality but well constrained (Fig. 3.7e).

The seventh peak in the COPD data is at 1000 m and is dated between 94 -130 k yrs BP from the long-term geologic slip-rate (Table 3.1). One of these surfaces has been dated using IRSL yielding a central age of 105 ± 5 k yrs BP (Walker et al., 2021). We observe three alluvial fan surfaces that are bound by the ~ 1000 m drainages that are assigned to the Qaf 4 unit. We therefore assign the 105 ± 5 k yrs BP to the Qaf 4 unit. Two of the three measurements are medium quality and well constrained, however the third measurement has error ranging from 900 m to almost 1100 m (Fig. 3.7e).

We cannot assign an offset measurement to Qaf 5 surface. We assume from the morphology of the surface and relationship to other alluvial units that this is older than the Qaf 4 surfaces. We observe that as the offset drainages increase the number of measurements decreases within our study area. We speculate that this is largely due reworking of sediment through time and the greater the period the higher chance of reworking. This results in a decrease in time resolution in the older units and wider errors and results are statistically less significant.

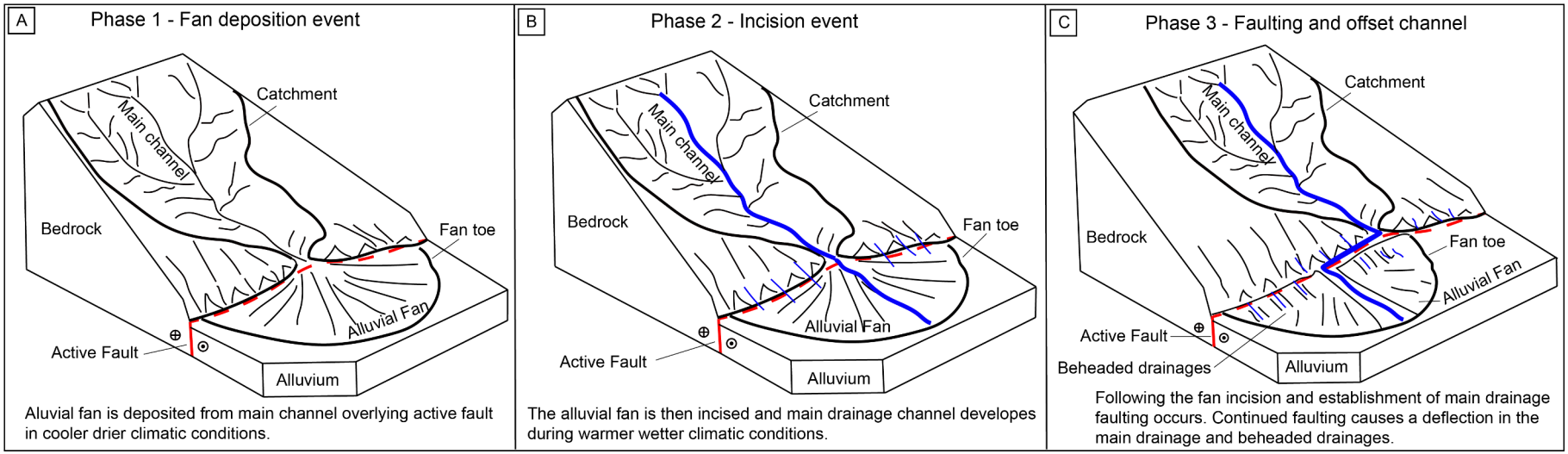


Figure 3.6: Simplified alluvial fan, incision and faulting schematic model for drainage channel offset measurements. Panel A shows alluvial fan deposition out of a catchment occurring during cooler and arid climatic conditions, the fan buries the active fault trace. Panel B shows the fan being incised by multiple drainages and the formation of a main channel during wetter climatic periods. Panel C shows the right-lateral movement on the fault beheading the drainages and offsetting the main channel through the alluvial fan. The main drainage is diverted along strike of the fault. The fault moves with a slip-rate, from this rate and measured offsets the minimum incision timing can be determined.

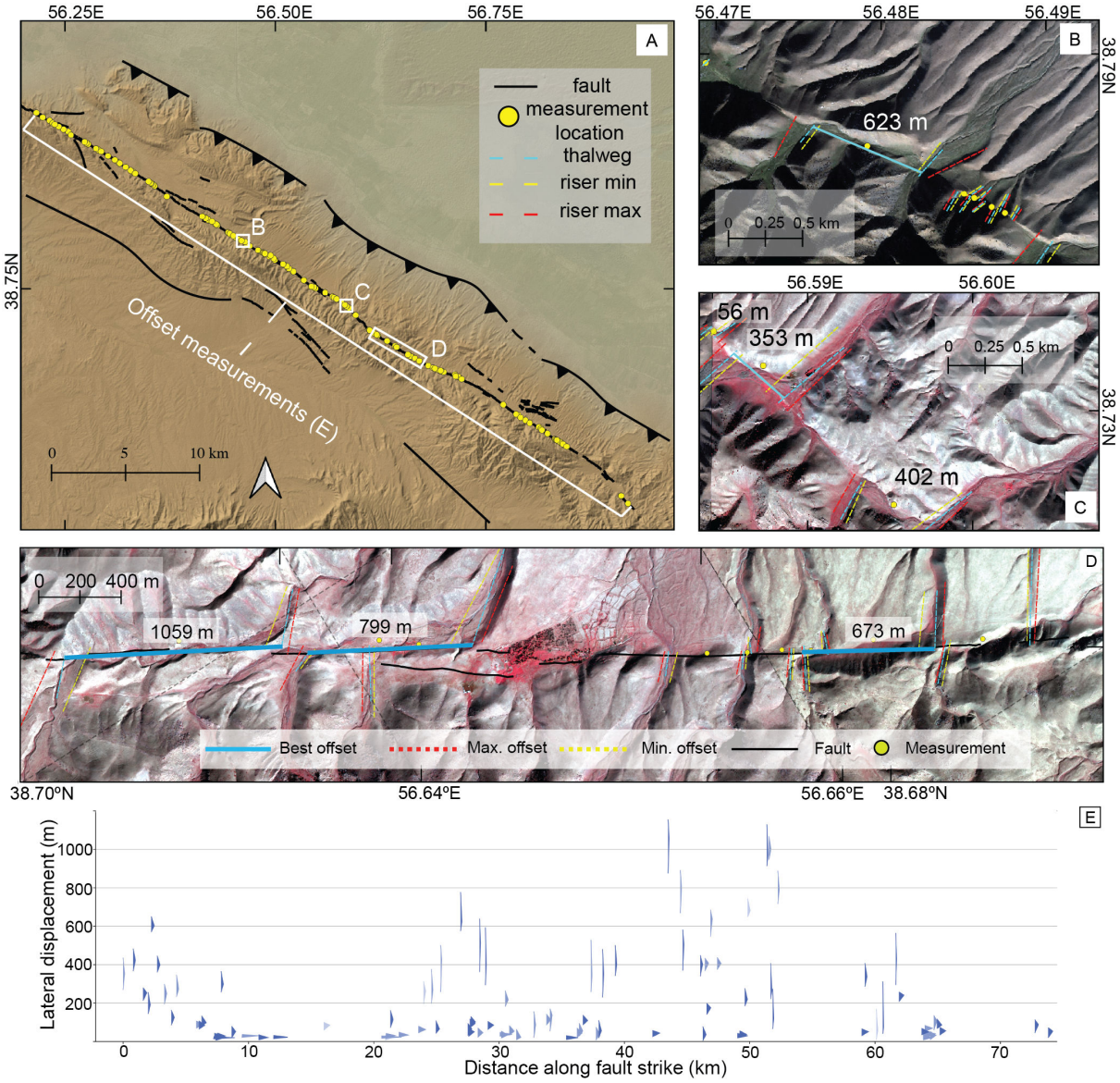


Figure 3.7: Panel A is an active fault map of the Main Kopeh Dagh Fault on SRTM derived DEM. Yellow dots show measured offset drainage and terrace riser sites. The white bracketed measurements are displayed on panel D. Panels B, C and D show the measurement method at two different sites shown on panel A. The blue lines are linear traces of the thalweg – this is our best offset measurement; the yellow lines trace the closest offset risers – representing the minimum offset; the red lines are the furthest risers – representing the maximum possible offset. Panel E shows the triangular Cumulative Offset Probability Distribution (COPD) for the section of the fault detailed in A. We show the combined COPD in Fig. 3.8 used to determine peaks in the COPD.

Table 3.1 shows the alluvial fan age based on slip-rate and peak fault offset displacement measurements shown in Figs 3.6, 3.7 and 3.8. We show the alluvial fan ages for the long-term geologic and geodetic slip-rates (this study and Dodds et al. (2022), respectively).

	Slip-rate: 9.2 ± 1.5 mm/yr			Dodds et al., 2022: 7.2 ± 2.4 mm/yr			Stratigraphic unit
Slip-rate (mm/yr)	7.7	9.2	10.7	4.8	7.2	9.6	
Peak Offsets (m)	Min. Age (kyrs)	**Age (kyrs)**	Max. Age (kyrs)	Min. Age (kyrs)	**Age (kyrs)**	Max. Age (kyrs)	
23.3	3	**3**	2	5	**3**	2	Qaf 1
30	4	**3**	3	6	**4**	3	Qaf 1 and 2
89	11	**10**	8	18	**12**	9	Qaf 3
256	33	**28**	24	53	**36**	27	Qaf 3
402	52	**44**	38	84	**56**	42	Qaf 4
600	78	**65**	56	125	**83**	63	Qaf 4
1000	130	**109**	93	208	**139**	104	Qaf 4

3.4.3 Age control

By combining the known IRSL ages for alluvial fan surfaces published in Walker et al. (2021) with our mapping we observe that the dated alluvial fans sit within the Qaf 4 unit. These deposits have been dated at between 117 ± 10 to 91 ± 9 kyrs BP, with a central age of 105 ± 5 kyrs BP. Two additional samples from a site outside our mapped area and yield ages of 37 - 34 ± 3 kyrs BP. The fan surface morphology is consistent with unit Qaf 3.

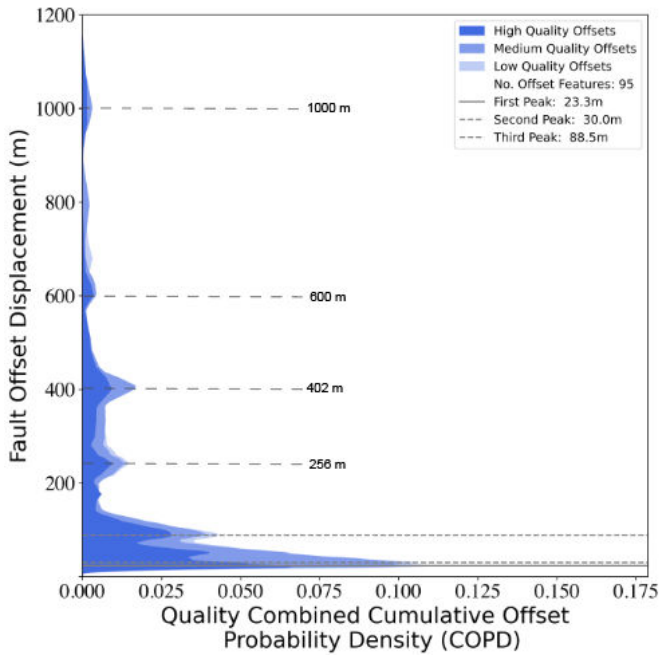


Figure 3.8: Shows the combined COPD results from our offset measurements. Quality has been assessed to each individual measurement as per the methods section. We see seven peaks in offset displacement at 23.3 m, 30 m, 88.5 m, 256 m, 402 m, 600 m and 1000 m. The number of measurements decreases as the offset displacement increases.

3.5 East Caspian lowlands

In this section of the study, we present new data acquired in the 2017 and 2019 field campaigns to the east Caspian lowlands, Turkmenistan. We present our findings from three sites near Oglanly, Belek Turrkmenskiy and Danata (Kum Dag) shown in Fig. 3.9.

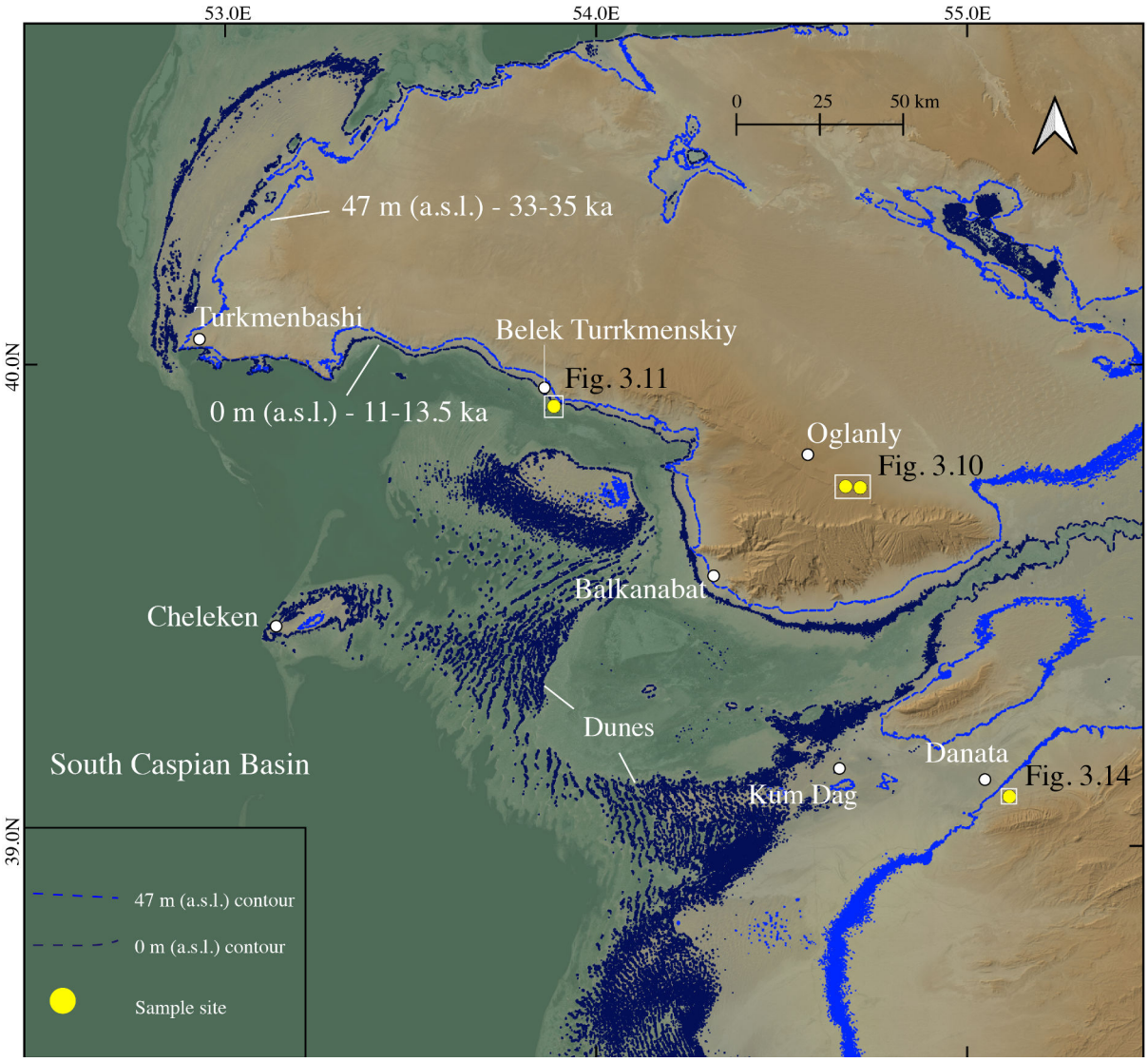


Figure 3.9: SRTM DEM (30 m resolution) of the East Caspian lowlands in Turkmenistan. The blues contours are at 0 m (a.s.l.) and 47 m (a.s.l.) and have been extracted from the SRTM DEM. We observe shoreline morphology at these contours that are from Caspian Sea highstands at 11-13.5 ka (0 m asl) and 33 - 35 ka (47 - 50 m asl) ((Leroy et al., 2020).

3.5.1 Oglanly

Oglanly is a small settlement to the north of Balkanabat and the northern front of the Balkan Mountain. There is a history of deep seismicity (depths > 20 km) with the last major earthquake occurring on the 6th December 2000 with a M7.0 at 25 km depth (Jackson et al., 2002). In November 2019 we undertook a field campaign evaluate possible fault scarps in the area (Figs 3.9 & 3.10).

Geomorphic surfaces

From our remote and field mapped we identify five generations of alluvial fan deposits at the Oglanly site (Fig. 3.10). We established relative age relationships based on the fan surface and cross-cutting relationships. Qaf 1 is youngest alluvial fan unit sitting northeast of the northern scarp. The fan surface is rough and incised by small streams and drainages. The drainage network appears immature and the unit crosscuts Qaf 2 and 4.

Qaf 2 is a smoother surface with less incision within the fan lobes than Qaf 1. It is deposited northeast of the northern scarp and is bound by the active drainage channels. Qaf 2 crosscuts Qaf 4 and 5.

Qaf 3 is a smooth surface with deeper incision than Qaf 2 and sits in the SE corner of Fig. 3.10 (a and b). It is crosscut by Qaf 2 and crosscuts Qaf 4.

Qaf 4 is a smooth surface with deeper incision than that of Qaf 2. It appears crosscut by Qaf 2 along the northern scarp. We obtained sediment samples from this surface (Fig. 3.10 c) which shows fan gravels at the base of the incision with river graves on top. IRSL dating yields a central age of 85.2 ± 5.5 k years BP (Table 3.3).

Qaf 5 is the oldest unit showing a smooth surface with deep well defined drainage channels. The surface terminates at the northern scarp with a clear change of unit (Qaf 2). The surface was sampled for IRSL dating and yields a central age of 99.7 ± 7.9 k years BP (Table 3.3).

Active faulting

We find evidence for active fault deformation at the Oglanly site. We observe two scarps, the first is at the foot of the bedrock mountain front, the second deforms the alluvial deposits to the north of the rangefront (Fig. 3.10). We see from SRTM 30 m elevation data the scarp shown in the topographic profile in Fig. 3.10 and this data give an approximate scarp height of 10-13 m.

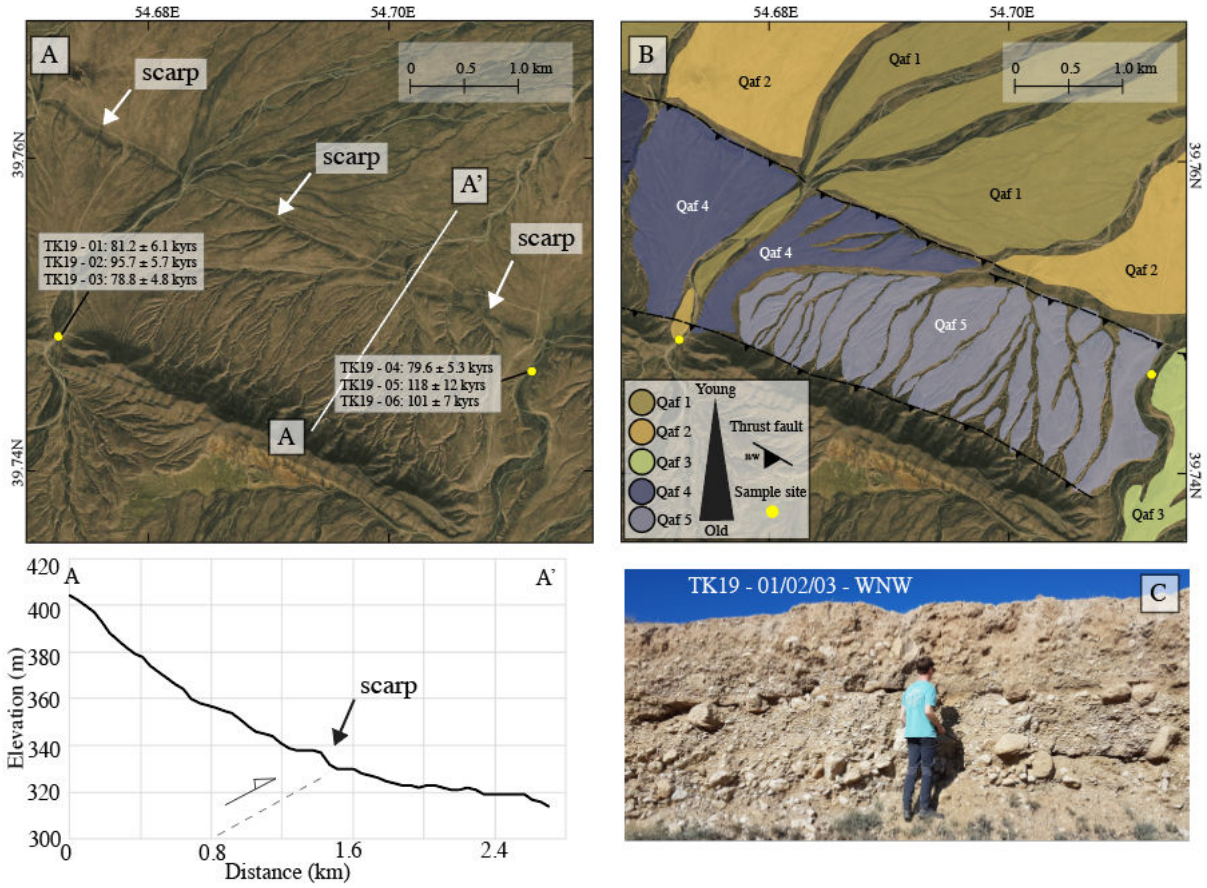


Figure 3.10: Panel A is a Bing Aerial image of the study area near Oglanly (Fig. 3.8). We observe two scarps and have sampled sediments for IRSL dating. Panel B shows a geomorphic map and we observe five different alluvial fan surfaces (Qaf 1-5). Yellow dots show sample sites. Panel C shows sample site TK19 – 01/02/03.

3.5.2 Belek Turrkmenskiy

About 80 km east of Turkmenbashi, the village of Belek Turrkmenskiy that sits at the edge of a coastal outlet into the Caspian Sea (Figs 3.9 & 3.11). East of the village are remnants of a small peninsular stepping out into the water channel. There are old gravel quarries on the peninsula and at the 0 m (a.s.l.) and 47 m (a.s.l.) contours towards Turkmenbashi.

Geomorphic surfaces

We identify four generations of beach deposits at the study area (Qb 1 – 4) and see two clear shorelines at 0 m (a.s.l.) and 47 - 50 m (a.s.l.) with evidence for at least three other shorelines at intermediate elevations. The 0 m (a.s.l.) and 47 - 50 m (a.s.l.) can be traced out to

Turkmenbashi to the west (Fig. 3.9). We also identify four generations of alluvial fan deposits (Qaf 1 - 4) with Qaf 1 is the youngest (Fig. 3.11).

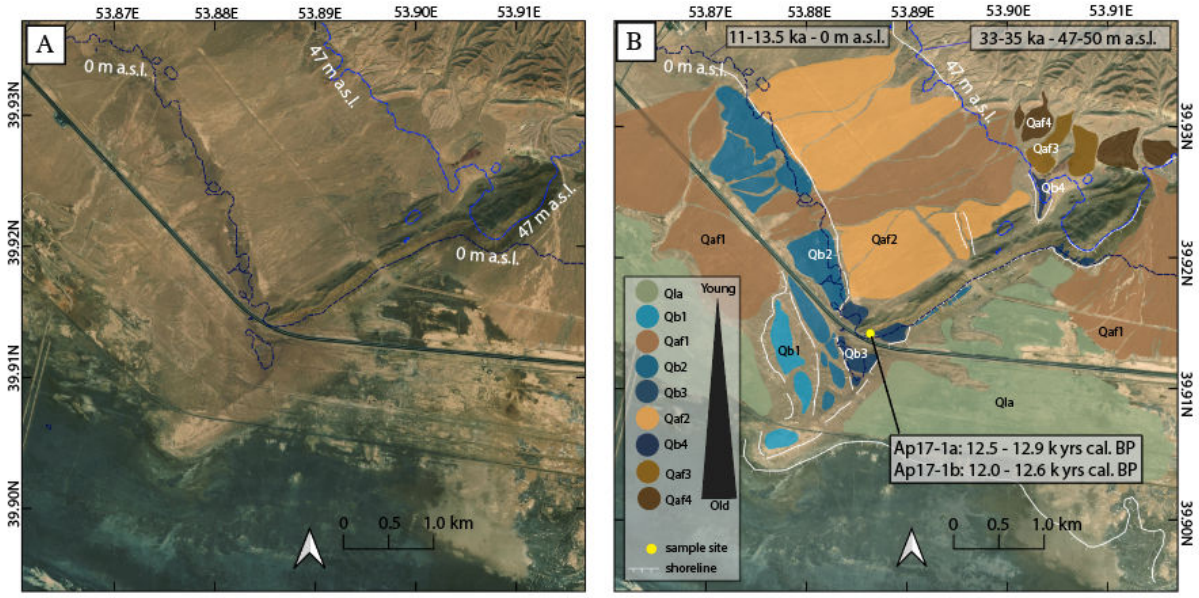


Figure 3.11: Panel A shows a Bing Aerial image of a shoreline sample site between Balkanabat and Turkmenbashi (Fig. 3.8). The blue contour lines show elevation at 0 m (a.s.l.) and 47 m (a.s.l.), the contours are at paleoshorelines. Panel B shows the Quaternary stratigraphy of the area. Qaf 1 – 4 are alluvial fan deposits; Qb 1 - 4 are beach deposits; and Qla is a lacustrine deposit. Age relationships are determined by elevation and cross-cutting relationships. Shorelines follow the 0 m and 47 m (a.s.l.) contours. Dated shells from Qb2 give a maximum age of 12.74 k cal. BP and are consistent with the end-Pleistocene high stand.

Qb 1 is identified on the peninsular between two shorelines and shows morphology consistent with a beach berm. Qb 2 sits above Qb1 and beneath the 0 m (a.s.l.) and is sandwiched between two shorelines on the peninsular. At the peninsular, Qb 2 shows beach berm morphology. The beach deposits continue to the east following the 0 m (a.s.l.) contour. We see evidence here both in the satellite imagery and in the field of quarrying and the sediments are shelly gravels (Fig. 3.11). Qb 3 sits at the 0 m (a.s.l.) and consists of shelly beach gravels and sands. Two bivalve shells were sampled from this unit and radiocarbon dating gives ages of at 12 – 12.9 k years cal. BP (Table 3.2, Figs 3.12 & 3.13). The sample site was a former gravel quarry and the main road to Turkmenbashi cuts through the deposit (Fig. 3.11a). The deposit has the morphology of a beach berm. Qb 4 sits at the 47 m (a.s.l.) and there is a clear shoreline shown in the alluvial fan surfaces that stretches out west towards Turkmenbashi (Figs 3.9 & 3.11). Field investigation of the deposits above Belek Turrkmenskiy show beach gravels with foresets capped with a horizontal gravel layer (Fig. 3.11). The Qb 4 deposit in Fig. 3.11 has a beach

berm morphology. We were not able to date shells from the site and we speculate from Caspian Sea level curves that this shoreline and beach deposit is most likely from 33 – 35 ka (Krijgsman et al., 2019).

Qaf 1 is the youngest alluvial fan deposit in the study area and crosscutting the Qb 2 beach deposit. Qaf 2 is older that Qaf 1 and has a smoother surface. Qaf 2 is cut at the 0 m (a.s.l.) shoreline suggesting that Qaf 2 predates or is concurrent with the Qb 3 deposits. There are two more generations of alluvial fans in the study area (Qaf 3 and 4). Qaf 3 is cut by the upper 47 m (a.s.l.) shoreline suggesting this unit predates or is concurrent with this high stand (Fig. 3.11). The Qaf 4 surface is a well incised surface that is crosscut by Qaf 3 suggesting it is an older unit.

The Qla surface is speculative, we interpret the flat surface as lacustrine deposits from a period with sea-level lower than the Qb 3 shoreline.

Table 3.2: Calibrated radiocarbon carbon ages at the sample location (Figs 3.11 and 3.12). The table shows the raw ages and calibrated date range using the Marine20 curve and ΔR value from sites around the Caspian. Samples are from shoreline deposits at 39.9142ºN/53.8864ºE, 0 m (asl).

Sample Name	Latitutde	Longitude	Elevation m (asl)	Age		sigma	Calibrated Modelled Age (cal. BP)
Ap17-1a	39.9142	53.8864	0	11,260	±	40	12,523 - 12,920
Ap17-1b	39.9142	53.8864	0	10,850	±	40	11,999 - 12,582

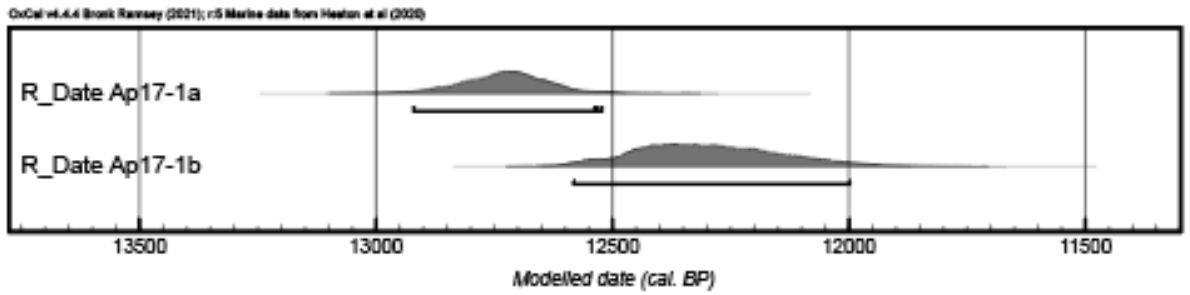


Figure 3.12: OxCal v4.4.4 probability distribution of calibrated age results from the Ap17-1a and b using the Marine20 curve.



Figure 3.13: A – Radiocarbon sample site for Ap17-1a/b, beach gravels and quarry site. B – shells sampled from beach gravels in A. C Shoreline deposit showing cross bedded gravels and sands capped with horizontal beach gravels. Interpreted as paleoshoreline at 47 m (asl).

3.5.3 Kum Dag

From satellite and field mapping we have mapped the Quaternary deposits near the village of Danata (50 km ESE of Kum Dag – Fig. 3.14). The study site sits on the western margin of the Kopeh Dagh mountains and the eastern edge of the Caspian lowlands. There are large scale anticline structures and active faulting appears to have a reverse sense of motion. We find three generations of alluvial deposit (Fig. 3.14b) that are labelled Qaf 1 to 3.

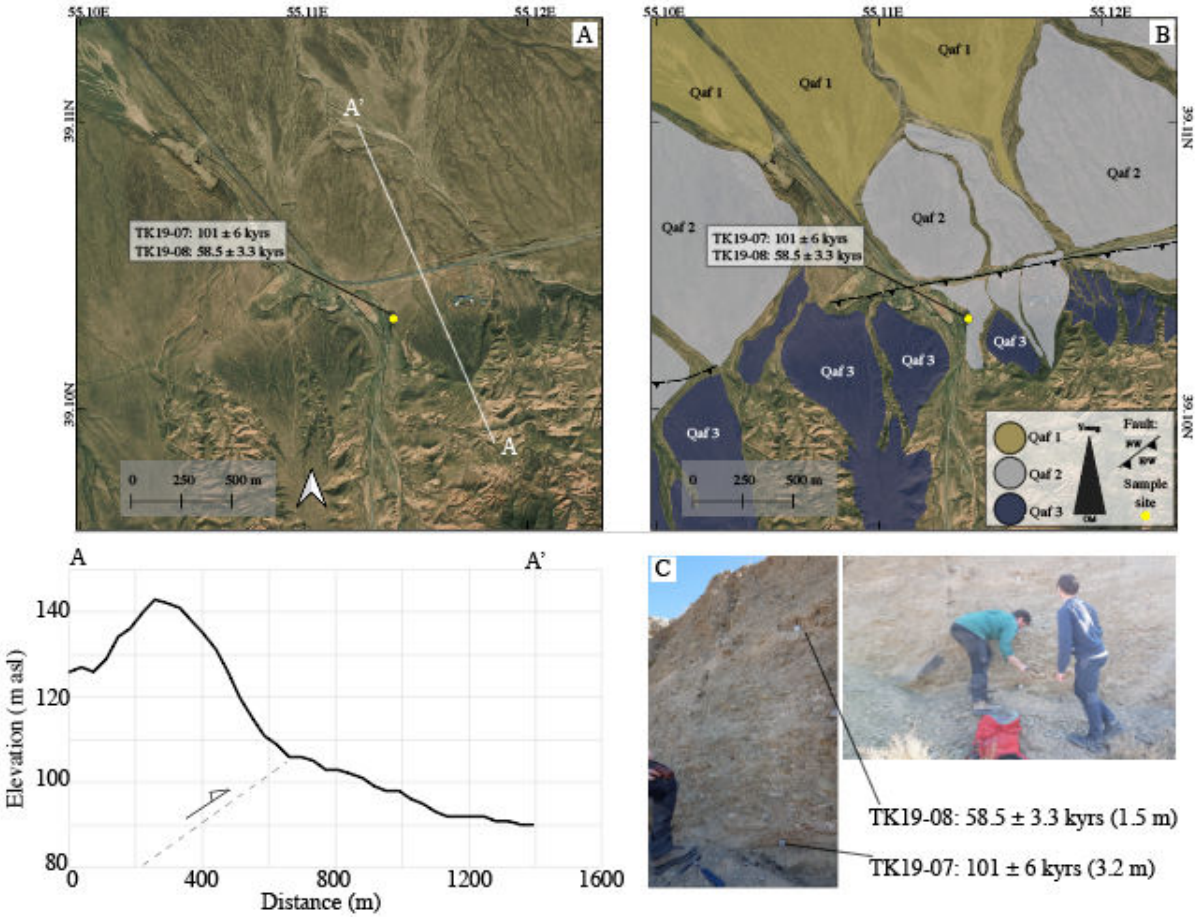


Figure 3.14: Panel A is a Bing Aerial image of the sample site to the southeast of Kum Dag (Fig. 3.8). Panel B shows the Quaternary stratigraphy and three generations of alluvial fan deposition (Qaf 1-3). We sampled sediments at the sample site (yellow dot) and use IRSL to constrain the age of deposition.

Geomorphic surfaces

Qaf 1 is the youngest surface which has a rough fan shaped surface with an immature shallow drainage network. Qaf 2 is the intermediate fan shaped surface which is smoother with a more well-established deeper drainage. It is crosscut by the Qaf 1 unit. We collected two samples

from a river cut in this surface from two silt lenses within the angular blocky/cobble layers that we interpret as alluvial coarse gravels. The samples were collected for IRSL dating and yield age constraints of the upper surface (1.5 m depth) at 58.5 ± 3.3 k years BP and the lower section (3.2 m depth) at 101 ± 6 kyrs BP (Table 3.3). We speculate that this surface was continuously active during the period 55 – 104 ka and then abandoned sometime after 55 ka. However, we cannot constrain the exact timing of abandonment from our results.

Qaf 3 is the oldest surface at the highest elevation at the study area and is a smooth surface with well-established drainage network bounding the sides of each surface (Fig. 3.14). The unit is crosscut by Qaf 1 and 2, suggesting that this is the oldest deposited unit. The IRSL dating of the younger Qaf 2 unit suggests that Qaf 3 was abandoned prior to 103 ka.

Active faulting

A clear scarp exists as a break in gradient of the hillslope shown in the profile A-A' (Fig. 3.14). There is a vertical offset in the Qaf 2 surface, and we speculate that this is fault related and the Qaf 2 surface south of the scarp has been uplifted by reverse faulting. From the SRTM elevation data we estimate a vertical scarp height of 7 - 10 m by projecting the Qaf 2 surface, which gives an uplift of 0.1 – 0.2 mm/yr. However, it should be noted that this measurement is based on low-resolution elevation data.

Table 3.3: Infrared Stimulated Luminescence results from sediment samples taken from alluvial fan sites at listed locations showing calculated group ages.

Latitude	Longitude	Elevation (m a.s.l.)	Field Code	Lab Code	Depth (m)	Sediment K (%)	Sediment U (µg/g)	Sediment Th (µg/g)	Dose rate mGy/yr		1 sigma uncertainty	Equivalent Dose (Gy)		1 sigma uncertainty	Age (kyr)		1 sigma uncertainty
39.748	54.673	399	TK19 -01	20094	1.90	1.6	6.25	9.00	4.18	±	0.18	340	±	21	81.2	±	6.1
39.748	54.673	398	TK19 -02	20095	1.32	1.8	7.19	8.50	4.55	±	0.20	435	±	18	95.7	±	5.7
39.748	54.673	400	TK19 -03	20096	3.30	1.9	5.13	8.50	4.15	±	0.18	327	±	14	78.8	±	4.8
39.746	54.673	400	TK19 -04	20097	2.30	1.9	7.13	9.00	4.63	±	0.20	369	±	18	79.6	±	5.2
39.746	54.673	400	TK19 -05	20098	1.50	1.4	5.8	6.20	3.74	±	0.16	442	±	40	118	±	12
39.746	54.673	360	TK19 -06	20099	4.10	1.8	4.02	8.80	3.82	±	0.17	388	±	18	101	±	7
39.103	55.114	90	TK19 -07	20100	3.20	1.8	2.18	7.50	3.35	±	0.15	340	±	12	101	±	6
39.103	55.114	90	TK19 -08	20101	1.50	1.7	2.3	9.40	3.44	±	0.15	201	±	7	58.5	±	3.3

3.6 Discussion

3.6.1 Paleoclimate in the late-Pleistocene

We interpret peaks in measured offset drainage channels along the Main Kopeh Dagh Fault as periods or pulses of increased incision (Fig. 3.6). Based on the long-term geologic and geodetic slip-rates we place constraints on the timing of increased incision (Table 3.1). The 1000 m peak corresponds to a central age of 105 ± 5 k years BP which puts this within MIS 5c – 5d (Fig. 3.14). From paleosol studies in the south Caspian lowlands (Iran) (e.g., Kehl, 2009; Kehl et al., 2021; Vlaminck et al., 2018, 2016) we speculate that this incision correlates to MIS 5c and increases in the global benthic $\delta^{18}O$ ($^{0}/_{00}$) curve (Lisiecki and Raymo, 2005) associated with relatively warmer and wetter conditions, with MIS 5a falling out of this age range (Fig. 3.15).

The 600 m peak corresponds to an age range of 56 - 78 ka using the geologic slip-rate putting these incisions within MIS 4 (Fig. 3.15). Previous studies of loess deposits in the south Caspian lowlands (Kehl et al., 2021) and stalagmites in the Alborz show drier stadial conditions during MIS 4. Alluvial fan abandonment, providing maximum age constraint on moister periods, in NE Iran show possible crossover with our incision dates towards the end of MIS 4 (Walker and Fattahi, 2011). We speculate that an increase in incision most likely occurred towards the end of MIS 4 which is towards the minimum end of our range (Fig. 3.15 and Table 3.1).

The next peak in our offset measurement results at 402 m can be dated between 38 - 52 ka (Table 3.1). Fan abandonment, constraining wetter periods in NE Iran is seen at Neyshabour (35 – 60 ka), Kashmar (40 - 60 ka) and Astaneh (55 ka) (Hollingsworth et al., 2010; Fattahi et al., 2007; Rizza et al., 2011; Walker and Fattahi, 2011). Additionally, intermittent poorly developed paleosols in the Caspian lowlands have been interpreted as relatively short-lived interstadial periods during MIS 3 (Karimi et al., 2011; Kehl, 2009; Vlaminck et al., 2018). We hypothesise that the 402 m offset peak could be associated to an increase in moisture due to intermittent interstadial conditions during this time.

We also observe another peak in the offset measurements at 256 m that dates at 24 – 33 ka using the geologic slip-rate (Table 3.1). Shoaee et al. (2023) also suggests that MIS 3 has short-

lived millennia scale wetter periods between 30 – 55 ka. Furthermore, the Caspian Sea is at high stand conditions between 33 – 35 ka (Krijgsman et al., 2019; Svitoch, 2013) with shorelines stretching well into Turkmenistan (Figs 3.2 & 3.9) at between 47 – 50 m (a.s.l.). This suggests there was an increased amount of water running into the Caspian in this period. Sediment studies from Lake Van (Turkey) show pulses of increased humidity during MIS 3 (e.g., McCormack et al., 2018). The 402 m and 256 m peaks in the offset measurements could be reflecting intermittent periods of increased precipitation during MIS 3.

We distinguish further peaks at 88.5 m, 30 m and 23.5 m with associated dates of 8 - 12 ka, 3 – 4 ka and 2 – 3 ka respectively. The 88.5 m peak (8 - 12 ka) corresponds to early MIS 1 and the start of the full interglacial period. Studies of Caspian Sea level show high stand conditions at 0m (a.s.l.) during this time that are supported by beach deposits dated in this study at 12.0 – 12.9 k years cal. BP at the same elevation in this study (Fig. 3.11). Additionally, well-developed paleosols from the Alborz, Kopeh Dagh and south Caspian lowlands have been correlated to this period (Karimi et al., 2011; Kehl et al., 2021) which also supports a hypothesis of increased moisture and warmer climatic conditions. Early Holocene (MIS 1) lake deposits from Nimbluk (Fattahi and Walker, 2015) and peat sequences from Neor Lake in the Alborz (Sharifi et al., 2015) have been dated at ~9 ka and are indicative of wetter conditions. Furthermore, alluvial fan abandonment is observed at Sabzevar (Fattahi et al., 2006), Kashmar (Fattahi, et al., 2007) and Astaneh (Rizza et al., 2011) during this period can be interpreted as indicative of wetter conditions. From the peaks in our offset measurement data, geomorphic mapping and other evidence from the region, we conclude that 8 – 12 ka is a period of increased incision and precipitation.

3.6.2 Caspian Sea level

From our geomorphic mapping we show two main shorelines at 47 - 50 m (a.s.l.) and 0 m (a.s.l.). Radiocarbon dating of shells in a beach berm deposit (Fig. 3.11) we suggest an age for the 0 m (a.s.l.) shoreline of around 12 – 12.9 k years cal. BP. This result does not agree with work by Svitoch (2009), Tudryn (2022) and Kuzucuoglu and Leroy (2023), who suggest lake levels nearer 50 m (a.s.l.) during the period 12 – 22 ka. Our results are consistent with work by Krijgsman et al. (2019) that suggests lake levels were nearer 0 m (a.s.l.) between 11 – 15 ka.

The geomorphic relationships suggest that the 47 – 50 m (a.s.l.) shoreline predates MIS 1 and most likely is associated with the Caspian high stand at 33 – 35 ka (Krijgsman et al., 2019; Svitoch, 2013). Our mapping of the 47 m (a.s.l.) contour line (Fig. 3.2) shows that Caspian Sea shoreline likely stretched further east of Serdar (Fig. 3.1). It is worth noting, however, that we did not date the 47 m (a.s.l.) shoreline and we cannot rule out that this shoreline formed in a later transgression.

Our findings reveal that the presence of the 256 m peak in channel offsets implies an increase in the incision of alluvial fans during the period 24 – 33 ka. This escalated incision may also be connected to a decline in the overall base level.

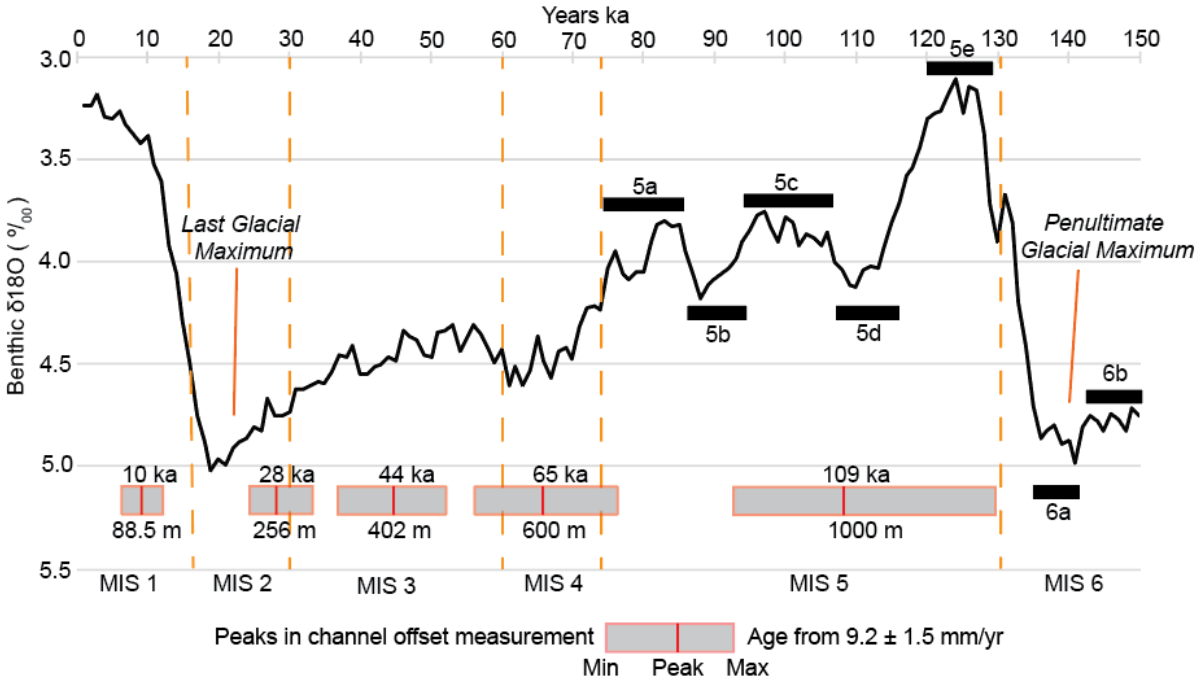


Figure 3.15: Benthic $\delta^{18}O$ ($^{0}/_{00}$) curve for the last 150 kyrs (Lisiecki and Raymo, 2005). Yellow dotted lines show Marine Isotope Stages and black bars show sub-stages. Grey blocks show minimum, best and maximum incision ages from peaks in the cumulative offset probability distribution (COPD) in Fig. 3.7 and Table 3.1. Red line is the age from the best measurement.

3.7 Conclusion

We build the first late-Quaternary stratigraphy in the Turkmen Kopeh Dagh and east Caspian lowlands. From relative dating and geomorphic relationships, we see five generations

of alluvial fan deposits in the Kopeh Dagh and Balkanabat mountains. We also find three clear alluvial fan generations in the east Caspian lowlands. From our on-fault offset drainage measurements we identify several peaks in incision, and we constrain timing from the long-term slip-rate at MIS 5 (e or c), late-MIS 4, MIS 3 and MIS 1. Our results agree with previous paleoclimate studies in NE Iran suggesting intermittent wetter periods during MIS 3 prior to the Last Glacial Maximum. Our results from the east Caspian lowlands show date a 0 m (a.s.l.) shoreline at 12 – 12.9 k years cal. BP consistent with a Caspian Sea level high stand in the early Holocene.

Acknowledgements

This work was supported by the Leverhulme Trust Research Project Grants 'EROICA' (RPG-2018-371) and 'NEPTUNE' (RPG-2018-243), by the NERC-ESRC Increasing Resilience to Natural Hazards program 'Earthquakes without Frontiers' (NE/J02001X/1), the NERC-funded COMET (GA/13/M/031), and allocation 0009090 from the Research England GCRF Support Fund. Pleiades satellite imagery was obtained through the Committee for Earth Observing satellites (CEOS) Seismic Hazard demonstrator.

Statement of Authorship for joint/multi-authored papers for PGR thesis

To appear at the end of each thesis chapter submitted as an article/paper

The statement shall describe the candidate's and co-authors' independent research contributions in the thesis publications. For each publication there should exist a complete statement that is to be filled out and signed by the candidate and supervisor **(only required where there isn't already a statement of contribution within the paper itself).**

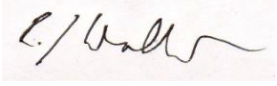
Title of Paper	Constraining landscape evolution of the Kopeh Dagh, Turkmenistan, using optical imagery and long-term geologic slip-rates.
Publication Status	□Unpublished and unsubmitted work written in a manuscript style
Publication Details	N. Marshall[1], G. Begenjev[2], Y. Bezmenov[2], N. Dodds[1], C. Gruetzner[3], R. Mirzin[2], E. Rhodes[4,5], R.T Walker[1] 1 - COMET, Department of Earth Sciences, Oxford University, Oxford, OX1 3AN, UK. 2 - Institute of Seismology and Physics of the Atmosphere, National Academy of Sciences of Türkmenistan, Aşgabat, Türkmenistan. 3 - Friedrich Schiller University Jena, Institute of Geological Sciences, Jena, Germany. 4 - Department of Geography, University of Sheffield, Sheffield, S10 2TN, UK. 5 - Department of Earth, Planetary, and Space Sciences, University of California Los Angeles, Los Angeles, CA 90095-1567, USA.

Student Confirmation

Student Name:	Neill Marshall		
Contribution to the Paper	Performed mapping and analysis on the topographic data, interpreted data and wrote the manuscript.		
Signature.	Neill Marshall	Date	04/10/23

Supervisor Confirmation

By signing the Statement of Authorship, you are certifying that the candidate made a substantial contribution to the publication, and that the description described above is accurate.

Supervisor name and title: Prof. Richard T. Walker			
Supervisor comments The student performed all analyses and interpretations			
Signature.		Date	05/10/23

This completed form should be included in the thesis, at the end of the relevant chapter.

Chapter 4

Paleoseismology of the Shirvan Strike-slip fault zone (West Caspian Fault), Azerbaijan: implications for seismic hazard and South Caspian tectonics.

Abstract

We provide the first robust geomorphic evidence for active dextral strike-slip faulting at the western and north-western margins of the South Caspian Basin, within the Kura basin of Azerbaijan. The Shirvan fault is one of several parallel strands and shows a number of right-lateral stream deflections and follows mud volcano alignments. Mud volcanoes occur predominantly at bends and anticlinal folding along the otherwise strike-slip trace, indicating a structural control on emplacement. Mud volcano distribution and alignments in seismicity allow us to infer a total fault length of ~150 km. We estimate a minimum slip-rate of 3.9-4.8 mm/yr averaged over the Holocene, based upon a displaced terrace riser of assumed age. Two paleoseismic trenches reveal between four and six surface rupture events over the last 3000 years, a seventh prior to that, and an average recurrence interval of 500-750 years. The events are unevenly spaced in time, with a significant cluster of 2 or 3 events in the last 600 years, and much longer intervals earlier. From earthquake scaling relationships we would expect rupture of the entire fault length to produce Mw 7.5 events with average slip of 3 m, which is consistent with the smaller lateral offsets (2-3 m) that we identify in imagery. However, a lack of historical earthquakes combined with inferences on fault behaviour within the fluid-rich Kura basin sediments lead us to speculate that the ruptures may represent aseismic slip events. The Shirvan and adjacent strike-slip faults play an important role in accommodating tectonic plate motion at the margin of the South Caspian Basin, and present a significant seismic hazard for communities and infrastructure in the vicinity.

4.1 Introduction

Determining the distribution, style, slip-rate, and earthquake history on major active faults is an essential step, both in understanding the hazard that they pose to local populations, and in determining the role that they play in accommodating regional tectonic motions (e.g. Molnar and Tapponnier, 1978; Walker et al., 2021). Nonetheless, there are many places globally where such information is lacking. The Kura basin of Azerbaijan is an important example. The active faulting within and around the basin is likely to play an important role in accommodating motion of the South Caspian Basin, which is an aseismic block within the Arabia-Eurasia collision zone that appears to move relative to its surroundings. Active faulting within the Kura basin also poses potential hazards to relatively large populations and important transport and energy infrastructure. However, rapid sedimentation within the Kura basin and multiple transgressions of the nearby Caspian Sea have acted to largely conceal the geomorphic expression of faulting, such that both the existence of major fault zones, and descriptions of their kinematic roles, are debated (e.g. Jackson et al., 2002; Vernant et al., 2004; Copley and Jackson, 2006; Reilinger et al., 2006; Kadirov et al., 2012; Gunnels et al., 2020).

In this paper we use observations from sub-metre resolution optical satellite imagery and digital elevation models derived from stereo satellite imagery, combined with published seismicity, and the distribution of mud volcanoes, to confirm the activity of north-south right-lateral strike-slip faults within the Kura basin. We undertake detailed field survey of one of the active faults, the Shirvan fault zone (Fig. 4.1), to determine slip-rate and paleoseismic history. We then discuss the role of the Shirvan fault in the regional tectonics and explore whether the faulting observed in the trench results from seismic or aseismic slip.

In the following sections we first introduce the regional geographical and tectonic setting (Section 4.2), and the methods used (Section 4.3), before describing the results of our regional survey of faulting (Section 4.4), paleoseismology and slip rate (Sections 4.5 and 4.6), and discussion (Section 4.7).

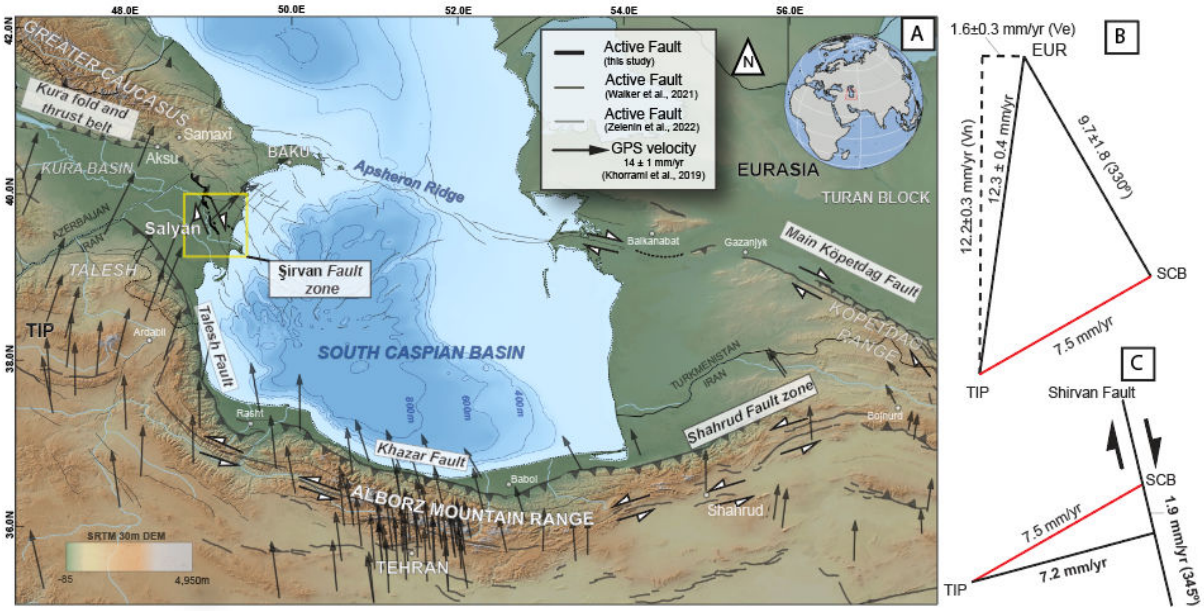


Figure 4.1. **A:** Tectonic map of the South Caspian Basin. Black arrows show GNSS velocity data relative to Eurasia is after Khorrami et al. (2019). Thick black lines are faults mapped in this study, black lines with teeth are active thrust fault, thick dark grey lines are from Walker et al. (2021), and thin light grey lines are taken from the Neotectonics Group, Moscow active fault map (Zelenin et al., 2022). The map shows the northern zone of Arabian-Eurasian collision with the main fault zones named in the white boxes. The yellow box is our study area. Note that GNSS velocity vectors drop significantly north of the Greater Caucasus. The motion of the GNSS and on the faults shows the westward extrusions of the South Caspian Basin and the subduction beneath the Alborz and Talesh. **B:** Velocity triangle showing motion of the South Caspian Basin relative to Eurasia (Dodds et al., 2022b). The Turkish-Iranian Plateau (TIP) motion is determined by averaging GNSS velocity vectors from Khorrami et al. (2019) relative to Eurasia. Solving between these two vectors gives SCB-TIP motion of 7.5 mm/yr. **C:** Takes the average strike of the Shirvan Fault (345°) to solve for the shortening (7.2 mm/yr) and 1.9 mm/yr of right-lateral shear.

4.2 Geographic and tectonic setting

4.2.1 The Kura Basin

The Shirvan fault zone is sited within the Kura Basin, a depression between the Greater Caucasus mountains to the north and Lesser Caucasus mountains to the south (Fig. 4.2). The sedimentary thickness of the Kura Basin is thought to be ~15 km (Piip et al., 2012), underlain by a granitic-metamorphic basement (Nadirov et al., 1997). Eastern Azerbaijan has a high concentration of mud volcanoes, distributed both in the Kura basin onshore and the offshore South Caspian Basin (Figs 4.2 & 4.3), with mud sourced from Oligocene Maykop formation, which underlies the ~10 km thickness of sands of the productive series (Abdullayev et al.,

2017; Allen et al., 2002; Mangino and Priestley, 1998; Piip et al., 2012). Mud volcanism results from sediment over-pressure and presence of hydrocarbons, combined with tectonic compression from the Arabia-Eurasia collision results in high pore pressure within the basins (Feyzullayev et al., 2015; Mazzini and Etiope, 2017).

Crustal thickness decreases, due to thinning, across the Kura Basin from ~60 km in the west to ~45 km in the east where it borders the South Caspian Basin (Mangino and Priestley, 1998). The Kura River flows eastwards through the basin to the Caspian Sea, leading to relatively high sedimentation rates at the present day. In the north, the Kura fold and thrust belt and Greater Caucasus are being actively uplifted by reverse faulting with seismicity focussed on the frontal thrusts (Fig. 4.2) (Allen et al., 2004; Copley and Jackson, 2006; Forte et al., 2013, 2010; Gunnels et al., 2020; Jackson et al., 2002). GNSS survey data by Kadirov et al. (2012) and Reilinger et al. (2006) shows northward motion of the Kura Basin with respect to Eurasia of 13.2 ± 0.5mm/yr (Figs 4.2 & 4.3).

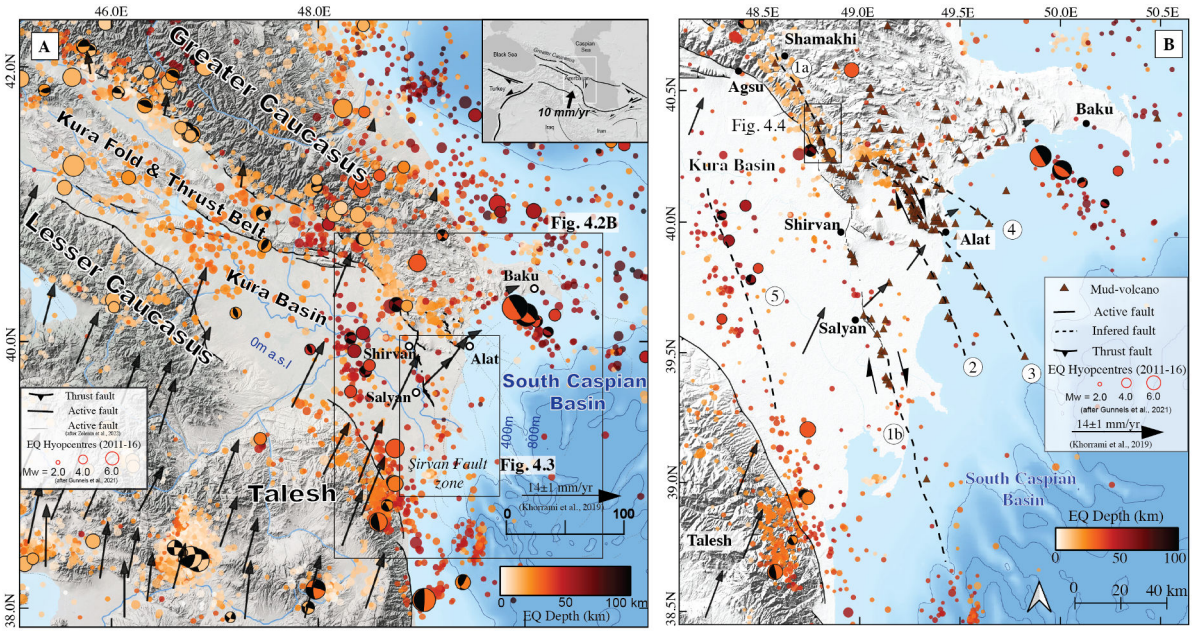


Figure 4.2 A - Seismotectonic map of Azerbaijan and Trans-Caspian region (inset). GNSS velocity vectors are from Khorrami et al. (2019), relocated seismicity is from Gunnels et al. (2021), and focal mechanisms are taken from the ISC catalogue. Black lines show the major faults and light grey shows active faults from Zelenin et al. (2022). Digital elevation data is from SRTM (30 m resolution) and Bathymetric data is from the Global Oceans (https://www.gebco.net/data_and_products/gridded_bathymetry_data/). B – Dotted black line show lineation of mud volcanoes in five main areas (1a – Shamakhi to Shirvan, 1b – Salyan to offshore South Caspian Basin, 2 – offshore southwest Alat, 3 – Alat (NW-SE) trend, 4 – north Alat offshore). Trend 5 is a linear NNW-SSE trend is seismicity with strike-slip focal mechanisms.

Most well-constrained earthquakes in the Kura Basin are moderate in magnitude and have depths that exceed 10 km (e.g., Copley and Jackson, 2006; Gunnels et al., 2020; Jackson et al., 2021, 2002; Engdahl et al., 2006). There are few recorded significant historical earthquakes on or near the Shirvan fault zone over the last 2000 years (Shebalin and Leydecker, 1997), with the exception of one event in the vicinity of Salyan in 1881 with magnitude 4.0 and intensity 5. Ambraseys and Melville (1982) report no earthquakes in the Shirvan region although there are two earthquakes in Azerbaijan of unknown origin in 1305 and 1436 (Ambraseys and Melville, 1982).

The active faulting in Azerbaijan and the Southeastern Caucasus is related both to north-south shortening within the Arabian-Eurasian continental collision zone, and to the motion of the South Caspian basin, which appears to be moving independently of the deforming regions that border it (e.g. Jackson and McKenzie, 1984; Jackson et al., 2002). Below, we describe the tectonics of the South Caspian Basin, which allows us to make inferences on the kinematics and tectonic role of faulting within adjacent regions of Azerbaijan. We also briefly describe the record of sea-level changes within the Caspian Sea, which has a large effect on the geomorphology of our study.

4.2.2 The South Caspian Basin (SCB)

The South Caspian Basin is bounded to east, south and west by the Kopeh Dagh, Alborz, and Talesh deforming belts, and its northern boundary is marked by the Apsheron ridge. Receiver function analysis and seismic reflections studies show a low velocity layer 15-20 km thick and 10-18 km high velocity basaltic-like layer beneath (Jackson et al., 2002). Additionally, reinterpretation of seismic refraction data reveals a thinned crustal thickness of 10 km and a Moho discontinuity at ~35-40 km deep (Piip et al., 2012). Above the basement, the 15-20 km low velocity layer is modelled as a series of sedimentary layers with the Miocene basin fill deposits starting at a depth of ~8-9 km (Abdullayev et al., 2017). The Quaternary layers make up the top 3 km of the basin fill (Abdullayev et al., 2017; Allen et al., 2002).

The basin is aseismic and thought to move independently of its surroundings, with a rate of 10.4 ± 1.1 mm/yr in direction 333° ± 5° relative to Eurasia, and 4.8 ± 0.8 mm/yr in direction

236° ± 14° relative to Iran (Copley and Jackson, 2006; Djamour et al., 2010; Jackson et al., 2002; Walker et al., 2021). North of the Apsheron ridge earthquakes with depths greater than 80 km occur, and are thought to be a result of the basement of the South Caspian subducting north beneath Eurasia (Jackson et al., 2021, 2002; Walker et al., 2021). Westward subduction of the SCB beneath the Talesh and Kura basin is also inferred from deep shallow-angle reverse faulting earthquakes (to depths of around 40 km) beneath these ranges (Jackson et al., 2002). The onset of subduction is often assumed to correlate to increased sediment accumulation in the basin at 5.5 Ma (Allen et al., 2002), though analysis of deep seismic lines through the Apsheron ridge and South Caspian instead suggest that the subduction dates earlier, to the Miocene (e.g. Green et al., 2006).

In the east, the motion of the SCB relative to Eurasia and Iran is accommodated via conjugate motion on the dextral Main Kopeh Dagh Fault and sinistral Shahroud Fault zone, as shown in Fig. 4.1, (Dodds et al., 2022b; Hollingsworth et al., 2008; Jackson et al., 2002; Walker et al., 2021). Faulting along the southern side of the SCB changes from east to west, with decreasing amounts of left-lateral slip and increasing shortening components as the Alborz ranges curve around the south side of the SCB. GNSS velocities indicate that the Talesh ranges and Kura basin move northwards relative to Eurasia at 10 – 13 mm/yr. GNSS studies by Kadirov et al. (2012) and Reilinger et al. (2006) show a north-eastwards directional change and decreasing magnitude of the velocity vectors between Salyan and Baku (Figs 4.1, 4.2, and 4.3). Kinematic modelling from GNSS data show that N-S strike-slip is possible (Djamour et al., 2010; Kadirov et al., 2012). By forming a velocity triangle from GNSS-derived Talesh-Eurasia velocity and the 9.7 ± 1.8 mm/yr SCB-EUR velocity (Dodds et al., 2022b) allows us to estimate ~ 7.5 mm/yr of motion between the SCB and the Turkish-Iranian Plateau (TIP) and Kura basin (Fig. 4.1). Resolving this velocity onto the north-south structures of the TIP results in 1.9 mm/yr of range-parallel right-lateral faulting, and 7.2 mm/yr of range-perpendicular shortening.

The structures on which relative motion between the Talesh mountains and Kura basin are accommodated are not well constrained, leading to continued debate about the kinematics of faulting, with some studies. A number of north-south right-lateral earthquakes are known from the Talesh region of Iran, including the Mw 6.1 Ardebil earthquake in 1997, and right-lateral geological and geomorphic displacements are mapped on north-south faults within the Talesh (Aziz Zanjani et al., 2013). Further north, we expect the right-lateral and reverse faulting to

continue across the Kura basin, though the rapid sedimentation has hindered efforts to identify active structures. Gunnels et al. (2020) show an NNW-SSE striking linear trend of seismicity (greater than 30 km deep) in the Kura Basin (Fig. 4.2) and interpret this as a dextral strike-slip fault zone, the West Caspian Fault. An abrupt alteration in sedimentary thickness (Allen et al., 2003) and gravity anomalies (Khain et al., 1966) are thought to be indicative of the presence of the West Caspian Fault. Trifonov (1978), Allen et al. (2003), and Khain et al. (1966) describe right-lateral shear and map active faults between topographic highs near Shirvan and Salyan, documenting evidence for én echelon folding. However, the existence of right-lateral faulting across the Kura basin is not certain. Copley and Jackson (2006) point out that available focal mechanisms indicate almost pure thrusting perpendicular to the Talesh margin, such that any right-lateral component is not reflected in seismicity.

4.2.3 Caspian Sea level

The Caspian Sea is the largest endorheic body of water globally, with occasional outflow to Black Sea at certain periods in its geologic history (Leroy et al., 2020). The closed nature of the Caspian Sea means that water levels vary depending on climatic and river inflow changes. The main sources of water into the Caspian are the Volga, Kura and Amu-Darya rivers and occasionally the Aral Sea. The southern Caspian Sea is deep water and overlies the South Caspian Basin. The northern part of the Caspian Sea is shallower, and overlies Eurasian basement.

The Caspian water level is presently at – 28 m and has changed dramatically since the Miocene, with transgressions peaking above 150m and regressions as low as -1500m (Forte and Cowgill, 2013; Kroonenberg et al., 1997). Radiocarbon dating of marine shells indicates two significant late Pleistocene transgressions at around 35ka and 11-13.5ka with high stands of 47-50 m and 0 m above global mean sea level (a.s.l.) respectively as discussed in Chapter 3 (Arslanov et al., 2016; Dolukhanov et al., 2010; Kakroodi et al., 2012; Kroonenberg et al., 1997; Pánek et al., 2016). During the Holocene, the Caspian Sea level has fluctuated with small-wavelength transgressions and regressions, and with high stands not exceeding -20 m a.s.l. (Kakroodi et al., 2012; Kroonenberg et al., 2007; Ollivier et al., 2016).

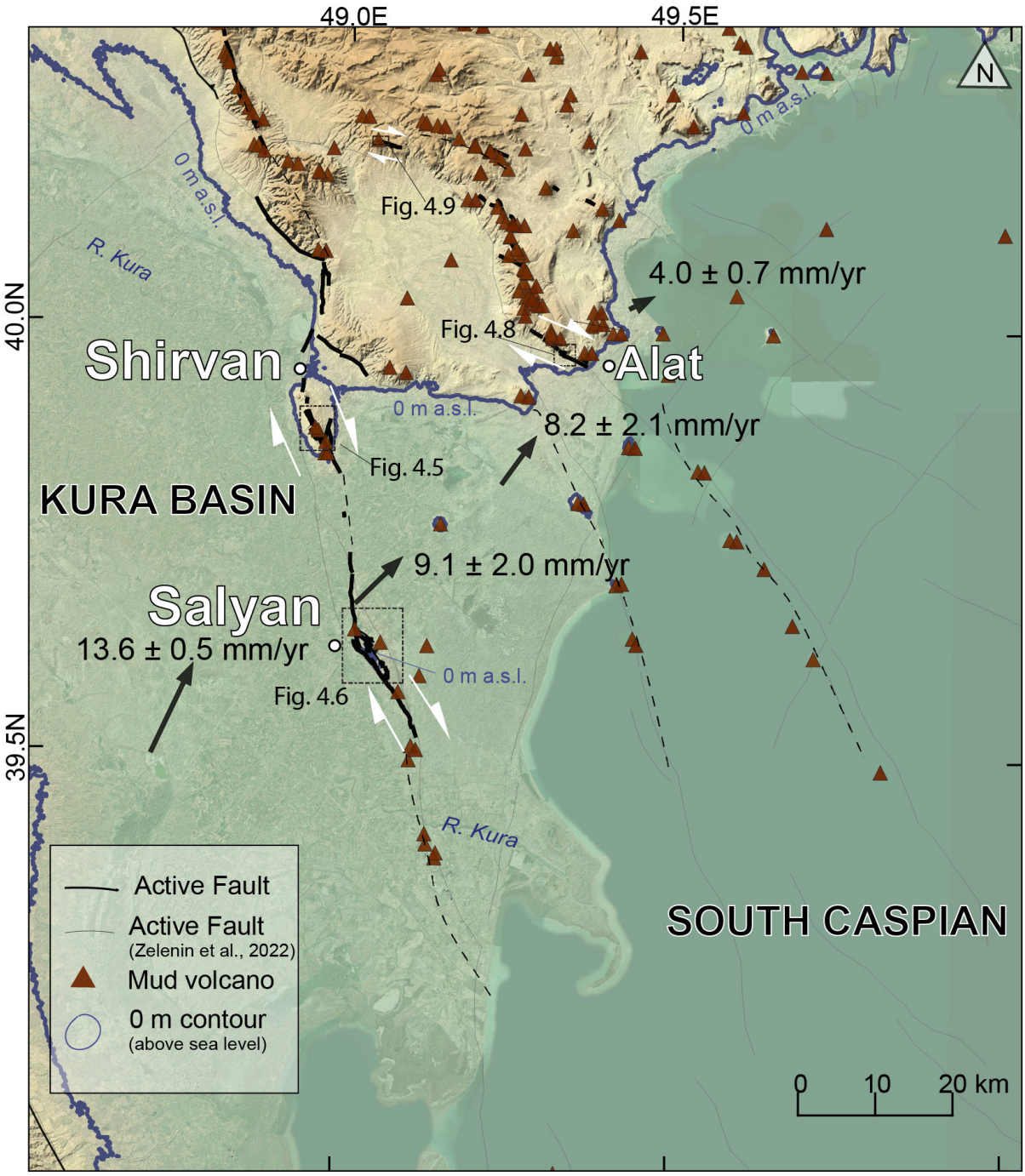


Figure 4.3. Active faults in the Shirvan region and GNSS velocity vectors for the area (after Khorrami et al. 2019). Brown triangles show the location of active mud volcanoes, black lines show the fault mapping in this study, grey lines are active faults from Zelenin et al. (2022). The blue line shows the 0 m above sea level (a.s.l.) contour which is dated at 11,000 – 13,500 years BP. Highlighted on this map are four study areas (see below). Elevation data is from SRTM and has been overlaid on to a Google Earth image.

4.3 Methods

4.3.1 Satellite imagery

We obtained high-resolution stereo imagery from the Pléiades satellite mission to build digital elevation models (DEMs) of onshore topography around the Shirvan fault zone (https://portal.opentopography.org/dataCatalog, 19/05/2021, SO21034807-2). We use Agisoft Metashape software to match points from pairs of images and calculate elevation point data. The point data is then interpolated to build a surface model or DEM with 1 m/pixel resolution. Faults were remotely mapped using hillshade images of Pléiades DEMs, Google Earth and Bing Aerial images prior to field mapping in May 2022. Using the satellite derived DEMs and photographs, we identified key sites for further field investigation. Elevation data is geoid adjusted using the emg2008-5 model derived by satellite gravity data and cubic interpolation (Karney, 2019). We use the geoid adjusted elevation data to determine topography heights relative to current sea level.

4.3.2 Structure from motion (Surveys using Unmanned Aerial Vehicle)

Key study sites in near Salyan (Fig. 4.3) were surveyed using a Teokit equipped DJI Phantom 4 Pro v2 drone, collecting ground surface images. The Teokit is a dGPS and provides precise photo locations that are corrected to the Emlid Reach RS2 dGPS base station (e.g., Zhang et al., 2019). We use Agisoft Metashape software to process the surveyed photographs into an Orthomosaic, and a DEM with a horizontal 2.6 cm/pixel resolution (https://portal.opentopography.org/dataCatalog).

4.3.3 Geomorphic and fault mapping

We undertook detailed geomorphic mapping using a combination of field observations, satellite imagery, and drone derived DEMs. At the Salyan site, we map identify fault scarps and measure offset drainage channels using a combination of field-based observation and drone imagery. Elevation data, measured from the dGPS, Teokit, and dGPS rover has been corrected using the emg2008-5 geoid model and cubic interpolation (Karney, 2019), giving the orthometric height.

We use abandoned terrace risers as piercing lines to measure offsets at the Salyan site (Fig. 4.6) as the thalweg is still the active channel at the site. We measure the preferred offset by measuring in QGIS the distance between the thalwegs and risers (e.g., (Kurtz et al., 2018) and the LaDiCaoz method (e.g., (Zielke and Arrowsmith, 2012). LaDiCaoz is a freely available Matlab programme that uses elevation data to best-fit and restore drainage channel and terrace riser offsets. We use elevation data from our UAV derived DEM and manually input the fault location, trace out the terrace riser and constrain the fault trace (from our fault mapping). The software then uses a best fit method to restore drainage channels and terrace riser slope.

Near Shirvan we measure offset drainage channel thalwegs along the surface rupture trace using the satellite derived DEMs. We use drainage channel thalwegs as piercing lines by projecting these into the fault trace. Where the piercing line meets the fault trace, we mark this as a piercing point. The distance between these piercing points is the offset measurement. We undertake the same process at the bottom of the channel risers either side of the measured thalweg. The distance between the two nearest offset risers represents a minimum displacement and the distance between the two furthest offset risers represents the maximum. The method is consistent with the method developed in Kurtz et al. (2018), and likewise we make qualitative assessments of the sinuosity and clarity of the measurements. We also assess the obliquity of the drainage to the fault trace. These assessments provide a qualitative weighting to our measurement to better constrain the uncertainty of the measurement.

4.3.4 Paleoseismic Trenching

Two paleoseismic trenches (Fig. 4.6, Trench 1 and Trench 2) were excavated, cleaned, gridded, photographed, and logged. As a tool for logging, we used an orthophoto mosaic constructed using photographs captured with a Samsung Galaxy S20 Ultra and processed in Agisoft Metashape software. The orthophoto has been scaled and orientated using reference points extracted from iPad-lidar scans of the trench walls (Pierce and Koehler, 2023). Logging was performed on an iPad using Adobe Illustrator software. Units, faults, and folds were distinguished, divided, and described following paleoseismic methods described in McCaplin, 2009. We use the Emlid Reach RS2 dGPS base station and rover to measure an elevation profile along each trench. We correct the elevation data using the emg2008-5 geoid model and cubic interpolation to give the orthometric height. In addition, a sediment sample pit 2.3 m deep was

excavated into a geomorphic surface at the Salyan site (Fig. 4.6), to obtain datable sediment to establish constraints on geologic slip.

4.3.5 Quaternary dating

Samples were collected for both radiocarbon and Infra-red stimulated luminescence (IRSL) dating. Stratified charcoal nodules in a burn layer were found in very fine aeolian sands at 2.1 m deep in the sample pit and sampled for radiocarbon dating. We also sampled an intact marine bivalve shell from the lower units (U65) of Trench 1. We excavated the charcoal nodules and shells from in-situ sediments using a cleaned metal trowel and placed these into a sealed zip-lock plastic bag. We sent the samples to Beta Analytic for pre-treatment and radiocarbon dating. The charcoal nodules and marine shells were analysed at Beta Analytic laboratory in Miami, Florida, using Accelerator Mass Spectrometry (AMS) dating. Results were calibrated using OxCal v4.4 (Bronk Ramsey, 1995) with the Marine 20 calibration curve and ΔR adjustment (-128) for the Caspian Sea shown in Table 2.

For IRSL dating we collected a total of 23 sediment tubes, 17 from Trench 1, 3 from Trench 2 and a further 3 from the sample pit. Plastic sample tubes were hammered horizontally into the sediment layer and sealed from light contamination. The ends of the tubes were wrapped in aluminium foil and taped to seal. Out of the 23 samples taken we processed 10 samples from Trench 1 and 3 from Trench 2. We did not process the IRSL samples from the sample pit as we had enough charcoal for radiocarbon dating. The samples were processed at the University of Sheffield and analysed using IRSL dating techniques on single feldspar grains (Rhodes, 2015). The samples were prepared by selecting a suitable grain size using wet sieving. A dilute HCl treatment was administered to samples to remove carbonate. The samples were then dried. K-feldspar fractions were separated from the quartz, plagioclase and heavier minerals by flotation in a centrifuge using a lithium metatungstate (LTM) solution. The samples were then rinsed to remove the LTM and the remaining grains were treated to remove their outer coating or staining. IRSL measurements were made using a a standard Risø TL-DA-20D automated luminescence reader. Details of the machine calibration and light filters are available in Rhodes (2015). The IRSL dating results are provided in full in Table 1 and are detailed on the trench logs. We apply the finite mixture model to identify grouping within the equivalent dose distributions (Galbraith and Green, 1990).

4.4 Right-lateral strike-slip faulting in the Kura basin

Continued debate about the existence and kinematics of faulting through the Kura basin justify detailed analysis of high-resolution satellite imagery and digital elevation models, in order to extract subtle indications of faulting within the low-relief geomorphology. We analyse satellite DEMs, a combination of Google Earth, Bing Aerial, and ERSI satellite imagery, and observations from field mapping to identify fault related scarps, offset drainages, pop-up and pull-apart structures consistent with active strike-slip faulting (Fig. 4.4). We first discuss a series of prominent fault scarps that run between the cities Salyan and Shirvan, and apparently further north towards Shamakhi, within the Caucasus (Fig. 4.2b, fault 1a-b). This fault, which we call the Shirvan fault system, is the focus of detailed field investigation in later sections. We then describe evidence for active right-lateral faulting close to Alat (Figs 4.2b, faults 2-4), and also the potential for further zones of faulting in the Kura basin interior inferred from seismicity.

4.4.1 The Shirvan fault zone

We describe three sections where the fault is clearly visible in the geomorphology. Each of these sections is associated with larger-scale topography in the form of anticlinal folding and mud volcanic activity. We infer that the fault zone extends between the three parts described here, but without geomorphic expression within the low-lying parts of the Kura basin. Mud volcanoes are aligned along the fault trace, with concentrations near bends in the fault, which also correspond to localised anticlinal folding. We note that the alignment in mud volcano activity extends south of the observable end of the fault zone, providing further evidence that the fault is longer than visible in the geomorphology. The fault zone also follows an ~150 km-long NNW-SSE alignment in seismicity, with depths of 40 km, which extends from Shamakhi through Shirvan and Salyan, and ~100 km offshore into the Caspian Sea.

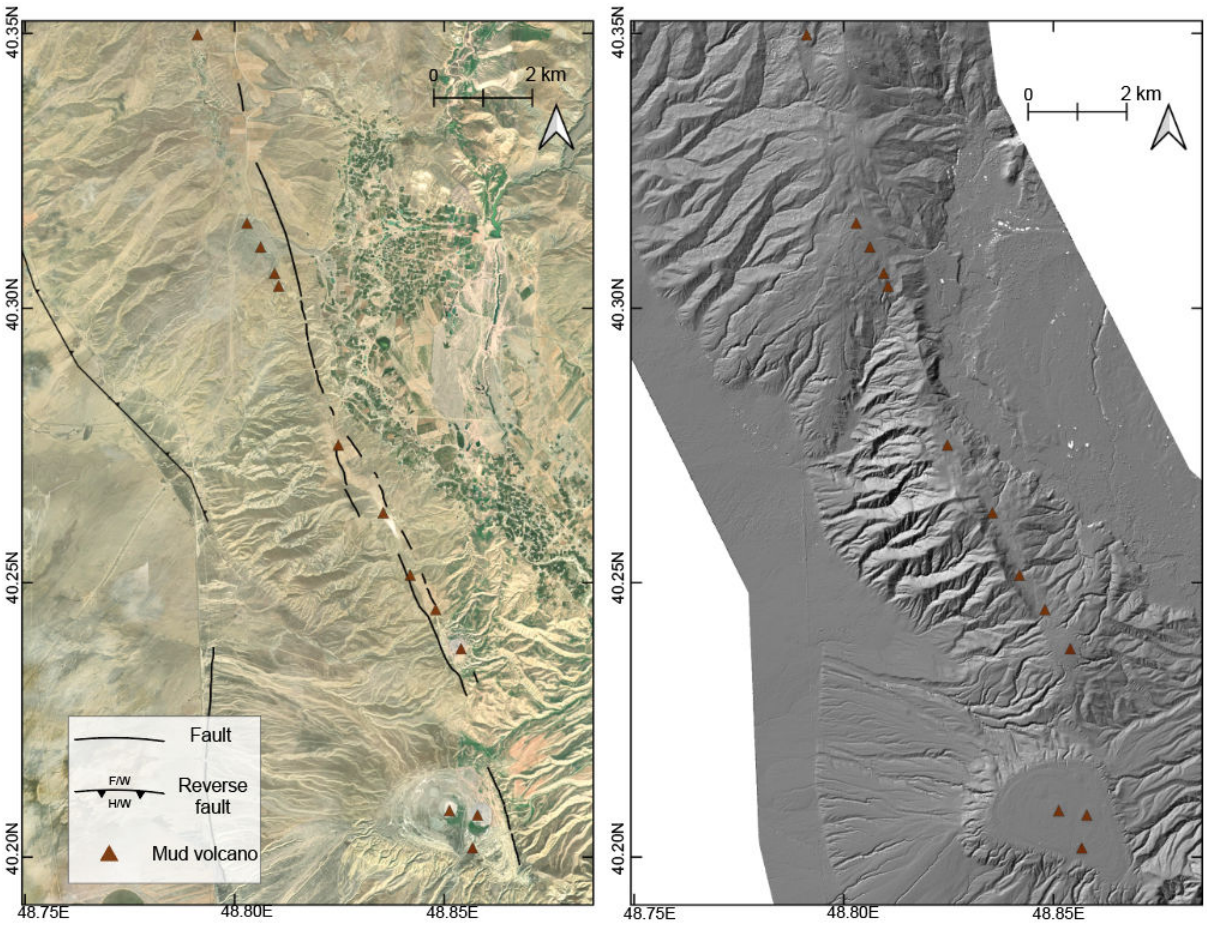


Figure 4.4: NNW-SSE striking strike-slip faulting between Shirvan and Shamakhi (Fig. 4.2). A - shows reverse and strike-slip faulting on Bing Aerial imagery. Mud volcanoes form in a lineation along fault strike. B – Pleiades stereo DEM showing a linear break in slope that crosscuts topography. The faulting forms a sharp linear scarp through the mud volcano at the SSE of the panel.

In Figs 4.3 & 4.4 we show east-facing scarps running along the apex of a line of anticlinal hills and mud volcanoes south of Shamakhi. Mud volcanoes are marked by brown triangles. No lateral displacements were identified across this section of the fault, though we infer that a major component of the slip is right-lateral, based upon observations further south near Shirvan.

Linear scarps cutting across an anticline adjacent to Shirvan are shown in Fig. 4.5. We find several right-laterally offset drainages (Fig. 4.5). There are too few identifiable offsets in our dataset to give a robust statistical analysis (e.g. Cumulative Offset Probability Distribution analysis).

We observe stepovers along the fault trace that are both left and right stepping (Fig. 4.5 b and c). At the left step we see an increase in elevation bound on each side by a rupture strand (Fig.

4.5b). An increase in elevation at a left step on an active strike-slip fault is indicative of right-lateral motion. We also see a right step in the surface rupture trace and observe that there is a drop in elevation in this zone (Fig. 4.5c), consistent with transtension and right-lateral faulting.

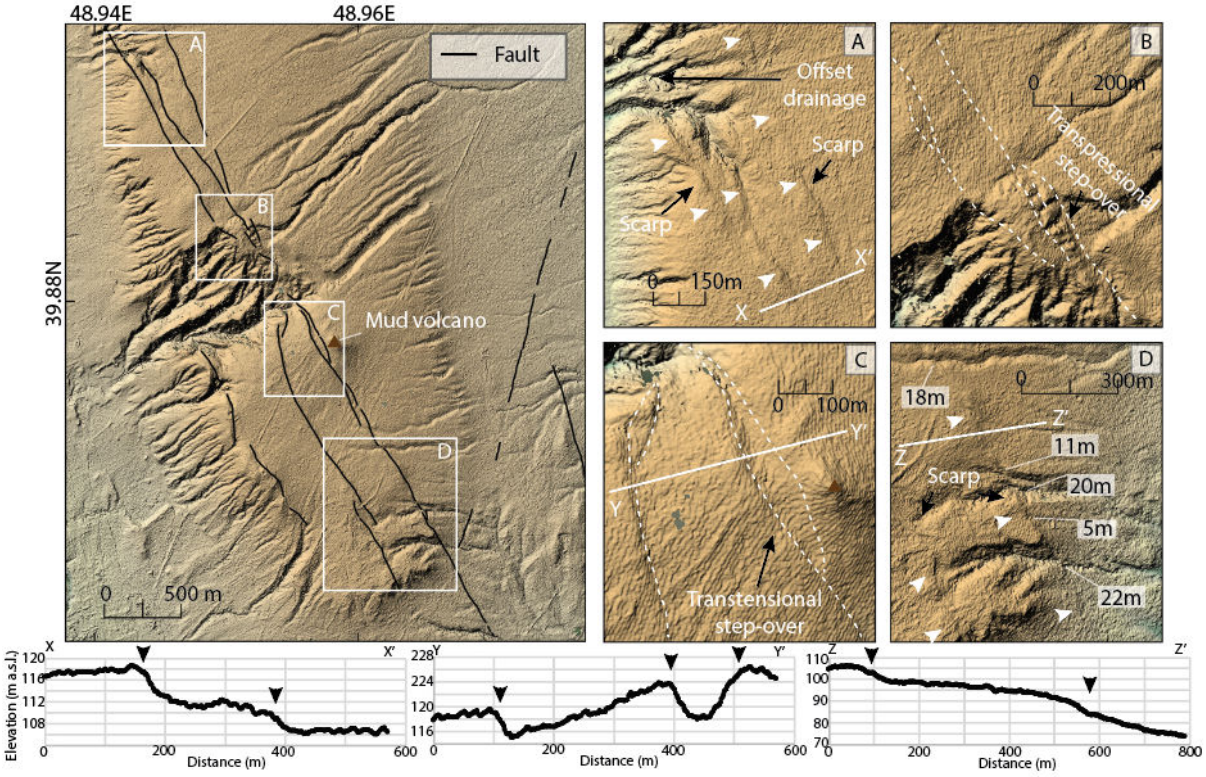


Figure 4.5: Rupture map from Shirvan. Panel D shows the rupture trace in three strands that have created scarps in the topography. The topographic profile XX' shows the scarps. There is also an offset drainage along strike of the rupture trace at the NW of the panel. Pleiades satellite derived DEM at 1 m resolution. Panel B shows the rupture trace and a transpresional step-over (pop-up) structure. Panel C – rupture trace showing scarps and trantensional pull-apart basin where there is a step-over in the rupture trace. This is seen in the topographic profile YY'. Panel D – two rupture traces, scarp and offset drainage channels with measurements between 5m and 22m. Scarps can be seen in the topographic profile ZZ'.

Near Salyan we identify a linear fault trace bounding the western side of a flat-topped region of raised topography, in which steeply dipping rocks outcrop, and which we interpret as an anticline that has been eroded during a sea-level highstand. Shelly marine terrace deposits are preserved on the surface in places.

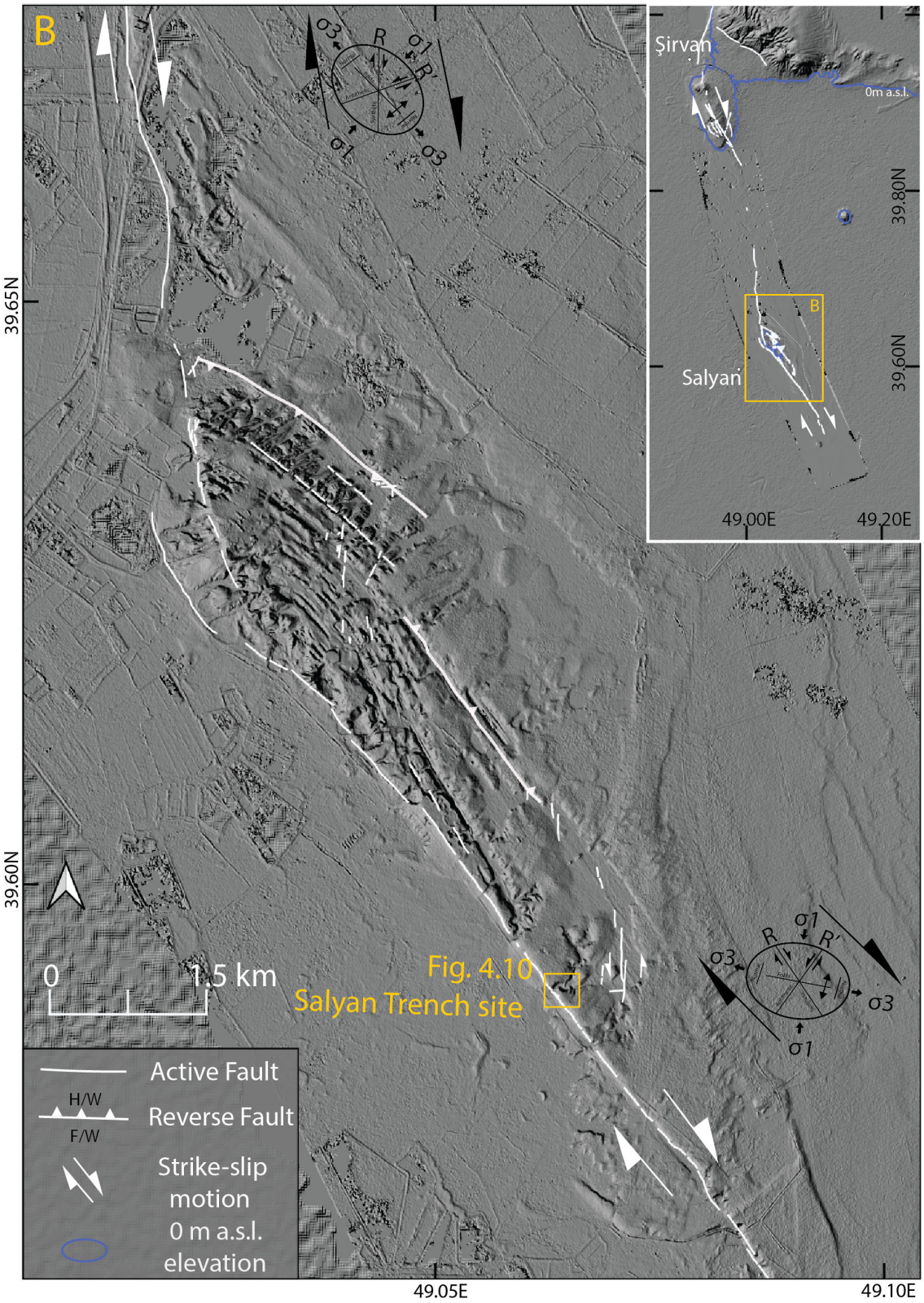


Figure 4.6. Pleiades derived DEM of the Salyan region of the Shirvan fault zone. White lines delineate active faulting from our field and remote mapping. We see the fault bend from a N-S to NW-SE trend. We see antithetic R' sinistral faulting (Fig. 4.7). Trench site is shown in the yellow box on panel B. Blue lines on inset panel show 0 m a.s.l.

The fault trace along the western side of the fold bends from almost N-S in the north of Fig. 4.6, to NW-SE in the south, with the fold axis parallel to the NW-SE trending section. Small antithetic left-lateral faults displace vertically-dipping beds within the anticline (Fig. 4.6).

We visited a section of the fault in the field, where the main fault trace runs along an ~8 m-high scarp with the marine terrace at the top. At this site we undertook a UAV survey, excavated paleoseismic trenches through the fault zone and opened a soil pit in an adjacent terrace surface. There are several other offset drainages to the southeast along the main fault trace with a range of dextral offsets although most are within the 7-10 m range.

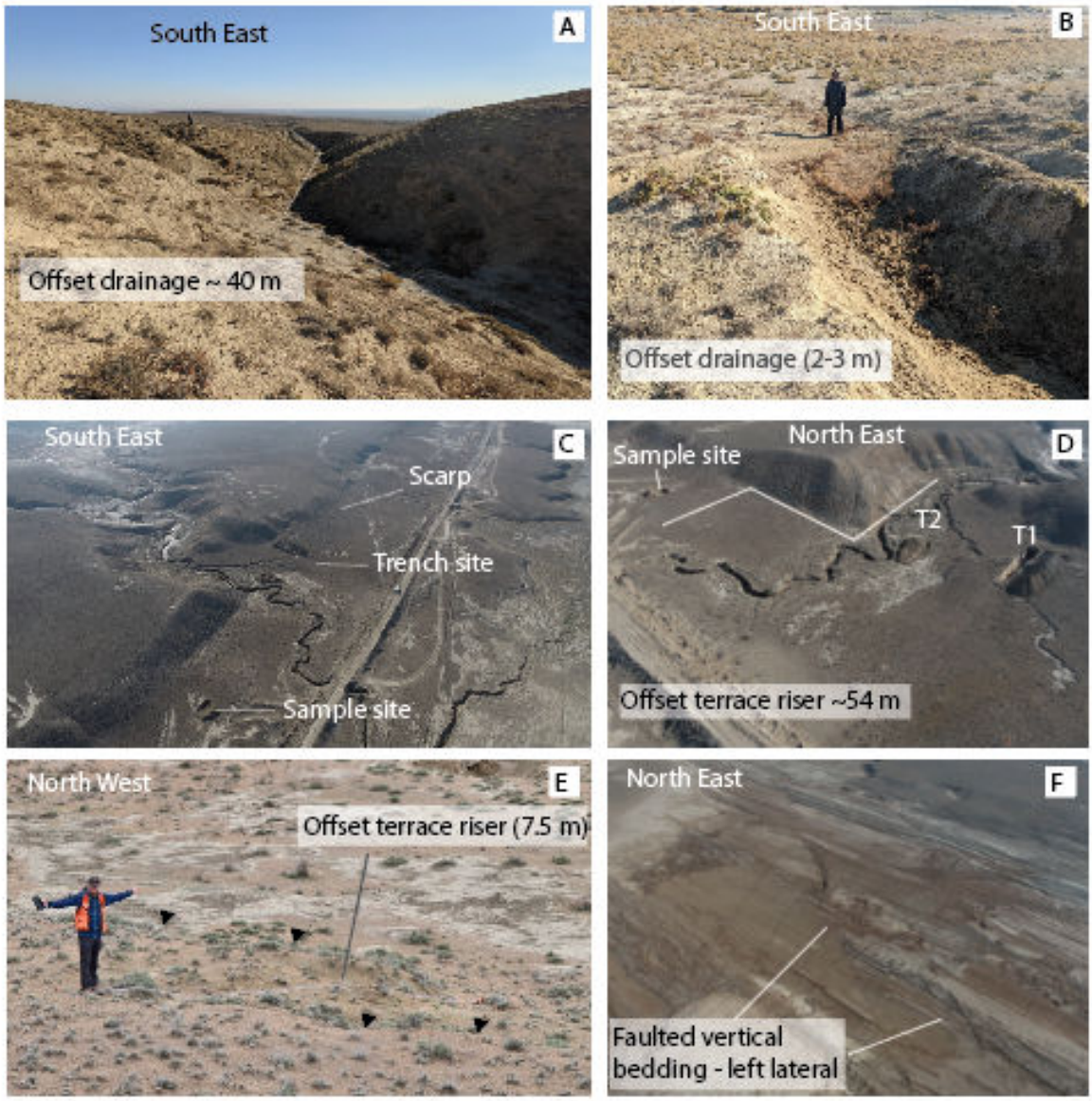


Figure 4.7. Field photographs of the Shirvan fault zone. A and B show two offsets at the Shirvan site in Fig. 4.5 (d). Panels C and D are oblique drone images of the trench site at Salyan (Fig. 4.6). E shows the 7.5 m offset riser. F shows an oblique drone image of antithetic left-lateral faulted vertical bedding planes.

4.4.2. The Alat fault system

To the west and northwest of Alat there are observable scarps with right-laterally offset drainage channels, trending NW-SE to NNW-SSE along the western margins of a range of anticlinal folds and mud volcanoes (Figs 4.8 & 4.9). The right-lateral displacements are particularly clear in the region shown in Fig. 4.9, where a sharp linear fault trace tracks across the slopes of a large mud volcano. A series of small channels and their interfluves are consistently displaced by ~10 m.

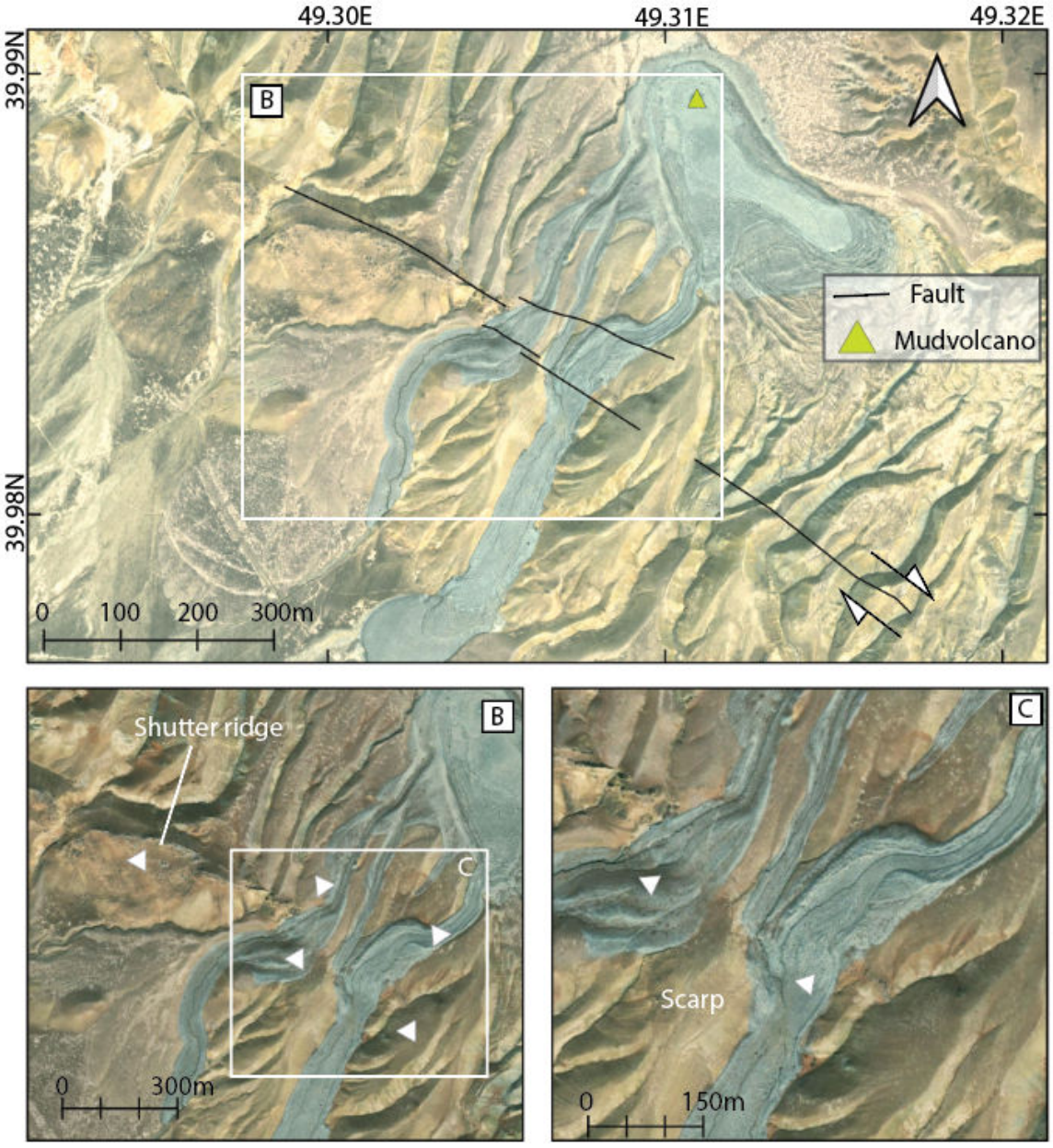


Figure 4.8. Fault trace near Alat (Fig. 4.3) shown on ERSI imagery. Shutter ridges, deflected drainage channels and scarps can be seen on panels B and C. We see a mud volcano near to the fault trace. Motion determined by offset drainages is consistent with dextral strike-slip faulting.

Further south, right-lateral offsets are again visible where the fault scarp cuts across the slopes of a mud volcano (Fig. 4.8). In this example the lateral offsets are less well defined, though larger, than in Fig. 4.9). Incised channels and their interfluves show displacements of several tens of metres.

The Alat fault system as mapped from the geomorphology coincides with an alignment in mud volcano activity, which extends offshore and splits into three separate trends, numbered 2, 3, and 4 in Fig. 4.2. There is also a close alignment between the mapped fault and an alignment in shallow seismicity, with depths to ~20 km (Fig. 4.2), and which appears to merge with the Shirvan fault zone seismicity near Shamakhi (Fig. 4.2).

4.4.3. Faulting inferred from mud volcanism and seismicity

We have described how the Shirvan and Alat fault systems (alignments 1-4 on Fig. 4.2), which are both visible in the geomorphology, align both with concentrations of mud volcanoes, and relocated seismicity in the Kura Basin between 2011-16 by Gunnels et al. (2020). We use these alignments to infer that the Shirvan and Alat faults are longer than mapped at the surface and extend offshore into the Caspian Sea.

Another alignment of seismicity with a NNW-SSE trend is observed parallel to those we have already described, but sited further west in the interior of the Kura basin (Fig. 4.2, alignment 5). Gunnels et al., (2020) and the ISC/GEM seismic catalogue also show strike-slip focal mechanisms along this trend, which are compatible with left-lateral faulting on their N-S nodal planes. The seismicity is mostly deep along this trend (>20 km). We see no surface expression of faulting, as might be expected due to the low relief and rapid sedimentation, nor not do we see evidence in the satellite imagery for mud-volcanism at the surface.

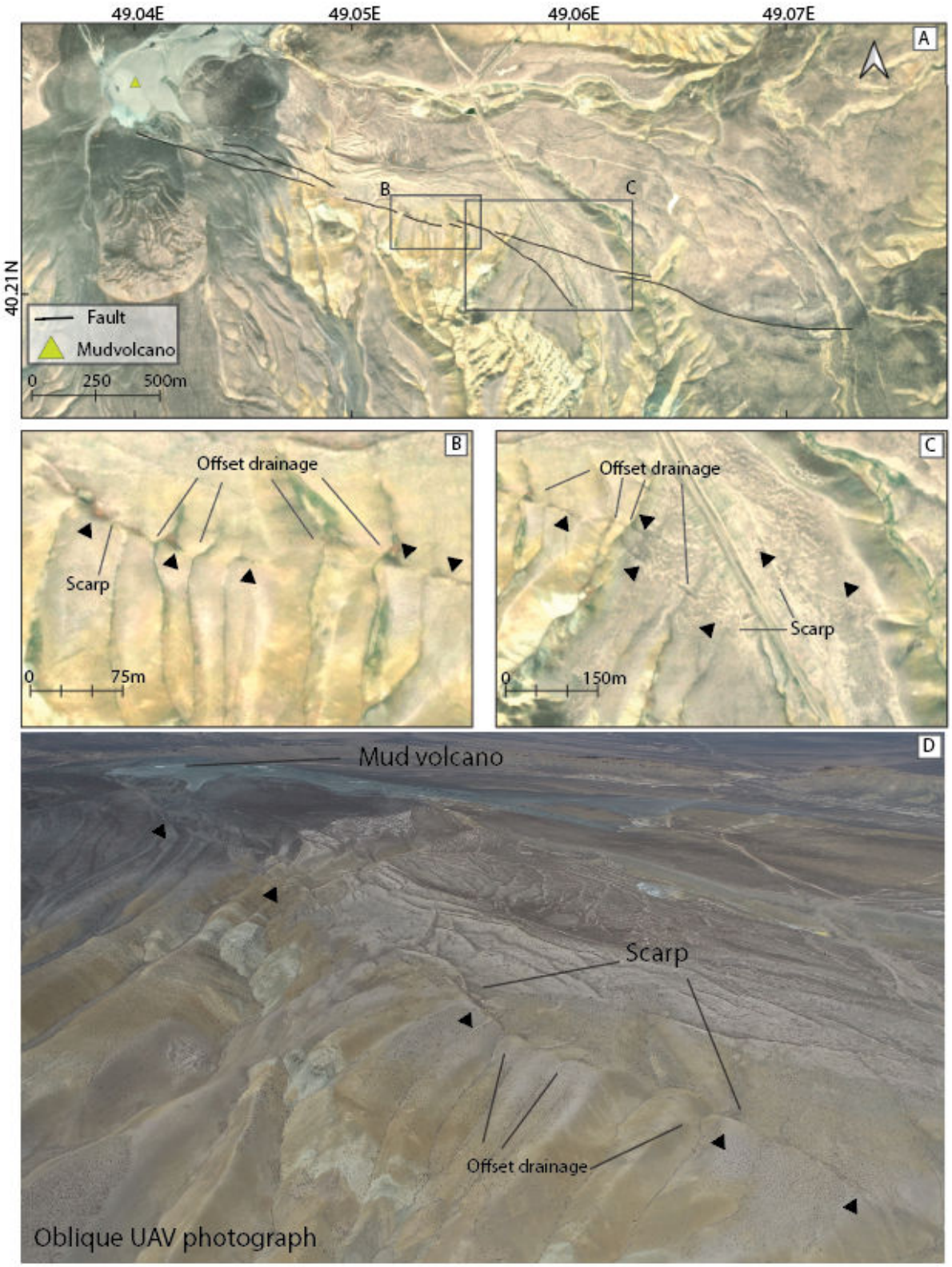


Figure 4.9. Northwest of Alat (Fig. 4.3) ERSI imagery showing fault scarps, offset drainages and a mud volcano at the NW end of the panel. Panel B shows a fault scarp with offset drainage channels. Panel C shows two parallel fault scarps and offset drainage channels. The offset drainage channels indicate a dextral motion of the fault. Panel D shows an oblique drone image of faulting. It shows offset drainages, scarps and mud volcanoes.

4.5 Paleoseismology of the Shirvan fault

We provide a detailed description of the site along the Shirvan fault that was selected for paleoseismic trenching and slip-rate determination. We first detail the geomorphology of the site, then we describe the trench stratigraphy's and quaternary dating results. Finally, we discuss the likely paleoseismic record and long-term slip-rate derived from our measurements.

4.5.1 Geomorphology

In the Salyan trenches we interpret fluvial, alluvial, aeolian, and marine deposits suggesting a complex geomorphic history (Fig. 4.10). Qt1 is the youngest fluvial terrace bound by the active channel and an older terrace riser. We observe flat laminae and small-scale undulating ripple marks on its surface. The grain size ranges from silt to medium sand containing some pebbles. The vegetation in mainly scrub bushes forming in mounds up to 0.5m wide, and we observe a change in the concentration of vegetation at a small scarp in the terrace. The top 1m of stratigraphy is exposed in Trench 2 (*see below*) and consists of fluvial sediments.

Qt2 is separated from Qt1 by a terrace riser and consists of brown silty soil with grass and small scrub bushes. The surface has a slight slope towards the active channel, and it has a smooth surface with little incision.

Qt3 sits at a higher elevation to Qt2 and is separated from Qt1 by a terrace riser. The surface consists of a brown silty soil with sparse grass and scrub bush vegetation and has a slight incline of 10º towards the north-west. To the south-east the surface is bound by a large terrace riser and a scarp to the south-west. We observe the Qt3 deposits at the top of the eastern end of Trench 1 (*see below*) and consists of laminated fluvial deposits and channel structures.

Qt4 is a flat 10x10m terrace deposit at a higher elevation to Qt1/2/3. It is bound to the south-east by a riser. There is sparse vegetation of grass and small scrub bushes and is composed of light brown silty soils that appear light grey at the surface.

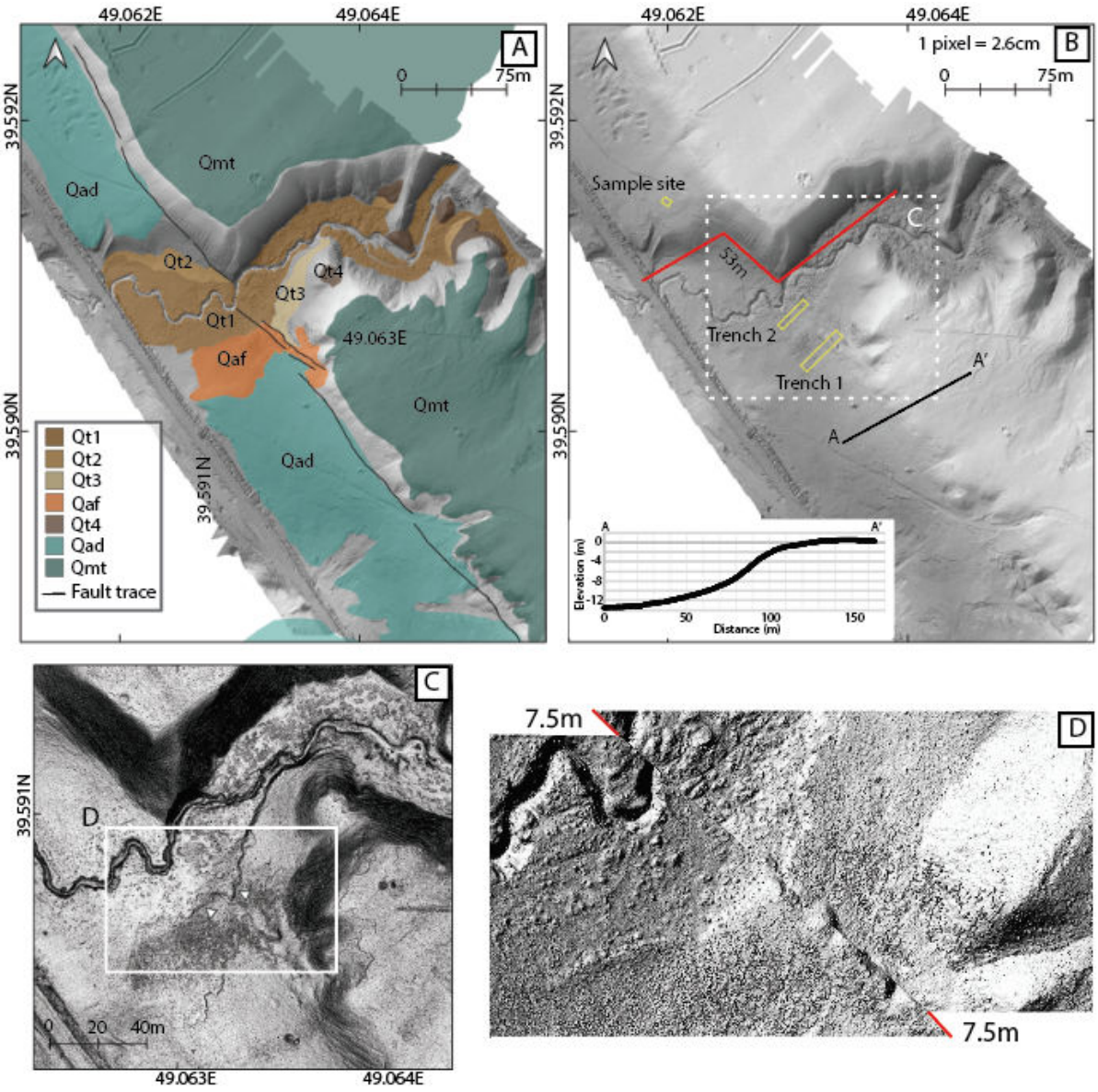


Figure 4.10. UAV derived DEM of the trench site near Salyan on the Shirvan fault zone. Panel 1 shows a geomorphic map and the fault trace. Panel 2 is a hillshade of the UAV DEM showing the sample site, Trench 1 and Trench 2. We see a dextral riser offset of 53 m. Profile AA' shows the marine terrace at an elevation of 0 m a.s.l. Panel C shows a slope map of from the UAV DEM data, showing the offset Qt1 riser and Qt1 tread. The matched riser profiles are restored using LaDiCoaz method, the result is shown in panel D showing a 7.5 m offset.

Qad is an undulating sparsely vegetated surface consisting of light brown to straw yellow silty sediments. Abundant marine shells are observed on its surface. From the elevation data we observe that this deposit ramps against a large riser to the east and the surface has a slight incline. A sample pit was excavated into this surface at the north-west of the study area (Fig. 4.10), we observe silts to very fine sands, with layers of pebbles and intact marine shells. We

also found a layer rich in charcoal nodules, which is beneath the layers containing marine fauna. We sampled and dated these charcoals from a depth of 1.4 m, yielding an age of 1744 - 2145 yrs cal BP. We also sampled and dated one of the marine shells on the terrace surface, yielding an age of 35280 ± 240 BP. Together, these age data suggest the terrace surface is reworked, and covered by material derived from elsewhere.

At the highest elevation in our study area (0 m a.s.l.) is a flat terrace we map as Qmt. There are several pits and small trenches previously excavated into this surface up to 30 cm deep and we observe silty brown soils containing broken marine shells in the surface. The overall morphology shows no incision and a flat smooth surface. We interpret this surface as a marine terrace. We did not sample in-situ shells from the Qmt surface to confirm its age. The surface elevation of 0 m a.s.l. is consistent with formation during the 11-13.5 ka transgression, however Qmt is a potential source of marine shells dated to ~35 ka on the lower surface (Qad) adjacent to it. Irrespective, Qmt is the oldest geomorphic surface in the Salyan study area. Also, as the most recent Caspian transgression at 11-13.5 ka would have inundated the study site, we assume that the geomorphology would have been reset at that time, with all terrace formation and incision (Qt1-4) being younger than the highstand.
Qaf sits above the Qt1 surface adjacent to the Qad surface. There is no riser between Qaf and Qad. A riser exists between Qt1 and Qaf suggesting that the former was incised into the latter. The Qaf surface slopes to the WNW and we observe that it traces back to the foot of the Qmt riser where there is a small incision. The majority of the Qaf surface is offset from this incision to the NW along the fault scarp. We observe the stratigraphy of Qaf in Trench 1, which consists of a fluvial base U30 and an alluvial silt deposit U80 (Fig. 4.11).

4.5.2 Trench 1

Trench 1 (Fig. 4.10) is 18 m long and 3 m deep from the top of scarp to the bottom of the excavation. Orthophoto mosaic and log of the northern wall is shown in Fig. 4.11. The trench exposes a sequence of sedimentary deposits that are cut by two distinct zones of vertical fractures either side of a 0.5 m topographic bulge. Either side of these fracture zones we observe sharp contacts and changes in the sedimentary deposits (Fig. 4.11).

Stratigraphy

There are four sedimentary facies in trench 1 (Fig. 4.11). At the base of the trench, we record the oldest facies (Facies 1) that consists of two units; chocolate clays (U10) and blue bedded sands (U20). Facies 2 (U50, U60 and U65) is found between the two fracture zones and sits above Facies 1. Facies 2 contains intact shells, coarse to fine sands (Fig. 4.11). U50 is a fine to medium tabular cross-bedded deposit that is capped by a ripple laminated sand unit (U60). We observe salt layers within units U60 and U65. We observe salts leaching from the trench wall in units U60 and U65. From the sedimentary structures and presence of shelly material we interpret the sands as a near shore or beach deposit.

Facies 3 consists of units U30, U40, U45, U70, U80, and U130. Grain size ranges from fine sands to silts. U30 is a bedded fine sand and silt deposit terminating at an angular unconformity with U60. The unit has a clear bedding between fine sand and silt layers and has an undulating contact with the blue sand (U20) unit at its base, we also observe channel structure within this unit cutting into U20. Above U30 there is a finer grained bedded silt unit (U40), this layer is truncated at a fracture zone. This unit is capped by a bedded block silt layer (U45) that also truncates at the fracture zone. Above U45 there is a blocky silty soil (U130) that almost tops the entire trench. Between the two fracture zones there is medium to fine sand unit (U70) sitting above the shelly sand unit (U65). The contact between these two units (U70 and U65) is sharp with an angular unconformity in the bedding planes at the eastern facture zone. Above U70 there is a distinct unit (U80) that has interstitial beds of fine sands and laminated silts. We interpret Facies 3 as fluvial/alluvial in origin, with sediment washing down from the marine terrace (Qmt) above.

Facies 4 consists of entirely of silts with differing sedimentary structures. At the base of the trench at the western end there is a thick unit of massive silts with no discernible bedding or lamination (U85). Above this unit there is a bedded massive silt unit (U90) with a variable thickness at the western facture zone. U100 sits above U90 and is a laminated silt layer with a varying thickness across the trench. U110 sits above U100 and is a thin deposit of massive silts with no lamination or apparent bedding. Above U110 there is a blocky silt deposit, U120, that shows some lamination. We interpret Facies 4 as a package of wind-blown dust deposited against a scarp.

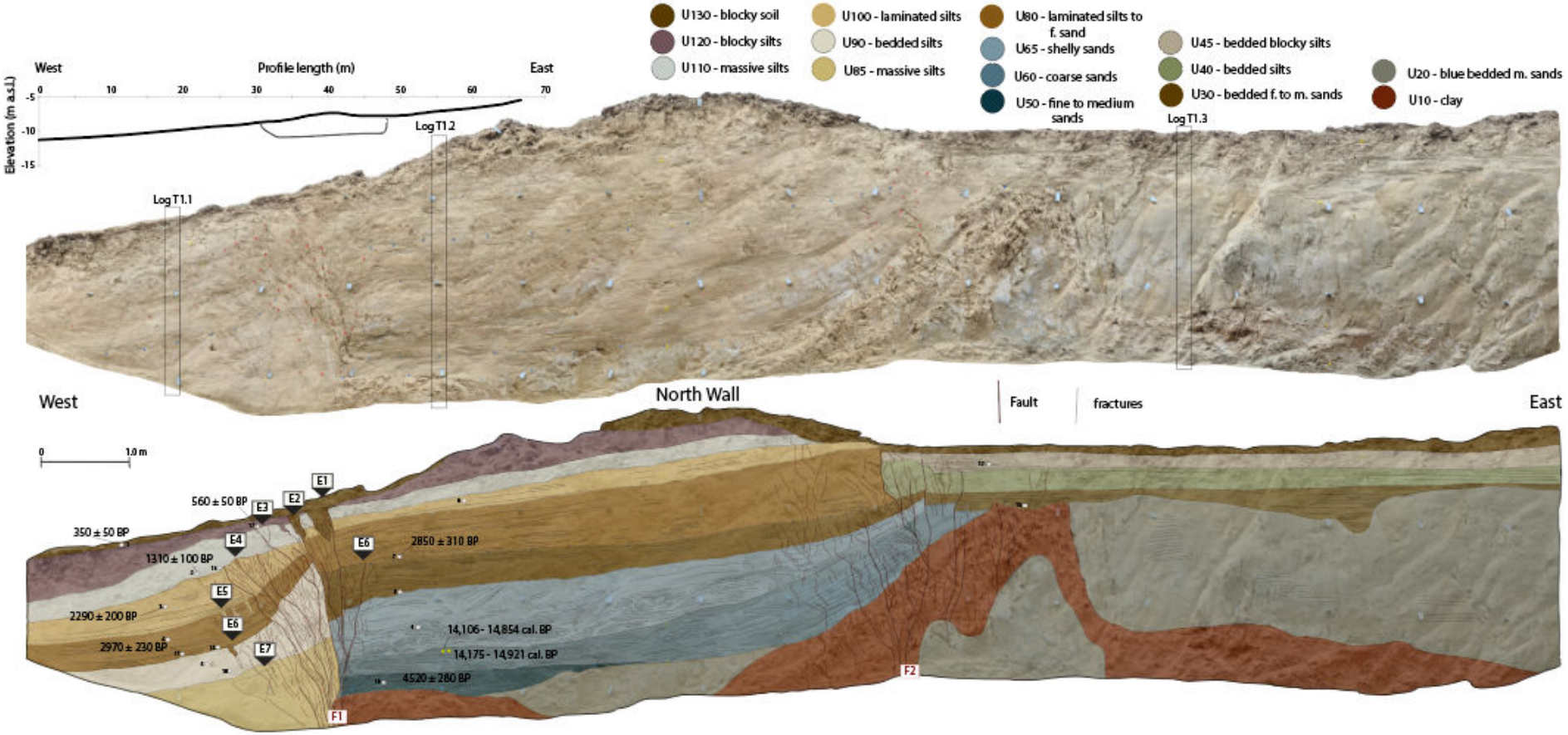


Figure 4.11. Trench 1 – photo-orthomosaic and trench log of the NNW wall of Trench 1 (Fig. 4.10). The trench has two fault zones (F1 and F2) and seven possible events (E1-7).

Faulting

The sediment deposits are truncated at two distinct vertical boundaries. The first boundary occurs at 4 to 5 m from the western end of the trench, the second boundary occurs at 11-12 m from the western end. Between the two vertical discontinuities, the surface topography is raised forming a 6 m long 0.5 m high scarp. The two vertical discontinuities show sealed and unsealed fractures fanning out laterally from the base of the trench to the top with a flower morphology. We observe vertical offsets and bedding thickness changes in the sedimentary layers (U80, U100, and U110) across these fractures at the western end of the trench. At the eastern end, the fracture zone truncates the sediment on each side. The lower units (U60 and U65) have variable dip from almost horizontal at the western end to 30°W towards the east and sit unconformably on top of the clay (U10) and blue sand (U20) units. At the eastern fracture zone, we observe angular unconformities between the coarse sand unit (U60) and the bedded silts and sands unit (U30/U40). There is also an angular unconformity between the marine sediments (U60/65) and the overlying laminated silts and sands (U70). We note that on the south wall of the trench, we see that the clay (U10) and blue sand (U20) units are folded and the eastern fracture zone cuts through this fold.

Given the vertical truncation of sediments, across fracture bed thickness changes, vertical offsets in sediment layers, and the flower structure we conclude that the two fracture zones are formed due to strike-slip faulting. We interpret that the clay (U10), blue sand (U20), and the shelly sands of Facies 2 (U50, U60, and U65) are folded. The sedimentary structures within facies 2 do not show evidence of onlap and do not appear to be high angle slope deposits so were most like deposited horizontally or on a slight incline.

A topographic profile parallel to the trench shows a bulge, bounded at either side by the two zones of deformation seen in the trench. The topography may indicate a pop-up structure or pressure ridge bounded by two superficial fault traces. The two fault zones displace sedimentary layers in an opposite sense to the bulging in the topography, suggesting a localised evolution in the fault zone structure. The orientation of this pressure ridge is consistent with right-lateral faulting.

4.5.3 Trench 2

We excavated an 11m long and 1.5m deep trench into the T1 geomorphic surface (Fig. 4.10). Orthophoto mosaic and trench log of the northern trench wall are shown in Fig. 4.12. At 6-7 m along the excavation there is a slight scarp in the surface shown in our dGPS profile along the trench.

Stratigraphy

In trench 2 (Fig. 4.12) there is one sedimentary facies of fluvial sediments consisting of seven units. The units fine upwards and all show sedimentary structures ranging from channel cross stratification to lamination in the upper units. Unit 1 (U1) consists of medium to coarse sands containing pebble layers, above this sits a coarse sand layer (U2) and then a medium layered sand deposit containing salts (U3). This is then topped by a relatively thick medium sand layer (U4). On the downthrown side of the fault U4 is capped by a laminated fine sand layer (U5), we cannot trace this layer on the eastern side of the fault. The length of the trench is then capped by laminated silts (U6) and a blocky soil (U7).

Faulting

We observe two zones of vertical fractures offsetting and truncating sedimentary units. The first zone is between trench wall markers 3 and 4 at the western end of the trench the fractures do not extend to the surface. The second zone is between trench wall markers 6 and 7 and is more complex. The fractures extend to the surface. Both fracture zones are vertically corrugated and have splays terminating in the lower units. We interpret these two fracture zones as faults. Both faults rupture layers U1 to U5 and with the easternmost fault also rupturing to the current ground surface in terrace T1 which is evidence of the most recent earthquake (MRE). Units U4 and U6 cap fault ruptures suggesting two earlier earthquakes. Overall, we interpret three events from the two fault zones (Fig. 4.13).

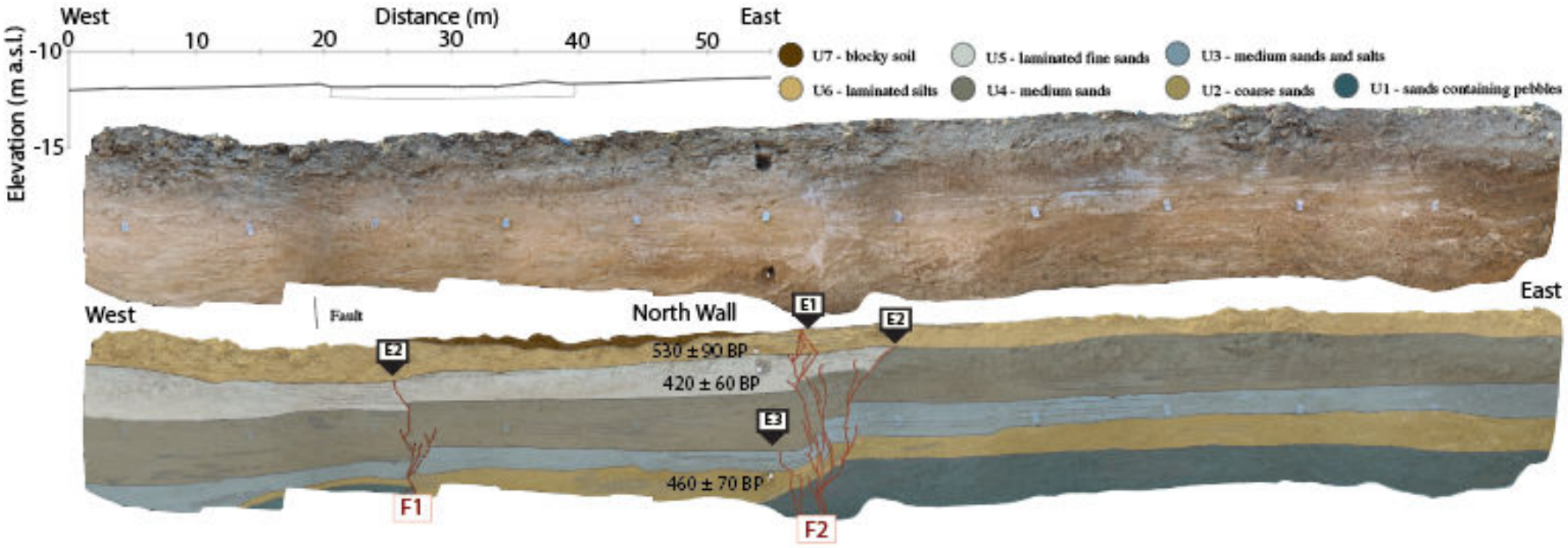


Figure 4.12. Trench 2 – photo-orthomosaic of the NNW wall of Trench 2. Trench log shows fluvial sediments in the Qt1 surface (Fig. 4.10). There are two fault zones (F1 and F2) and up to three events (E1-3).

4.5.4. Age control

Our age control comes predominantly from infra-red stimulated luminescence dating, due to the absence of suitable organic remains for radiocarbon dating in most of the stratigraphic layers. The detailed results of the 13 IRSL samples we processed and analysed are shown in Table 1. The results from Trench 1 show a good stratigraphic order increasing in age with depth (Fig. 4.11). At the western side of fault (F1) sediment age increases by ~1000 years per 0.5 m of depth. Across F1 we see good agreement in age between the base of U80, supporting our interpretation that these layers are part of the same deposit.

Near the bottom of Trench 1 we sampled a fine to medium tabular cross-bedded shallow deposit of facies 2 (U50) yielding an age of 4520 ± 280 BP years. Above this sample two intact marine shells were extracted from U65 and dated using radiocarbon (Table 4.2), yielding an ages of 14175 – 14921 and 14106 – 14854 cal. BP at an elevation of -13.8 m (a.s.l.) (Fig. 4.14). The sedimentary structures within facies 1 are consistent with a shallow marine or shoreface environment, and the elevation is consistent with the high stand at 11,000-13,500 years ago, but the IRSL age suggests instead that the deposit is younger (4520 ± 280 BP years) and postdates all major Caspian transgressions. In the following sections we assume that the IRSL ages are correct, and that the facies 2 units represent reworked marine debris. We also consider the alternative interpretation of IRSL results underestimating deposition ages, favouring our interpretation of a shallow marine or beach setting for the facies 2 units.

We correlate sediments at the Salyan trench site based on age control (Fig. 4.14). We find that the fluvial sediments in trench 2 were deposited during the same period as unit U120 in trench 1 (blue dotted line Fig. 4.14). The difference in thickness is as a result of different sedimentary environments (fluvial and soil/slope deposit). We also correlate between the layers in the sample pit and the deposits in trench 1 based on the age of dated charcoal and IRSL samples (red line Fig. 4.14). The sediment logs with elevation in m a.s.l. show the correlations within trench 1 and 2 (Fig. 4.14). In trench 1 we can constrain units U40 and U45 between 2850 ± 310 BP and 350 ± 50 BP, which constrains the Qt3 terrace to this range (Fig. 4.10). Therefore, the 7.5 m offset in the Qt3 terrace riser must have occurred during this period.

4.6 Paleo-earthquakes and slip-rate of the Shirvan fault zone

4.6.1. Paleo-earthquake history

We have evidence of four to seven events in Trench 1 and one to three events in Trench 2 (Fig. 4.13). We now bracket the ages of these events based upon our IRSL age results. Although the IRSL ages are in stratigraphic order, they are younger than two radiocarbon ages extracted from marine shells in deeper parts of the trench. It is possible, therefore, that the age brackets given below underestimate the true ages.

Event 1: The most recent surface rupturing earthquake is constrained in Trench 1 within 350 ± 50 yrs BP (Figs. 4.11 & 4.13). The morphology of the active channel thalweg and terrace risers does not show a clear across fault offset related to this most recent event, and the slip magnitude at the site is therefore unknown. Further to the south at Salyan we see two offset drainage channels that are smaller than 3 m which are possibly associated to the most recent event (Fig. 4.16).

Event 2: The penultimate earthquake is marked by filled fissures in Trench 1 (Figs 4.11 & 4.13) and capped fault terminations in Trench 2 (Figs 4.12 & 4.13). The fissure fill material in Trench 1 is the same blocky soil unit (U130) and has been dated at 350 ± 50 years BP. The U120 blocky silt layer sitting beneath (U130) is dated at 560 ± 50 years BP. This constrains the age of event 2 sometime between 610 – 300 years BP. The capped fault rupture termination in Trench 2 is bracketed by two dated sedimentary layers between 440-480 years BP (Figs 4.11 & 4.12). As the IRSL ages in Trench 2 are inverted in the stratigraphy (i.e. older above younger ages) we have a good constraint on the E2 (Fig. 4.11) event horizon. We therefore conclude that the penultimate most likely occurred between 440-460 years BP, bracketed by the ages in Trench 1 of 350 ± 50 and 560 ± 50 years BP.

Event 3: We observe evidence for the third most recent event in both Trench 1 and 2. In Trench 1, IRSL dating provides age constraint on the layer (U120) capping fault rupture terminations and a small fissure at 560 ± 50 years BP (Figs 4.11 & 4.13). Trench 2 shows faults terminating and capped bedding in layer U4 (Figs 4.12 & 4.13). Age constraints from Trench 2 suggest that

this event occurred between 420 ± 60 and 460 ± 70 years BP. The vertical offsets at fault F1 in unit U3 is greater than U5, which also supports the hypothesis of an additional event.

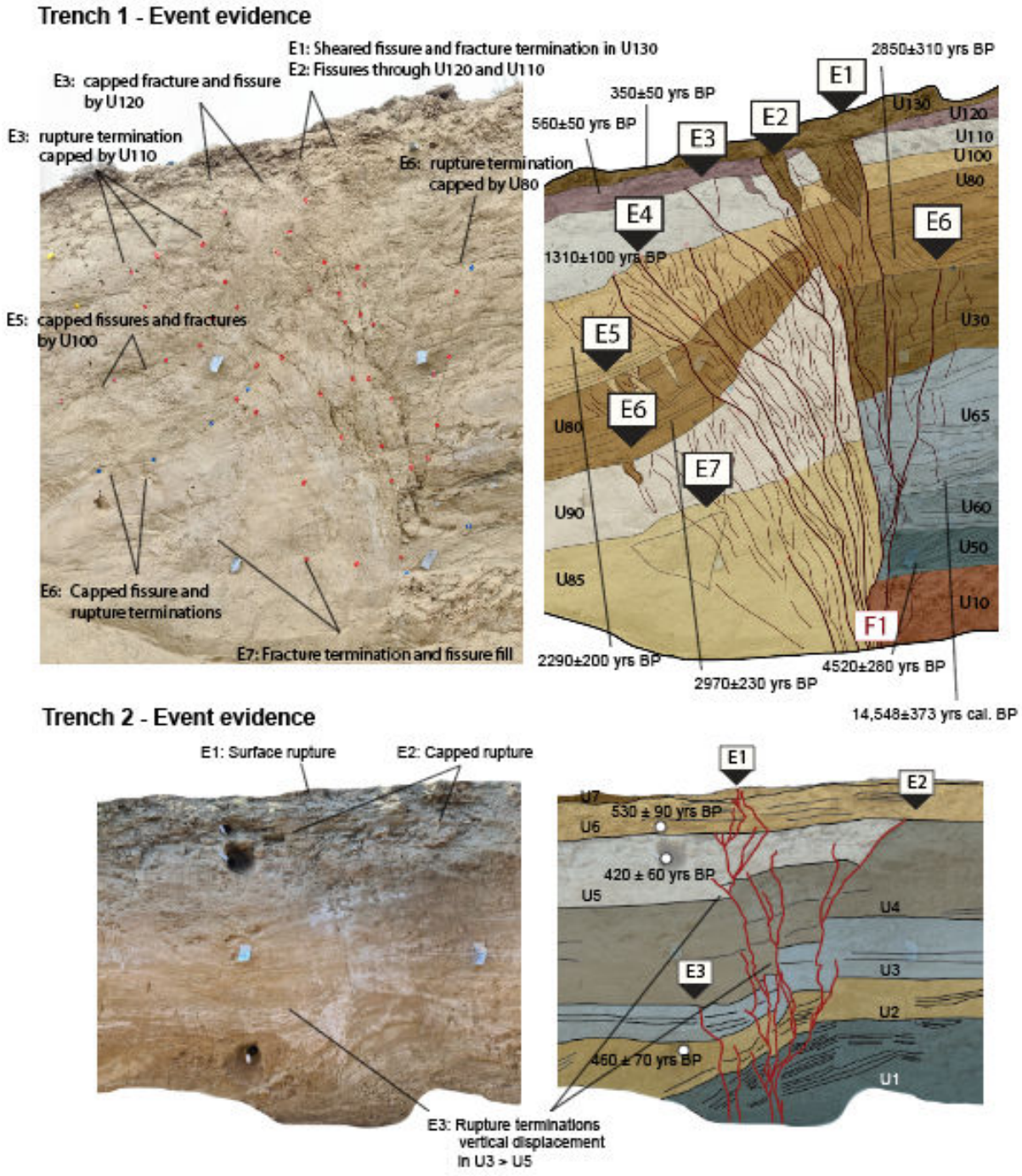


Figure 4.13. Event evidence from trenches 1 and 2. Units and event labels are consistent with the trench logs in Figs 4.11 & 4.12. Trench 1 has evidence for at least 4 and up to 7 events. Ages are from IRSL and radiocarbon dating techniques (Tables 4.1 & 4.2).

Event 4: We observe a fourth event on F1 in Trench 1. The massive silt layer (U110) caps fault rupture terminations and a cluster of fractures (Figs 4.11 & 4.13). The capping layer is dated at 1310 ± 100 years BP, with the layer beneath (U100) is dated at 2290 ± 200 years BP. Therefore, we have constraint on the timing of event 4 at between 1310 ± 100 and 2290 ± 200 years BP. From the termination of the fault rupture in the stratigraphy the event timing is closer to 1310 ± 100 years BP.

Event 5: The fifth event in Trench 1 occurs at the boundary between the two silt units U100 and U80. There is a cluster of sealed fractures in U80 capped by bedded silt layers in U100, we also observe a series of small fissures at the boundary. We cannot see a terminated fault trace at this boundary. The middle of U100 is dated at 2290 ±200 years BP and the base of U80 has an age of 2970 ± 230 years BP (Figs 4.11 & 4.13). Assuming the rate of sedimentation remains the same we expect that this event occurred somewhere in the middle of these two dates. We cannot constrain the timing of this event further.

Event 6: The base of U80 is the capping layer of another set of clustered fractures and a small fissure in a bedded silt layer U75. The sample at the base of U80 gives an age of 2970 ± 230 years BP at the western side of F1. On the eastern side of F1 we observe a fault strand terminating at the top of U70 and is also capped at the base of U80. IRSL dating of a sediment sampled at the base of U80 gives an age of 2850 ± 310 years BP. The dating shows good agreement either side of the fault (Figs11 & 4.13). Based on the position of the samples relative to the fault and fractures suggests a probable age between 2740-3160 years BP of event 6.

Event 7: At the base of the western side of fault F1 we observe a capped fissure and sealed fractures. We do not have age constraint of this event evidence other than it occurred sometime before 2970 ± 230 years BP. Therefore, we do not consider this event in our earthquake recurrence estimates.

When combining the event horizons from both trenches we evaluate that there is firm evidence to support at least four events in last 3000 years BP with a possible the possibility of three

others. Events 2, 3, 4 and 6 provide the most compelling evidence with larger uncertainty on events 1, 5 and 7.
The evidence for event 1 is a surface rupture in Trench 2 and sheared fissures in Trench 1. The sheared fabrics are subtle, and we cannot rule out that surface rupture cracks are attributed to other further afield earthquakes. Event 5 in Trench 1 is based on a series of small fissures and sealed fractures. We cannot see a terminated fault strand associated with these fractures and fissures which provides an uncertainty of the origin. The evidence for event 7 is based entirely of our interpretation of a capped fissure filled with material of the same unit, we cannot rule out that this pattern in the sediments could be caused by other processes such as soft sediment deformation.

There are therefore between four and six earthquakes in the last 3000 years BP giving a recurrence of surface rupturing event every 500-750 years on average. We exclude event 7 from the estimate as we are unable to constrain the age of the capping deposit. However, the intervals between successive events are far from equal, with 2 or 3 of the events apparently occurring within the last 500 years, and earlier events being much more widely spaced in time.

We have only a few constraints on the possible amounts of slip in each event, as measurements are restricted to those few places where the landscape is both unaltered by human activities, and where there is relief across the fault. We observe twenty offsets of variable size that are clustered at local topographic highs (Fig. 4.15). At the Salyan trench site, we measured a 7.5 m offset terrace riser in the field (Fig. 4.10), which we confirmed by restoring the slope of the terrace riser using the LaDiCoaz method (Fig. 4.10). We were not able to achieve accurate age constraint on terrace by direct sampling or obtain reasonable constraint from Trench 1. From our observations and remotely measured across fault offset drainage channels, we see six other offsets within error that fall into the 7.5 m range southeast of the Salyan trench site and north near Shirvan (Fig. 4.15). Near Shirvan (Fig. 4.5 & 4.15), we measured a 3.0 m offset in a young drainage channel in the field (Fig. 4.7b), but this channel is not visible in satellite imagery. From the satellite imagery we measure a 4.6 m offset north of Shirvan and two 2.0 m offsets southeast of the Salyan trench site (Fig. 4.15). However, these measurements are poorly constrained in the satellite imagery. We infer that the 2-3 m offsets occurred in the MRE, and the 7.5 m displacement at our trench site is representative of at least two events, though with the amount and quality of measurements that we have we are unable to assess quantitatively.

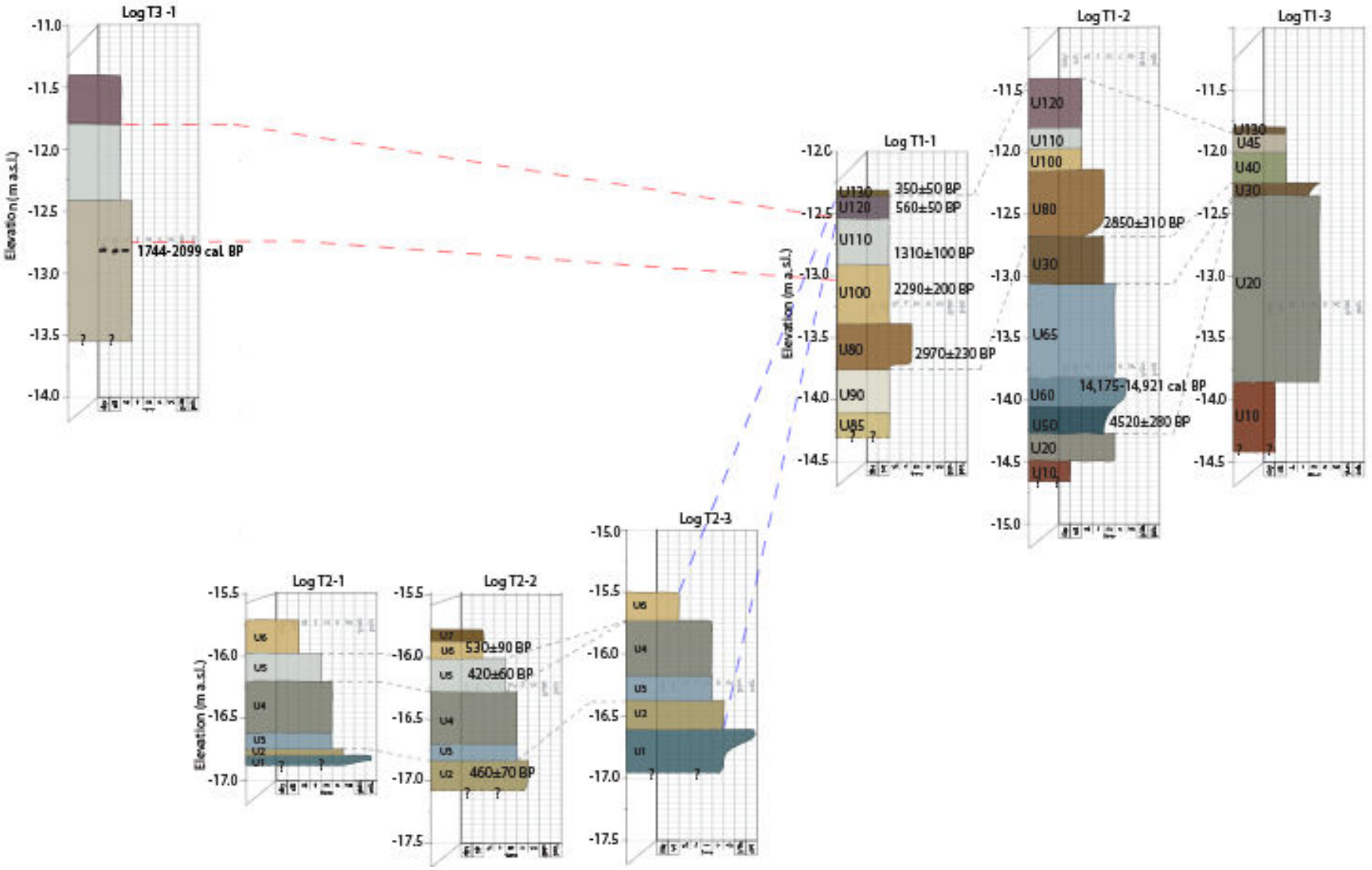


Figure 4.14. Stratigraphic log of the sample site, Trench 1 and Trench 2. Unit descriptions in the text section 3.2.1. Red and blue lines show sediment ages that match at the different trenches.

4.6.2. Slip-rate estimate

To determine slip-rate on the fault we use the 53 ± 4 m right-lateral displacement of a riser between Qad (upper surface) and Qt2 (lower surface). We dated charcoals from a sample pit excavated into the Qad terrace at 1744 – 2099 and 1824 - 2145 years cal. BP (Fig. 4.10 and 4.14), which yields a slip-rate of 29.4mm/yr if the sample age is representative of the terrace formation age (Fig. 4.3). We also dated a marine shell from the present-day surface of Qad at ~35 ka, which yields a slip rate of less than 2 mm/yr. However, the inconsistency between the two sample ages indicates that the sediments overlying Qad are reworked and incorporates much older detrital material. The last major highstand in the Caspian Sea is thought to be between 11,000 - 13,500 cal BP, with sea level reaching an elevation of 0 m relative to global levels during this time (Arslanov et al., 2016; Dolukhanov et al., 2010; Kakroodi et al., 2012; Kroonenberg et al., 1997; Pánek et al., 2016), which would have covered the trench sites. We assume that geomorphic surfaces pre-dating this last highstand would have been reset, such that all fluvial incision and terrace formation must postdate the last highstand. If the offset of the terrace riser started to accumulate at a maximum of 11,000 - 13,500 cal BP it allows us to infer a minimum geologic slip-rate between 3.9 - 4.8 mm/yr.

4.7. Discussion

The Shirvan fault zone, along with the Alat fault and potentially a further parallel strand within the Kura basin interior, together accommodate right-lateral faulting between the South Caspian Basin and onshore regions. At bends in the Shirvan fault zone we observe folding from metre to kilometre scales, suggesting that these folds are building topography as the principal compressive stress direction changes. Our data also shows a relationship between strike-slip faulting and mud-volcanism in this region. We observe that active faults are coincident with mud volcano vents, which suggests there is a structural control on emplacement.

From velocity triangles and GNSS measurements we estimate that the right-lateral shear should total to 1.9 mm/yr. We have determined a probable maximum slip-rate of 3.9 - 4.8 mm/yr for the Shirvan fault, showing that it is an important structure within regional tectonics. This slip-rate is also supported by the earthquake recurrence captured of the last 3000 years from our interpretations of the trench logs. If we assume that each event has 2 - 3 m of slip in each event and have 5 earthquakes in the last 3000 years, we have an estimated slip-rate of 3 – 5 mm/yr.

The Shirvan fault is also an important element in assessments of earthquake hazard, passing close to large population centres in east Azerbaijan (Shirvan and Salyan) and within ~30 km of Shamakhi and Qobustan to the north (Fig. 4.2). The region is also an important gateway linking Central Asia to the ports and infrastructure in the Black Sea and eastern Mediterranean, the so-called "middle corridor", and contains concentrations of energy and transport infrastructure that may be vulnerable to fault rupture. It is therefore important to assess the earthquake potential upon the fault.

We have mapped the Shirvan fault system in detail for a length of 60km, through seismicity and mud volcano alignments suggest the fault is likely to be 150 km in length, stretching at least 30 km offshore to the south, and merging northwards with the Greater Caucasus (Fig. 4.1), in agreement with the mapping of Zelenin et al. (2022). If the entire 150 km fault were to rupture in an earthquake, log-linear scaling relationships for strike-slip faults in Wesnousky (2008) suggest a maximum slip of 5.9m, an average slip of 3.0m and a moment-magnitude of 7.5, using a rigidity modulus of 30 GPa and a seismogenic thickness of 15 km. These figures are consistent with the limited number of stream offset measurements that we have measured along the fault. An important result from our Quaternary dating is that although the average recurrence interval is 500-750 years, the slip events are far from even in timing and show an apparent clustering of two or three events within the last 500 years, so in the historical period.

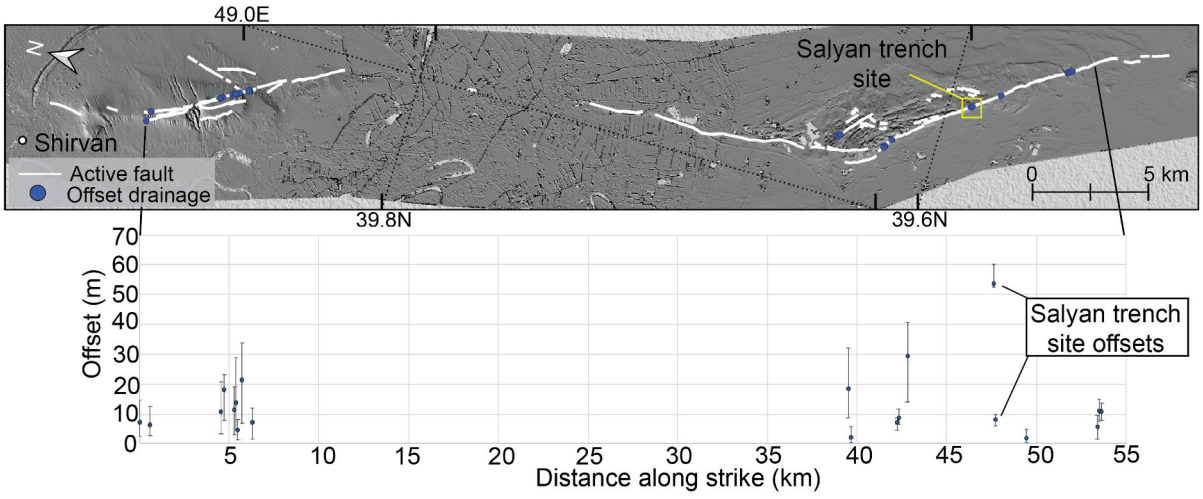


Figure 4.15. Offset drainage measurements along fault strike in the Shirvan and Salyan sections. Blue circles are offset measurements and yellow line shows the Shirvan fault trace.

Gunnels et al. (2020) and the ISC database (International Seismic Center, 2022) show shallow seismicity along the fault zone, but with no event larger than M_w6. The pre-instrumentational earthquake catalogue shows no large events within the Salyan-Shirvan region, which conflicts with evidence for earthquake clustering over the last 500 years. It is feasible that the absence of major historical earthquakes results from a lack of documentation in this area due to its remoteness. Alternatively, it is possible that the absence of large earthquakes is real, with the surface ruptures resulting from an aseismic process.

Aseismic slip along the Shirvan fault is plausible, as it cuts through ~15 km thickness of sediments of the Kura basin, with high fluid pressures and overpressure demonstrated through active mud-volcanism. Our trenches do not rule out continuous creep deformation, but the sedimentation and structure are suggestive of punctuated fault movement in discrete events, with successive sediment packages capping discrete fracture zones. The slip events seen in our trenches may result from triggered aseismic slip in discrete events, triggered either during fluid mobilization events, or by deeper earthquakes within the basement beneath the Kura basin, such as the deep thrust events that accommodate shortening between the South Caspian and adjacent onshore regions (Figs 4.1 & 4.2). The 1983 M_w5.8 Kum Dag earthquake, in the Caspian lowlands of Turkmenistan, is a possible analogy for this type of behaviour (e.g. Jackson et al., 2002). This moderate magnitude earthquake had a hypocentral depth of 27 km and yet created a 20 km surface rupture and maximum dextral slip of 0.5 m (Trifonov et al., 1986). The surface slip following the Kum Dag earthquake is inferred to have been aseismic, and triggered by the deep moderate-magnitude earthquake in the underlying basement. Physical factors such as lithology, sedimentary overpressure and pore fluid pressure can lead to aseismic slip on faults (e.g., (Harris, 2017). Examples of aseismic creep on the Philippine Fault (Leyte Island) shows correlation to higher fluid pressures in a hydrothermal system.

Mud volcanism is a surface phenomenon that occurs in zones of high pore pressure believed to be derived from overpressure, natural gases and tectonic compressive forces (Mazzini and Etiope, 2017). Compressive tectonic stresses, acting on sediments increases pore pressure, creates favourable conditions for eruptions and controls mud volcano emplacement. In compressional regions, mud volcanoes are found along the top of anticlines with subsurface pathways controlled by the regional stress field (Bonini, 2012). The relationship between

strike-slip faulting and mud volcano emplacement is widespread. We see examples on the South Coast and Central Range Faults in Trinidad-Tobago (Deville and Guerlais, 2009; Dia et al., 1999; Weber et al., 2020), in the Gulf of Cadiz offshore Spain (Hensen et al., 2015), on the Watukosek fault in Indonesia (Mazzini et al., 2009) and at the southern Salton Sea in California (Onderdonk et al., 2011). These examples suggest that vertically dipping strike-slip faults provide a structural control on mud volcano emplacement. Additionally, where faults bend localised compressive stresses cause folding (Cunningham and Mann, 2007). We observe a correlation between active strike-slip faulting and mud volcano emplacement shown on Fig. 4.2b and these appear to cluster at fault bends. We speculate that strike-slip faults and folding from fault bends are controlling the emplacement of mud volcanoes.

Our investigation on the Shirvan fault zone has wider implications for the methods of assessing seismic hazard within regions of sparse paleoseismic data, historical archives, and with potentially long recurrence intervals between major earthquakes. In Azerbaijan there are additional challenges posed by the complexity of faulting with strike-slip faults in the basin sediments overlying thrusts in the basement below, and with the potential for fault slip to occur through aseismic processes given high fluid pressures in the surrounding rocks. Effective assessment of earthquake risk requires detailed assessment of the hazard posed by the faulting, bringing together geologic data, geodetic investigation of fault slip behaviour, and the building of appropriately long earthquake catalogues through the use of archive documents.

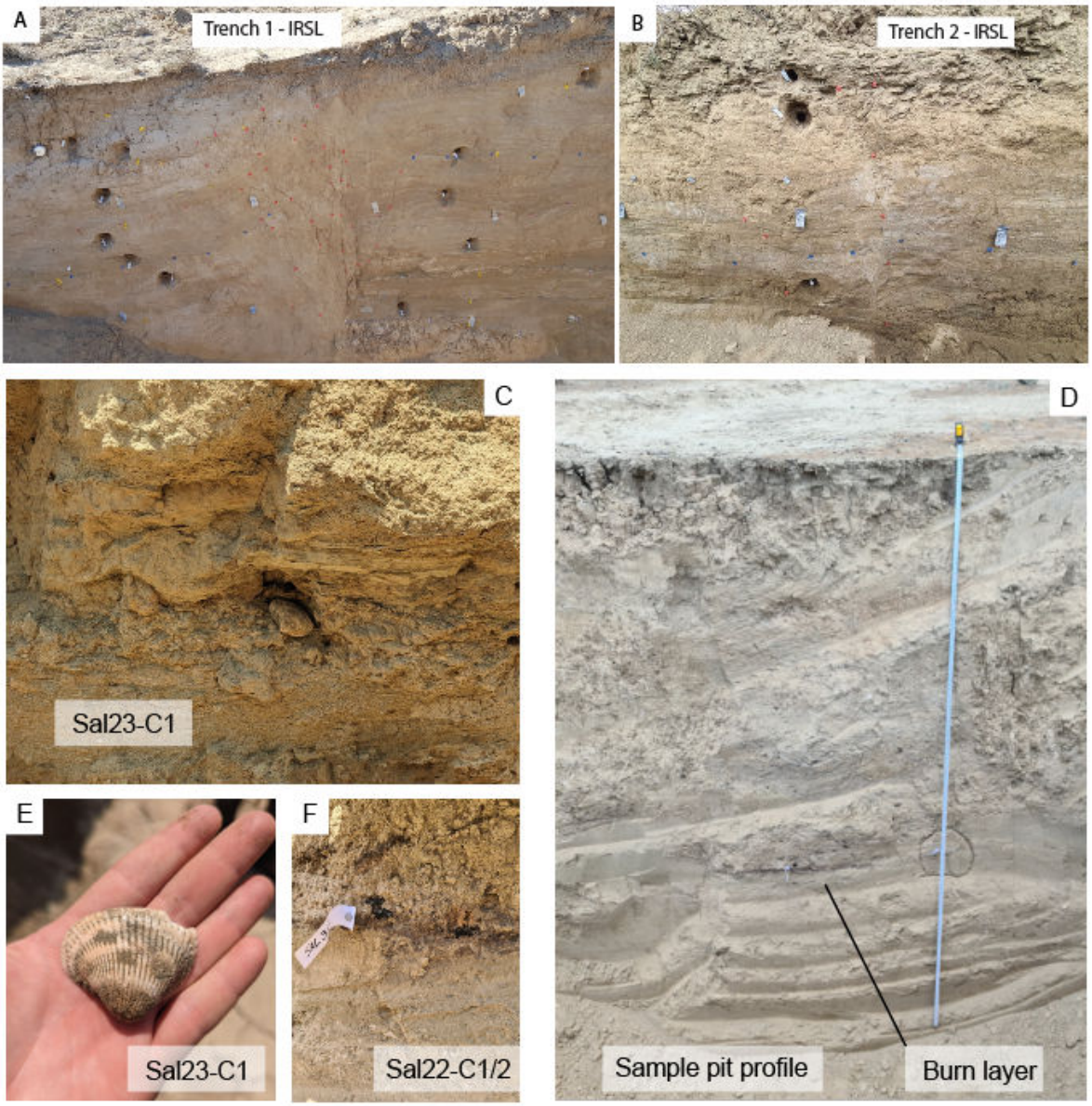


Figure 4.16. A – Fault 1 (F1) Trench 1 (Fig. 4.11) IRSL sample locations detailed in the trench log. B – Fault 2 (F2) Trench 2 (Fig. 4.12) IRSL sample locations detailed in trench log 2 (Fig. 12). C – Shell in situ taken from the top of U60 in Trench 1 (Fig. 11) calibrated ages in Table 4.2. D – photo of sample pit wall (Fig. 6) with a charcoal burn layer sampled and dated using radiocarbon (Table 2). E – close photo of removed (C) in tact shell from U60. F – Close up photo of burn layer in D.

4.8 Conclusion

We have shown geomorphic evidence for active right-lateral strike-slip faulting through the Kura basin of Azerbaijan, which accommodates lateral motion between the South Caspian Basin and adjacent onshore areas and forms a potential hazard to populations and infrastructure. We provide the first constraints on geologic slip-rate of 3.9 – 4.8 mm/yr, based on the assumed age of an offset terrace. From paleoseismic trenching we show evidence for between four and seven paleo-earthquakes in the Holocene, with three of these events occurring within the last 600 years BP. The Shirvan fault therefore shows irregular recurrence of slip events, with a distinct clustering in the last millennium. No large earthquakes are recorded in the region over this time frame, raising the possibility that the slip may have occurred aseismically, in events triggered by deeper seismicity or by fluid pressures in surrounding rocks.

Acknowledgements

We thank the Republican Seismic Survey, Azerbaijan, for their continued collaborative support. We also thank BP Azerbaijan. The paper was aided through discussions with Rich Koehler, Gordon Seitz and James Jackson. Satellite imagery was obtained through the Committee for Earth Observing Satellites (CEOS) Seismic Hazards Demonstrator and through funding from St. Edmund Hall, Oxford. Our work was funded through BP Azerbaijan, CASP through a fieldwork award to Neill Marshall, through the NERC-funded COMET (GA/13/M/031), the NERC-ESRC Increasing Resilience to Natural Hazards program "Earthquakes without Frontiers" (NE/J02001X/1), allocation 0009090 from the Research England GCRF Support Fund, and the Leverhulme Trust through research grants EROICA (RPG-2018-371) and NEPTUNE (RPG-2018-243).

Data Tables

Table 4.1 shows the location and age of the IRSL samples from trenches 1 and 2. The location in the cross section is shown in Figs 4.11, 4.12, and 4.13. Pictures of sample site in Fig. 4.16.

Trench	Latitude	Longitude	Elevation (m a.s.l.)	Field Code	Lab Code	Depth (m)	Age (kyr)		1 sigma uncertainty
Trench 1	39.5906	49.0633	-13.764	SAL1 - 1	22148	0.05	350	±	50
Trench 1	39.5906	49.0633	-13.764	SAL1 - 2	22149	0.45	1310	±	100
Trench 1	39.5906	49.0633	-13.764	SAL1 - 3	22150	0.85	2290	±	200
Trench 1	39.5906	49.0633	-13.764	SAL1 - 7	22154	0.84	2850	±	310
Trench 1	39.5906	49.0633	-13.764	SAL1 - 10	22157	2.37	4520	±	280
Trench 1	39.5906	49.0633	-13.764	SAL1 - 11	22158	1.45	2970	±	230
Trench 1	39.5906	49.0633	-13.764	SAL1 - 17	22164	0.10	560	±	50
Trench 2	39.5908	49.0631	-13.463	SAL2 - 2	22167	0.15	530	±	90
Trench 2	39.5908	49.0631	-13.463	SAL2 - 3	22168	0.27	420	±	60
Trench 2	39.5908	49.0631	-13.463	SAL2 - 4	22169	1.30	460	±	70

Table 4.2 shows the location and type of material sampled for radiocarbon dating. The ages have been calibrated using the OxCal v4.4.4 model using the Marine 20 curve and delta R adjustment from previous studies around the Caspian Sea. Pictures of sample sites in Fig. 4.16.

Name	Location	Latitutde (°)	Longitude (°)	Elevation (m asl)	Material	Calibrated Age (years cal. BP)
Sal23-C1	Salyan Trench 1	39.5906	49.0633	-13.8	Shell	14175 - 14921
Sal23-C2	Salyan Trench 1	39.5906	49.0633	-13.8	Shell	14106 - 14854
Sal22-C1	Salyan Sample pit	39.5914	49.062	-12.8	Charcoal	1744 - 2099
Sal22-C2	Salyan Sample pit	39.5914	49.062	-12.8	Charcoal	1824 - 2145
Sal21-S1	Salyan Qad surface	39.5914	49.062	-11.4	Shell	35040 - 35520
Shi21-S2	Shirvan surface	39.8663	48.9676	64	Shell	35570 - 36070

Statement of Authorship for joint/multi-authored papers for PGR thesis

To appear at the end of each thesis chapter submitted as an article/paper

The statement shall describe the candidate's and co-authors' independent research contributions in the thesis publications. For each publication there should exist a complete statement that is to be filled out and signed by the candidate and supervisor **(only required where there isn't already a statement of contribution within the paper itself).**

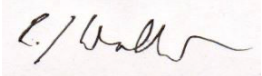
Title of Paper	Paleoseismology of the Shirvan Strike-slip fault zone (West Caspian Fault), Azerbaijan: implications for seismic hazard and South Caspian tectonics.
Publication Status	□Unpublished and unsubmitted work written in a manuscript style
Publication Details	N. Marshall[1], S. Kazimova[3], I. Pierce[1], E. Rhodes[4,5], R.T Walker[1], R. Javanshir[1,2], B. Johnson[1], G. P. De Pascale[6], I. Guliyev[2], G. Yetirmishli[3], R. Muradov[3]. *[1]COMET, Department of Earth Sciences, Oxford University, Oxford, OX1 3AN, UK.* [2]Azerbaijan National Academy of Science, Baku, Azerbaijan. [3]Republican Seismic Survey Center of Azerbaijan National Academy of Science, Baku, Azerbaijan *[4]Department of Geography, University of Sheffield, Sheffield, S10 2TN, UK.* *[5]Department of Earth, Planetary, and Space Sciences, University of California Los Angeles, Los Angeles, CA 90095-1567, USA.* *[6]School of Engineering and Natural Sciences, University of Iceland, Reykjavík, Iceland.*

Student Confirmation

Student Name:	Neill Marshall		
Contribution to the Paper	Performed mapping and analysis on the topographic data, logged and sampled trench sites, interpreted data and wrote the manuscript.		
Signature.	Neill Marshall	Date	04/10/23

Supervisor Confirmation

By signing the Statement of Authorship, you are certifying that the candidate made a substantial contribution to the publication, and that the description described above is accurate.

Supervisor name and title: Professor Richard T. Walker			
Supervisor comments The student made all analysis and interpretation			
Signature.		Date	05/10/23

This completed form should be included in the thesis, at the end of the relevant chapter.

5 Concluding Remarks

5.1 Conclusions from the Thesis

By investigating active faulting and earthquakes, this thesis aims to expand our knowledge and understanding of the active tectonic processes and inherent seismic hazards in the South Caspian region.

Chapter 2 focusses on active faulting and earthquakes in the region surrounding Ashgabat, home to around 1 million people. The investigation concentrates on the devastating 1948 M_w7.3 Ashgabat earthquake using a combination of remote sensing, seismology and field observations. The analysis of digitised seismograms provides a well constrained focal mechanism solution and location. The results show that this earthquake was most-likely a strike-slip event with an epicentre just to the northwest of Ashgabat. From the digitised seismograms, an estimate of M_w yields a result of 7.3 ± 1.4, in agreement with previous estimates. By digitising and georeferencing earthquake rupture maps from 1949 and comparing with my fault mapping, I have identified sites of earthquake rupture approximately 80 km in length. I show evidence for right-lateral offset drainage channels on faults near to the reported ruptures and combining this evidence with the strike-slip focal mechanism solution conclude that the earthquake was right-lateral strike-slip. The earthquake ruptures are complex, and I interpret this as a multi-segment/fault event that did not rupture the Main Kopeh Dagh Fault but secondary structures. There is additional evidence for multiple earthquakes in the vicinity of Ashgabat, highlighted by right-lateral offsets in qanats (~5 m) and the walls of the ancient city of Nisa (~18 m).

Chapter 3 looks further west at faulting on the Main Kopeh Dagh Fault and east Caspian lowlands. I find peaks in right-lateral offset drainages at 23.5, 30, 88, 256, 402, 600 and 1000m. The long-term geologic slip-rate of 9.2 ± 1.5 mm/yr provides age constraints on these peaks in incision events during MIS 1, end-MIS 2, mid-MIS 3, start-MIS 3, MIS 5a and MIS 5c-e and these are interpreted as increased levels of moisture and precipitation. The age ranges coincide with paleoclimate records in northeast Iran and the Caspian lowlands. Based on paleoclimate records, the study shows that the slip-rate is more likely to be in the lower range of 7.2 – 9.2

mm/yr. Radiocarbon dating of shells in a paleoshoreline deposit at 0m (a.s.l.) yields a maximum age of 12.7 k years cal. BP. This agrees with Caspian Sea level curves showing a 0 m (a.s.l.) highstand after the Last Glacial Maximum (end-MIS 2) and correlates with the incision event calculated from slip-rate and offset drainage channels.

Chapter 4 shows active right-lateral faulting on the western and north-western margins of the South Caspian Basin. The study identifies previously unknown strike-slip faults that step out into the Caspian Sea, and these correlate the alignment of mud volcanoes. From paleoseismic investigation the Shirvan Fault zone has hosted 4 – 7 earthquakes during the Holocene and has a slip-rate of 3.9 - 4.8 mm/yrs (based on the assumption that incision started after the last highstand end-MIS 2). From active fault mapping and the location of mud volcanoes, the total fault length is estimated at 150 km and is capable of hosting M 7.5 events. The Shirvan fault has irregular recurrence of slip with a distinct clustering of events in the last millennium (three earthquakes in the last 600 years BP). As there are no large earthquakes recorded during this period there is a possibility that slip may have occurred aseismically, in events triggered by deeper seismicity or by fluid pressures in surrounding sediments.

5.2 Suggestions for Future Work

The findings of this thesis suggest the need for several lines of research to be pursued. Firstly, the thesis demonstrates the utility of using satellite remote sensing in combination with seismic, paleoclimate and archaeological data to evaluate active faulting, paleoearthquakes and tectonics. To gain a comprehensive understanding of fault patterns, rupture processes and distributions wider areas of satellite imagery can be utilised in the investigation of the Main Kopeh Dagh Fault (Turkmenistan). When combined with field-based investigation, as described in Chapter 4, a higher resolution record of past earthquakes can be achieved. For a major active strike-slip fault, there have been only two paleoseismic trenches that identifies the most recent earthquake on the Main Kopeh Dagh Fault and this fault remains poorly understood. In order to build a better understanding of this fault zone, more paleoseismic trenches are required, specifically to target events prior to the most recent, and to examine the earthquake history of other unstudied segments. This will help construct better longer-term earthquake records and answer questions relating to the segmentation, rupture processes and spatial and temporal clustering of large seismicity.

The thesis highlights the potential effect that fluid rich over-pressured sedimentary basins have on earthquake rupture processes. The findings show the possibility that lower magnitude and/or deep seismicity can trigger surface rupture that currently falls outside of rupture length to magnitude scaling relationships. Currently, these findings are speculative and further investigation is required. Combining the paleoseismic results in Chapter 4 with further geodetic investigations using GNSS and InSAR timeseries, will help to establish if the fault is creeping and help determine the distribution of strain within the region. Further paleoseismic work in the northern area of the Shirvan Fault zone and fault ruptures in the east Caspian lowlands will provide a new dataset of fault ruptures in over-pressured sediments. This data can be compared with regions showing similar behaviour, notably the Salton Sea (California, USA) and the Central Range Fault (Trinidad and Tobago), addressing globally applicable questions regarding low magnitude event rupture processes, fault creep and rheologically weak faults capacity for large earthquakes. By targeting earthquake recurrence in the northern section of the Shirvan fault we will also be able to compare with the event chronology we observe near Salyan at our trench site. This will help address question of earthquake rupture length and if we see temporal clustering of earthquakes in the last 600 years.

Chapter 3 has developed a novel new method for building Quaternary stratigraphy using fault slip-rate near to north-eastern Iran. There is potential to reverse this method and date peaks in offset measurements with the paleoclimate records. From this data constraints slip-rates can be obtained for active faults in northern Iran (e.g., the Shahrud Fault zone) and other arid regions with well-preserved fault offsets.

Finally, the east Caspian lowlands shows and preserves many possible shoreline features marking past Caspian Sea level. There is still debate in the literature as to the timing and level of highstand conditions during the late-Pleistocene. By accurately measuring the elevation and mapping these shorelines alongside dating the deposits, a new sea level curve for the Caspian can be constructed.

References

Abdullayev, N.A., Kadirov, F., Guliyev, I.S., 2017. Subsidence history and basin-fill evolution in the South Caspian Basin from geophysical mapping, flexural backstripping, forward lithospheric modelling and gravity modelling. Geological Society, London, Special Publications 427, 175–196. https://doi.org/10.1144/SP427.5

AgiSoft PhotoScan Professional (Version 2.0) (Software). (2021). Retrieved from http://www.agisoft.com/downloads/installer/

Allen, M., Jackson, J., Walker, R., 2004. Late Cenozoic reorganization of the Arabia-Eurasia collision and the comparison of short-term and long-term deformation rates. Tectonics. https://doi.org/10.1029/2003TC001530

Allen, M.B., Jones, S., Ismail-Zadeh, A., Simmons, M., Anderson, L., 2002. Onset of subduction as the cause of rapid Pliocene-Quaternary subsidence in the South Caspian basin. Geology 30, 775. https://doi.org/10.1130/0091-7613(2002)030<0775:OOSATC>2.0.CO;2

Ambraseys, Jackson, 1998. Faulting associated with historical and recent earthquakes in the Eastern Mediterranean region. Geophys J Int 133, 390–406. https://doi.org/10.1046/j.1365-246X.1998.00508.x

Ambraseys, N.N., 1997. The Krasnovodsk (Turkmenistan) Earthquake of 8 July 1895. Journal of Earthquake Engineering 1, 293. https://doi.org/10.1142/S1363246997000131

Ambraseys, N.N., Melville, C.P., 1982. A history of Persian earthquakes. Cambridge University Press, Cambridge.

Antoine, S.L., Klinger, Y., Delorme, A., Wang, K., Bürgmann, R. and Gold, R.D., 2021. Diffuse deformation and surface faulting distribution from submetric image correlation along the 2019 Ridgecrest, California, ruptures. Bulletin of the Seismological Society of America, 111(5), pp.2275-2302.

Arslanov, Kh.A., Yanina, T.A., Chepalyga, A.L., Svitoch, A.A., Makshaev, R.R., Maksimov, F.E., Chernov, S.B., Tertychniy, N.I., Starikova, A.A., 2016. On the age of the Khvalynian deposits of the Caspian Sea coasts according to 14C and 230Th/234U methods. Quaternary International 409, 81–87. https://doi.org/10.1016/j.quaint.2015.05.067

Aziz Zanjani, A., Ghods, A., Sobouti, F., Bergman, E., Mortezanejad, G., Priestley, K., Madanipour, S., Rezaeian, M., 2013. Seismicity in the western coast of the South Caspian Basin and the Talesh Mountains. Geophys J Int 195, 799–814. https://doi.org/10.1093/gji/ggt299

Barbot, S., Luo, H., Wang, T., Hamiel, Y., Piatibratova, O., Javed, M. T., Braitenberg, C., & Gurbuz, G., 2023. Slip distribution of the February 6, 2023 Mw 7.8 and Mw 7.6, Kahramanmaraş, Turkey earthquake sequence in the East Anatolian Fault Zone. Seismica, 2(3). https://doi.org/10.26443/seismica.v2i3.502

Berberian, M., Yeats, R.S., 1999. Patterns of historical earthquake rupture in the Iranian Plateau. Bulletin of the Seismological Society of America 89, 120–139. https://doi.org/10.1785/BSSA0890010120

Bergman, E., Benz, H., Yeck, W., Karasözen, E., Engdahl, E.R., Ghods, A., Hayes, G., Earle, P., 2022. A Global Catalog of Calibrated Earthquake Locations. Seismological Research Letters; 94 (1): 485–495. doi: https://doi.org/10.1785/0220220217

Biasi, G.P, Wesnousky, S.; Steps and Gaps in Ground Ruptures: Empirical Bounds on Rupture Propagation. Bulletin of the Seismological Society of America 2016;; 106 (3): 1110–1124. doi: https://doi.org/10.1785/0120150175

Bonini, M., 2012. Mud volcanoes: Indicators of stress orientation and tectonic controls. Earth Sci Rev 115, 121–152. https://doi.org/10.1016/j.earscirev.2012.09.002

Bormann, P. & Saul, J., 2008. The new IASPEI standard broadband magnitude m(B). Seismological Research Letters - SEISMOL RES LETT. 79. 698-705. 10.1785/gssrl.79.5.698

Bronk Ramsey, C., 1995. Radiocarbon Calibration and Analysis of Stratigraphy: The OxCal Program. Radiocarbon 37, 425–430. https://doi.org/10.1017/S0033822200030903

Butovskaya, E. M. & Kovalenko, YA. G., 1955. Osobennosti karty isoseist Ashkhabadskovo zemletryasenya 5-6 Oktyabrya 1948 goda i deformaziya zemnoi poverkhnosti v rayone Ashkhabada po dannym nivelirovok 1942-1952 gg. In Meterologiya i gidrologiya v Uzbekistane. Tashkent: Izd. Akad. Nauk Uzb. S.S.R.

Caporali, A., Zurutuza, J., & Bertocco,M. (2019). A time-dependent model ofelastic stress in the Central Apennines,Italy.Journal of Geophysical Research:Solid Earth,124, 9852–9869. https://doi.org/10.1029/2019JB01780

Carolin, S.A., Ersek, V., Roberts, W.H.G., Walker, R.T., Henderson, G.M., 2019. Drying in the Middle East During Northern Hemisphere Cold Events of the Early Glacial Period. Geophys Res Lett 46, 14003–14010. https://doi.org/10.1029/2019GL084365

Charlier, C. H. & Van Gils, J. M., 1953. Liste des stations seismologiques mondiales. L'Association Internationale de Seismologie, Observatoire Royal de Belgique a Uccle Service Seismologique.

Cooke, M.L. and Pollard, D.D., 1997. Bedding-plane slip in initial stages of fault-related folding, Journal of Structural Geology, Volume 19, Issues 3–4, p567-581, https://doi.org/10.1016/S0191-8141(96)00097-1.

Copley, A., Jackson, J., 2006. Active tectonics of the Turkish-Iranian Plateau. Tectonics. https://doi.org/10.1029/2005TC001906

Cunningham, W.D., Mann, P., 2007. Tectonics of strike-slip restraining and releasing bends. Geological Society, London, Special Publications 290, 1–12. https://doi.org/10.1144/SP290.1

Deville, E., Guerlais, S.-H., 2009. Cyclic activity of mud volcanoes: Evidences from Trinidad (SE Caribbean). Mar Pet Geol 26, 1681–1691. https://doi.org/10.1016/j.marpetgeo.2009.03.002

Davidovich A., 1951. Report on the 1947 excavations in the area of the Square Hall of Old Nisa, Ashgabat, Proc. South Turkmenistan Archaeological Complex Expedition, 108–142.

Di Giacomo, D., Engdahl, E.R., Storchak, D.A., 2018. The ISC-GEM Earthquake Catalogue (1904–2014): status after the Extension Project. Earth Syst Sci Data 10, 1877–1899. https://doi.org/10.5194/essd-10-1877-2018

Dia, A.N., Castrec-Rouelle, M., Boulègue, J., Comeau, P., 1999. Trinidad mud volcanoes: where do the expelled fluids come from? Geochim Cosmochim Acta 63, 1023–1038. https://doi.org/10.1016/S0016-7037(98)00309-3

Djamali, M., de Beaulieu, J.L., Shah-hosseini, M., Andrieu-Ponel, V., Ponel, P., Amini, A., Akhani, H., Leroy, S.A.G., Stevens, L., Lahijani, H., Brewer, S., 2008. A late Pleistocene long pollen record from Lake Urmia, NW Iran. Quat Res 69, 413–420. https://doi.org/10.1016/J.YQRES.2008.03.004

Djamour, Y., Vernant, P., Bayer, R., Nankali, H.R., Ritz, J.-F., Hinderer, J., Hatam, Y., Luck, B., Le Moigne, N., Sedighi, M., Khorrami, F., 2010. GPS and gravity constraints on continental deformation in the Alborz mountain range, Iran. Geophys J Int 183, 1287–1301. https://doi.org/10.1111/j.1365-246X.2010.04811.x

Dodds, Nicholas, Begenjev, G., Bezmenov, Y., Gruetzner, C., Mirzin, R., Rhodes, E., Walker, R.T., Wordsworth, P., 2022a. A Major Medieval Earthquake on the Main Köpetdag (Kopeh Dagh) Fault, Turkmenistan. Bulletin of the Seismological Society of America 112, 2189–2215. https://doi.org/10.1785/0120210195

Dodds, N, Daout, S., Walker, R.T., Begenjev, G., Bezmenov, Y., Mirzin, R., Parsons, B., 2022b. Interseismic deformation and strain-partitioning along the Main Köpetdag Fault, Turkmenistan, with Sentinel-1 InSAR time-series. Geophys J Int 230, 1612–1629. https://doi.org/10.1093/gji/ggac139

Dolukhanov, P.M., Chepalyga, A.L., Lavrentiev, N. V., 2010. The Khvalynian transgressions and early human settlement in the Caspian basin. Quaternary International 225, 152–159. https://doi.org/10.1016/j.quaint.2009.10.039

Elliott, J.R., Nissen, E.K., England, P.C., Jackson, J.A., Lamb, S., Li, Z., Oehlers, M. and Parsons, B., 2012. Slip in the 2010–2011 canterbury earthquakes, New Zealand. Journal of Geophysical Research: Solid Earth, 117(B3).

Engdahl, E.R., van der Hilst, R., Buland, R., 1998. Global teleseismic earthquake relocation with improved travel times and procedures for depth determination. Bulletin of the Seismological Society of America; 88 (3): 722–743. doi: https://doi.org/10.1785/BSSA0880030722

Engdahl, E.R., Jackson, J.A., Myers, S.C., Bergman, E.A., Priestley, K., 2006. Relocation and assessment of seismicity in the Iran region. Geophys J Int 167, 761–778. https://doi.org/10.1111/j.1365-246X.2006.03127.x

England, P., Jackson, J., 2011. Uncharted seismic risk. Nat Geosci 4, 348–349. https://doi.org/10.1038/ngeo1168

Fattahi, M., Walker, R., Hollingsworth, J., Bahroudi, A., Nazari, H., Talebian, M., Armitage, S., Stokes, S., 2006. Holocene slip-rate on the Sabzevar thrust fault, NE Iran, determined using optically stimulated luminescence (OSL). Earth Planet Sci Lett. https://doi.org/10.1016/j.epsl.2006.03.027

Fattahi, M., Walker, R.T., 2015. Optical dating of Holocene lake bed sediments of the Nimbluk Plain, Khorasan, Northeast Iran: Implications for the climate change and palaeo-environment. Environmental Science.

Fattahi, M., Walker, R.T., Khatib, M.M., Dolati, A., Bahroudi, A., 2007. Slip-rate estimate and past earthquakes on the Doruneh fault, eastern Iran. Geophys J Int 168, 691–709. https://doi.org/10.1111/j.1365-246X.2006.03248.x

Fedorov, P.V., 1998. Ashgabat-1948. Recollection of an eyewitness, Vestn. Otd. Geol. Geofiz. Geokhim. Gorn. Nauk Ross. Akad. Nauk, no. 2, pp. 20–25.

Feyzullayev, A.A., Tagiyev, M.F., Lerche, I., 2015. On the Origin of Hydrocarbons in the Main Lower Pliocene Reservoirs of the South Caspian Basin, Azerbaijan. Energy Exploration & Exploitation 33, 1–13. https://doi.org/10.1260/0144-5987.33.1.1

Field, E.H., Arrowsmith, R.J., Biasi, G.P., Bird, P., Dawson, T.E., Felzer, K.R., Jackson, D.D., Johnson, K.M., Jordan, T.H., Madden, C., Michael, A.J., Milner, K.R., Page, M.T., Parsons, T., Powers, P.M., Shaw, B.E., Thatcher, W.R., Weldon, R.J., Zeng, Y., 2014. Uniform California Earthquake Rupture Forecast, Version 3 (UCERF3)--The Time-Independent Model. Bulletin of the Seismological Society of America 104, 1122–1180. https://doi.org/10.1785/0120130164

Forte, A.M., Cowgill, E., 2013. Late Cenozoic base-level variations of the Caspian Sea: A review of its history and proposed driving mechanisms. Palaeogeogr Palaeoclimatol Palaeoecol 386, 392–407. https://doi.org/10.1016/j.palaeo.2013.05.035

Forte, A.M., Cowgill, E., Bernardin, T., Kreylos, O., Hamann, B., 2010. Late Cenozoic deformation of the Kura fold-thrust belt, southern Greater Caucasus. Geol Soc Am Bull 122, 465–486. https://doi.org/10.1130/B26464.1

Forte, A.M., Cowgill, E., Murtuzayev, I., Kangarli, T., Stoica, M., 2013. Structural geometries and magnitude of shortening in the eastern Kura fold-thrust belt, Azerbaijan: Implications for the development of the Greater Caucasus Mountains. Tectonics 32, 688–717. https://doi.org/10.1002/tect.20032

Galbraith, R.F., Green, P.F., 1990. Estimating the component ages in a finite mixture. Int J Rad Appl Instrum D 17, 197–206. https://doi.org/10.1016/1359-0189(90)90035-V

Ghassemi, M.R., Garzanti, E., 2019. Geology and geomorphology of Turkmenistan: A review. Geopersia 9, 125–140. https://doi.org/10.22059/geope.2018.265613.648416

Golinskiy, G. L., and Nepesov, R. D., 1968. Seismicity characteristics of Turkmenistan and adjacent Iran regions on the macroseismic materials, in Seysmichnost, Turkmeniyi. pp. 51-151, Ylym, Ashkhabad.

Gorshkov, G. P., 1984. Seismotectonics of the Kopet Dagh, 272 pp., Nauka, Moscow.

Grützner, C., Carson, E., Walker, R.T., Rhodes, E.J., Mukambayev, A., Mackenzie, D., Elliott, J.R., Campbell, G., Abdrakhmatov, K., 2017. Assessing the activity of faults in continental interiors: Palaeoseismic insights from SE Kazakhstan. Earth Planet Sci Lett 459, 93–104. https://doi.org/10.1016/j.epsl.2016.11.025

Gunnels, M., Yetrimishli, G., Kazimova, S., Sandvol, E., 2020. Seismotectonic evidence for subduction beneath the Eastern Greater Caucasus. Geophys J Int 224, 1825–1834. https://doi.org/10.1093/gji/ggaa522

Hamling, I.J., Hreinsdóttir, S., Clark, K., Elliott, J., Liang, C., Fielding, E., Litchfield, N., Villamor, P., Wallace, L., Wright, T.J., D'Anastasio, E., Bannister, S., Burbidge, D., Denys, P., Gentle, P., Howarth, J., Mueller, C., Palmer, N., Pearson, C., Power, W., Barnes, P., Barrell, D.J.A., Van Dissen, R., Langridge, R., Little, T., Nicol, A., Pettinga, J., Rowland, J., Stirling, M., 2017. Complex multifault rupture during the 2016 Mw 7.8 Kaikōura earthquake, New Zealand. Science (1979) 356. https://doi.org/10.1126/science.aam7194

Hanks, T. C. and Kanamori, H., 1979. A Moment Magnitude Scale. Journal of Geophysical Research, 84 (B5), 2348– 2350, doi:10.1029/JB084iB05p02348.

Harris, R.A., 2017. Large earthquakes and creeping faults. Reviews of Geophysics 55, 169–198. https://doi.org/10.1002/2016RG000539

Hayes, G. P., Bergman, E., Johnson, K. L., Benz, H. M., Brown, L., & Meltzer, A. S., 2013. Seismotectonic framework of the 2010 February 27 MW 8.8 Maule, Chile earthquake sequence. Geophysical Journal International, 195(2), 1034–1051. doi:10.1093/gji/ggt238

Heaton, T.J., Köhler, P., Butzin, M., Bard, E., Reimer, R.W., Austin, W.E.N., Bronk Ramsey, C., Grootes, P.M., Hughen, K.A., Kromer, B., Reimer, P.J., Adkins, J., Burke, A., Cook, M.S., Olsen, J., Skinner, L.C., 2020. Marine20—The Marine Radiocarbon Age Calibration Curve (0–55,000 cal BP). Radiocarbon 62, 779–820. https://doi.org/10.1017/RDC.2020.68

Heimann, S., Kriegerowski, M., Isken, M., Cesca, S., Daut, S. Grigoli, F., Juretzek, C., Megies, T., Nooshiri, N., Steinberg, A., Sudhaus, H., Vasyura-Bathke, H., Willey, T., Dahm, T., 2017. Pyrocko – An open-source seismology toolbox and library.

Hensen, C., Scholz, F., Nuzzo, M., Valadares, V., Gràcia, E., Terrinha, P., Liebetrau, V., Kaul, N., Silva, S., Martínez-Loriente, S., Bartolome, R., Piñero, E., Magalhães, V.H., Schmidt, M., Weise, S.M., Cunha, M., Hilario, A., Perea, H., Rovelli, L., Lackschewitz, K., 2015. Strike-slip faults mediate the rise of crustal-derived fluids and mud volcanism in the deep sea. Geology 43, 339–342. https://doi.org/10.1130/G36359.1

Hollingsworth, J., Fattahi, M., Walker, R., Talebian, M., Bahroudi, A., Bolourchi, M.J., Jackson, J., Copley, A., 2010a. Oroclinal bending, distributed thrust and strike-slip faulting, and the accommodation of Arabia-Eurasia convergence in NE Iran since the Oligocene. Geophys J Int. https://doi.org/10.1111/j.1365-246X.2010.04591.x

Hollingsworth, J., Jackson, J., Walker, R., Nazari, H., 2008. Extrusion tectonics and subduction in the easter South Caspian region since 10 Ma. Geology. https://doi.org/10.1130/G25008A.1
Hollingsworth, J., Jackson, J., Walker, R., Reza Gheitanchi, M., Javad Bolourchi, M., 2006. Strike-slip faulting, rotation, and along-strike elongation in the Kopeh Dagh mountains, NE Iran. Geophys J Int. https://doi.org/10.1111/j.1365-246X.2006.02983.x

Hollingsworth, J., Nazari, H., Ritz, J.F., Salamati, R., Talebian, M., Bahroudi, A., Walker, R.T., Rizza, M., Jackson, J., 2010b. Active tectonics of the east Alborz mountains, NE Iran: Rupture of the left-lateral Astaneh fault system during the great 856 A.D. Qumis earthquake. J Geophys Res Solid Earth. https://doi.org/10.1029/2009JB007185

Hollingsworth, J., Jackson, J., Walker, R., Reza Gheitanchi, M. and Javad Bolourchi, M., 2006. Strike-slip faulting, rotation, and along-strike elongation in the Kopeh Dagh mountains, NE Iran. Geophysical Journal International, 166(3), pp.1161-1177.

International Seismological Centre, 2022. On-line Bulletin, https://doi.org/10.31905/D808B830

Jackson, J., McKenzie, D., 1984. Active tectonics of the Alpine--Himalayan Belt between western Turkey and Pakistan. Geophys J Int 77, 185–264. https://doi.org/10.1111/j.1365-246X.1984.tb01931.x

Jackson, J., McKenzie, D., Priestley, K., 2021. Relations between earthquake distributions, geological history, tectonics and rheology on the continents. Philosophical Transactions of the Royal Society A: Mathematical, Physical and Engineering Sciences 379, 20190412. https://doi.org/10.1098/rsta.2019.0412

Jackson, J., Priestley, K., Allen, M., Berberian, M., 2002. Active tectonics of the South Caspian basin. Geophys J Int. https://doi.org/10.1046/j.1365-246X.2002.01588.x

Jordan, T. H. & Sverdrup, K. A., 1981. Teleseismic location techniques and their application to earthquake clusters in the South-Central Pacific. Bulletin of the Seismological Society of America. 71 (4): 1105–1130. doi: https://doi.org/10.1785/BSSA0710041105

Kadirov, F., Floyd, M., Alizadeh, A., Guliev, I., Reilinger, R., Kuleli, S., King, R., Nafi Toksoz, M., 2012. Kinematics of the eastern Caucasus near Baku, Azerbaijan. Natural Hazards 63, 997–1006. https://doi.org/10.1007/s11069-012-0199-0

Kakroodi, A.A., Kroonenberg, S.B., Hoogendoorn, R.M., Mohammd Khani, H., Yamani, M., Ghassemi, M.R., Lahijani, H.A.K., 2012. Rapid Holocene sea-level changes along the Iranian Caspian coast. Quaternary International 263, 93–103. https://doi.org/10.1016/j.quaint.2011.12.021

Karasözen, E., Nissen, E., Bergman, E. A., & Ghods, A., 2019. Seismotectonics of the Zagros (Iran) from orogen-wide, calibrated earthquake relocations. Journal of Geophysical Research: Solid Earth, 124(8), 9109–9129. doi:10.1029/2019jb017336

Karimi, A., Frechen, M., Khademi, H., Kehl, M., Jalalian, A., 2011. Chronostratigraphy of loess deposits in northeast Iran. Quaternary International 234, 124–132. https://doi.org/10.1016/j.quaint.2009.08.002

Karney, C.F.F., 2019. GeographicLib (Version 1.51) [WWW Document]. https://geographiclib.sourceforge.io/1.51.

Kehl, M., 2009. Quaternary climate change in Iran – the state of knowledge. Erdkunde 63, 1–17. https://doi.org/10.3112/erdkunde.2009.01.01

Kehl, M., Vlaminck, S., Köhler, T., Laag, C., Rolf, C., Tsukamoto, S., Frechen, M., Sumita, M., Schmincke, H.-U., Khormali, F., 2021. Pleistocene dynamics of dust accumulation and soil formation in the southern Caspian Lowlands - New insights from the loess-paleosol sequence at Neka-Abelou, northern Iran. Quat Sci Rev 253, 106774. https://doi.org/10.1016/j.quascirev.2020.106774

Kennett, B. L. N., Engdahl, E. R., Buland, R, 1995.. Constraints on seismic velocities in the Earth from traveltimes, Geophysical Journal International, Volume 122, Issue 1, July 1995, Pages 108–124, https://doi.org/10.1111/j.1365-246X.1995.tb03540.x

Khorrami, F., Vernant, P., Masson, F., Nilfouroushan, F., Mousavi, Z., Nankali, H., Saadat, S.A., Walpersdorf, A., Hosseini, S., Tavakoli, P., Aghamohammadi, A., Alijanzade, M., 2019. An up-to-date crustal deformation map of Iran using integrated campaign-mode and permanent GPS velocities. Geophys J Int 217, 832–843. https://doi.org/10.1093/gji/ggz045

Kolibacv, V . A. 1962. O smcshcnii geodezicheskikh punktov v rayonc Ashkhabadskovo zcm lctryascnya 1948 g. Geode zia i Kartografia 5, Geodezizdat.

Krijgsman, W., Tesakov, A., Yanina, T., Lazarev, S., Danukalova, G., Van Baak, C.G.C., Agustí, J., Alçiçek, M.C., Aliyeva, E., Bista, D., Bruch, A., Büyükmeriç, Y., Bukhsianidze, M., Flecker, R., Frolov, P., Hoyle, T.M., Jorissen, E.L., Kirscher, U., Koriche, S.A., Kroonenberg, S.B., Lordkipanidze, D., Oms, O., Rausch, L., Singarayer, J., Stoica, M., van de Velde, S., Titov, V.V., Wesselingh, F.P., 2019. Quaternary time scales for the Pontocaspian domain: Interbasinal connectivity and faunal evolution. Earth Sci Rev 188, 1–40. https://doi.org/10.1016/j.earscirev.2018.10.013

Kroonenberg, S.B., Abdurakhmanov, G.M., Badyukova, E.N., van der Borg, K., Kalashnikov, A., Kasimov, N.S., Rychagov, G.I., Svitoch, A.A., Vonhof, H.B., Wesselingh, F.P., 2007. Solar-forced 2600 BP and Little Ice Age highstands of the Caspian Sea. Quaternary International 173–174, 137–143. https://doi.org/10.1016/j.quaint.2007.03.010

Kroonenberg, S.B., Rusakov, G.V., Svitoch, A.A., 1997. The wandering of the Volga delta: a response to rapid Caspian sea-level change. Sediment Geol 107, 189–209. https://doi.org/10.1016/S0037-0738(96)00028-0

Kulikova, G. and Krüger, F., 2015. Source process of the 1911 M 8.0 Chon-Kemin earthquake: Investigation results by analogue seismic records. Geophysical Journal International, 201(3), pp.1891-1911.

Kulikova, G. and Krüger, F., 2017. Historical seismogram reproductions for the source parameters determination of the 1902, Atushi (Kashgar) earthquake. Journal of Seismology, 21(6), pp.1577-1597.

Kulikova, G., Schurr, B., Krüger, F., Brzoska, E. and Heimann, S., 2016. Source parameters of the Sarez-Pamir earthquake of 1911 February 18. Geophysical Journal International, 205(2), pp.1086-1098.

Kulikova, G. and Krüger, F., 2017. Historical seismogram reproductions for the source parameters determination of the 1902, Atushi (Kashgar) earthquake. Journal od Seismology, 21(6):1577-1597.

Kurtz, R., Klinger, Y., Ferry, M., Ritz, J.-F., 2018. Horizontal surface-slip distribution through several seismic cycles: The Eastern Bogd fault, Gobi-Altai, Mongolia. Tectonophysics 734–735, 167–182. https://doi.org/10.1016/j.tecto.2018.03.011

Kurushin, R.A., Bayasgalan, A., Ölziybat, M., Enhtuvshin, B., Molnar, P., Ch. Bayarsayhan, Kenneth W. Hudnut, Jian Lin, 1998. The Surface Rupture of the 1957 Gobi-Altay, Mongolia, Earthquake. GSA Special Papers, v. 320, DOI: https://doi.org/10.1130/0-8137-2320-5.1

Kuzucuoğlu, C., Leroy, S., 2023. Geographic and geomorphologic context of Caspian Sea level fluctuations over the Late Pleistocene and Holocene. Quaternaire 71–92. https://doi.org/10.4000/quaternaire.17991

Laske, G., Masters, G., Ma, Z., & Pasyanos, M., 2013. Update on crust1.0—A 1-degree global model of Earth's crust. Abstract EGU2013-2658 presented at 2013 Geophys. Res. Abstracts 15.

Leroy, S.A.G., Lahijani, H.A.K., Crétaux, J.-F., Aladin, N. V., Plotnikov, I.S., 2020. Past and Current Changes in the Largest Lake of the World: The Caspian Sea, in: Large Asian Lakes in a Changing World. pp. 65–107. https://doi.org/10.1007/978-3-030-42254-7_3

Liapin A., 2006. The excavations of A. A. Marushchenko at Ak-Tepe. Problems of history, philology, Culture 16, no. 1, 267–292.

Lisiecki, L.E., Raymo, M.E., 2005. A Pliocene-Pleistocene stack of 57 globally distributed benthic δ18O records. Paleoceanography 20, n/a-n/a. https://doi.org/10.1029/2004PA001071

Mackey, K. G., & Bergman, E., 2014. Ground-truth locations for the mangyshlak peaceful nuclear explosion sequence, western Kazakhstan. Bulletin of the Seismological Society of America, 104(4), 2116–2119. doi:10.1785/0120130330

Mangino, S., Priestley, K., 1998. The crustal structure of the southern Caspian region. Geophys J Int 133, 630–648. https://doi.org/10.1046/j.1365-246X.1998.00520.x

Mazzini, A., Etiope, G., 2017. Mud volcanism: An updated review. Earth Sci Rev 168, 81–112. https://doi.org/10.1016/j.earscirev.2017.03.001

Mazzini, A., Nermoen, A., Krotkiewski, M., Podladchikov, Y., Planke, S., Svensen, H., 2009. Strike-slip faulting as a trigger mechanism for overpressure release through piercement structures. Implications for the Lusi mud volcano, Indonesia. Mar Pet Geol 26, 1751–1765. https://doi.org/10.1016/J.MARPETGEO.2009.03.001

Masson, M.E., 1949. 'Gorodishcha Nisy v Selenii Bagir i Ikh Izuchenie'. In Trudy IUTAKE 1, edited by M.E. Masson, 16–115. Ashgabat: Izdatel'stvo Turkmenskogo Filiala Akademii Nauk SSSR.

McCaplin, J.P., 2009. Paleoseismology, 2nd ed. Academic Press, London-Amsterdam.

McCormack, J., Bontognali, T.R.R., Immenhauser, A., Kwiecien, O., 2018. Controls on Cyclic Formation of Quaternary Early Diagenetic Dolomite. Geophys Res Lett 45, 3625–3634. https://doi.org/10.1002/2018GL077344

McGill, S., Sieh, K., 1993. Holocene slip rate of the Central Garlock Fault in southeastern Searles Valley, California. J Geophys Res Solid Earth 98, 14217–14231. https://doi.org/10.1029/93JB00442

McKenzie, D., 1972. Active Tectonics of the Mediterranean Region, Geophysical Journal International, Volume 30, Issue 2, December 1972, Pages 109-185, https://doi.org/10.1111/j.1365-246X.1972.tb02351.x

Molnar, P., Tapponnier, P., 1978. Active tectonics of Tibet. J Geophys Res 83, 5361. https://doi.org/10.1029/JB083iB11p05361

Mousavi, Z., Walpersdorf, A., Walker, R.T., Tavakoli, F., Pathier, E., Nankali, H.R.E.A., Nilfouroushan, F. and Djamour , Y., 2013. Global Positioning System constraints on the active tectonics of NE Iran and the South Caspian region. Earth and Planetary Science Letters, 377, pp.287-298.

al-Muqaddasī., 2001. The Best Divisions for Knowledge of the Regions: Aḥsan al-Taqāsīm Fī Maʿrifat al-Aqālīm. Translated by Basil Collins. Reading: Garnet.

Nadirov, R.S., Bagirov, E., Tagiyev, M., Lerche, I., 1997. Flexural plate subsidence, sedimentation rates, and structural development of the super-deep South Caspian Basin. Mar Pet Geol 14, 383–400. https://doi.org/10.1016/S0264-8172(96)00054-2

Nicol, A. & Nathan, S., 2001. Folding and the formation of bedding-parallel faults on the western limb of Grey Valley Syncline near Blackball, New Zealand, New Zealand Journal of Geology and Geophysics, 44:1, 127-135, DOI: 10.1080/00288306.2001.9514929

Nikonov, A.A., 1998. Aşgabat Earthquake: Half a Century Later. Bulletin of the Russian 1068 Academy of Sciences 68, 789–797.

Okal, E.A., 2015. Historical seismograms: Preserving an endangered species. GeoResJ, 6, pp.53-64.

Ollivier, V., Fontugne, M., Lyonnet, B., Chataigner, C., 2016. Base level changes, river avulsions and Holocene human settlement dynamics in the Caspian Sea area (middle Kura valley, South Caucasus). Quaternary International 395, 79–94. https://doi.org/10.1016/j.quaint.2015.03.017

Onderdonk, N., Mazzini, A., Shafer, L., Svensen, H., 2011. Controls on the geomorphic expression and evolution of gryphons, pools, and caldera features at hydrothermal seeps in the Salton Sea Geothermal Field, southern California. Geomorphology 130, 327–342. https://doi.org/10.1016/J.GEOMORPH.2011.04.014

Ou, Q., Kulikova, G., Yu, J., Elliott, A., Parsons, B. and Walker, R., 2020. Magnitude of the 1920 Haiyuan earthquake reestimated using seismological and geomorphological methods. Journal of Geophysical Research: Solid Earth, 125(8), p.e2019JB019244.

Pánek, T., Korup, O., Minár, J., Hradecký, J., 2016. Giant landslides and highstands of the Caspian Sea. Geology 44, 939–942. https://doi.org/10.1130/G38259.1

Petersen MD, Moschetti MP, Powers PM, et al. The 2014 United States National Seismic Hazard Model. Earthquake Spectra. 2015;31 S1-S30. doi:10.1193/120814EQS210M

Pho, H-T. & Behe, L., 1972. Extended distances and angles of incidence of P waves. Bulletin of the Seismological Society of America, 62 (4): 885–902. doi: https://doi.org/10.1785/BSSA0620040885

Pierce, I., Koehler, R., 2023. 3D Paleoseismology from iOS Lidar and Structure from Motion Photogrammetry: a case study on the Dog Valley fault, California. Seismica 2. https://doi.org/10.26443/seismica.v2i1.208

Pierce, I. K. D. (2022). Spatiotemporal clustering of paleoseismicity in the Walker Lane, USA: An extensional supercycle? Geophysical Research Letters, 49, e2022GL099078

Piip, V.B., Rodnikov, A.G., Buvaev, N.A., 2012. The deep structure of the lithosphere along the Caucasus-South Caspian Basin-Apsheron Threshold-Middle-Caspian Basin-Turan plate seismic profile. Moscow University Geology Bulletin 67, 125–132. https://doi.org/10.3103/S0145875212020068

Pilipko V. N., 2007. Some results of the archaeological investigations at Old Nisa, Rossiyskaya Arkheologiya 1, 150–158.

Pilipko, V. N., 2010. Stratigrafiia i Topografiia Gorodishcha Novaia Nisa. In Drevnie Tsivilizatsii Na Srednem Vostoke. Arkheologiia, Istoriia, Kul'tura, edited by S.B. Bolelov. Moscow: Gosudarstvennyĭ muzeĭ Vostoka.

Pugh, D. J., White, R. S. and Christie, P. A. F., 2016. A Bayesian method for microseismic source inversion. Geophysical Journal International, 206(2), 1009-1038.

Pugh, D. J. and White, R. S., 2018. MTfit: A Bayesian Approach to Moment Tensor Inversion, Seismological Research Letters, 89, 1507–1513.

QGIS Development Team, 2021. QGIS Geographic Information System. Open Source Geospatial Foundation Project. https://qgis.org.

Reilinger, R., McClusky, S., Vernant, P., Lawrence, S., Ergintav, S., Cakmak, R., Ozener, H., Kadirov, F., Guliev, I., Stepanyan, R., Nadariya, M., Hahubia, G., Mahmoud, S., Sakr, K., ArRajehi, A., Paradissis, D., Al-Aydrus, A., Prilepin, M., Guseva, T., Evren, E., Dmitrotsa, A., Filikov, S. V., Gomez, F., Al-Ghazzi, R., Karam, G., 2006. GPS constraints on continental deformation in the Africa-Arabia-Eurasia continental collision zone and implications for the dynamics of plate interactions. J Geophys Res Solid Earth 111, n/a-n/a. https://doi.org/10.1029/2005JB004051

Reimer PJ, Reimer RW, 2001. A marine reservoir correction database and on-line interface. Radiocarbon 43:461-3.

Reitman, N.G., Klinger, Y., Briggs, R.W., Gold, R.D., 2023. Climatic influence on the expression of strike-slip faulting. Geology 51, 18–22. https://doi.org/10.1130/G50393.1

Rhodes, E.J., 2015. Dating sediments using potassium feldspar single-grain IRSL: Initial methodological considerations. Quaternary International 362, 14–22. https://doi.org/10.1016/j.quaint.2014.12.012

Rezanov, I. A., 1957. The Ashkhabad Earthquake of 1948 and its geological background, Academy of Science USSR.

Rizza, M., Mahan, S., Ritz, J.-F., Nazari, H., Hollingsworth, J., Salamati, R., 2011. Using luminescence dating of coarse matrix material to estimate the slip rate of the Astaneh fault, Iran. Quat Geochronol 6, 390–406. https://doi.org/10.1016/j.quageo.2011.03.001

Robert, A.M.M., Letouzey, J., Kavoosi, M.A., Sherkati, S., Müller, C., Vergés, J., Aghababaei, A., 2014. Structural evolution of the Kopeh Dagh fold-and-thrust belt (NE Iran) and

interactions with the South Caspian Sea Basin and Amu Darya Basin. Mar Pet Geol 57, 68–87. https://doi.org/10.1016/J.MARPETGEO.2014.05.002

Rogozhin, E.A., 1995. Tectonic position and geologic manifestations of the Ashkhabad 1948 earthquake. Izvestiya Physics of the Solid Earth, 30(9), pp.747-758.

Rogozhin, E.A., 2012. Ocherki regional'noi seismotektoniki (Overviews of Regional Seismotectonics), Moscow: Inst. Fiz. Zemli Ross. Akad. Nauk. ISBN 978-5-91682-017-1

Rustanovich, D. N., 1967. Seismicity of the Turkmen Territory and 1948 Ashkhabad Earthquake, Voprosy Inzhenernoy Seysmologiyi, vol. 12, 95 pp., Nauka, Moscow.

Rustanovich, D. N., and Shirokova, E. I., 1964. Some results of a study of the Ashkhabad earthquake of 1948, Izv. Akad. Nauk S.S.S.R. (ser. Geofiz.) 12, 1077-1080. (Transl. by Am. Geoph. Union).

Schweitzer, J., 2001. HYPOSAT – An Enhanced Routine to Locate Seismic Events. Pure and Applied Geophysics, 158 (1). 277-289 doi:10.1007/pl00001160

Shabanian, E., Siame, L., Bellier, O., Benedetti, L., Abbassi, M.R., 2009. Quaternary slip rates along the northeastern boundary of the Arabia-Eurasia collision zone (Kopeh Dagh Mountains, Northeast Iran). Geophys J Int. https://doi.org/10.1111/j.1365-246X.2009.04183.x

Sharifi, A., Pourmand, A., Canuel, E.A., Ferer-Tyler, E., Peterson, L.C., Aichner, B., Feakins, S.J., Daryaee, T., Djamali, M., Beni, A.N., Lahijani, H.A.K., Swart, P.K., 2015. Abrupt climate variability since the last deglaciation based on a high-resolution, multi-proxy peat record from NW Iran: The hand that rocked the Cradle of Civilization? Quat Sci Rev 123, 215–230. https://doi.org/10.1016/j.quascirev.2015.07.006

Shebalin, N. V., 1974. Foci of large earthquakes at the USSR territory, 53 pp., Nauka, Moscow.

Shebalin, N.V. and Tatevossin, R.E., 1996. Catalogue of strong earthquakes (M≥6.0) for the Global Seismic Hazard Assessment Program test area 'CAUCASUS.' Historical and Prehistorical Earthquakes in the Caucasus.

Shirokova, E. I., 1967. General Features in the orientation of principal stresses in earthquake foci in the Mediterranean-Asia seismic belt, USSR Academy of Sciences, Institute of Physics of the Earth, 12-22

Shoaee, M.J., Breeze, P.S., Drake, N.A., Hashemi, S.M., Vahdati Nasab, H., Breitenbach, S.F.M., Stevens, T., Boivin, N., Petraglia, M.D., 2023. Defining paleoclimatic routes and opportunities for hominin dispersals across Iran. PLoS One 18, e0281872. https://doi.org/10.1371/journal.pone.0281872

Sidorin, A.Ya., 2019. Effects and Lessons of the 1948 Ashgabat Earthquake. Seismic Instruments 55, 271–282. https://doi.org/10.3103/S0747923919030113

M.F. Sohn, S.A. Mahan, J.R. Knott, D.D. Bowman, 2007. Luminescence ages for alluvial-fan deposits in Southern Death Valley: Implications for climate-driven sedimentation along a tectonically active mountain front. Quaternary International, 166, 49-60. https://doi.org/10.1016/j.quaint.2007.01.002

Sukacheva, M. P., and Kazanli, D. N., 1949. Report on the Geologic Studies of the October 6th 1948 Ashkhabad Earthquake, 123 pp., Ashkhabad.

Svitoch, A.A., 2013. The Pleistocene Manych straits: Their structure, evolution and role in the Ponto-Caspian basin development. Quaternary International 302, 101–109. https://doi.org/10.1016/j.quaint.2012.03.015

Tchalenko, J.S., Skempton, A.W., 1975. Seismicity and structure of the Kopet Dagh (Iran, U. S. S. R.). Philosophical Transactions of the Royal Society of London. Series A, Mathematical and Physical Sciences 278, 1–28. https://doi.org/10.1098/rsta.1975.0019

Tchalenko, J.S. and Ambraseys, N., 1970. Structural analysis of the Dasht-e Bayaz (Iran) earthquake fractures. Geological Society of America Bulletin 81, 41 - 60.

Trifonov, V.G., Vostrikov, G.A., Lykov, V.I., Orazsakhatov, Kh., Skobelev, S.F., 1986. TECTONIC ASPECTS OF THE 1983 KUM-DAG EARTHQUAKE, WEST TURKMENIA. Int Geol Rev 28, 377–389. https://doi.org/10.1080/00206818609466278

Tsai, C. -H., Abdrakhmatov, K., Mukambayev, A., Elliott, A.J., Elliott, J.R., Grützner, C., Rhodes, E.J., Ivester, A.H., Walker, R.T., Wilkinson, R., 2022. Probing the Upper End of Intracontinental Earthquake Magnitude: A Prehistoric Example From the Dzhungarian and Lepsy Faults of Kazakhstan. Tectonics 41. https://doi.org/10.1029/2022TC007300

Tudryn, A., Gibert-Brunet, E., Tucholka, P., Antipov, M.P., Leroy, S.A.G., 2022. Chronology of the Late Pleistocene Caspian Sea hydrologic changes: A review of dates and proposed climate-induced driving mechanisms. Quat Sci Rev 293, 107672. https://doi.org/10.1016/j.quascirev.2022.107672

Ventra, D, Clarke, L.E., 2018. Geology and geomorphology of alluvial and fluvial fans: current progress and research perspectives. Geological Society, London, Special Publications, 440, 1 – 21. https://doi.org/10.1144/SP440.16

Viaz'mitina, M.I. 1951. 'Arkheologicheskoe Izuchenie Gorodishcha Novaia Nisa v 1947 Godu'. In Trudy IUTAKE 2, edited by Mikhail Evegen'ievich Masson, 147–69. Ashgabat: Izdatel'stvo Turkmenskogo Filiala AN SSSR.

Vlaminck, S., Kehl, M., Lauer, T., Shahriari, A., Sharifi, J., Eckmeier, E., Lehndorff, E., Khormali, F., Frechen, M., 2016. Loess-soil sequence at Toshan (Northern Iran): Insights into late Pleistocene climate change. Quaternary International 399, 122–135. https://doi.org/10.1016/j.quaint.2015.04.028

Vlaminck, S., Kehl, M., Rolf, C., Franz, S.O., Lauer, T., Lehndorff, E., Frechen, M., Khormali, F., 2018. Late Pleistocene dust dynamics and pedogenesis in Southern Eurasia – Detailed insights from the loess profile Toshan (NE Iran). Quat Sci Rev 180, 75–95. https://doi.org/10.1016/j.quascirev.2017.11.010

Walker, R.T., Bezmenov, Y., Begenjev, G., Carolin, S., Dodds, N., Gruetzner, C., Jackson, J.A., Mirzin, R., Mousavi, Z., Rhodes, E.J., 2021. Slip-Rate on the Main Köpetdag (Kopeh Dagh) Strike-Slip Fault, Turkmenistan, and the Active Tectonics of the South Caspian. Tectonics 40, 1–27. https://doi.org/10.1029/2021TC006846

Walker, R.T., Fattahi, M., 2011. A framework of Holocene and Late Pleistocene environmental change in eastern Iran inferred from the dating of periods of alluvial fan abandonment, river terracing, and lake deposition. Quat Sci Rev 30, 1256–1271. https://doi.org/10.1016/j.quascirev.2011.03.004

Walker, R. T., Bergman, E. A., Szeliga, W., & Fielding, E. J., 2011. Insights into the 1968-1997 dasht-e-bayaz and Zirkuh earthquake sequences, eastern Iran, from calibrated relocations, Insar and high-resolution satellite imagery. Geophysical Journal International, 187(3), 1577–1603. doi:10.1111/j.1365-246x.2011.05213.x

Walters, R. J., Elliott, J. R., Li, Z., & Parsons, B., 2013. Rapid strain accumulation on the Ashkabad fault (Türkmenistan) from atmosphere-corrected InSAR. Journal of Geophysical Research: Solid Earth, 118(7), 3674–3690. https://doi.org/10.1002/jgrb.50236

Weber, J., Geirsson, H., La Femina, P., Robertson, R., Churches, C., Shaw, K., Latchman, J., Higgins, M., Miller, K., 2020. Fault Creep and Strain Partitioning in Trinidad-Tobago: Geodetic Measurements, Models, and Origin of Creep. Tectonics 39. https://doi.org/10.1029/2019TC005530

Wesnousky, S. Predicting the endpoints of earthquake ruptures. Nature 444, 358–360 (2006). https://doi.org/10.1038/nature05275

Wesnousky, S.G., 2008. Displacement and Geometrical Characteristics of Earthquake Surface Ruptures: Issues and Implications for Seismic-Hazard Analysis and the Process of Earthquake Rupture. Bulletin of the Seismological Society of America 98, 1609–1632. https://doi.org/10.1785/0120070111

Wimpenny, S., and Watson, S.C., 2020. gWFM: A Global Catalog of Moderate-Magnitude Earthquakes Studied Using Teleseismic Body Waves. Seismological Research Letters 2020;; 92 (1): 212–226. doi: https://doi.org/10.1785/0220200218

Yeck, W. L., Weingarten, M., Benz, H. M., McNamara, D. E., Bergman, E. A., Herrmann, R. B., … Earle, P. S., 2016. Far-field pressurization likely caused one of the largest injection induced earthquakes by reactivating a large pre-existing basement fault structure. Geophysical Research Letters, 43(19). doi:10.1002/2016gl070861

Zelenin, E., Bachmanov, D., Garipova, S., Trifonov, V., Kozhurin, A., 2022. The Active Faults of Eurasia Database (AFEAD): the ontology and design behind the continental-scale dataset. Earth Syst Sci Data 14, 4489–4503. https://doi.org/10.5194/essd-14-4489-2022

Zhang, H., Aldana-Jague, E., Clapuyt, F., Wilken, F., Vanacker, V., Van Oost, K., 2019. Evaluating the potential of post-processing kinematic (PPK) georeferencing for UAV-based structure- from-motion (SfM) photogrammetry and surface change detection. Earth Surface Dynamics 7, 807–827. https://doi.org/10.5194/esurf-7-807-2019

Zielke, O., Arrowsmith, J.R., Ludwig, L.G., Akçiz, S.O., 2010. Slip in the 1857 and Earlier Large Earthquakes Along the Carrizo Plain, San Andreas Fault. Science (1979) 327, 1119–1122. https://doi.org/10.1126/science.1182781

Zielke, O., Arrowsmith, R., 2012. LaDiCaoz and LiDARimager—MATLAB GUIs for LiDAR data handling and lateral displacement measurement. Geosphere 8, 206. https://doi.org/10.1130/GES00686.1